Modeling of Mode-Locking Regimes in Lasers

D I S S E R T A T I O N

zur Erlangung des akademischen Grades

doctor rerum naturalium
(Dr. rer. nat.)
im Fach Physik

eingereicht an der
Mathematisch-Naturwissenschaftlichen Fakultät
Humboldt-Universität zu Berlin

von
Magister der Physik Rostislav Arkhipov

Präsident der Humboldt-Universität zu Berlin:
Prof. Dr. Jan-Hendrik Olbertz

Dekan der Mathematisch-Naturwissenschaftlichen Fakultät:
Prof. Dr. Elmar Kulke

Gutachter:
1. PD Dr. Uwe Bandelow
2. Prof. Dr. Kurt Busch
3. Prof. Dr. Kathy Lüdge

eingereicht am: 23. September 2014
Tag der mündlichen Prüfung: 3. March 2015

Abstract

In this thesis current problems related to the generation of short optical pulses in mode-locked lasers are considered in a theoretical context. We use numerical and analytical methods to study these problems. Additionally, the problem of resonant medium radiation excited by ultrashort light pulse propagating at superluminal velocity is investigated.

In all existing mode-locked lasers discussed in the literature, the bandwidth of the laser pulses is limited by the bandwidth of the gain medium. In Chapter 2 of this thesis we investigate the possibility of passive mode-locking based on the coherent interaction of light with the amplifying and absorbing media in lasers with ring and linear cavities. We consider the realistic and practically interesting case when the absorbing and amplifying media are separated in the cavity space but not homogeneously mixed in the volume of the cavity, as was considered earlier in the literature. It was shown that other, not soliton scenarios of passive mode-locking exist, and that coherent mode-locking is self-starting (lasing without an injection seeding pulse is possible). We point to the fact that the spectral width of the laser generation can be significantly larger than the spectral bandwidth of the gain medium. This is only possible due to the coherent interaction between light and matter. Our theoretical consideration is based on the system of Maxwell-Bloch equations using the slowly varying envelope approximation.

Passively mode-locked semiconductor lasers are convenient and compact sources of short optical pulses with a high repetition rate. To reduce pulse timing jitter in these lasers, hybrid mode-locking technique is commonly used. In Chapter 3 hybrid mode-locking in a two-section edge-emitting semiconductor laser is studied using a set of three delay differential equations. In these equations the external modulation applied to the saturable-absorber section is modeled by the modulation of the carrier relaxation rate. An estimation of the locking range where the pulse repetition frequency is synchronized with the frequency of the external modulation is performed numerically and analytically. Our numerical simulations indicate that hybrid mode-locking can be also achieved in cases when the frequency of the external modulation is approximately twice or a half of that of the pulse repetition frequency of the free-running passively mode-locked laser. An asymptotic analysis of the dependence of the locking range width on the laser parameters is carried out in the limit of small-signal modulation. Numerical and analytical estimations of the locking range performed in the present work are in qualitative agreement with the experimental data obtained with passively mode-locked semiconductor quantum dot lasers.

Another technique for the stabilization of pulse repetition frequency of mode-locked semiconductor lasers is based on the injection of two coherent sidebands into a laser (dual-mode injection). In Chapter 4 we study the dynamics of a passively mode-locked semiconductor laser with dual frequency coherent optical injection using a delay differential equation model. Namely, we investigate the phenomenon of synchronization of pulse repetition rate to the difference of the two injected frequencies. The locking range is calculated numerically and estimated asymptotically in the limit of small injection field amplitude and zero linewidth enhancement factors. The dependence of the locking range on the model parameters is studied.

Pulse repetition frequency multiplication in mode-locked lasers is an important issue in optical communications. In Chapter 5 of this thesis using a delay differential

equation model with two time delays, we investigate the dynamics of a semiconductor laser with an active cavity coupled to an external passive cavity. Our numerical simulations indicate that when the coupling between the two cavities is strong enough and the round-trip time of the active cavity is an integer multiple of the round-trip time of the external passive cavity, a harmonic mode-locking regime can develop in the laser with a pulse repetition period close to the passive cavity round-trip time. We also demonstrate that the laser output field intensity is sensitive to the relative phase between the electric fields in the two cavities and exhibits a resonant behavior. The period and width of these resonances depends on the round-trip times of the two cavities and the coupling strength between them. The existence of optical bistability between different dynamical regimes was demonstrated numerically.

In Chapter 6 the optical response of a one-dimensional resonant medium made of dipoles with a periodically varying density excited by a spot of light moving along the medium at superluminal (subluminal) velocity is studied. We demonstrated that the Cherenkov radiation in such a system is rather unusual, possessing both a transient and resonant character. We show that, under certain conditions, another Doppler-like frequency appears in the radiation spectrum in addition to the resonant Cherenkov peak. Both linear (small-signal) and nonlinear regimes as well as different medium topologies are considered.

Zusammenfassung

In dieser Arbeit werden einige Probleme im Zusammenhang mit der Erzeugung ultrakurzer Pulse in modengekoppelten Lasern unter Verwendung analytischer und numerischer Methoden theoretisch untersucht. Weiterhin werden einige Resultate über die Strahlung resonanter Medien, welche durch einen ultrakurzen Überlichtgeschwindigkeits-Lichtpuls angeregt werden, dargestellt.

In allen konventionellen modengekoppelten Lasern, welche in der gängigen Literatur diskutiert werden, ist die Bandbreite des Pulses durch die Bandbreite des Verstärker-Mediums limitiert. Die Möglichkeit passiver Modenkopplung durch kohärente Wechselwirkung des Lichts mit einem absorbierenden und einem verstärkenden Lasermedium in linearen und ringförmigen Kavitäten wird in Kapitel 2 theoretisch untersucht. Insbesondere der interessante Fall, in welchem das absorbierende und das verstärkende Medium in der Kavität räumlich separiert (und nicht homogen vermischt) sind, wird untersucht. Es wird gezeigt, dass nicht-Soliton-artige Szenarien existieren und Lasertätigkeit ohne einen extern injizierten Puls möglich ist. Weiterhin kann gezeigt werden, dass die spektrale Breite des Lasers deutlich größer als die spektrale Breite des Verstärker-Mediums sein kann, abhängig von den Parametern des Verstärker- und Absorber-Mediums. Grundlage dieses Effekts ist die kohärente Wechselwirkung von Licht und Materie. Die theoretische Behandlung basiert auf der Untersuchung eines Systems von Maxwell-Bloch-Gleichungen unter Verwendung einer Näherung für langsam veränderliche Einhüllende.

Passiv modengekoppelte Halbleiterlaser sind zuverlässige und kompakte Quellen kurzer optischer Pulse mit hoher Wiederholungsrate. Allerdings zeigen solche Laser Timing-Jitter, wodurch Stabilisierungstechniken notwendig sind. Die hybride Modenkopplung ist gegenwärtig ein sehr aktives Forschungsgebiet. In Kapitel 3 wird die hybride Modenkopplung in einem kantenemittierenden Zwei-Sektions-Halbleiterlaser anhand eines Systems von drei gekoppelten Delay-Differentialgleichungen untersucht. In diesen Gleichungen wird das externe Signal, welches an die Absorber-Sektion gekoppelt wird, durch die Modulation der Ladungsträger-Relaxationsraten modelliert. Abschätzungen des Synchronizationbereichs, in welchem die Pulswiederholungsfrequenz mit der Frequenz der externen Modulation synchronisiert, werden anhand numerischer und analytischer Rechnungen gewonnen. Die numerischen Simulationen zeigen, dass hybride Modenkopplung sogar in Fällen erreicht werden kann, in denen die Frequenz der externen Modulation zweieinhalb mal so groß wie die Pulswiederholungsfrequenz des frei laufenden passiv modengekoppelten Lasers ist. Im Grenzfall kleiner Modulationssignale wird durch asymptotische Analysis die Abhängigkeit der Breite des Kopplungsregimes von den Laser-Parametern nachvollzogen. Die in dieser Arbeit dargestellten numerischen und analytischen Abschätzungen des Kopplungsbereichs sind in guter qualitativer Übereinstimmung mit experimentellen Beobachtungen in passiv modengekoppelten Quantenpunkt-Halbleiterlasern.

Eine weitere Methode zur Stabilisierung der Pulswiederholungsfrequenz modengekoppelter Halbleiterlaser basiert auf der Injektion zweier kohärenter Seitenbänder in den Laser. Die Dynamik passiv modengekoppelter Halbleiterlaser, welche durch zwei kohärente Frequenzen optisch gepumpt werden, wird in Kapitel 4 anhand eines Delay-Differentialgleichungsmodells untersucht. Die Kopplungsregime, in welchen der Laser mit den beiden injizierten Frequenzen synchronisiert, werden numerisch und analytisch berechnet. Durch asymptotische Analysis für den Grenzfall

schwacher Injektionsfeldamplituden lässt sich die Abhängigkeit der Synchronizationbereiche von den Modellparametern, wie z. Bsp. der optischen Bandbreite, der Absorber-Recovery-Zeit und den linearen Verlusten ermitteln.

Das Problem der Vervielfachung der Pulswiederholungsrate ist bedeutend für Anwendungen in der optischen Kommunikation. In Kapitel 5 dieser Arbeit wird die Dynamik eines Halbleiterlasers mit einer aktiven Kavität, welche an eine passive, externe Kavität gekoppelt ist, anhand eines Delay-Differentialgleichungsmodells mit 2 Zeitverzögerungen untersucht. Die numerischen Simulationen zeigen, dass sich ein harmonisches Modenkopplungsregime ausbilden kann, dessen Pulswiederholungszeit etwa der Umlaufzeit der passiven Kavität entspricht, falls eine ausreichend starke Kopplung der beiden Kavitäten vorliegt und falls die Umlaufzeit der aktiven Kavität ein ganzzahliges Vielfaches der Umlaufzeit der passiven Kavität ist. Weiterhin wird ein Resonanzphänomen diskutiert, demzufolge die Intensität des ausgekoppelten Laserfelds empfindlich von der Relation der Phasen der elektrischen Felder in den beiden Kavitäten abhängt. Die Periodendauer und Breite der Resonanzen hängt vom Verhältnis der Umlaufzeiten und der Kopplung der beiden Kavitäten ab. Die Existenz optisch bistabiler dynamischer Regime wird numerisch nachgewiesen.

Kapitel 6 dieser Arbeit beinhaltet eine theoretische Studie der optischen Antwort eines eindimensionalen resonanten Mediums, welches aus Dipolen mit periodisch veränderlicher Dichte aufgebaut ist, auf einen Lichtpuls, welcher sich mit Überlichtgeschwindigkeits durch das Medium bewegt. Die Cherenkov-Strahlung eines solchen Systems besitzt untypische Eigenschaften und zeigt sowohl transienten als auch resonanten Charakter. Unter bestimmten Bedingungen kann im Spektrum neben dem resonanten Cherenkov-Signal eine weitere Doppler-artige Frequenz auftreten. Hier werden sowohl das lineare (kleine Signale) als auch nichtlineare Regime, sowie verschiedene Topologien des Mediums betrachtet.

Dedicated to my parents...

Contents

1 Introduction

The current work is devoted to the theoretical study of mode-locked lasers. These lasers are used for generation of short optical pulses that find applications in different areas ranging from real-time monitoring of chemical reactions to high-bit-rate optical communications [1–26]. The main focus of this thesis lies on the analysis of fundamental and practical dynamical properties of the mode-locking techniques such as coherent mode-locking, hybrid mode-locking, dual mode optical injection, and mode selection in mode-locked lasers. These techniques can be used for the improvement of the mode-locked pulse characteristics and for the control of the pulse repetition frequency, in particular, frequency stabilization and multiplication. In the last chapter a new type of Cherenkov radiation from the resonant medium excited by an ultrashort light pulse propagating at superluminal velocity is discussed. This phenomenon opens the possibility of generation of new frequencies in resonant medium, which are contained in the radiation spectrum of a mode-locked laser.

The development of ultrashort laser pulse sources has been an area of scientific and technological interest in optics since the 1960s [1–26]. Such ultrashort laser pulse sources with stabilized high peak power and repetition rate have many practical applications in different areas of physics and chemistry, for example in real-time monitoring of ultrafast processes in matter, ultrahigh-bit-rate optical communications, high-capacity telecommunication systems, optical clocks, metrology, etc. [21–25]. The principles of operation for different types of ultrashort pulse lasers are described in many papers and monographs [1, 3–9, 12–26].

A well known method for generating high power short optical pulses is called Q-switching, see Refs. [1, 20, 21]. The technique is based on the incorporation of an optical switch into the laser cavity. This device can rapidly change the transmission of light. When the switch is off, the cavity Q-factor is very small and lasing is impossible. When the switch is on, the Q-factor is high and lasing becomes possible. The pump radiation produces a high population inversion in the active medium when the switch is off. After the maximum population inversion is achieved, the switch is rapidly opened, the cavity Q-factor increases and the energy stored in the active medium radiates as so-called giant pulse of light with a high peak power. A disadvantage of this method is that it does not allow for generation of pulses with sufficiently high repetition rates.

An alternative technique to obtain short optical pulses with high repetition rates is mode-locking. The basic idea here is as follows. Assume we have a laser with the spectrum of generation consisting of a set of longitudinal modes. The frequency separation between any two adjacent cavity modes is $\Delta\nu = \frac{1}{T}$, where T is the cavity round-trip time of light, see Fig. 1.1. Let N denote the total number of modes and ν_0 the carrier frequency. Consider the electric field of laser radiation at a fixed point of space. This

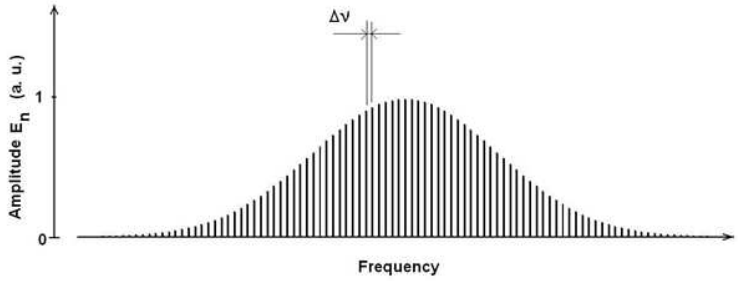

Figure 1.1: Spectrum of laser radiation. Laser radiation contains a set of longitudinal modes with the frequency separation between any two adjacent modes $\Delta\nu$.

field can be represented in the form:

$$E(t) = \sum_{n=-N/2}^{N/2} E_n(t) \cos[2\pi\nu_0 t + 2\pi(n-1)\Delta\nu t + \phi_n(t)]. \tag{1.1}$$

In general, the mode amplitudes $E_n(t)$ and phases $\phi_n(t)$ vary with time. Suppose for simplicity that mode amplitudes E_n and phases ϕ_n do not depend on time. If phases ϕ_n are random numbers the laser output should exhibit a random peak pattern, see Fig. 1.2a. On the contrary, when phases ϕ_n are equal to each other in (1.1) then the time dependence of laser radiation intensity has the form of a pulse train with the time period T, see Fig. 1.2b. In order to obtain the conditions under which the phase difference between laser modes is fixed, different mode-locking techniques are used. Well known mode-locking methods are: active mode-locking, passive mode-locking, coherent mode-locking, and hybrid mode-locking.

In active mode-locking the active element, an optical modulator (that can change amplitude or phase of light under external control) is introduced into a laser cavity, see Refs. [2, 17, 20, 21]. To achieve a mode-locking regime the frequency of modulation should be close to (or a multiple of) the intermode frequency interval $\Delta\nu$. Modulation at the frequency $\Delta\nu$ results in the parametric enhancement of the adjacent modes with the required phases, whose modulation enhances, in turn, the next adjacent modes, etc.

In order to achieve passive mode-locking, a nonlinear absorbing medium is placed into the laser cavity [4–9, 11–26]. The system behavior strongly depends on the ratio of two parameters: pulse duration τ_p and damping time T_2 of the polarization of the medium, where typically the relation $\tau_p > T_2$ holds. The case when this inequality is satisfied is referred to as an incoherent interaction of a light pulse with a medium. Polarization of the medium follows the optical field in a quasi-stationary manner and can be adiabatically eliminated from the model [10, 18]. The nonlinearity of the amplification/absorption in the case of incoherent interaction results from the change in the population differ-

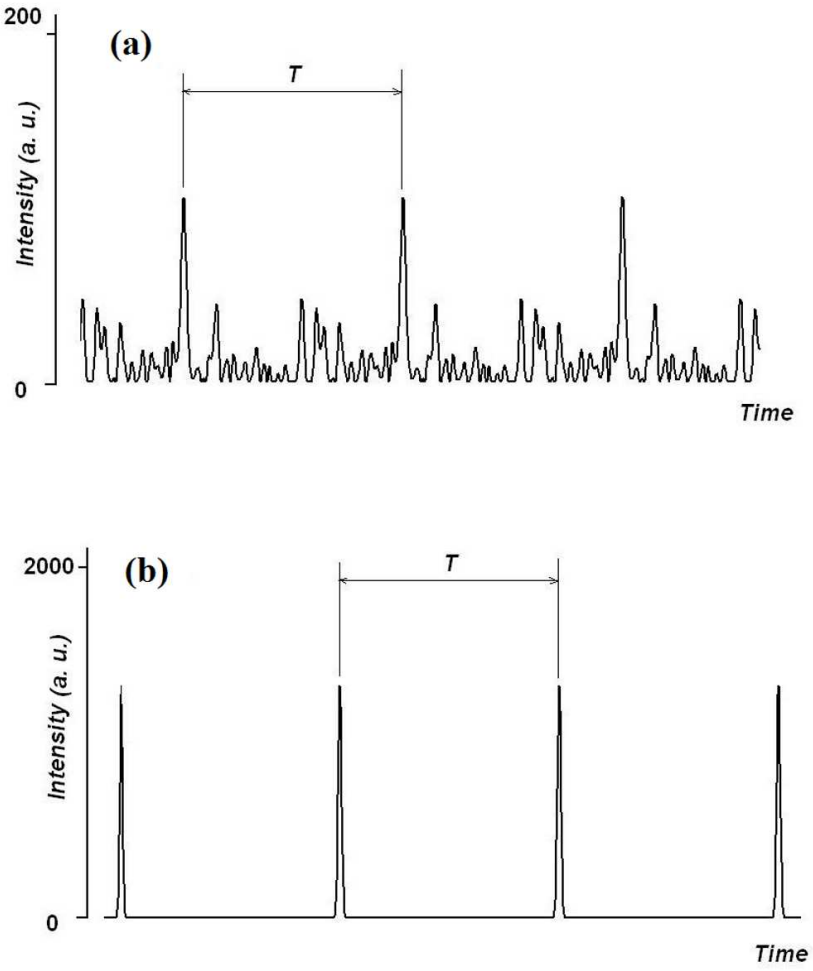

Figure 1.2: Time dependence of radiation intensity $|E(t)|^2$: (a): chaotic spikes in the case of random phases; (b): short optical pulses in the case of equal phases (mode-locking regime).

ence of the levels under the influence of the intense optical field. In particular, the absorber saturates when the electric field is strong. Therefore, the term saturable absorber is used in the literature. Physical mechanisms of passive mode-locking in lasers are well-understood in the incoherent case, see Refs. [12–26]. The saturable absorber is an element with a transmission depending on the laser radiation intensity propagating through it. The saturable absorber absorbs the low intensity portions of the light propagating through it and transmits the high intensity portions. In such a way the absorber acts as a nonlinear modulator of the losses in the cavity and periodic pulse trains can appear. This technique was successfully realized in different types of lasers: Ruby lasers [3], neodymium glass lasers [4], dye lasers [11], and semiconductor lasers [22–26]. The passive mode-locking technique allows to obtain optical pulses with the duration reduced to a few hundreds of femtoseconds in solid state lasers and semiconductor lasers [17–26]. The pulse duration of passively mode-locked (PML) lasers with a saturable absorber is limited by the inverse gain bandwidth of the active medium.

Another interesting type of interaction between a short light pulse and a resonant medium arises when pulse duration is shorter than polarization relaxation time, $\tau_p < T_2$. Such interaction is called coherent [10, 18, 27–29]. In this case the polarization of the medium does not follow the field in a quasistationary manner and depends on the field in the previous time moments. Moreover, the presence of a phase memory changes qualitatively the picture of the evolution of the pulse. For example, a soliton-like pulse propagation in the absorbing medium (2π pulse of self-induced transparency) and in the gain medium (π pulse) becomes possible under such conditions [10, 18, 27–29]. Recently this phenomenon was used to develop a theory of coherent passive mode-locking in Refs. [30–36]. This type of mode-locking is based on the coherent interaction between light with absorber and gain, which leads to the formation of 2π pulse of self-induced transparency in absorber and π pulse in the gain media. Contrary to the usual PML lasers, where the ultimate limit on the output pulse duration is set by the inverse bandwidth of the gain medium, coherently mode-locked lasers can generate optical pulses with a duration much shorter than the medium coherence time T_2, i.e. the spectral width of the lasing is larger than the bandwidth of the gain medium.

In Refs. [30–36] theoretical study of coherent mode-locking was performed for a laser with amplifier and absorber implemented within the same sample. This assumption was crucial for the observation of the soliton regimes. However, gain and absorber are typically separated in space. Discovery and characterization of the coherent mode-locking in this situation theoretically and experimentally is an open problem. Potentially, with the help of coherent mode-locking one can obtain ultrashort pulses with spectral bandwidth wider than the gain spectrum, and the inverse bandwidth of the gain medium will not be the ultimate limit of the output pulse duration anymore.

Passive mode-locking in semiconductor lasers has a number of important applications. PML semiconductor lasers are widely used for the generation of short optical pulses with high repetition rates ranging from a few GHz to hundreds of GHz [22–26]. Such lasers contain forward biased gain section and reverse biased saturable absorber section. Due to their compact size, low cost and reliability, they are prominent candidates for a number of different applications, in particular, in high-speed communication systems [22–

26]. PML quantum dot lasers are particularly good candidates for this purpose [24, 25]. The advantages of such lasers in comparison to quantum well devices are broadband high gain amplification, ultrafast carrier dynamics, and a very low threshold current for lasing [24, 25]. Moreover, further development of stabilized semiconductor light sources is a great demand for the use in a range of applications such as optical telecommunications, frequency metrology, optical sampling, and clock recovery [22–26]. Due to some technical factors, PML semiconductor lasers exhibit significant timing jitter which limits their performance in these applications. For stabilization of the pulse repetition frequency a hybrid mode-locking technique [26, 37–42] and coherent dual mode optical injection from an external laser [43–47] are used.

Hybrid mode-locking is a combination of active and passive mode-locking techniques [22–26]. In hybrid mode-locked semiconductor lasers, external voltage modulation is applied to the saturable absorber section. If the frequency of this modulation is close to the pulse repetition frequency of the laser, the latter frequency becomes locked to the external one. The interval of modulation frequencies, where this synchronization takes place, is usually referred to as the locking range. Locking range in semiconductor lasers strongly depends on the characteristics of the voltage modulation - modulation amplitude, modulation frequency, as well as parameters of the gain and absorber sections. Characterization of this dependence can be used to provide recommendations on locking range enlargement.

The disadvantage of hybrid mode-locking technique is that it does not influence the individual line's frequency noise [43–47]. For various optical communication systems, optical frequency combs with narrow optical linewidths are desirable. Therefore, another technique leading to stabilization of pulse repetition frequency and individual line's frequency noise reduction was used in [43–47]. This technique is based on the injection of two coherent spectral lines (dual-mode injection) into a PML laser [43–47]. When the frequency separation of two injected frequencies is close to the pulse repetition frequency of the free-running PML laser, the latter frequency is synchronized to this separation frequency. Locking range in this situation strongly depends on the relative positions of two injected frequencies with respect to the PML laser spectrum, frequency separation between two injected tones, and injected field power. Analysis of this dependence is important for the improvement of the characteristics of PML laser pulses, reduction frequency noise, and suppression of waveform instabilities.

The problem of pulse repetition frequency multiplication in semiconductor lasers is very important for the increase of data transmission rate in various optical communication systems [48–57]. In practice laser repetition rate is limited by the operational frequencies of the optical modulators [48] and by the fact that the active medium length must be sufficiently large to achieve laser generation. A mode selection technique to increase the pulse repetition frequency using an external Fabry-Perot filter was successfully realized in solid state femtosecond laser systems [53–57]. Application of mode selection technique in the PML semiconductor lasers has high potential in ultrahigh-bit-rate optical communication systems.

In 1930th P. A. Cherenkov and S. I. Vavilov discovered a radiation arising when electron moves in a pure liquid with the velocity larger than the phase velocity of light in the

liquid [58–64]. This radiation received the name of Cherenkov radiation. The Cherenkov radiation typically has a conical shape with the angle depending on the ratio of the electron velocity and the speed of light in the medium. Moving spot of light created by a rotating source on a distant screen [65–67], gradient of the refractive index or population inversion, and other medium characteristics depending on the radiation intensity can propagate at superluminal velocity [10, 68]. This in principle can lead to a number of effects similar to the Cherenkov radiation. Note, that superluminal motions are not prohibited if they are not associated with the signal (information) transfer [66, 67, 69–74]. Recent investigations demonstrated the appearance of conical emission similar to Cherenkov radiation when an ultrashort pulse from a mode-locked laser propagates in resonant atomic vapors [75–79]. Another example of superluminal propagation appears when a light pulse is incident obliquely on a thin layer containing resonant particles. In this case the intersection of the pulse and the layer (light spot) moves along the layer with the velocity $V = c/\sin\beta > c$, where β is the angle between the pulse wavevector and the vector normal to the layer [65–67]. Superluminal pulse propagation along a layer of resonant particles can lead to an excitation of Cherenkov radiation. In particular, the case when the resonant particles are distributed periodically along the layer is of particular interest and has not been systematically studied so far. Experimental realization of Cherenkov radiation in this case opens the possibility for the determination of a spatial structure of the scattering system from the spectrum of the scattered wave.

This thesis consist of five original chapters.

In Chapter 2 a theoretical study of coherent mode-locking in two-section lasers is presented. Qualitative consideration of the coherent passive mode-locking basing on the area theorem of McCall and Hahn facilitates the discovery of the stable limit cycles that correspond to mode-locking regime in the system. The diagram technique considered in Chapter 2 reveals the main features of coherent passive mode-locking such as the dependence of pulse duration on the ratio absorber/gain transition dipole moments and the possibility of existence of multiple pulses per cavity round-trip. Numerical simulations are performed for the lasers with ring and linear cavities with the help of Maxwell-Bloch equations under the slowly varying envelope approximation. Results of these simulations confirm the predictions based on the McCall and Hahn area theorem. All numerical simulations in Chapter 2 are performed for realistic parameter values typical for different types of lasers, in particular, for semiconductor lasers. This analysis is closely related to the recent progress in the investigation of coherent phenomena in semiconductor lasers [80–82], self-induced transparency in semiconductors [83, 84], and coherent pulse propagation in quantum cascade lasers (QCL) [85, 86]. Coherently mode-locked two-section lasers studied in Chapter 2 can be used to obtain ultrashort optical pulses with high repetition rate.

In Chapter 3 using a delay differential equation model (DDE) a detailed theoretical analysis of hybrid mode-locking in semiconductor lasers is performed. Existence of hybrid mode-locking regimes in the cases when the frequency of the external signal is close to the second-harmonic of the PML laser pulse repetition frequency and to half of the laser repetition rate is demonstrated for the first time. The recent experimental evidence of such half-frequency modulation hybrid mode-locking provided by TU Berlin

is discussed [87]. Moreover, an asymptotic analysis of model equations performed in Chapter 3 allows to estimate the locking range width at small modulation amplitudes. The analysis performed in Chapter 3 reveals the possible reasons of the asymmetry of the locking regions that was observed experimentally in mode-locked quantum dot lasers [42].

In Chapter 4 semiconductor mode-locked lasers with coherent dual mode optical injection are studied using a DDE model. Locking range is calculated numerically and estimated asymptotically for the cases when the frequency separation between the two injected tones is varied. Results of numerical simulations are in qualitative agreement with the recent experimental data obtained with mode-locked quantum dot lasers [88]. Using an asymptotic analysis the dependence of locking range width on the model parameters is studied.

In Chapter 5 a PML semiconductor laser coupled to an external passive cavity is studied theoretically using a DDE model with two time delays. The external cavity in this case is used as a filter which suppresses certain longitudinal modes of the PML laser. Increase of pulse repetition frequency by a factor of 2 and 3 when the external cavity length is 2 and 3 times smaller than the active cavity is demonstrated. Dependence of the characteristics of these harmonic mode-locking regimes on the model parameters and coupling coefficients between the two cavities is studied. Existence of optical bistability in the model equations is demonstrated numerically.

In Chapter 6 an interesting phenomenon that can be implemented experimentally with ultrashort pulse sources is studied. It can arise when radiation of a resonant medium is excited by an ultrashort light pulse propagating at superluminal velocity [65–67, 74]. Superluminal excitation of resonant medium occurs when a short plane-wave pulse crosses a flat screen. Appearance of a new type of Cherenkov radiation in the resonant medium excited by such a pulse is demonstrated. This radiation has unusual properties: it arises in a transient regime and possesses a narrowband spectrum with the central frequency at the resonance of the particles of which the medium is comprised. Moreover, it is demonstrated that if medium particles are distributed periodically, a second Doppler-like frequency appears in the spectrum of medium radiation. This additional frequency emerges in the linear regime, when the pump remains weak, and in the nonlinear regime, when the pump radiation is strong. Intensity of radiation at this additional frequency can be much larger than the intensity of radiation at the resonance frequency.

The thesis closes with the summary and concluding remarks.

This thesis was carried out in the Weierstrass Institute for Applied Analysis and Stochastics (WIAS) and funded by the EU Project ITN Prophet, Grant No. 264687. All simulations were performed at WIAS using FORTRAN codes developed by the author and A. Pimenov.

2 Theoretical analysis of coherent mode-locking in lasers

In the present chapter the theoretical background of mode-locked lasers is discussed along with a brief introduction of efforts to model their behavior. Furthermore, coherent passive mode-locking in two-section lasers with either ring or linear cavity is studied numerically.

2.1 Passive mode-locking in lasers, basic theoretical approaches

Investigations of mode-locking in lasers began as soon as the first lasers were developed in the 1960s [3–9]. As we mentioned in the introduction, discovering mode-locking led to a great success in the realization of extremely short laser pulses with high peak power. Below we consider the basic approaches that are used to describe theoretically passive mode-locking regimes in lasers.

The primary element allowing periodic pulse generation is the nonlinear absorber. A nonlinear absorber is a material where the absorption decreases with increase of the light intensity. Such materials as dyes, crystals or semiconductors with strong resonant absorption can be used for this purpose. The latter are most actively used nowadays, because of their significant advantages in comparison to dye absorbers and other solid state materials used before (see Refs. [22–25, 89]). As an example of the recent progress in this area, the discovery of so-called semiconductor saturable absorber mirror (SESAM) [89, 90] can be mentioned. In this device, semiconductor absorber material is integrated into the laser mirror which results in dependence of the mirror reflectivity on the light intensity. Such a technique allows for the creation of passively mode-locked solid state lasers generating light pulses with a duration from femtoseconds to nanoseconds [89, 90].

Passive mode-locked semiconductor lasers are actively studied today. In such lasers, quantum dot and quantum well materials can be used for both gain and absorbing sections, resulting in short optical pulses with a repetition rate in the range from few to hundreds GHz [22–26]. Due to their compact size and high repetition rate they are considered as promising candidates for optical communication systems.

Before the detailed discussion of theoretical approaches to passive mode-locking mechanism, an important remark is to be mentioned. Short pulse propagation occurring in a resonant medium strongly depends on the ratio between the two parameters: pulse duration τ_p and polarization relaxation time T_2. There are two general situations that can be imagined in this context, typically referred to as an incoherent interaction of a

light pulse with medium, and the coherent interaction [10, 18, 29]. In the former case the pulse duration is much larger than the polarization relaxation time, $\tau_p >> T_2$. Polarization of the medium "follows" the optical field in a quasi-stationary manner and can be adiabatically eliminated from the model equations describing interaction of the light with medium [10, 18]. During the pulse propagation, it reduces the population difference in the medium, thus making it saturated. Therefore, the term "saturable" is used in the literature to denote such absorber. Due to the lack of instantaneous nontrivial dynamics of the atomic polarization, such type of mode-locking will be called “incoherent” in the following, in contrast to “coherent” mode-locking considered below. The majority of the papers considering theoretically passive mode-locking are based on an incoherent approximation. We briefly overview this class of theories.

P. G. Kryukov and V. S. Letokhov explained mode-locking using so-called fluctuation mechanism [20, 21, 91, 92]. According to this model the laser radiation at the low-intensity linear stage contains a lot of chaotic ultrashort spikes. At the next, nonlinear, stage, when the intensity of radiation increases, the absorbing medium bleaches. This leads to a faster amplification of the spikes having the highest intensity, and, simultaneously, to their compression. Thus, a periodic sequence of mode-locked ultrashort pulses appears. This model was successfully applied to an explanation of mode-locking regimes in Ruby, Nd-glass and other lasers.

Analytical study of passive mode-locking was first performed by H. Haus, see Refs. [93, 94] and review [95]. His theory was developed for so-called fast and slow saturable absorbers and contains significant simplifications. In the case of fast saturable absorber (see Ref. [94]) its population difference relaxation time must be much smaller than the pulse duration. Another simplification is that the pulse shape does not change significantly per cavity round-trip and that the absorber saturation is relatively weak. In Ref. [93] an analytical study of passive mode-locking with so-called slow saturable absorber was performed. In this theory the pulse duration is assumed to be much smaller than the absorber recovery time. Besides, the approximation of a weak gain and absorption were assumed. In Ref. [96] New also developed an analytical theory of mode-locking. He demonstrated that combined action of the absorption and saturation in the amplifier can lead to a pulse compression. The results obtained by New were applied to explain the picosecond pulse generation in mode-locked dye lasers. Further development and analysis of the mode-locking models were performed in Refs. [97–99]. This analysis was based mainly on the numerical simulations.

The disadvantages of the Haus and New approaches were elucidated in Refs. [100–102]. In particular, the ability of the models of Haus and New to adequately describe real laser systems were questioned for many practical situations. For example, semiconductor mode-locked lasers have rather high gain and losses per cavity round-trip. To overcome this limitation, in Refs. [100–102] a delay differential equations (DDE) model was developed by A. G. Vladimirov with coauthors. This model is able to describe mode-locking in the parameter range typical for semiconductor lasers. The only essential assumption of this model was a ring-cavity geometry with unidirectional lasing. Nevertheless, the approximation of slow saturable absorber, typical for semiconductor lasers was utilized there. An analytical and numerical study of such a model is possible using bifurcation

analysis and asymptotic techniques. Furthermore, the DDE model and some its generalizations were successfully applied to study different dynamical regimes in passively mode-locked lasers [42, 87, 102–105]. We will apply the DDE model to the theoretical analysis of hybrid mode-locked, dual mode optically injected semiconductor lasers and coupled cavity semiconductor lasers in Chapters 3-5 of the thesis.

Let us consider a qualitative physical picture of the pulse evolution in a mode-locked laser [10, 17]. After the pulse passes through the absorber, its leading edge is strongly attenuated. On the other hand, the trailing edge propagates in the medium which is already saturated and thus experiences weaker absorption rate. As a result, the laser pulse shape becomes asymmetric, see Fig. 2.1a. Note that the pulse maximum is shifted backward during this process, meaning that it moves at a velocity smaller than the velocity of light in vacuum c.

In the amplifying medium the situation changes significantly. The pulse front propagates in a still unsaturated medium and thus is strongly amplified. The gain becomes saturated, and the trailing edge grows slower, as illustrated in Fig. 2.1b. As a result of nonlinear amplification, the pulse maximum is shifted forward. Therefore, the velocity of the pulse maximum is larger than the light velocity in vacuum c. This, of course, does not contradict the causality principle. The possibility of superluminal propagation of the pulse maxima in an amplifying medium was demonstrated experimentally and theoretically in Refs. [10, 106–109]. As a result of this process the resulting pulse is narrowed and achieves its stationary shape after many round-trips. This process is illustrated in Fig. 2.2.

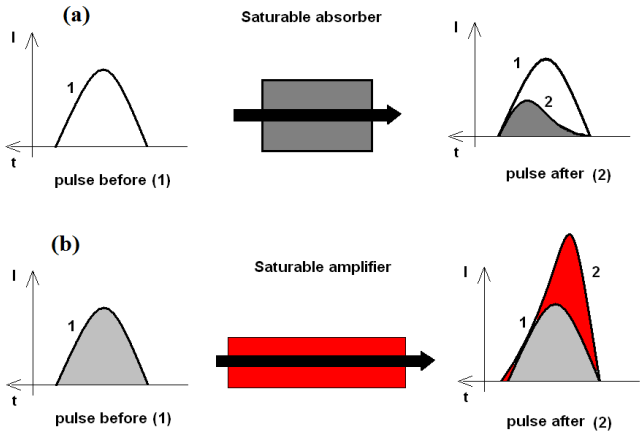

Figure 2.1: Illustration of the pulse shape evolution in a saturable absorber (a) or saturable amplifier (b) [10, 17].

In contrast to previous considerations, if the pulse duration is short enough, the dipole moment (medium polarization) induced in the nonlinear medium does not have time to decay during the interaction time. This happens if the pulse duration τ_p is much less than the polarization relaxation time, $\tau_p << T_2$, i.e. "coherent" interaction of light with

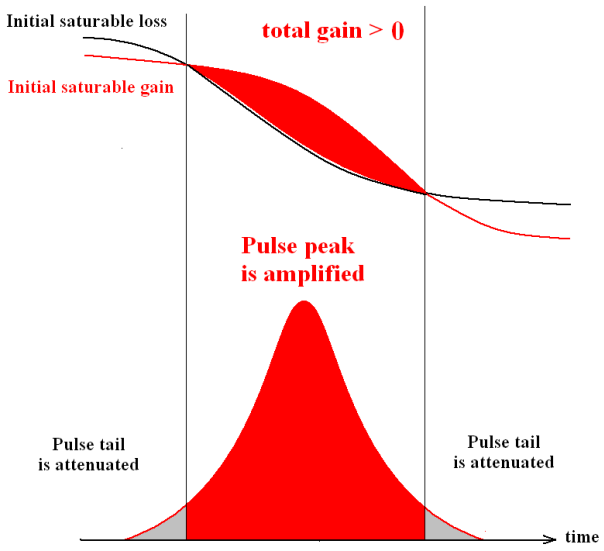

Figure 2.2: Pulse-shortening process by simultaneous action of the absorber and amplifier [17].

a medium takes place. In this case the polarization of the medium is determined by the field values in the previous time moments and does not "follow" the field, as in the case of incoherent interaction. In other words, the medium possesses a "phase memory" during the relaxation time T_2, which strongly changes the picture of the pulse propagation.

Coherent pulse propagation in amplifying and absorbing media is well-studied currently, see Refs. [10, 27–29, 80–86, 110, 111]. In the case of such coherent interaction, an interesting phenomenon of self-induced transparency (SIT) may arise. SIT was discovered by S. L. McCall, E. L. Hahn in Refs. [27, 28] and observed experimentally in different media. The influence of SIT on the pulse propagation is the following: the leading edge of the pulse transfers the particles from the ground energy state to a coherent superposition of the ground and excited states. Thus, some part of the field energy is stored in the medium. The trailing edge of the pulse causes the atoms to emit electric field and thus the energy stored in the medium returns back to the field. In this way, the atoms are excited at the leading edge of the pulse and move back to the ground state at the trailing edge. In this way, the pulse may restore its initial shape during the propagation and thus travel in the nonlinear medium without loss of energy. This leads, however, to the decrease of the pulse velocity. The important quantity describing the pulse dynamics in the coherent regime is the pulse area, defined as [28] (for more detailed explanation see Chapter 6 of the thesis):

$$\Phi(t,z) = \frac{d_{12}}{\hbar}\int_{-\infty}^{t} \mathcal{E}(t',z)dt', \tag{2.1}$$

where d_{12} is the transition dipole moment of the two-level atom, and $\mathcal{E}(t,z)$ is the pulse

envelope. The area Φ of a stable SIT-induced soliton is 2π. An important result of the SIT theory is the so-called pulse area theorem. This theorem governs the evolution of the pulse area Φ during its propagation in a two-level absorbing (or amplifying) medium with an inhomogeneity broadened line [10, 28, 29, 110]:

$$\frac{d\Phi}{dz} = -\frac{\alpha_0}{2}\sin\Phi, \tag{2.2}$$

where

$$\alpha_0 = \frac{8\pi^2 N_0 d_{12}^2 \omega_{12} T_2^*}{\hbar c}, \tag{2.3}$$

is the absorption coefficient per unit length, N_0 is the concentration of two-level atoms, ω_{12} is the medium transition frequency and $1/T_2^*$ is the width of inhomogeneously broadened line. The solution of (2.2) is

$$\tan(\Phi/2) = \tan(\Phi_0/2)e^{-\alpha_0 z/2}, \tag{2.4}$$

where Φ_0 is the initial pulse area. The solution of (2.2) is presented in Fig. 2.3a. According to Fig. 2.3 the area of pulses with Φ_0 smaller than π tends toward 0 during propagation in the medium (see also Fig. 2.3b). If the pulse area is slightly larger than π (for example $\Phi_0 = 1.1\pi$ as in Fig. 2.3a), the pulse area tends to a stationary value 2π and a stable soliton is formed. Besides, the pulse duration increases simultaneously, see Fig. 2.3c. In contrast, if the initial pulse area $2\pi < \Phi_0 < 3\pi$ as in Fig. 2.3d, pulse narrowing takes place. And finally, if the Φ_0 close to 4π initial pulse may split into 2 separate 2π pulses, see Fig. 2.3e, where the evolution of pulse shape for $\Phi_0 = 3.6\pi$ is illustrated.

Coherent pulse propagation in an amplifying medium can be also described by (2.2) taking into account the fact that α_0 changes its sign. From Eq. (2.2) it follows that the same diagram Fig. 2.3a can be used, only the opposite z-direction must be taken. Accordingly (see Fig. 2.3), a pulse with the initial area $\Phi_0 < \pi$ (or 2π) approaches a steady-state with the area π. During this process, the pulse duration decreases. Note that such π-pulse leaves the initially excited two-level atoms in the ground level after its passage.

Thus, a stable 2π soliton in an absorbing medium, and a stable π soliton in a gain medium can be formed. This fact was first noted in Ref. [10] where a coherent pulse propagation in a two-component medium containing a gain and absorbing material was studied theoretically.

This observation led to the proposal of so called coherent passive mode-locking, a theory developed in Refs. [30, 31] and later expanded upon in recent papers [32–36]. In order to achieve 2π and π pulse areas in the absorbing and gain medium respectively, it is necessary to take the dipole moment of the absorbing medium two times larger than the dipole moment of the gain medium. In contrast to the case of usual passive mode-locking, coherent mode-locking allows for the generation of optical pulses with spectral bandwidth larger than the bandwidth of the gain medium. On the other hand, in Refs. [30–36] it was assumed that both the absorbing and amplifying media are

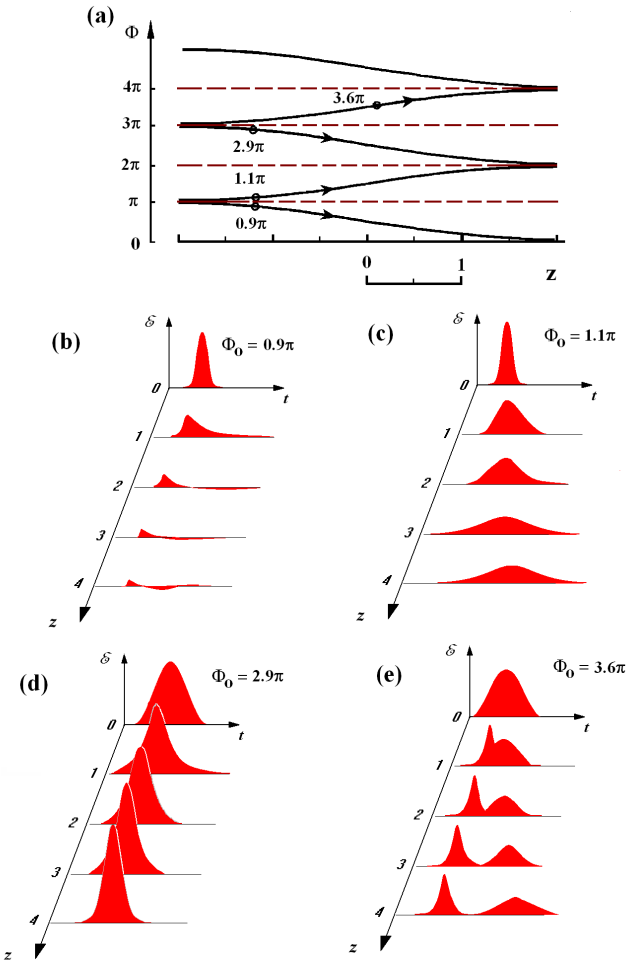

Figure 2.3: (a) Branches of solution of Eq. (2.2). For an absorbing (amplifying) medium with $\alpha_0 > 0$ ($\alpha_0 < 0$), the pulse area evolves in the direction of increasing (decreasing) distance z toward the nearest even (odd) multiple of π. (b)-(d): Evolution of pulses with the initial areas $\Phi_0 = 0.9\pi$, $\Phi_0 = 1.1\pi$, 2.9π, 3.6π respectively, with distance and time [28].

homogeneously "mixed" in the same sample. This is difficult to realize for most of passively mode-locked laser systems [22–26], with the exception of a quantum cascade laser structure developed in [32, 33]. Because of this, below in this Chapter we will extend the theoretical analysis of the coherent mode-locking to the case when both absorber and gain medium are placed separately in the cavity. Some results of this Chapter are included in a common publication [112], which is currently under preparation and in a recent publication: R. M. Arkhipov, M. V. Arkhipov, I. V. Babushkin "On coherent mode-locking in a two-section laser", JETP Letters, Vol. 101(3), pp. 149-153 (2015).

Before proceeding further with numerical analysis, let us consider the pulse evolution qualitatively, using a drawing showing the evolution of the pulse area in different parts of the cavity, which we refer to as McCall-Hahn diagrams in the following. It allows us for better understanding of basic mechanisms responsible for the pulse generation in a situation when the gain and absorber sections are separated, as well as to estimate the range of parameters where the coherent mode-locking is possible. We note that such an analysis, to the best of our knowledge, have never been considered in the literature before.

2.2 Area theorem and coherent mode-locking

In this section we present analysis of coherent mode-locking using the graphical representation technique which we call "McCall and Hahn diagrams".

Consider the situation when the absorbing and amplifying media are separated in space and the dipole moment of the absorber is twice that of the amplifier. Let us plot the solutions of Eq. (2.2) for the absorber and amplifier on the same plane for the case when the coefficient α_0 determined by Eq. (2.3) is the same for both media (in this case N_0 in the amplifier is four time that of the absorber). The branches of solutions of Eq. (2.2) placed in this way are shown in Fig. 2.4. Importantly, we can chose the direction of motion along the branch of the absorber (blue curves noted as $1a$, $2a$, $3a$, $4a$) from left to right, whereas for the amplifier it is opposite, from right to left (red curves noted as $1g$, $2g$), which is explained by the opposite signs of α_0 in both sections.

Using such diagram technique we are able to see immediately the most important peculiarities of the pulse area evolution. Let us assume that we have a laser with a ring cavity operating in a unidirectional lasing regime, see Fig. 2.5. In this laser a short pulse satisfying the condition of coherent interaction passes through the amplifier, is reflected from the mirror 1 with the reflection coefficient for the field R, and then enters the absorber. Assume that the other mirrors do not produce any energy loss. We also assume that the pulse travels long enough in every cavity section such that both the gain and absorber are able to recover to their equilibrium values between the pulse passages. Let us now suppose that a short pulse with the initial area $\Phi_0 = 0.25\pi$ enters the amplifier (cf. Fig. 2.6). This area corresponds to the point $G1$ on the red (amplifier) curve. Propagation in the amplifier corresponds to a shift of this point from right to left along the amplifier branch (red curve in Fig. 2.6) to $G2$, which is accompanied by an increase of the pulse area. After the pulse passes the amplifier, it is reflected by a

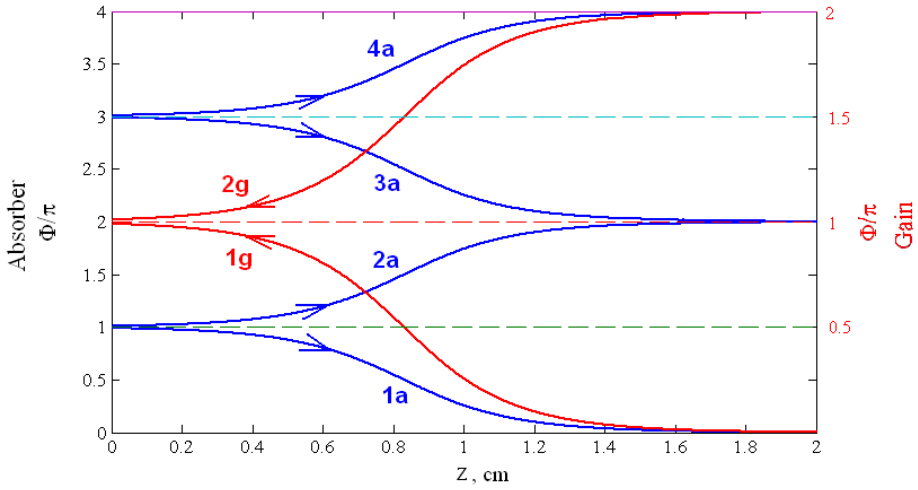

Figure 2.4: Branches of solution of Eq.(2.2) for the absorber 1a, 2a, 3a, 4a (blue lines) and the amplifier 1g, 2g (red line) for $|\alpha_0| = 10$ cm^{-1}.

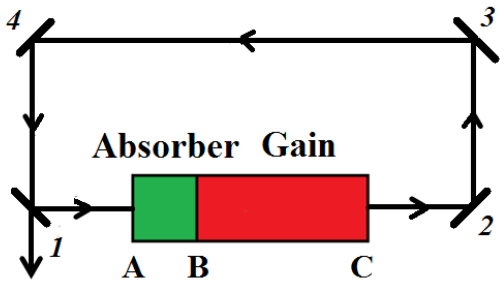

Figure 2.5: Schematic representation of mode-locked laser with a ring cavity where unidirectional counter clockwise lasing is assumed.

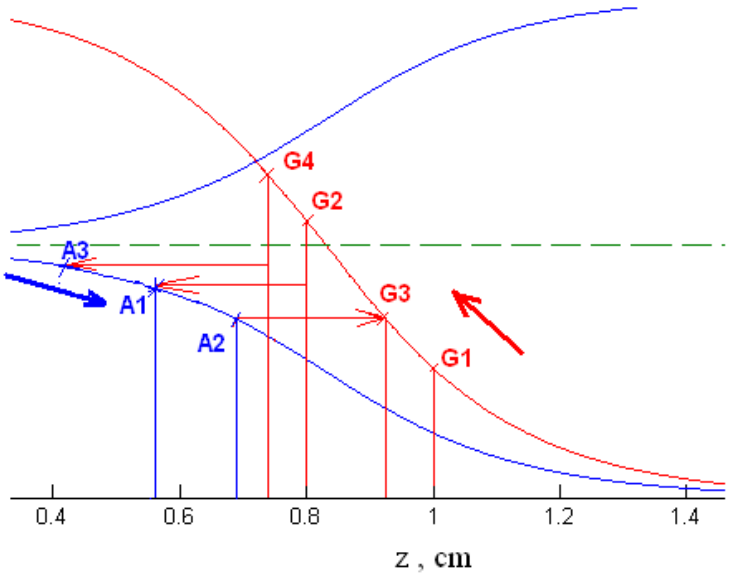

Figure 2.6: Using the McCall and Hahn diagrams from Fig. 2.4 for illustration of the pulse area evolution. The pulse evolution follows the path $G1 \rightarrow G2 \rightarrow A1 \rightarrow A2 \rightarrow G3 \rightarrow G4 \rightarrow A3$ in the gain (along red line) and in the absorber (along the blue line) sections in z-direction, backward and forward, correspondingly, which reflects different signs of α in both sections. The vertical sections of the path correspond to the reflection from the mirror, when the pulse area decreases.

non-ideal mirror and its area is thus reduced. Hence, the working point moves down vertically from $G2$ by the distance corresponding to the pulse area decrease caused by the reflection. Then, moving along the straight line parallel to the horizontal axis one arrives to the point $A1$, which now describes the pulse entering the absorber. Evolution of the pulse in the absorber is described by moving from left to right along the blue branch until the point $A2$. Now one returns back to the gain branch in $G3$. The point $G3$ is located above the initial point $G1$, meaning the overall increase of the pulse area after the whole cycle.

Now we repeat the cycle by moving from $G3$ again along the gain curve, arriving to $G4$, then descend down to $A3$ on the absorber curve, and so on. Note that the pulse area increases because the slope of the gain curve (and its length) is larger than that of the absorption curve. Finally, after long run the pulse area at the output of the amplifier and absorber will approach π and 2π, respectively, leading to a stationary pulsating regime. Note that if we decrease the mirror reflection coefficient strongly enough, or, alternatively, increase the absorber length, the working point might now move down every cycle thus tending toward zero, meaning the pulse decay.

Using such an approach one can predict whether a stable limit cycle exists and can be achieved from an initial pulse with the small area. The appearance of such limit cycles can be confirmed by numerical simulations. An example of such cycle and its development is presented in Fig. 2.7. For the exemplary parameters a regime develops from the initial pulse with the small area $\Phi_0 = 0.001\pi$ in 50 round-trips times as shown in Fig. 2.7a, which approaches the limit cycle depictured separately in Fig. 2.7b.

The difference between the slopes of the amplifier and absorber curves allows us to start the iteration process from very small pulse areas and approach finally the nonzero limit cycle. That in particularly means, that an injection of a seed pulse is not always necessary to achieve the stationary short-pulse regime. This is in contrast to the scheme with "mixed" absorber and gain used in previous considerations of coherent mode-locking, where the initial pulse is absolutely necessarily to achieve the pulsed regime.

Nevertheless, if we increase the absorber length, the low-signal limit becomes purely absorbing, thus requiring injection of a seed pulse to start generation. Fig. 2.7 illustrates this point. In particular, Fig. 2.8a illustrates the evolution of the pulse area with the absorber length increased 2 times in comparison to that in Fig. 2.7 and initial pulse area $\Phi_0 = 0.15\pi$. In this case the system tends to zero pulse area. On the other hand, if one starts from $\Phi_0 = 0.2\pi$, the system approaches a nonzero limit cycle after 7 round-trips, as shown in Fig. 2.8b.

Using the area theorem Eq. (2.4) one can easily obtain the condition of lasing self-starting for coherent mode-locking. Suppose that the gain and absorber sections have the lengths L_g, L_a and the gain (absorption) coefficients α_{0g} and α_{0a} respectively, and the process starts from a weak pulse with the initial area $\Phi_0 \ll 1$, meaning that the working point is on the lower part of the red branch in Fig. 2.6. Since in the lower part of the branches $\Phi \ll 1$, $\tan(\Phi) \approx \Phi$, the area theorem Eq. (2.4) can be rewritten in the form:

$$\Phi \approx \Phi_0 e^{-\alpha_0 z/2}. \tag{2.5}$$

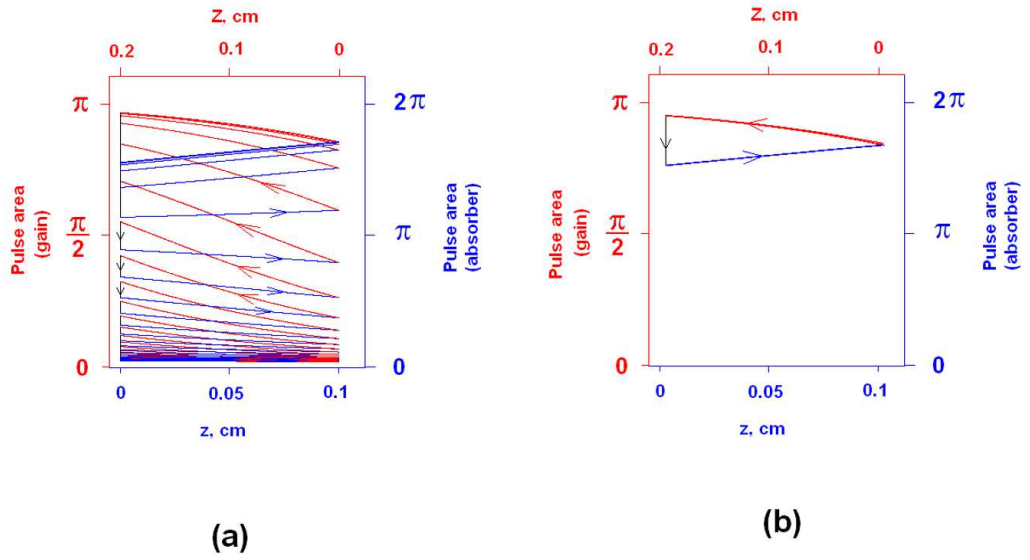

Figure 2.7: Evolution of the pulse area Φ in the absorber and gain medium (a) from the initial value $\Phi_0 = 0.001\pi$ to a limit cycle (b) in a ring cavity geometry. The blue and red curves corresponds to the pulse propagation in the absorber and gain sections, correspondingly.

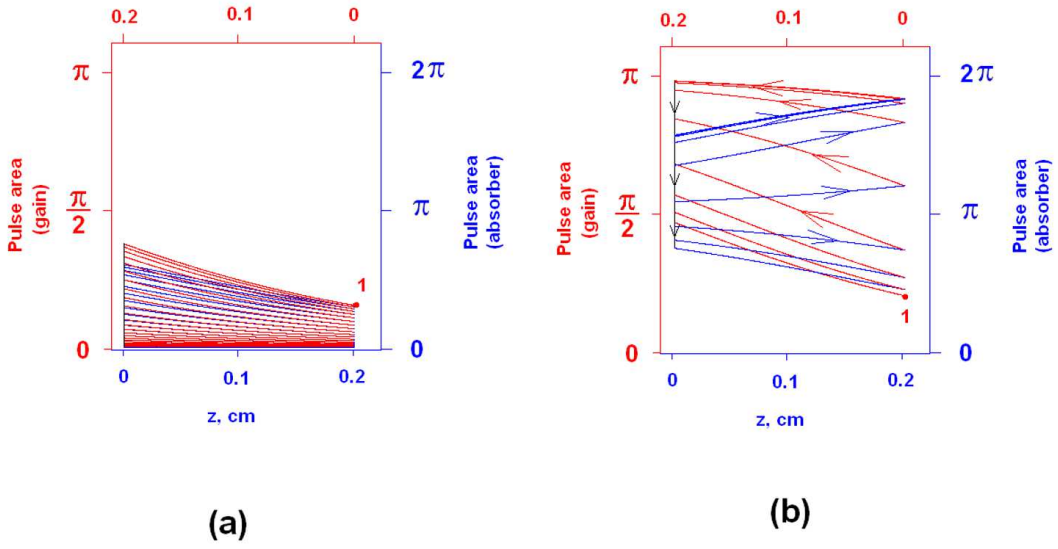

Figure 2.8: Evolution of the pulse area Φ in the ring cavity geometry for large length of the gain section. The evolution starts from the point 1, which corresponds to $\Phi_0 = 0.15\pi$ in (a) and $\Phi_0 = 0.2\pi$ in (b). In the former case, the system approaches zero, whereas in the later one it moves toward a nonzero limit cycle.

Assume that a seed pulse with the initial area for gain medium $\Phi_{0B} \ll 1$ starts propagating in the amplifier at the point B, see Fig. 2.5. At the output of the gain section (point C) the pulse area according to Eq. (2.5) will be

$$\Phi_C = \Phi_{0B} e^{\alpha_{0g} L_g/2}.$$

Since only the part of the radiation is reflected from the mirror 1, the initial pulse area for absorber (point A in Fig. 2.5) is given by $\Phi_A = R m_d \Phi_C$, where $m_d = d_{12a}/d_{12g}$ the ratio of absorber/gain dipole moments. After passing through the absorber (point B) the pulse area will be:

$$\Phi_B = \Phi_A e^{-\alpha_{0a} L_a/2} = R m_d \Phi_{0B} e^{\alpha_{0g} L_g/2} e^{-\alpha_{0a} L_a/2}. \tag{2.6}$$

In order to self-start the lasing one must have $\Phi_B \geq m_d \Phi_{0B}$. This condition can be rewritten in the form:

$$R e^{\alpha_{0g} L_g/2} e^{-\alpha_{0a} L_a/2} \geq 1. \tag{2.7}$$

With the help of the diagrams introduced above (and Fig. 2.3 where the MCall and Hahn solution is illustrated) we will now analyze the situation, when the ratio of the dipole moments is not equal to two. First, we consider the case when $m_d < 1$. The corresponding diagram for $m_d = 0.5$ is shown in Fig. 2.9a. In this case the limit cycle is realized with the branch $1g$ of the amplifier and $1a$ of the absorber. On the amplifier branch, the pulse with the area tending to π is formed, whereas the absorber will decrease the pulse area. Because of the energy conservation, decrease of the pulse area means that the pulse envelope must change its sign. Thus, the generated pulse must have at least one point of zero intensity. Experimental observation and theoretical study of such zero-area (0π) formation in the absorber medium was presented in [113, 114].

In the example presented in Fig. 2.9b we set $m_d = 1.5$. In this case, the branch $1g$ of amplifier and one of the branches $1a$ or $2a$ of the absorber can take part in the generation. A limit cycle formed with $1g$ and $2a$ has the following feature: when moving along $2a$, the pulse area tends to 2π and its duration increases in contrast to the cycle with $1g$ and $1a$.

The situation when $2 < m_d < 3$, namely, $m_d = 2.5$ is shown in Fig. 2.9c. One branch of the amplifier $1g$ and one of the three branches of the absorber $1a$, $2a$ or $3a$ will be involved in this case. The cycle formed on the branch $3a$ yields a reduction of the pulse duration. This happens because the pulse moving from amplifier to absorber has the area $\Phi > 2\pi$. During its propagation in the absorber Φ will tend to 2π and the pulse duration will decrease. Thus, the ratio of the dipole moments influences the duration of the laser pulse in a coherent mode-locking.

In the situation when $m_d > 3$ (not shown) the branch $4a$ can participate in generation. On this branch, the formation of radiation with area 4π takes place, which must split into two 2π pulses which might have different amplitudes and durations. Thus, in this situation two pulses will arise over a single cavity round-trip.

It is to be remarked that the McHall and Hahn diagrams demonstrated above were first introduced in the present work and provide a unifying framework allowing better un-

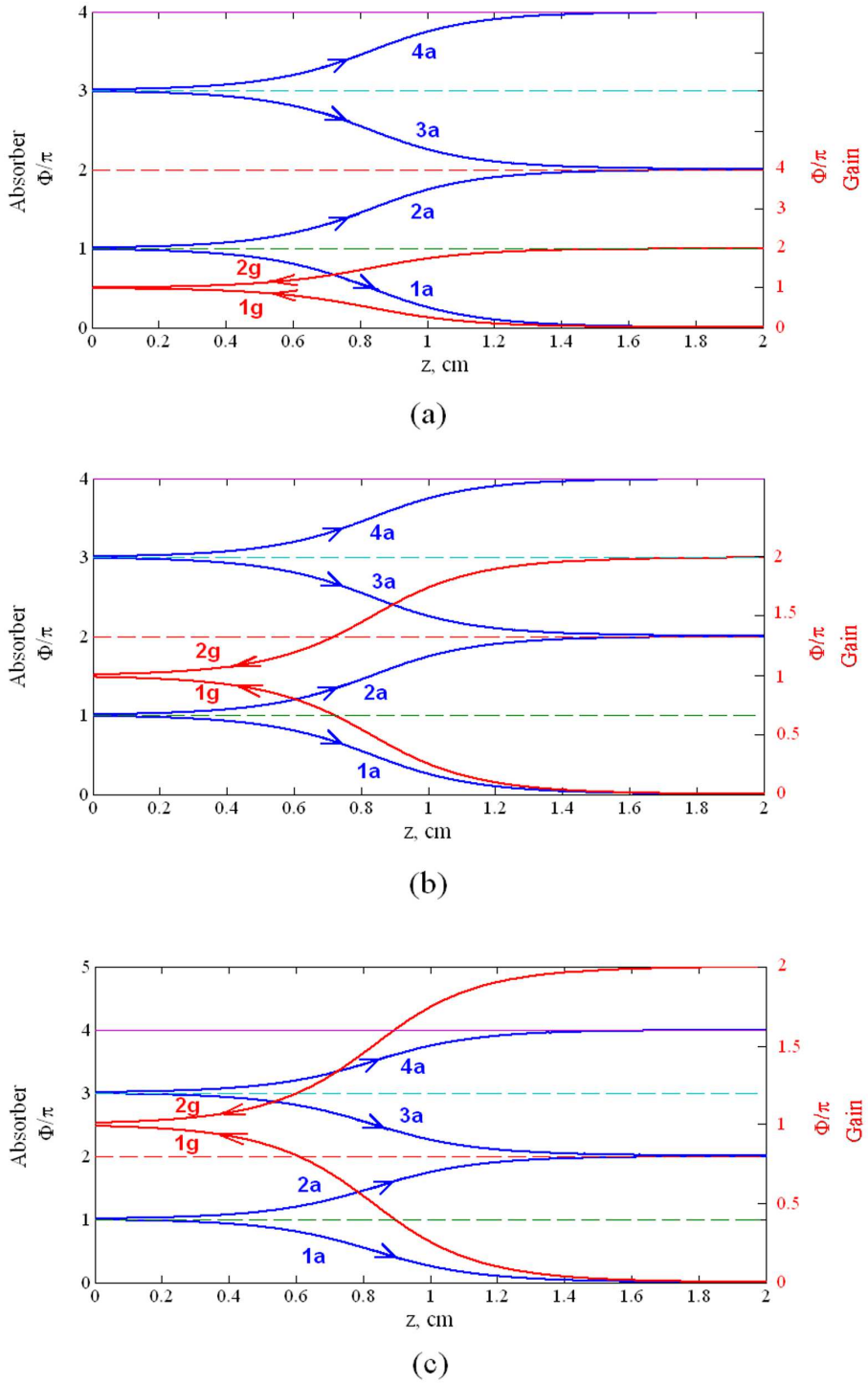

Figure 2.9: Branches of solution of Eq. (2.2) for an absorber (blue lines) and amplifying medium for different ratios m_d. (a): $m_d = 0.5$, (b): $m_d = 1.5$, (c): $m_d = 2.5$.

derstanding of the passive mode-locking process in the coherent regime. It demonstrates the stability of the pulsating regimes over the wide range of parameters. Sometimes such stable pulsations are obtained even without an external seed.

2.3 Fundamental equations for laser model

To study the mechanism of mode-locking in a two-section laser we carry out numerical experiments based on a set of Maxwell-Bloch equations describing propagation of light in a two-level medium in a slow-varying envelope approximation for the field and for the atomic polarization [10, 12, 16, 18, 29, 81, 110, 115, 116].

The set of equations governing its evolution has the form:

$$\frac{d}{dt}P_c^{\pm}(z,t) = -\frac{P_c^{\pm}(z,t)}{T_2} - \Delta\omega P_s^{\pm}(z,t) - \frac{d_{12}}{2\hbar}\Delta\rho(z,t)B^{\pm}(z,t), \tag{2.8}$$

$$\frac{d}{dt}P_s^{\pm}(z,t) = -\frac{P_s^{\pm}(z,t)}{T_2} + \Delta\omega P_c^{\pm}(z,t) + \frac{d_{12}}{2\hbar}\Delta\rho(z,t)A^{\pm}(z,t), \tag{2.9}$$

$$\begin{aligned}\frac{d}{dt}\Delta\rho(z,t) = -\frac{\Delta\rho(z,t)-\Delta\rho_0}{T_1} - \frac{2d_{12}}{\hbar}(A^+(z,t)P_s^+(z,t) + A^-(z,t)P_s^-(z,t) + \\ +B^+(z,t)P_c^+(z,t) + B^-(z,t)P_c^-(z,t)),\end{aligned} \tag{2.10}$$

$$\frac{\partial A^{\pm}(z,t)}{\partial t} \pm c\frac{\partial A^{\pm}(z,t)}{\partial z} = -4\pi\omega d_{12}N_0P_s^{\pm}(z,t), \tag{2.11}$$

$$\frac{\partial B^{\pm}(z,t)}{\partial t} \pm c\frac{\partial B^{\pm}(z,t)}{\partial z} = 4\pi\omega d_{12}N_0P_c^{\pm}(z,t). \tag{2.12}$$

Equations (2.8)-(2.10) describe the evolution of slowly varying envelopes of two counter-propagating waves (in-phase $P_c^{\pm}(z,t)$ and quadrature $P_s^{\pm}(z,t)$ components) of real and imaginary parts of non-diagonal element of the quantum mechanical density matrix, as well as the population difference $\Delta\rho$ between the lower and upper energy levels of the medium. Equations (2.11) and (2.12) govern the evolution of amplitudes (in-phase $A^{\pm}(z,t)$ and quadrature $B^{\pm}(z,t)$ components) of the two counter-propagating optical waves. The propagation direction is denoted by $(+)$ and $(-)$ respectively. The derivation of the model equations is given in Appendix A. The equations include parameters of the two-level system, such as transition dipole moment d_{12}, concentration of two-level atoms N_0, population difference relaxation time T_1, polarization relaxation time T_2, carrier frequency of the optical field ω, frequency detuning $\Delta\omega$ of the radiation field from transition frequency of the two-level medium ω_{12}, and population difference at the equilibrium $\Delta\rho_0$. For the amplifying medium, $\Delta\rho_0 = -1$, for the absorbing medium, $\Delta\rho_0 = 1$. We make all these parameters depending on the space coordinate z, so that these equations can be applied to the description of the gain and the absorbing medium located in different sections of the cavity. The set of equations (2.8)-(2.12)

affords sufficiently complete modeling of evolution of extended two-level media in a cavity, taking into account multi-mode character of radiation and the nonlinear coherent effects accompanying interaction of the light with the two-level medium. It was also used in our recent study of lasing without population inversion in a two-level optically dense medium [117], and spectral condensation phenomenon arising when narrow-band absorbing medium is placed in the resonator with broad-band amplifying medium [118].

We apply the system of equations (2.8)-(2.12) to analyze the situation when both laser gain and absorber media are placed in the ring optical cavity in the case of unidirectional propagation, as well as the case of a linear cavity. In our analysis below we will assume that resonance frequencies in the gain and absorber are equal to each other and to the carrier frequency of the electric field, i.e. $\Delta\omega = 0$. The simplified system of Maxwell-Bloch equations under these conditions can be written in the form:

$$\frac{\partial A^{\pm}(z,t)}{\partial t} \pm \frac{\partial A^{\pm}(z,t)}{\partial z} = 4\pi\omega_{12} d_{12} N_0 P_s^{\pm}(z,t), \tag{2.13}$$

$$\frac{d}{dt} P_s^{\pm}(z,t) = -\frac{P_s^{\pm}(z,t)}{T_2} + \frac{d_{12}}{2\hbar}\Delta\rho(z,t) A^{\pm}(z,t), \tag{2.14}$$

$$\frac{d}{dt}\Delta\rho(z,t) = -\frac{\Delta\rho(z,t) - \Delta\rho_0}{T_1} - \frac{2d_{12}}{\hbar}\left(A^{+}(z,t)P_s^{+}(z,t) + A^{-}(z,t)P_s^{-}(z,t)\right). \tag{2.15}$$

2.4 Coherent mode-locking in lasers with a ring cavity

In the case of a ring cavity we put in Eqs. (2.8)-(2.12) $A^{-}(z,t) = 0$, assuming thus unidirectional propagation and using the notation $A^{+}(z,t) \equiv A(z,t)$. First, we consider the case when the ratio of the transition dipole moments absorber/gain $m_d = 2$. We perform numerical simulations of the model equations (2.8)-(2.12) for the parameter values given in Table 2.1 and Table 2.2.

Table 2.1: Parameter values used in the numerical simulations

Parameter	Gain	Absorber
central wave length of the medium	$\lambda_{12g} = 0.7\ \mu m$	$\lambda_{12a} = 0.7\ \mu m$
length of the medium	$L_g = 0.15$ cm	$L_a = 0.45$ cm
concentration of two-level atoms	$N_{0g} = 12.5 \cdot 10^{14}$ cm^{-3}	$N_{0a} = 12.5 \cdot 10^{14}$ cm^{-3}
transition dipole moment	$d_{12g} = 5$ Debye	$d_{12a} = 10$ Debye
population difference at equilibrium	$\Delta\rho_{0a} = 1$	$\Delta\rho_{0g} = -1$
population difference relaxation time	$T_{1g} = 0.16$ ns	$T_{1a} = 0.16$ ns
polarization relaxation time	$T_{2g} = 40$ ps	$T_{2g} = 40$ ps

Assuming also the initial conditions with the constant amplitude close to non-lasing solution, we perform numerical simulations showing that after a transition process taking a few tens of cavity round-trip times, regular sequence of short optical pulses appears. The pulse-to-pulse period of this pulse train is larger than the cold cavity round-trip

Table 2.2: To Table 2.1

cavity length $L = 0.6$ cm
reflectivity of the mirror $R = 0.8$
initial pulse area $\Phi_0 = 10^{-10}\pi$

time $T = L/c = 20$ ps. Since we assumed $T_{2g} = T_{2a} = 40$ ps, which is larger than T and also an order of magnitude more than the pulse duration (1 ps), the interaction of light and matter is in coherent regime and accompanied by the formation of pulses with the area close to 2π in the absorber and π in the amplifier.

Fig. 2.10a,b illustrates the spatial distribution of $A(z)$, $\Delta\rho(z)$ and $P_s(z)$. In Fig. 2.10a the laser pulse passes through the absorber whereas in Fig. 2.10b it is located in the amplifier (the pulse moves from left to right during the propagation). Fig. 2.10 shows the pulse at the time moment close to the 100th round-trip after the beginning of the numerical simulations, when the stable pulsing regime is already established. At the leading edge of the pulse the population difference $\Delta\rho$ decreases until the value close to -0.8. $P_s > 0$ in this interval, hence, absorption of the radiation takes place. At the trailing edge $P_s < 0$, and the population difference increases and is recovered to its initial value. The absorber starts to radiate, returning energy to the trailing edge of the pulse. Thus the pulse shown in Fig. 2.10 has all the features of the SIT one.

After passing through the absorber the pulse propagates in the amplifier, see Fig. 2.10b. It can be seen that at the trailing edge of the pulse the population inversion $\Delta\rho$ becomes positive. P_s is, on the other hand, negative, therefore, the medium gives the energy to the field. The gain medium becomes absorbing after the pulse passage. This behavior is typical for the π pulse propagating in the amplifying medium.

Fig. 2.10c illustrates the dependence of the pulse area inside the cavity during a single pass. It is clearly seen that, as it was predicted in the previous section, the pulse area is close to 2π in the absorber and to π in the gain. A pulse with the area noticeably smaller than 2π arrives to the entrance of the absorber and then its area rapidly grows. Interestingly, the pulse area in the amplifier increases somewhat but then start to decrease. The initial increase above the value of π is because of the finite relaxation time of the media. The subsequent decrease is due to self-stabilization mechanism of the π-pulse area.

Fig. 2.10d shows the distribution of the electric field amplitude $A(z)$ in the cavity over four round-trips. It demonstrates one more feature of the pulse propagation inside the cavity, namely that the pulse velocity in the absorber is smaller than in the amplifier, which manifests itself in a bend of the pulse propagation trajectory on the boundary between the absorber and amplifier.

Another important feature should be mentioned in this case. The spectrum of the laser generation is much broader than the width of the gain (absorption) profile since pulse duration $\tau_p \sim 1$ ps is smaller than medium coherence time $T_{2g} = T_{2a} = 40$ ps in this case. This can be seen from Fig. 2.11a,b, where the time dependence of the output field intensity $|A|^2$ and its spectrum together with the Lorentzian gain and absorption line

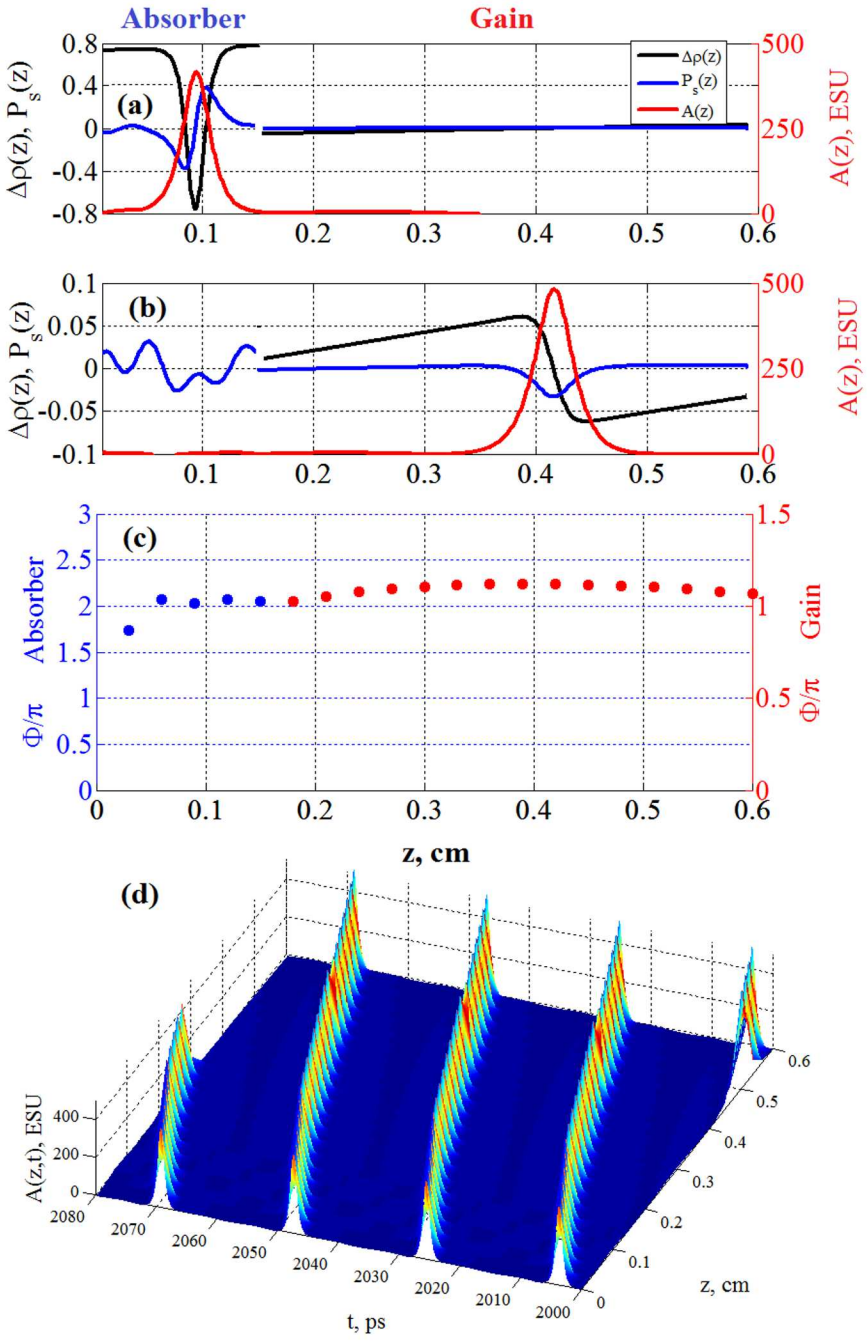

Figure 2.10: (a), (b) Distribution of the electric field amplitude $A(z)$ in the cavity (red line), $P_s(z)$ (blue line) and population difference $\Delta\rho(z)$ (black line) when pulse is located in the absorber (a) and in the gain (b) sections. (c) Evolution of the pulse area in the cavity during one round-trip. (d) Distribution of the electric field amplitude $A(z)$ field in the cavity. The parameter values given in Table 2.1 and in Table 2.2.

shapes are plotted. In the usual passive mode-locking theory the situation is different — the pulse duration is determined by the bandwidth of the gain medium. Also, it is seen from Fig. 2.11b that the pulse repetition frequency is smaller than cold-cavity one (50 GHz) because of the fact that pulse in the absorber propagates with the velocity smaller than c. In the amplifier π-pulse propagates with the velocity of light c.

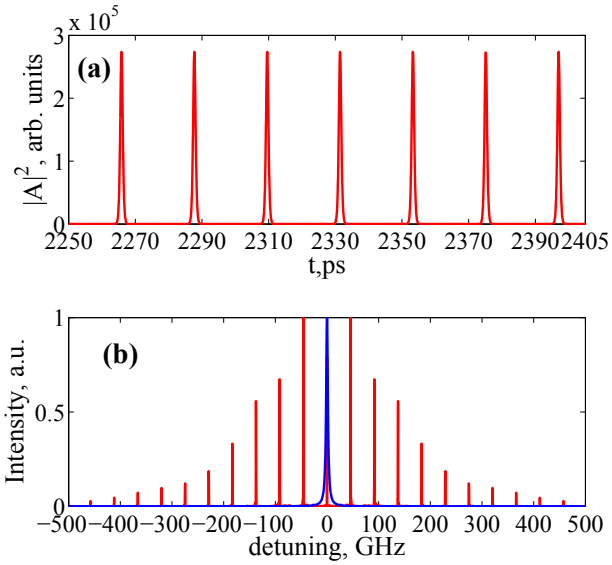

Figure 2.11: (a) Time dependence of the output field intensity. (b) Its spectrum (red) and normalized Lorentzian gain and absorption line shapes (blue) for the example illustrated in Fig. 2.10.

Fig. 2.10b shows that the value of polarization in the absorber after the pulse passage is not equal to zero due to the fact that some of the pulse energy is left in the absorber [28]. It changes its sign along the medium and has relatively large value resulting in an additional light emission by the absorber. This is so-called "coherent optical ringing" of the field and polarization [119]. Coherent ringing creates radiation that propagates in the direction of the amplifier. However, immediately after the passage of the pulse the amplifier is still absorbing, resulting in attenuation of this radiation. Besides, the radiation remaining in the absorber will affect the propagation of the pulse when it appears in the absorber again. This fact can be seen from our simulations on the behavior of the pulse area in the absorber (see Fig. 2.10c), which is non-monotonic. One can see an increase of such “jitter” with the increase of the absorber length. On the other hand, the effect of coherent ringing decreases with decrease of T_2. Note that such “noise of polarization” created by a laser pulse in the absorber is characteristic for the coherent mode-locking. And its influence on the coherent mode-locking regime we report for the first time. Numerical simulations for the case of mixed gain and absorber in the soliton laser shows a large value of such ringing. A detailed quantitative analysis of the

impact of coherent ringing on the pulse dynamics is a subject of a separate study and is not considered in this thesis.

The example presented above demonstrates the existence of coherent mode-locking in a ring optical laser geometry with unidirectional lasing and the gain spatially separated from absorber, in contrast to previous works. One of the most important parameters influencing the dynamics is the time relaxation of polarization in the gain and absorber. In the example shown in Fig. 2.10 $T_{2a} = T_{2g} = 40$ ps. Our numerical simulations show that the regime of short optical pulses is preserved if these times are independently varied from 2 ps until 50 ps. Influence of the relaxation time $T_2 = T_{2g} = T_{2a}$ on the pulse parameters in the coherent mode-locking regime is shown in Fig. 2.12, where the half-width pulse maximum duration τ_p, its peak intensity I_p, and energy density W is shown in the steady state regime after 100 round-trips times.

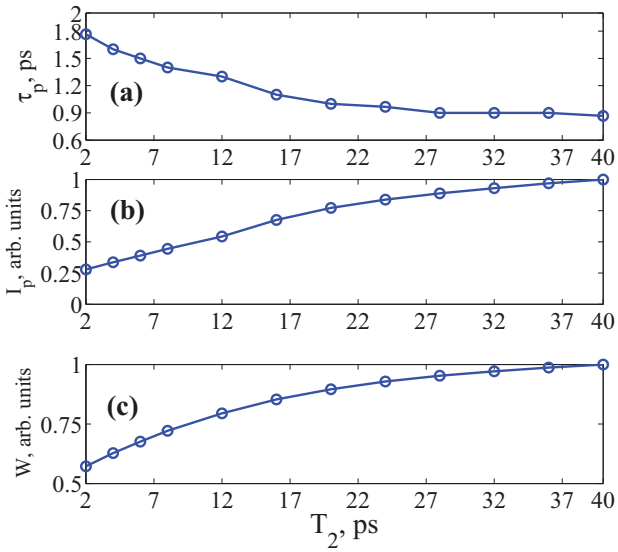

Figure 2.12: Dependence of the pulse duration τ_p (a), the peak intensity I_p (b) and energy density of the pulse W (c) on the polarization relaxation time $T_2 = T_{2g} = T_{2a}$. Other parameter values are as in Table 2.1 and Table 2.2.

It is seen from Fig. 2.12 that the pulse duration increases with the decrease of T_2, whereas the peak intensity and the energy density decreases. This behavior can be explained by the fact that with decrease of the "phase memory time" T_2 the part of the energy transferred to the absorber at the leading edge and coming back at the trailing edge decreases, which in turn influences the gain. The behavior of the pulse area in the cavity under different values of T_2 is further illustrated in Fig. 2.13. One can see that this dynamics is quite similar for very different values of T_2.

Fig. 2.14 presents the dependence of the pulse duration τ_p (a), peak intensity I_p (b) and pulse energy density W (c) on the ratio of the dipole moments of the absorber and amplifier m_d. We see that with increasing of d_{12a} the pulse duration decreases from 1.35

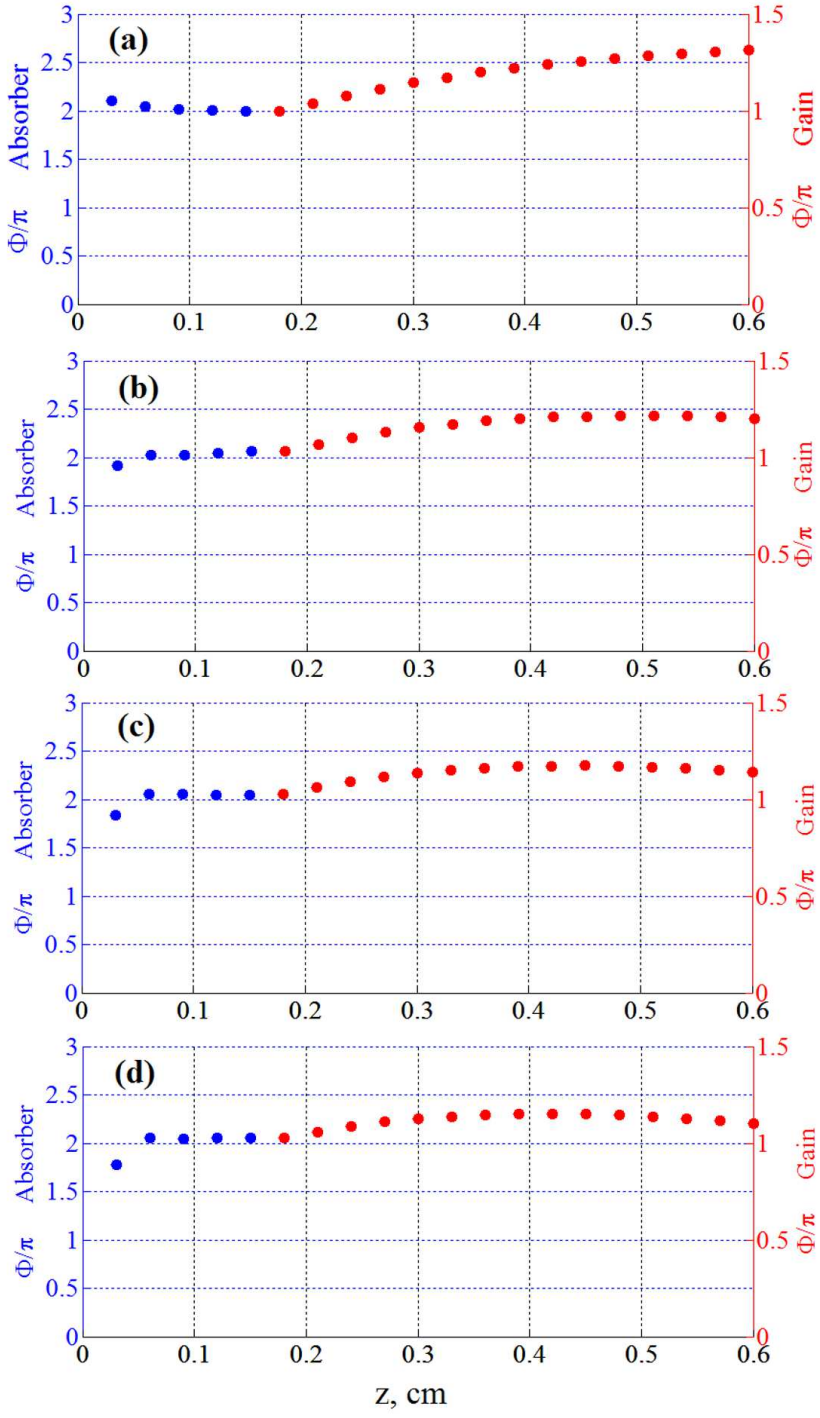

Figure 2.13: Dependence of the pulse area in the cavity Φ under different values of $T_2 = T_{2g} = T_{2a}$. (a): $T_2 = 4$ ps, (b): $T_2 = 8$ ps, (c): $T_2 = 12$ ps, (d): $T_2 = 16$ ps. Other parameter values are as in Table 2.1 and Table 2.2.

ps to 200 fs. This leads to the increase of the peak intensity approximately 4 times, thus keeping the pulse energy approximately constant, see Fig. 2.14c. Numerical simulations were performed using the parameter values $T_{2g} = 20$ ps, $N_{0g} = N_{0a} = 18 \cdot 10^{14}$ cm^{-3}. Other parameter values are as in Table 2.1 and in Table 2.2.

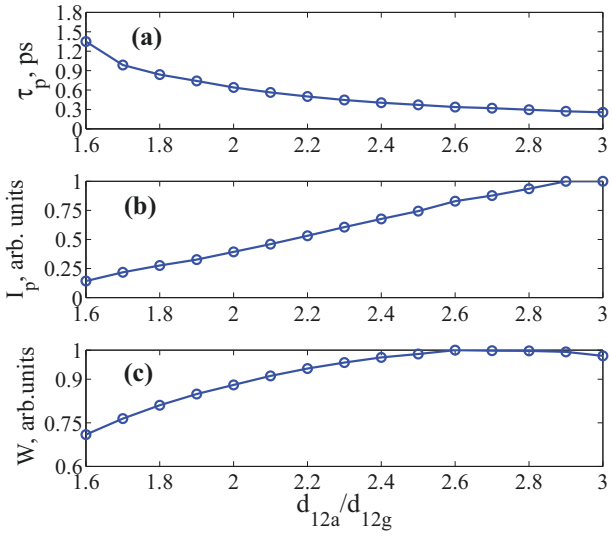

Figure 2.14: Dependence of the pulse duration τ_p (a), the peak intensity of the pulse I_p (b) and energy density of the pulse W (c) on the ratio of the dipole moment of the absorber and gain medium m_d. $T_{2g} = 20$ ps, $N_{0g} = N_{0a} = 18 \cdot 10^{14}$ cm^{-3}. Other parameter values are as in Table 2.1 and Table 2.2.

Let us consider the case when the ratio of the dipole moments of the absorber/gain $m_d < 1$. In this case, according to the area theorem, the pulse area in the absorber must tend to zero. The example of the numerical simulations of the model equations (2.8)-(2.12) when $d_{12a} = 2.5$ Debye ($m_d = 0.5 < 1$) with other parameters are as in Table 2.1 is given in Fig. 2.15. Fig. 2.15a illustrates the distribution of the pulse amplitude in the different parts of the cavity. In particular, in the absorber, according to the area theorem, the pulse area tends to zero and increases to π in the gain section, see Fig. 2.15b. Our numerical simulations indicate that there are two pulses with different values of the peak intensity for one round-trip time at the output from the gain medium, see Fig. 2.15c.

Finally, let us consider the case when the ratio of dipole moments $m_d > 3$, namely $m_d = 4$. In this situation McCall and Hahn diagrams predict appearance of two pulses. Fig. 2.16 illustrates the results of numerical simulations when $d_{12a} = 20$ Debye with other parameters are as in Table 2.1. Generation has the form of a periodic train of pulse pairs, one for each cavity round-trip time, see Fig. 2.16c. The pulse area in the absorber is close to 4π and tends to π in the gain section as shown in Fig. 2.16c.

In conclusion, numerical experiments using the system of Maxwell-Bloch equations in the slowly varying envelope approximation shows the presence of a stable coherent mode-

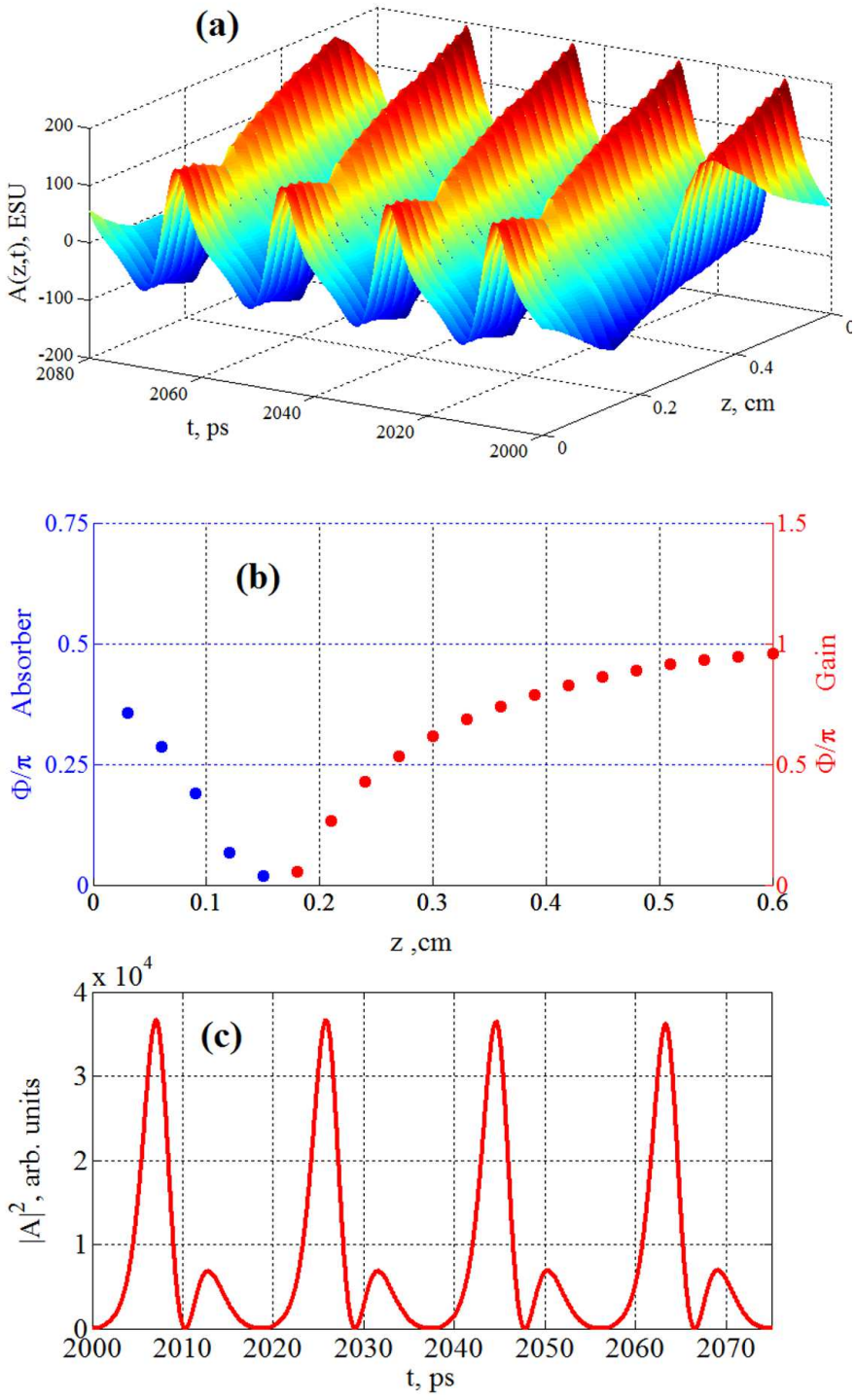

Figure 2.15: Evolution of the electric field amplitude in the cavity $A(z,t)$ (a), Dependence of the pulse area $\Phi(z)$ inside the cavity (b) and the temporal dependence of the output intensity $|A|^2$ (c) for $d_{12a} = 2.5$ Debye and other parameter values given in Table 2.1 and Table 2.2.

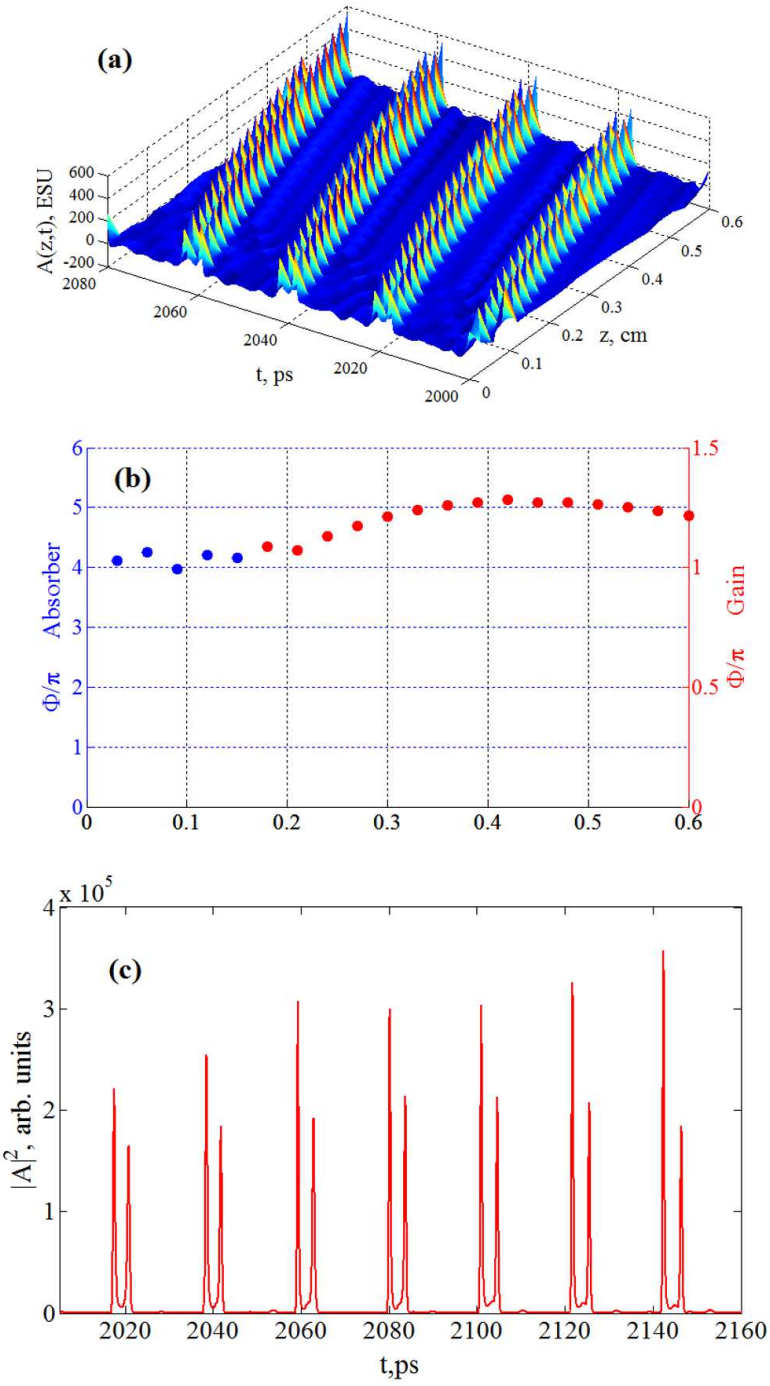

Figure 2.16: Evolution of the electric field amplitude in the cavity $A(z,t)$ (a), Dependence of the pulse area $\Phi(z)$ inside the cavity (b) and the temporal dependence of the output intensity $|A|^2$ (c) for $d_{12a} = 20$ Debye and other parameters given in Table 2.1 and Table 2.2.

locking in a two-section ring-cavity laser with absorbing and amplifying media separated in space. Mixing of these media, as it was done in the pioneer works in Refs. [30, 31] is not necessary for the coherent mode-locking to arise. Moreover, in such two-section laser injection of a seed pulse is also not a necessary condition for the appearance of pulsed regime. In contrast, self-starting from noise is possible. Remarkably, the width of the lasing spectrum can be significantly broader than the width of the gain line. Coherent mode-locking regime is preserved even if the relaxation time of the polarization in the amplifier and absorber either larger or smaller than the round-trip time of the cavity. In examples presented above T_2 of the media varied from 40 ps to 2 ps at a cavity round-trip time 20 ps.

We also have demonstrated the influence of the dipole moments absorber/gain ratio m_d on the coherent mode-locking regime. In the range $1.5 < m_d < 3$ an increase of m_d leads to a decrease of the laser pulse duration. Our numerical simulations indicate that the coherent mode-locking regime is also possible if $m_d < 1.5$ and $m_d > 3$. However, in this case several pulses per cavity round-trip time occur.

2.5 Modeling coherent mode-locking in a laser with a linear cavity

In the previous sections we considered a two-section laser with a circular geometry. Here we consider an another scheme namely a linear laser geometry. To perform numerical simulations, we use the system (2.13)-(2.15) with both propagation directions retained.

There is an important difference between a laser with a linear cavity and a ring one. In case of a ring cavity (Fig. 2.17a) a pulse coming out of the gain medium passes first the absorber section and only then reenters the gain. In such a way, some time is gained for the relaxation processes in the gain section. During this time the gain in the medium recovers under the action of pumping, and the medium becomes an amplifier again.

Another situation arises in the linear cavity, see Fig. 2.17b. Consider what happens in the amplifying medium when it almost completely fills the cavity. Assume that a pulse propagates in the amplifying medium from the point A to B. This pulse, leaving the point B, is reflected from the mirror and goes back to the point B again. At this time the gain medium near B has not recovered yet, and thus no amplification arises. As a result, intensity of the pulse does not increase near the point B. In contrast, near A the gain has already recovered, so that finally net amplification may still take place in the amplifier. Amplification around point B will also takes place for the pulse, when it comes from the opposite direction. As a consequence, the existence of two counter-propagating pulses is possible in this situation, which is shown in this section by the means of numerical simulations.

In the numerical simulations we consider a situation when the amplifier section is placed in the center of the cavity (as Fig. 2.18a but without absorber), and the cavity mirrors have the same reflection coefficients. Numerical experiment visualized in Fig. 2.18a demonstrates a stable self-mode-locking regime with the pulse-to-pulse distance equal to the half of the cavity round-trip time. The pulse repetition rate is explained by the

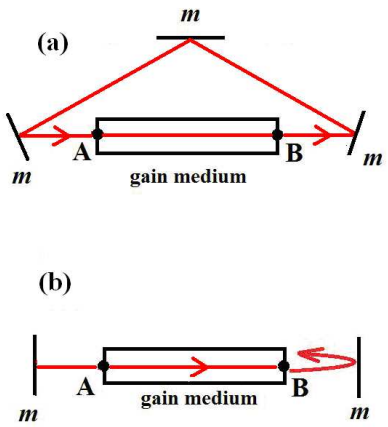

Figure 2.17: Schematic representation of pulse motion in a ring (a) and linear lasers (b). by m the cavity mirrors are marked.

appearance of pulses in both of the counter-propagating waves.

In order to suppress one of the pulses we may, for instance, introduce an external modulation of the reflectivity of one of the mirrors with the period close to the cold-cavity repetition period $2L/c$. In this way we introduce elements of active mode-locking. In this case due to competition between the pulses in the cavity there remains only one pulse, for which the mirror reflectivity is maximal at the moment of the pulse incidence, see Fig. 2.18b. The counter-propagating wave can also be suppressed if an absorbing section is placed between one of the mirrors and the amplifier, as shown in Fig. 2.18c.

The solutions presented in Fig. 2.18 shows that the absorber creates a regime in which only one pulse propagates in the cavity. The peak amplitude value of this single pulse is larger and pulse duration is smaller than in the case of two pulses.

One should note that in the situation considered above the laser operates in incoherent regime, since the laser pulse duration is larger than the medium coherence time T_2. In particular, the population difference does not change its sign (because $\Omega_R \cdot T_{2g} \simeq 1$ in Fig. 2.18). The electric field amplitude A, slow envelope of the imaginary part of the non-diagonal element of density matrix P_s as well as population difference $\Delta\rho$ for the case given in Fig. 2.18c are shown in Fig. 2.19 for various positions and directions of the pulse propagation inside the cavity.

One can expect the appearance of coherent mode-locking if we increase significantly the amplitude of the pulse. For this, we may increase the concentration of the particles in the amplifier and absorber (and set them equal to each other) and make the dipole moment of the absorber twice larger than that of the amplifier. The later is very important for the realization of coherent mode-locking as shown in the previous section. The results of numerical simulations in such modified system are shown in Fig. 2.20. By changing the model parameters in this way mode-locking is in the regime of coherent interaction of light and matter, both in the amplifier and in the absorber.

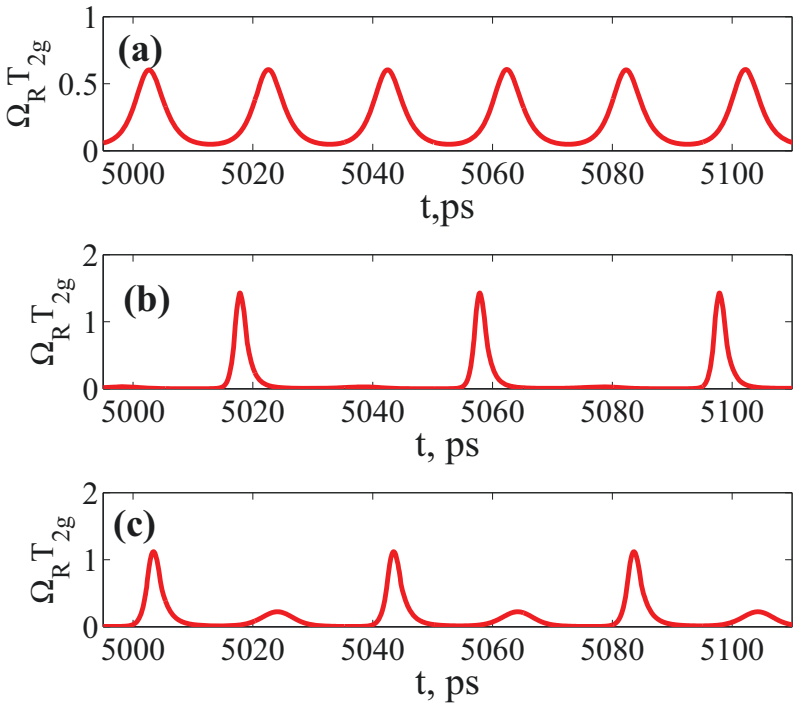

Figure 2.18: Results of the numerical simulations of the laser generation with a linear cavity. On the y-axis is the value of the Rabi frequency $\Omega_R = d_{12g}A/\hbar$ normalized to T_{2g}. Parameters of the model: cavity length $L = 0.6$ cm, length of the gain medium $L_g = 0.15$ cm, optical wavelength $\lambda = 0.7\mu$m, reflectivity of the laser mirrors: $R = 0.6$, $T_{1g} = 0.5$ ns, $T_{2g} = 1$ ps, $d_{12g} = 5$ Debye, $N_{0g} = 15 \cdot 10^{15}$ cm^{-3}. (a) The stable pulsation regime in the case when only the gain section is present in the cavity. The period of the pulse train is 20 ps and equal to the half of the round-trip time. (b) Active mode-locking due to modulation of the reflectivity of one of the cavity mirrors with 20 percent depth and the period equal to the cavity round-trip time (40 ps). The repetition rate of the pulse train is now equal to the one of external modulations. (c) Passive mode-locking in a two-section laser shown in Fig. 2.18a. The length of the absorber is L_a=0.15 cm, and $T_{1a} = 0.6$ ns, $T_{2a} = 0.5$ ps, $d_{12a} = 5$ Debye, $N_{0a} = 5 \cdot 10^{15}$ cm^{-3}.

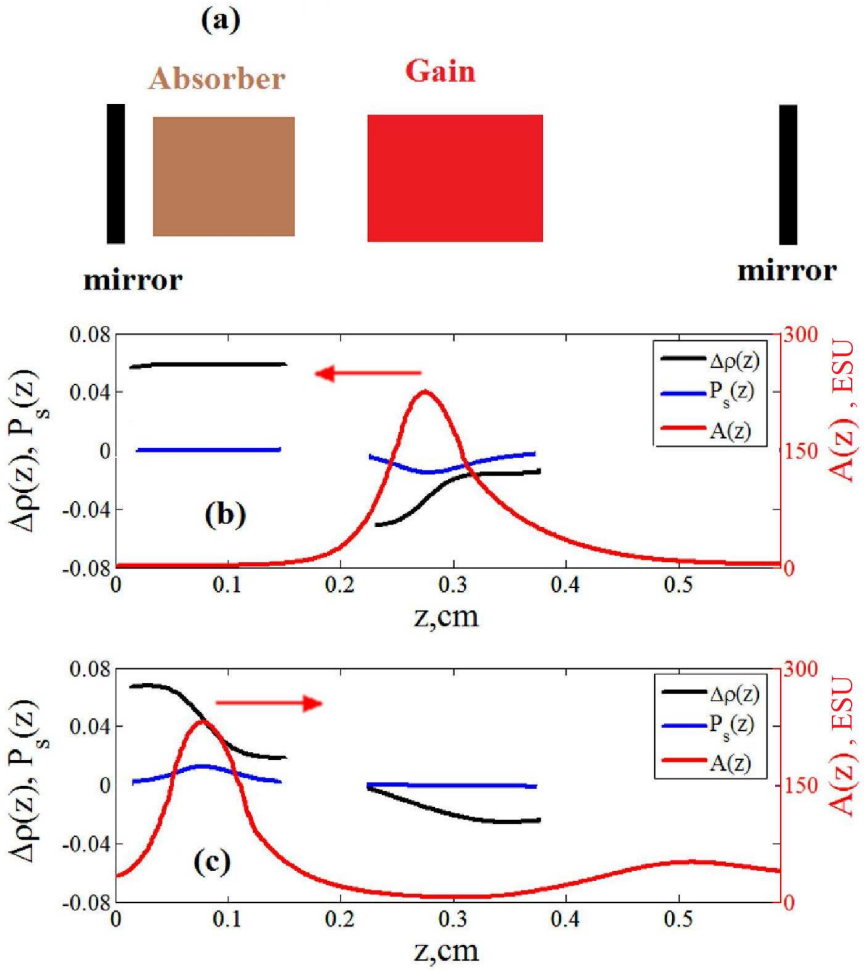

Figure 2.19: Distribution $A(z) = A^+(z) + A^-(z)$, $P_s(z) = P_s^+(z) + P_s^-(z)$ and $\Delta\rho(z)$ in the laser with the linear cavity in the regime of steady-state generation during a single pass. All the parameters are the same as in Fig. 2.18. (a) The scheme of the laser. The pulse is shown as it propagates from right to left and is located in the gain medium (b) and, at the later time moment, when it propagates from left to right and is located in the absorbing medium (c). Red arrow indicates the direction of pulse propagation.

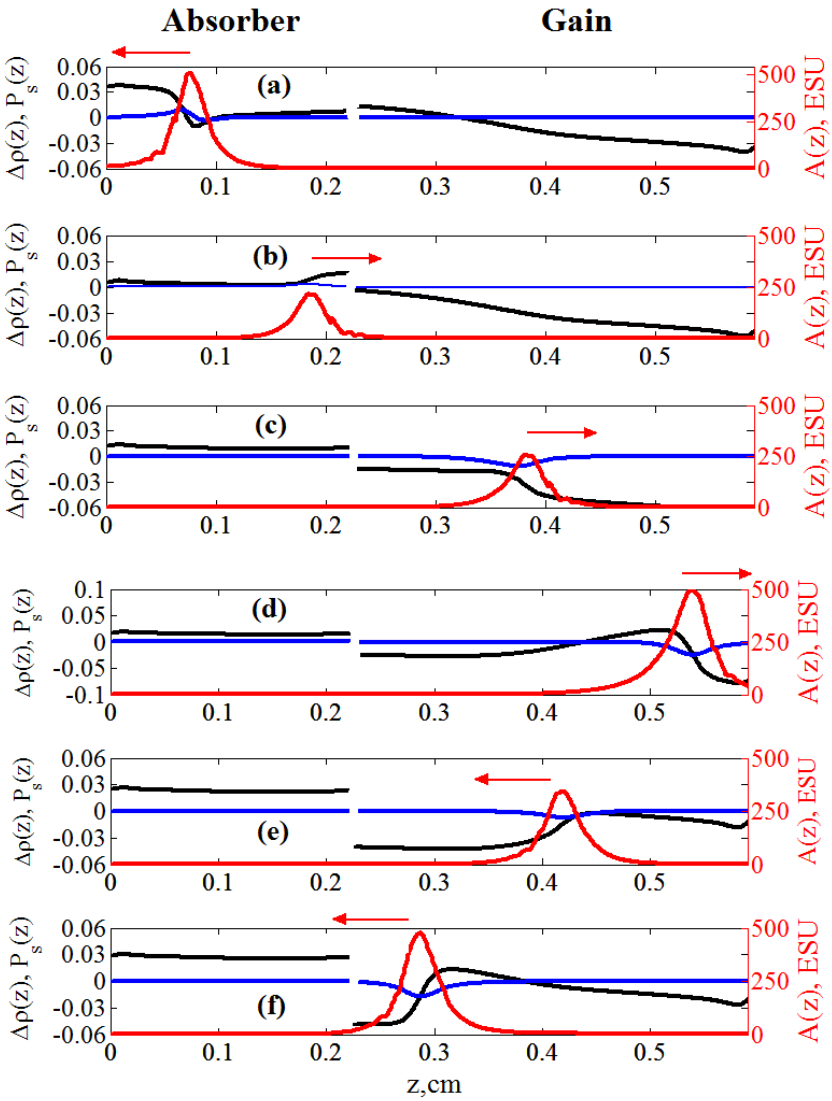

Figure 2.20: Distribution of the electric field amplitude $A(z) = A^+(z) + A^-(z)$ (red line), $P_s(z) = P_s^+(z) + P_s^-(z)$ (blue line) and $\Delta\rho(z)$ in the laser with the linear cavity in the regime of steady-state generation during one pass ($\lambda = 0.7\mu m$, $R = 0.6$, $T_{1g} = 0.5$ ns, $T_{2g} = 1$ ps, $d_{12g} = 5$ Debye, $L_g = 0.36$ cm, $T_{1a} = 1$ ns, $T_{2a} = 0.4$ ps, $d_{12a} = 10$ Debye, $L_a = 0.22$ cm, $N_{0g} = N_{0a} = 15 \cdot 10^{15}$ cm^{-3}). In (a) - (f) the consequent stages of the pulse propagation are shown, with different propagation direction (which is alternated by reflections) and pulse position in the absorber and amplifier. Red arrow indicates the direction of pulse propagation.

Another example of the coherent mode-locking regime is given in Fig. 2.21. In contrast to the previous case the polarization relaxation time in the absorber T_{2a} and the concentration of absorbing particles N_{0a} were increased. Such parameter modifications do not lead to disappearance of passive mode-locking, but modify the scenario of the pulse propagation in the cavity in the mode-locking regime and the pulse shape at the output of the laser. During the evolution the pulse exits the amplifier and enters the absorber with the area close to 2π (for the absorber), see Fig. 2.21a. Due to the losses at the left mirror ($R = 0.6$) during the back trip the pulse propagates in the absorber as a π-pulse. The leading edge of the pulse loses energy and inverts the medium. Behind the pulse, coherent polarization begins to emit electromagnetic radiation which is in anti-phase to the pulse, see Fig. 2.21b. As a result, at the input of the amplifier the pulse has the area close to zero, see Fig. 2.21c. Propagation of this pulse in the amplifying medium has the following features: the part of the pulse envelope with a negative sign is amplified not so efficiently as the leading edge, Fig. 2.21d. In the amplifier the pulse area increases and tends to π. As a result, at the laser output a train of intense short pulses with a small burst at the trailing edge is observed. After the reflection from the mirror the pulse area decreases, but during the pulse propagation in the amplifier it tends to a π pulse again, see Fig. 2.21e-Fig. 2.21f.

The burst at the trailing edge of the pulse disappears if the reflectivity on the left facet of the laser is 1. The scenario of the pulse propagation changes in the following way: from the amplifier to the absorber comes a pulse, which behaves in the absorber like 2π pulse, see Fig. 2.22a. After the reflection from the left-side mirror the pulse does not change its area and propagates as a 2π-like pulse in the absorber, Fig. 2.22b. Due to the finite relaxation time of the absorber the pulse area changes only slightly during the propagation in the absorber, and the sign change of the field envelope does not occur, see Fig. 2.22b. Then the pulse propagates in the gain section as a π pulse, see Fig. 2.22c-Fig. 2.22d. After the reflection from the mirror and propagation through the amplifying medium (Fig. 2.22e) a π pulse is formed (Fig. 2.22f). This pulse propagates as a 2π pulse in the absorber and the propagation cycle is repeated again.

In these examples the relaxation time of polarization was very close to the pulse duration (~ 1 ps). In this situation the coherent mechanism of the light-matter interaction plays a major role. However, the scenario of pulse formation differs from the case of a ring laser, considered in the previous section. The particular difference is that the existence of π (2π) pulses along the whole length of the amplifier (absorber) is not required for a passive mode-locking to arise.

Importantly, the examples of the coherent mode-locking presented in this section were reproduced by us in the large parameter range, in particular for the parameter values typical for semiconductor, solid states and gas lasers.

Besides, our numerical experiments show that the regime of coherent mode-locking is preserved if the T_2 is larger or comparable with the pulse duration and cavity round-trip time. In the linear cavity laser, analogously to the ring cavity one, the pulse duration depends on the dipole moment ratio m_d. This ratio may influence also the existence of single or multiple pulses per round-trip time. Thus, the predictions provided by the McCall and Hahn diagrams are well reproduced by numerical experiments.

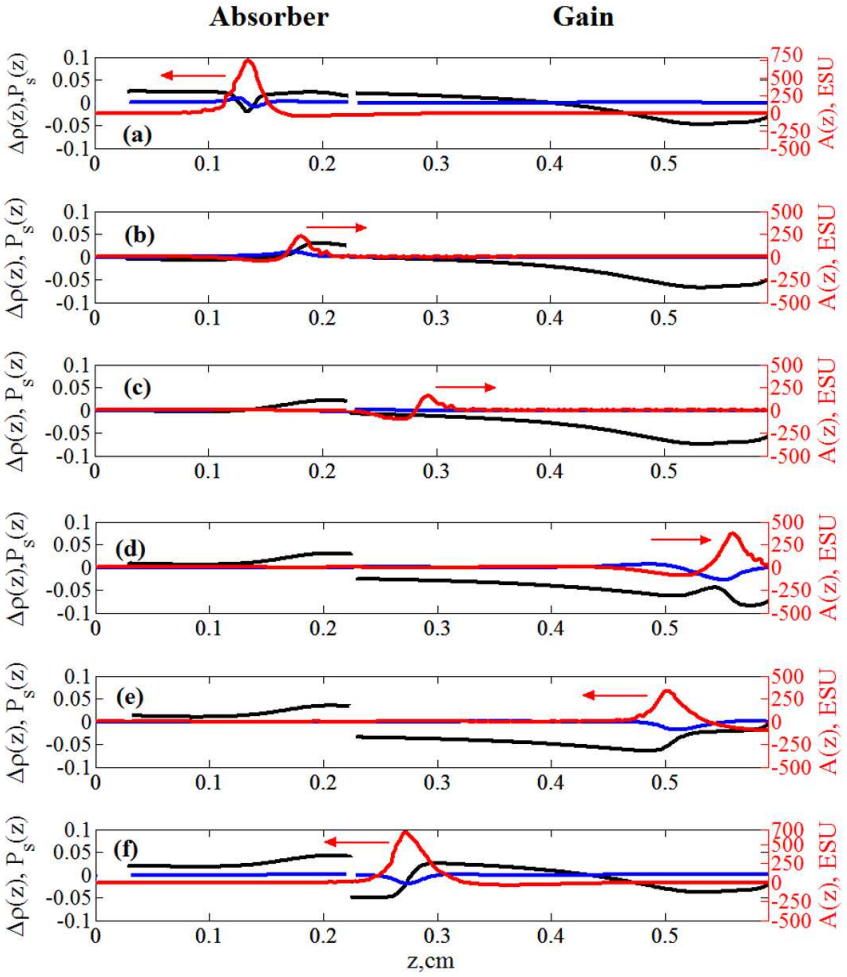

Figure 2.21: (a)-(f) Distribution of the electric field amplitude $A(z)$ (red line), polarization amplitude $P_s(z)$ (blue line) and population difference $\Delta\rho(z)$ in the laser with a linear cavity in the coherent mode-locking regime during a single round-trip for different pulse positions and propagation directions for $\lambda = 0.7\mu m$, $R = 0.6$, $T_{1g} = 0.5$ ns, $T_{2g} = 1$ ps, $d_{12g} = 5$ Debye, $L_g = 0.36$ cm, $N_{0g} = 15 \cdot 10^{15}$ cm^{-3}, $T_{1a} = 1$ ns, $T_{2a} = 1.2$ ps, $d_{12a} = 10$ Debye, $N_{0a} = 18 \cdot 10^{15}$ cm^{-3}, $L_a = 0.22$ cm. Red arrow indicates the direction of pulse propagation.

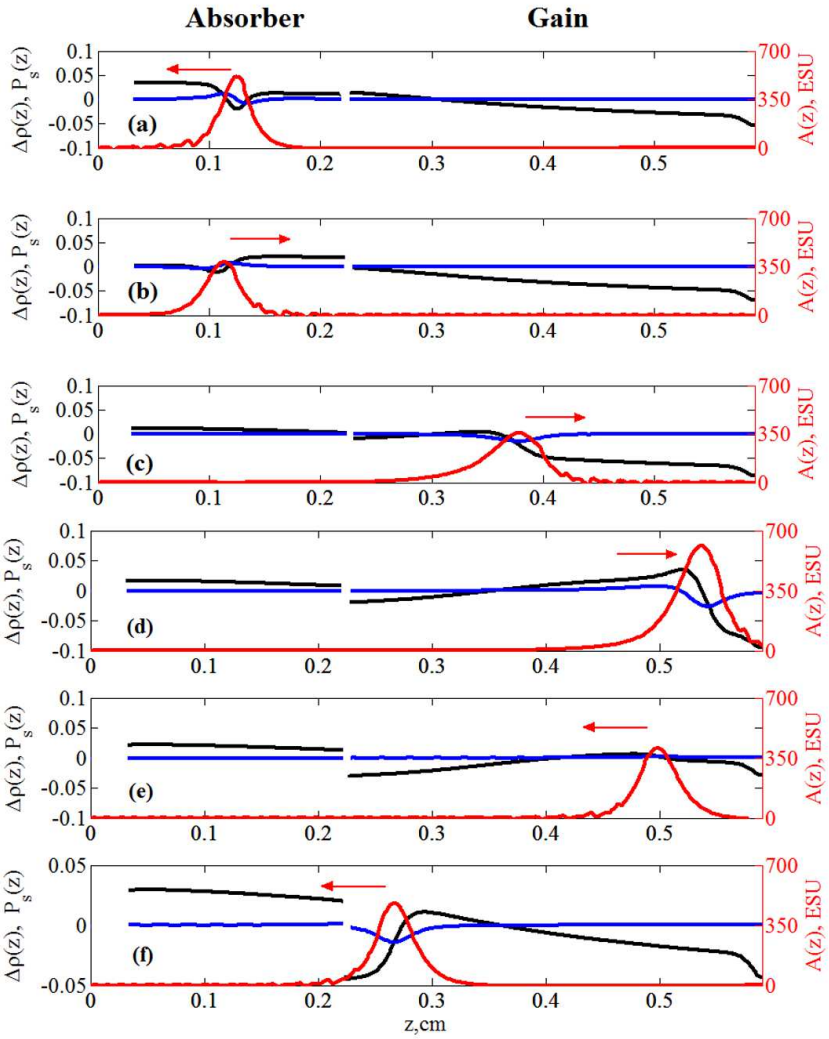

Figure 2.22: (a)-(f) Distribution of the electric field amplitude $A(z)$ (red line), polarization amplitude $P_s(z)$ (blue line) and population difference $\Delta\rho(z)$ (black line) in the linear cavity laser in the coherent passive mode-locking regime during a single round-trip for different positions and directions of propagation of pulse in the gain and absorbing sections. The reflectivity of the left mirror $R = 1$. Other parameters are as in Fig. 2.21. Red arrow indicates the direction of pulse propagation.

In summary, in this section we demonstrated a possibility of coherent mode-locking in a two-section linear cavity laser. The particular pulse regimes are quite different from the ones appearing in the ring cavity laser.

2.6 Conclusions

In this section we summarize the results of the present chapter. We have presented a theoretical justification of the possibility of coherent passive mode-locking in a two-section laser, appearing due to the coherent character of light-matter interaction. An important feature of coherent mode-locking is the possibility to generate short optical pulses with spectral bandwidth wider than the gain bandwidth of the active medium.

Qualitative consideration of the coherent passive mode-locking based on the area theorem of McCall and Hahn and its graphical representation has been performed here. We developed a diagram technique, allowing to elucidate the resulting regime qualitatively, in particular to find stable limit cycles in the system. Examples of such stable pulsed limit cycles have been presented. It has been shown that the regime of the coherent mode-locking can occur, depending on the parameters, via self-starting, or via an injection of an external seed pulse. The parameters of the pulses depend heavily on the ratio of the transition dipole moments of the absorber and the gain media. The duration of the pulse decreases if this ratio increases. When it is smaller than 1 or more than 3, multiple pulses on a single cavity round-trip arise.

To perform numerical experiments, a model of a two-section laser has been developed, which is based on Maxwell-Bloch equations in the slowly varying envelope approximation. The results of numerical experiments have demonstrated the existence of coherent mode-locking regimes in a two-section laser with a ring or linear cavity in a wide range of parameters. The regime of coherent mode-locking can be realized in semiconductor lasers, solid-state or gas lasers. The results of the numerical simulations show also that certain amount of energy is saved in the absorber in between the pulse passages, allowing for complicated pulse-to-pulse dynamics. The scenarios of coherent mode-locking which have been considered in this chapter differ from those previously proposed in the literature. In particular, to realize stable coherent mode-locking regime in a two-section laser the injection of an external seeding pulse has been shown to be unnecessary. Our numerical simulations show also that the coherent mode-locking exists in the lasers with cavities having low Q factors, unlike the earlier proposal of a soliton laser in [30].

Finally, it is to be mentioned that the effect of SIT was discovered and explained by McCall and Hahn more than 40 years ago. However, the SIT has not found up to now significant applications in photonics because of high powers and high instrumental precision needed for this technique. From the practical point of view, the incoherent mode-locking schemes have been up to now superior over coherent ones. Nevertheless we believe that implementation of the coherent mode-locking in two-section lasers proposed here allows to overcome the fundamental limits of the “classical” mode-locking techniques and to use such lasers as sources of ultrashort pulses with high repetition rate.

3 Theoretical investigation of hybrid mode-locking in semiconductor lasers

In the following chapter the theoretical modeling of hybrid mode-locking in semiconductor lasers is considered.

3.1 Hybrid mode-locking

Due to the presence of noise sources, pulses emitted by PML lasers usually exhibit a considerable timing jitter that can be of the order of 10 ps for 40-GHz PML lasers [120]. An effective method for suppressing this jitter down to hundreds of femtoseconds is based on hybrid mode-locking (HML) which is a combination of active and passive mode-locking techniques. In hybrid mode-locked lasers the reverse bias applied to the saturable absorber (SA) section is modulated at the frequency f_M close to the pulse repetition frequency f_P of the free-running PML laser [37–42]. A schematic representation of a hybrid mode-locked laser is given by in Fig. 3.1.

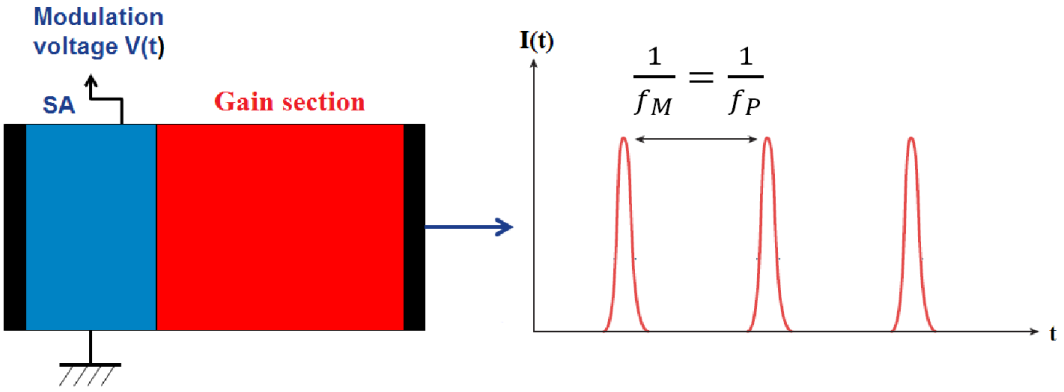

Figure 3.1: Schematic representation of a hybrid mode-locked semiconductor laser. External radio frequency voltage modulation is applied to the saturable absorber section.

When the frequency detuning $\delta f = f_M - f_P$ becomes sufficiently small, the pulse repetition frequency synchronizes to the frequency f_M of the external modulation. The interval of detunings δf, where this synchronization takes place is usually referred to as the locking range.

Experimental studies of HML were performed in different types of semiconductor lasers, see Refs. [40–42, 121, 122]. In Ref. [121] hybrid mode-locking was achieved in quantum dot lasers. Experiments provided in Ref. [40, 41, 121] demonstrated a significant reduction of the pulse jitter using HML down to hundreds of fs for mode-locked quantum dot lasers. In [42, 122] an experimental study of HML in quantum dot laser with a pulse repetition rate of 40 GHz was reported. It was demonstrated experimentally in Ref. [122] that HML has a small influence on the pulse shape and chirp and only leads to decrease of the the pulse timing jitter.

In Ref. [42] an evolution of the locking range with an increase of the external RF voltage modulation amplitude was investigated experimentally and theoretically. Experimental investigations provided in Ref. [42] were performed using a monolithic 40-GHz two-section quantum dot laser diode with total length of 1 mm. The saturable absorber length was 1/10 of the total length. Modulation voltage applied to the SA section had a harmonic form and contained DC component of the reverse bias applied to the SA section. The locking range was investigated for different values of injection current in the gain section and reverse bias applied to the absorber section. The frequency of the external voltage f_M was varied around the pulse repetition frequency of the PML laser f_P. Locking was observed when the frequency $f_M \approx f_P$. It was demonstrated experimentally that the locking range increases almost linearly with the modulation amplitude and exhibits a strong asymmetry with respect to the frequency f_P.

The theoretical study of the HML performed in Ref. [42] was based on the set of delay differential equations describing the dynamics of a quantum dot mode-locked laser taking into account the carrier exchange between carrier reservoir and discrete levels in quantum dots, see Ref. [123]. Numerical simulations showed qualitative agreement with the experimental data. It was demonstrated theoretically that for sufficiently large values of modulation amplitude the locking range is strongly asymmetric with respect to the frequency f_P. It was reported in Ref. [42] that this asymmetry is related to the nonlinear dependence of the pulse repetition frequency on the modulation amplitude. Detailed analysis of the possible reasons for this asymmetry will be performed in this chapter (see Section 3.7).

The dependence of the locking range on the reverse bias applied to the SA section was also studied experimentally in [42]. It was found that the locking range increases linearly with modulation amplitude for all values of the reverse bias applied to the absorber section. When reverse bias was varied between -4 to -8 V the locking range decreases with the bias. Further increase of negative bias up to -10 V leads to increase of the locking range, i.e. locking range has parabolic dependence on the reverse bias.

In this chapter we perform a detailed theoretical analysis of hybrid mode-locking in semiconductor lasers. Our analysis is based on a set of three delay differential equations describing time evolution of the field amplitude, saturable gain, and saturable absorption. In our analysis we will use the system of delay differential equations derived in Refs. [100–102]. We present numerical estimates of the locking range width of a fundamental mode-locking regime (where pulsation frequency f_P is close to the inverse cavity round-trip time) for three different cases of harmonic voltage modulation. In addition to the standard case, where the frequency of the external modulation is close to the

pulse repetition frequency, $f_M \approx f_P$, we consider the cases when the frequency of the external signal is close to second-harmonic of the frequency f_P, $f_M \approx 2f_P$, [second harmonic modulation (SHM)] and to half of the frequency f_P, $f_M \approx f_P/2$, [half frequency modulation (HFM)]. Our simulations show that in the standard and SHM cases the locking regions grow almost linearly with the modulation amplitude a and have nearly the same width. In contrast to that, the HFM provides a smaller and strongly nonlinear locking region. In Section 3.5 we perform an asymptotic analysis of model equations and obtain estimates for the locking range width at small modulation amplitudes. We demonstrate that these estimates are valid at moderate and even large modulation amplitudes not only for standard, but also for SHM hybrid mode-locking and analyze the impact of different laser parameters on the locking range. In Section 3.7 we discuss the possible reasons of the asymmetry of the locking regions. We show that this asymmetry can be related to the dependence of the pulse repetition frequency on the modulation amplitude. Finally, in Section 3.8 we discuss the results of experimental investigations which provide evidence of HFM hybrid mode-locking in a 20-GHz quantum dot laser. In line with theoretical predictions these results demonstrate that the HFM hybrid mode-locking region is sufficiently smaller than that of the standard case. Experiment was performed at TU Berlin by Dejan Arsenijević. The majority of the results presented in this chapter below were published in own publication, Ref. [87]:
R. Arkhipov, A. Pimenov, M. Radziunas, D. Rachinskii, A. G. Vladimirov, D. Arsenijević, H. Schmeckebier, and D. Bimberg. Hybrid mode-locking in semiconductor lasers: simulations, analysis and experiments, IEEE Journal of Selected Topics in Quantum Electronics, Vol. 19, p.100208, 2013

3.2 Theoretical model

To study the dynamics of two-section hybrid mode-locked semiconductor lasers, we use a dimensionless system of delay differential equations (DDE) describing unidirectional lasing in a ring PML laser. The DDE model governs the time evolution of the complex optical field amplitude $A(t)$ at the entrance of the absorber section as well as the saturable gain $G(t)$ and saturable absorption $Q(t)$ functions in the gain and saturable absorber sections of the device. It can be written in the form [100–102]:

$$\frac{1}{\gamma}\frac{dA}{dt} = -A + \sqrt{\kappa} e^{\frac{(1-i\alpha_g)G(t-T)-(1-i\alpha_q)Q(t-T)}{2}} A(t-T), \tag{3.1}$$

$$\frac{dG}{dt} = g_0 - \gamma_g G - e^{-Q}\left(e^{G}-1\right)|A|^2; \tag{3.2}$$

$$\frac{dQ}{dt} = \gamma_q(1+aF(t))(q_0-Q) - s\left(1-e^{-Q}\right)|A|^2. \tag{3.3}$$

Here α_g and α_q are the linewidth enhancement factors in the gain and absorber sections, respectively, the delay parameter T is equal to the cold cavity round-trip time, γ is the spectral filtering bandwidth, κ is the attenuation factor describing linear non-resonant intensity losses per cavity round trip, and s is the ratio of the saturation intensities in

the gain and absorber sections. The pump parameter g_0 is proportional to the injection current in the gain region, q_0 is the unsaturated absorption parameter, γ_g and γ_q are the relaxation rates of the gain and the saturable absorber, respectively. The parameters used in simulations were similar to those in Ref. [42] used for simulations of 40 GHz PML laser. Without the loss of generality, by scaling the time variable, the cold cavity field round-trip time T in the Eq. (3.1) was set to unity. Typical values of the model parameters are given in Table 3.1. In our simulations and analysis, we first start with the simplest case of zero linewidth enhancement factors, $\alpha_{g,q} = 0$. The case of non-zero linewidth enhancement factors α_g, α_q in the gain and absorber sections will be considered in the Section 3.6.

Table 3.1: Typical parameter values used in simulations

cold cavity round-trip time	T	1
linewidth enhancement factor in the gain section	α_g	1.7
linewidth enhancement factor in the SA	α_q	1
spectral filtering bandwidth	γ	37.5
non-resonant field intensity attenuation factor per cavity round-trip	κ	0.3
pump parameter	g_0	1.25
unsaturated absorption	q_0	2
gain relaxation rate	γ_g	0.025
SA relaxation rate	γ_q	2.5
ratio of gain/absorber saturation intensities	s	10

Following Refs. [42, 124], we assume that the reverse bias modulation affects only the SA absorber relaxation rate γ_q. Therefore, in the model equation (3.3) this rate is multiplied by the factor $1 + aF(t)$. The function F represents a periodic voltage modulation (VM) with the frequency f_M and the modulation amplitude a.

3.3 Locking regions in a parameter plane

In this section we describe the results of numerical simulations of the domains of hybrid mode-locking where the pulse repetition frequency is locked to the frequency of the external harmonic modulation.

First, we integrated numerically the model equations (3.1)-(3.3) with the parameter values given in Table 3.1 and zero amplitude of the voltage modulation ($a = 0$). As a result we obtained the passive mode-locking pulsations with pulse repetition frequency $f_P \approx 0.9723$.

Next, we studied the case when modulation of the SA reverse bias take the harmonic form:

$$F = F_0(t) = \cos(2\pi f_M t), \tag{3.4}$$

where the frequency is $f_M = f_P + \delta f$ and δf is a small frequency detuning. Let us

describe the procedure we used in order to calculate the width of the locking range for a fixed value of modulation amplitude $a > 0$. For each value of the frequency detuning δf from some interval we performed a long-term numerical integration of the model equations (3.1)-(3.3) taking the solution calculated at the previous value δf as the initial condition.

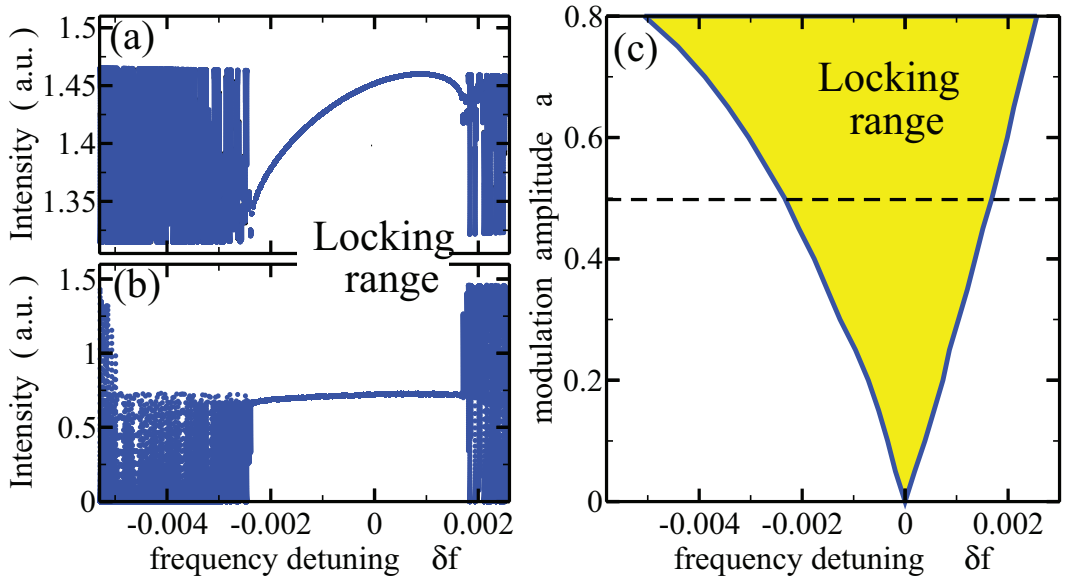

Figure 3.2: Numerical estimate of the locking range of a hybrid mode-locked laser. (a): Local maxima of the intensity time trace and (b): $1/f_M$-periodic stroboscopic map points of emitted field intensity at fixed modulation amplitude $a = 0.5$. In the locking range all mode-locked pulses have the same peak intensity at fixed given δf. (c): Locking tongue in the plane of two parameters: frequency detuning δf and modulation amplitude a. Other parameter values are as in Table 3.1.

The results of numerical simulations are illustrated in Fig. 3.2(a,b). Fig. 3.2a shows the local maxima of the laser field intensity time trace for the 200 last time units of the integration interval versus δf. When detuning $|\delta f|$ is sufficiently small we observe locking of the pulse repetition frequency to the frequency of the external modulation f_M . The resulting hybrid mode-locking regime is strictly $1/f_M$ - periodic and all the recorded field maxima at a fixed δf have the same value. On the other hand, for frequency detuning outside of the locking interval, we observed irregular or quasi-periodic dynamical regimes in the numerical simulations. This case corresponds to the multiple intensity peak values (cloud of points) for each value of the corresponding frequency detuning δf. In Fig. 3.2b we present the optical field component of the stroboscopic map for each δf. Here, for all considered values of detuning δf we have collected the field intensities separated from each other in time by the interval $1/f_M$. Once locking is achieved and the pulse repetition period is equal to $1/f_M$, all stroboscopic map points have the same value.

Outside of the locking region, multiple values of this map at a given δf are observed in the numerical simulations. Both diagrams in Fig. 3.2(a,b) were used to estimate the locking interval (locking range) boundaries.

By estimating the locking range at different values of the modulation amplitude a we obtain the domain of HML (the locking tongue) in the two parameter plane δf and a, see Fig. 3.2(c). One can see that the locking range increases almost linearly with the modulation amplitude a.

3.4 Second-harmonic and half frequency modulations

In this section we consider the cases when the external modulation frequency f_M is close either to the second harmonic of the frequency f_P, i.e., $\delta f = f_M/2 - f_P \ll f_P$, or to the first subharmonic of this frequency, $\delta f = 2f_M - f_P \ll f_P$. We show that in both these cases the pulse repetition frequency can be synchronized with the external modulation. Typical examples of the second-harmonic modulation (SHM), half frequency modulation (HFM), and standard HML states are represented in Fig. 3.3a, b and c.

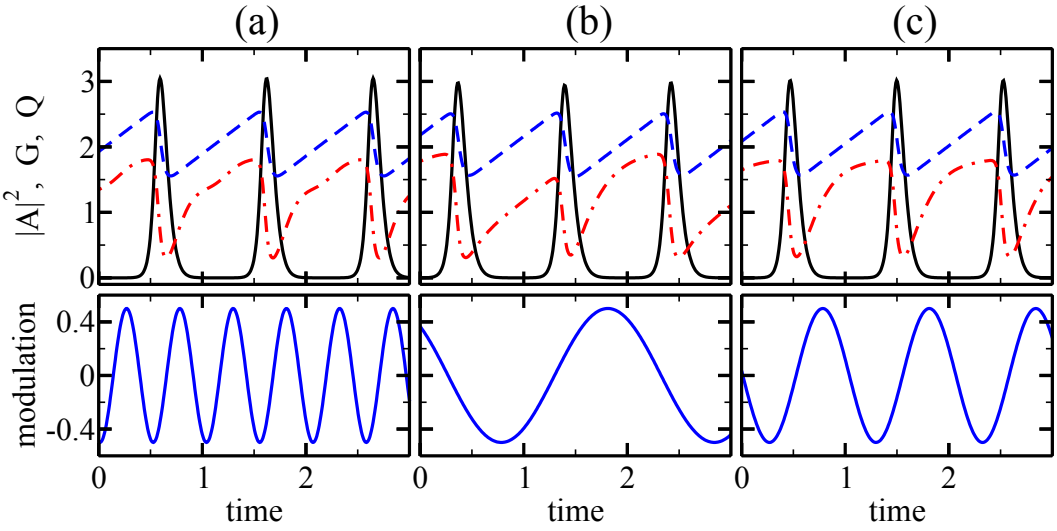

Figure 3.3: Hybrid mode-locked regimes for modulation amplitude $a = 0.5$ and (a): $f_M = 1.945 \approx 2f_P$, (b): $f_M = 0.48625 \approx f_P/2$, and (c): $f_M = 0.9725 \approx f_P$. Other parameter values are as in Table 3.1. Black solid, blue dashed, and red dash-dotted curves in the upper panels represent the field intensity $|A(t)|^2$, gain $G(t)$, and absorption $Q(t)$, respectively. Solid blue curve in the lower panels represents the time dependence of the modulation function $F(t)$ (3.4).

In all the cases shown in Fig. 3.3 the frequency detuning δf is small and the pulse repetition frequency is close (or equal) to the f_P. In the case of standard modulation [panel (c)] and SHM [panel (a)] the period of the mode-locked solution is close to the pulse repetition period $1/f_P$ of the free-running PML laser. In the case of SHM this

period contains exactly two modulation cycles of the function $F(t)$, see the blue solid curve in the lower panel of Fig. 3.3(a). In contrast to this, in the case of HFM we have $1/f_M \approx 2/f_P$. Therefore in this case, the exact period of hybrid mode-locked solution is also approximately two times larger than $1/f_P$ and contains a pair of slightly different mode-locked pulses, see Fig. 3.3(b), where the difference between the two consequent pulses can be better seen in the time-trace of the saturable absorption $Q(t)$ (red dashed-dotted curve) and Fig 3.4. Since the external modulation gives rise to a difference in the peak values between two subsequent pulses, this difference will increase with the modulation amplitude a.

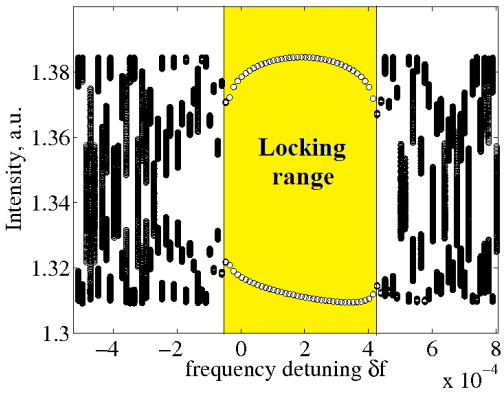

Figure 3.4: Local maxima of the intensity timetrace. Modulation amplitude $a = 0.5$. In HFM case locking range is characterized by a pair of slightly different pulse maxima. Other parameter values are as in Table 3.1.

Fig. 3.5 shows the domains of HML (locking tongues) in the plane of two parameters: frequency detuning δf and modulation amplitude a, for all the three cases mentioned above. One can see from Fig. 3.5 that the locking range of the standard modulation and the SHM have almost equal widths, and the locking tongues are nearly symmetric with respect to $\delta f = 0$. On the other hand, the locking tongue corresponding to the HFM case is located within a significantly smaller and strongly asymmetric domain. Moreover, the numerically calculated boundaries of this locking tongue are strongly nonlinear. Therefore, it is difficult to calculate numerically this quite narrow locking range when modulation amplitude a is small. Such nonlinear dependence of the locking range on the modulation amplitude is typical for the subharmonic resonance 1:2 [125]. A similar behavior of the HML domains was found in the case of non-zero linewidth enhancement factors, $\alpha_g = 1.7, \alpha_q = 1$.

3.5 Asymptotic analysis

Here, using a perturbative approach, we derive an analytical expression for the locking range width δf_{LR} in the case of a weak harmonic modulation of the absorber relaxation

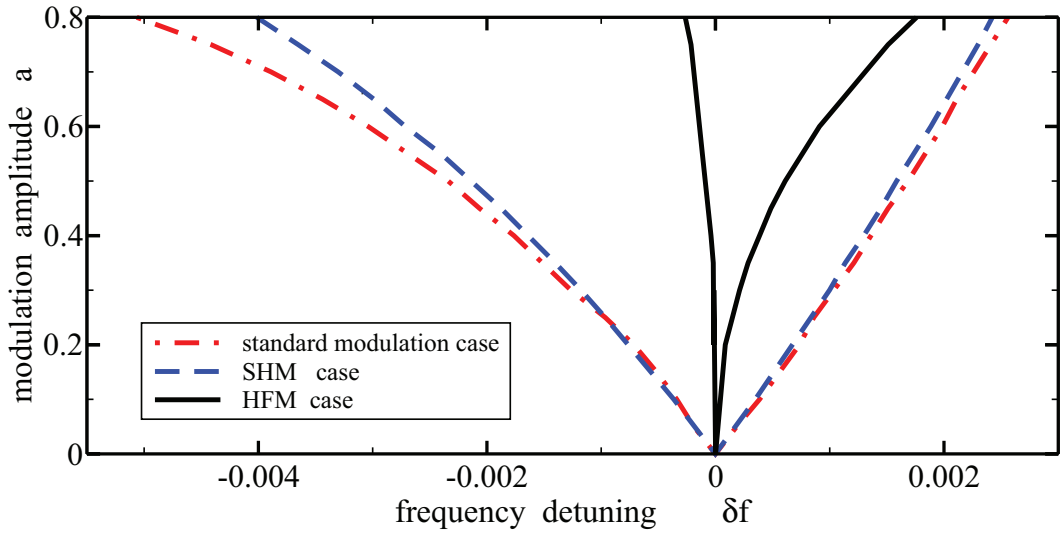

Figure 3.5: Domains of hybrid mode-locking in the plane of two parameters: frequency detuning and modulation amplitude. Red dashed-dotted, blue dashed, and solid black curves represent boundaries of standard, SHM, and HFM hybrid mode-locking in the case of $\alpha_g = \alpha_q = 0$. Other parameter values are as in Table 3.1.

rate with the frequency $f_M = f_P + \delta f$, $\delta f \ll f_P$. We consider the situation when for zero modulation amplitude $a = 0$, the model (3.1)-(3.3) has a fundamental mode-locking solution

$$A(t) = A_0(t)e^{i\Omega t}, \quad G(t) = G_0(t), \quad Q(t) = Q_0(t), \tag{3.5}$$

where $A_0(t)$, $G_0(t)$, and $Q_0(t)$ are periodic functions with the period $T_0 = 1/f_P$ close to 1 and the value of Ω depends on the linewidth enhancement factors in the gain and absorber sections, α_g and α_q.

For nonzero modulation amplitudes a the time shift invariance $A(t) \to A(t + t')$, $G(t) \to G(t + t')$, $Q(t) \to Q(t + t')$ of the model equations Eqs. (3.1)-(3.3) is broken and a synchronization of the pulse repetition frequency f_P to the external modulation frequency f_M can take place. When the frequency detuning $\delta f = f_M - f_P$ is sufficiently small, the hybrid mode-locking regime with the pulse repetition frequency f_M can appear. We use perturbation analysis to estimate the width of the locking range δf_{LR} at small modulation amplitudes $a \ll 1$. This perturbation analysis is based on the method of multiple time scales [87, 105, 126]. We introduce two time scales $\tau_0 = t$ and $\tau_1 = at$ with operators of differentiation $D_0 = \frac{\partial}{\partial \tau_0}$ and $D_1 = \frac{\partial}{\partial \tau_1}$. Time derivatives are given by: $\frac{dA}{dt} = D_0 A + aD_1 A$, $\frac{dG}{dt} = D_0 G + aD_1 G$ and $\frac{dQ}{dt} = D_0 Q + aD_1 Q$.

We are looking for the solutions of Eqs. (3.1)-(3.3) in the form: $A(t) = A_0[\tau_0 + \theta(\tau_1)]e^{i\varphi(\tau_1)} + aA^1[\tau_0 + \theta(\tau_1), \tau_1]e^{i\varphi(\tau_1)} + ...$, $G(t) = G_0[\tau_0 + \theta(\tau_1)] + aG^1[\tau_0 + \theta(\tau_1), \tau_1]e^{i\varphi(\tau_1)} + ...$, and $Q(t) = Q_0[\tau_0 + \theta(\tau_1)] + aQ^1[\tau_0 + \theta(\tau_1), \tau_1]e^{i\varphi(\tau_1)} + ...$, where A^1, G^1, Q^1 are the small perturbations, and θ and φ are slowly varying functions of time. By substitut-

ing these expansions into Eqs. (3.1)-(3.3) and collecting first order terms in the small parameter a, we obtain an inhomogeneous linear equation for the real vector of small perturbations $\delta\psi = \left(ReA^1, ImA^1, G^1, Q^1\right)^t$ (superscript t denotes transposition):

$$-\frac{d}{dt}\delta\psi + \mathcal{L}(t)\delta\psi + \mathcal{M}(t-T)\delta\psi(t-T) = \mathcal{F}(t). \tag{3.6}$$

Using the following notations $A_{r0} = ReA_0$, $A_{i0} = ImA_0$ Jacobian matrices $\mathcal{L}$ and $\mathcal{M}$ can be written in the form:

$$\mathcal{L} = \begin{pmatrix} -\gamma & \Omega & 0 & 0 \\ -\Omega & -\gamma & 0 & 0 \\ -2e^{-Q_0}(e^{G_0}-1)A_{r0} & -2e^{-Q_0}(e^{G_0}-1)A_{i0} & -\gamma_g - e^{G_0-Q_0}|A_0|^2 & e^{-Q_0}(e^{G_0}-1)|A_0|^2 \\ -2s(1-e^{-Q_0})A_{r0} & -2s(1-e^{-Q_0})A_{i0} & 0 & -\gamma_q - se^{-Q_0}|A_0|^2 \end{pmatrix}. \tag{3.7}$$

$$\mathcal{M} = \gamma\sqrt{\kappa}e^{(G_0-Q_0)/2}\begin{pmatrix} 2\cos\alpha & 2\sin\alpha & \mathcal{M}_{13} & \mathcal{M}_{14} \\ -2\sin\alpha & 2\cos\alpha & \mathcal{M}_{23} & \mathcal{M}_{24} \\ 0 & 0 & 0 & 0 \\ 0 & 0 & 0 & 0 \end{pmatrix}. \tag{3.8}$$

where $\alpha = (\alpha_g G_0 - \alpha_q Q_0)/2 + \Omega T$, $\mathcal{M}_{13} = (A_{r0} + \alpha_g A_{i0})\cos\alpha + (A_{i0} - \alpha_g A_{r0})\sin\alpha$, $\mathcal{M}_{14} = -(A_{r0} + \alpha_q A_{i0})\cos\alpha - (A_{i0} - \alpha_q A_{r0})\sin\alpha$, $\mathcal{M}_{23} = -(A_{r0} + \alpha_g A_{i0})\sin\alpha + (A_{i0} - \alpha_g A_{r0})\cos\alpha$, $\mathcal{M}_{24} = (A_{r0} + \alpha_q A_{i0})\sin\alpha - (A_{i0} - \alpha_q A_{r0})\cos\alpha$.

The homogeneous Eq. (3.6) with $\mathcal{F}(t) = 0$ has two vector solutions χ_φ and χ_θ associated with the phase shift $A \to Ae^{i\phi}$, $G \to G$, $Q \to Q$ and time shift $A(t) \to A(t+t')$, $G(t) \to G(t+t')$, $Q(t) \to Q(t+t')$ symmetries of Eqs. (3.1)-(3.3) with $a = 0$. These solutions can be written as [87, 105]: $\chi_\varphi(t) = (-ImA_0, ReA_0, 0, 0)^t$, and $\chi_\theta = \frac{d}{dt}\psi_0$, where $\psi_0 = (ReA_0, ImA_0, G_0, Q_0)^t$. The adjoint neutral vector-functions $\chi^\dagger_\varphi(t)$ and $\chi^\dagger_\theta(t)$ are defined as periodic solutions of the adjoint linear problem:

$$\frac{d}{dt}\delta\psi^\dagger + \mathcal{L}^t(t)\delta\psi^\dagger + \mathcal{M}^t(t)\delta\psi^\dagger(t+T) = 0. \tag{3.9}$$

These modes satisfy the orthonormalization conditions

$$\langle\chi_j, \chi^\dagger_k\rangle := \int_0^{T_0}\sum_{s=1}^{4}\chi_{js}(t')\chi^\dagger_{ks}(t')dt' = \delta_{kj}, \tag{3.10}$$

where $j, k = \varphi, \theta$, and δ_{kj} is the Kronecker symbol.

The right side of the Eq. (3.6) is

$$\mathcal{F} = \begin{pmatrix} -(\dot{A_{r0}} + T\ddot{A_{r0}} + T\gamma\dot{A_{r0}} - \Omega T\dot{A_{i0}})D_1\theta + (A_{i0} + T\dot{A_{i0}} + T\gamma A_{i0} + \Omega T A_{r0})D_1\varphi \\ -(\dot{A_{i0}} + T\ddot{A_{i0}} + T\gamma\dot{A_{i0}} + \Omega T\dot{A_{r0}})D_1\theta - (A_{r0} + T\dot{A_{r0}} + T\gamma A_{r0} - \Omega T A_{i0})D_1\varphi \\ -\dot{G_0}D_1\theta \\ -\dot{Q_0}D_1\theta + \gamma_q a F(t)(q_0 - Q_0) \end{pmatrix} \tag{3.11}$$

Here we used notations: $\dot{A_{r0}} = \frac{dA_{r0}}{d\tau_0}$, $\ddot{A_{r0}} = \frac{d^2A_{r0}}{d\tau_0^2}$ and $\dot{A_{i0}} = \frac{dA_{i0}}{d\tau_0}$, $\ddot{A_{i0}} = \frac{d^2A_{i0}}{d\tau_0^2}$.

To calculate the adjoint neutral modes $\chi^\dagger_\varphi(t)$ and $\chi^\dagger_\theta(t)$ we solve Eq. (3.9) numerically in reverse time with two linearly independent initial conditions $(0,0,0.1,0)^t$ and $(2,0,1,1)^t$ and obtain the solutions $Y = (Y_1, Y_2, Y_3, Y_4)^t$ and $Z = (Z_1, Z_2, Z_3, Z_4)^t$. The desired adjoint functions $\chi^\dagger_\theta(t)$ and $\chi^\dagger_\varphi(t)$ can be represented as a linear combination of Y and Z: $\chi^\dagger_\varphi(t) = c_1^\varphi Z + c_2^\varphi Y$ and $\chi^\dagger_\theta(t) = c_1^\theta Z + c_2^\theta Y$. Using the biorthogonality conditions Eq. (3.10)we obtain the coefficients $c_{1,2}^{\varphi,\theta}$:

$$c_1^\varphi = \frac{1}{\langle Z, \chi_\varphi\rangle - \langle Y, \chi_\varphi\rangle\langle Z, \chi_\theta\rangle / \langle Y, \chi_\theta\rangle}, \tag{3.12}$$

$$c_2^\varphi = \frac{1}{\langle Y, \chi_\varphi\rangle - \langle Z, \chi_\varphi\rangle\langle Y, \chi_\theta\rangle / \langle Z, \chi_\theta\rangle}, \tag{3.13}$$

$$c_1^\theta = \frac{1}{\langle Z, \chi_\theta\rangle - \langle Y, \chi_\theta\rangle\langle Z, \chi_\varphi\rangle / \langle Y, \chi_\varphi\rangle}, \tag{3.14}$$

$$c_2^\theta = \frac{1}{\langle Y, \chi_\theta\rangle - \langle Z, \chi_\theta\rangle\langle Y, \chi_\varphi\rangle / \langle Z, \chi_\varphi\rangle}. \tag{3.15}$$

According to the Fredholm alternative, the equation Eq. (3.6) is solvable provided its inhomogeneous part $\mathcal{F}$ is orthogonal to the adjoint neutral modes $\chi^\dagger_\theta$ and $\chi^\dagger_\varphi$. Since our functions are T_0-periodic, we can apply inner product in the following way:

$$\langle u(t+\theta), v(t+\theta)\rangle = \int_\theta^{T_0+\theta} u(t+\theta)v^t(t+\theta)dt = \int_0^{T_0} u(t)v^t(t)dt. \tag{3.16}$$

Orthogonality condition $\langle \chi^\dagger_\varphi, \mathcal{F}\rangle = 0$ leads to the following equation:

$$c_1 D_1\theta + c_2 D_1\varphi = a\gamma_q c_3, \tag{3.17}$$

where

$$c_1 = T\int_0^{T_0} (\ddot{A_{r0}} + \gamma\dot{A_{r0}} - \Omega\dot{A_{i0}})\chi^\dagger_{\varphi 1} + (\ddot{A_{i0}} + \gamma\dot{A_{r0}} + \dot{\Omega_{r0}})\chi^\dagger_{\varphi 2}dt, \tag{3.18}$$

$$c_2 = \int_0^{T_0} -(A_{i0} + \gamma T\dot{A_{i0}} + \Omega T A_{r0})\chi^\dagger_{\varphi 1} + (A_{r0} + T\dot{A_{r0}} + \gamma T A_{r0} - \Omega T A_{i0})\chi^\dagger_{\varphi 2}dt, \tag{3.19}$$

$$c_3 = \int_\theta^{T_0+\theta} \cos\left(2\pi(f_P + \delta f)t\right)(q_0 - Q_0(t+\theta))\chi^\dagger_{\varphi 4}(t+\theta)dt. \tag{3.20}$$

According to Eq. (3.16) formula (3.20) can be rewritten as:

$$c_3 = \int_{\theta}^{T_0+\theta} \cos\left(2\pi(f_P+\delta f)t\right)\left(q_0 - Q_0(t+\theta)\right)\chi^{\dagger}_{\varphi 4}(t+\theta)dt \simeq$$
$$\simeq \int_{0}^{T_0} \cos\left(2\pi(f_P+\delta f)(t-\theta)\right)\left(q_0 - Q_0(t)\right)\chi^{\dagger}_{\varphi 4}(t)dt.$$

After shifting the time variable $t \to t-\theta$ the expression under the integral in Eq. (3.20) becomes:

$$\cos(2\pi f_P t + 2\pi\delta f t - 2\pi\theta f_P)(q_0 - Q_0(t))\chi^{\dagger}_{\varphi 4}(t), \tag{3.21}$$

where we have neglected the term $\theta\delta f$ in the cos argument using the relation $\delta f \ll f_P$. In the locked state

$$\Theta \equiv 2\pi\delta f t - 2\pi f_P\theta = const, \tag{3.22}$$

as the frequency of the solution is synchronized to the external modulation frequency. Therefore, for the locked state we obtain the following equation:

$$c_1 D_1\theta + c_2 D_1\varphi = a\gamma_q(c_{3c}\cos\Theta + c_{3s}\sin\Theta), \tag{3.23}$$

where

$$c_{3c} = \int_0^{T_0} \cos(2\pi f_P t)(q_0 - Q_0(t))\chi^{\dagger}_{\varphi 4}dt,$$

$$c_{3s} = \int_0^{T_0} \sin(2\pi f_P t)(q_0 - Q_0(t))\chi^{\dagger}_{\varphi 4}dt.$$

From the orthogonality condition $\langle\chi^{\dagger}_{\theta}, \mathcal{F}\rangle = 0$ we get:

$$c_4 D_1\theta + c_5 D_1\varphi = a\gamma_q\left(c_{6c}\cos\Theta + c_{6s}\sin\Theta\right), \tag{3.24}$$

where

$$c_4 = \int_0^{T_0} [(T\ddot{A}_{r0} + \gamma T\dot{A}_{r0} - \Omega T\dot{A}_{i0})\chi^{\dagger}_{\theta 1} + (T\ddot{A}_{i0} + \gamma T\dot{A}_{i0} + \Omega T\dot{A}_{r0})\chi^{\dagger}_{\theta 2} + 1]dt,$$

$$c_{6c} = \int_0^{T_0} \cos(2\pi f_P t)(q_0 - Q_0(t))\chi^{\dagger}_{\theta 4}dt,$$

$$c_{6s} = \int_0^{T_0} \sin(2\pi f_P t)(q_0 - Q_0(t))\chi^{\dagger}_{\theta 4}dt.$$

Expressions (3.23) and (3.24) are the system of linear algebraic equations on $D_1\varphi$ and $D_1\theta$. Solving this system with respect to the derivatives $D_1\theta$ and $D_1\phi$ we find that θ satisfies the following differential equation:

$$D_1\theta = a\gamma_q\left(k_{1c}\cos\Theta + k_{1s}\sin\Theta\right), \tag{3.25}$$

where

$$k_{1c} = \frac{c_{6c}c_4 - c_{3c}c_1}{c_1c_5 - c_2c_4},$$
$$k_{1s} = \frac{c_{6s}c_4 - c_{3s}c_1}{c_1c_5 - c_2c_4}.$$

Using Eq. (3.22) and the expression for $D_1\theta$ from (3.25) we obtain the locking condition in the form:

$$\delta f = af_P\gamma_q\left(k_{1c}\cos\Theta + k_{1s}\sin\Theta\right) = af_P\gamma_q\sqrt{k_{1c}^2 + k_{1s}^2}\sin(\Theta + \phi_s), \tag{3.26}$$

where $\phi_s \equiv \arctan\frac{k_{1c}}{k_{1s}}$. This condition gives us, finally, the estimate for the width of the locking range:

$$\delta f_{LR} = 2af_P\gamma_q\sqrt{k_{1c}^2 + k_{1s}^2}. \tag{3.27}$$

It follows from Eq. (3.27) that locking range is proportional to the modulation amplitude a and absorber relaxation rate γ_q. This proportionality was observed experimentally and in numerical simulations.

The numerical estimation of the locking range width using asymptotic formula (3.27) was performed by A. Pimenov and reported in common publication [87]. In Fig. 3.6(a) we compare the results of this estimate with those obtained by direct integration of Eqs. (3.1)-(3.3). It is seen that the asymptotic relation (3.27) gives a good approximation of δ_{LR} even for relatively large modulation amplitudes a.

Similar techniques can be used for estimating the locking range in the case of SHM [Fig. 3.6(b)] considered in the previous section, but not for HFM, since for the latter type of modulation the dependence of the locking range width on the modulation amplitude is nonlinear at small a, $\delta f_{LR} = \mathcal{O}(a^2)$, see Fig. 3.6(c).

For SHM $\delta f = f_M/2 - f_P \ll 1$ and the period of the locked solution $2/f_M$ is close to 1. Thus, the only difference in derivation of the locking estimate coefficients k_{1c} and k_{1s} in Eq. (3.27) occurs due to a different expression for the function $F(t) = \cos[4\pi(f_P + \delta f)t)]$ in Eq. (3.11) and Eq. (3.20). Similarly to the standard hybrid mode-locking case, the resulting estimate can be also applied for relatively large a, see Fig. 3.6(b).

3.6 Parameter study

In this section we present the dependence of the ratio $\delta f_{LR}/a$ characterizing the locking tongue width on the model parameters. This dependence is illustrated in Figs. 3.7 and 3.8, for different values of the pump parameter g_0. These curves were calculated by asymptotic formula Eq. (3.27). The case of vanishing α-factors is represented in Fig. 3.7. It follows from Fig. 3.7a that for sufficiently large g_0 the locking range is inversely proportional to the square of the spectral filtering bandwidth, $\delta f_{LR} \propto \gamma^{-2}$. Fig. 3.7b illustrates the dependence of $\delta f_{LR}/a$ on the ratio of saturation intensities s. One can see that the locking range width is a decreasing function of this parameter. A

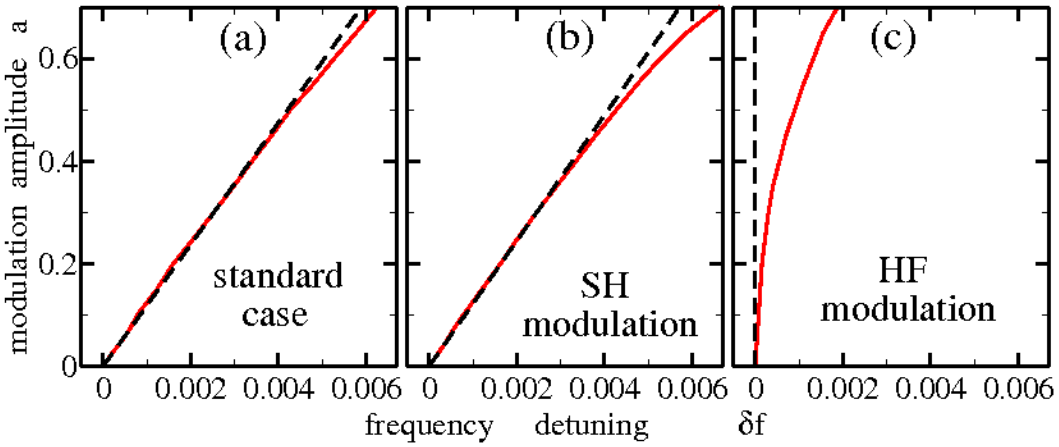

Figure 3.6: Estimation of δ_{LR} of the hybrid mode-locked regions as a function of the modulation amplitude a for (a): standard hybrid mode-locking, (b): SHM hybrid mode-locking and (c): HFM hybrid mode-locking. Thick solid red curves show numerical integration of Eqs. (3.1)-(3.3). Thin black dashed lines show the asymptotic estimates for $a \ll 1$. $\alpha_g = 1.7$, $\alpha_q = 1$. Other parameters are as in Table 3.1.

similar decrease of the locking range takes place with an increase of the linear attenuation factor κ, see Fig. 3.7c.

Assuming that the bias applied to the SA section affects only the relaxation rate γ_q we study the impact of the SA bias on the locking range width by changing γ_q. Fig. 3.7d illustrates the increase of locking range with the absorber relaxation rate γ_q. The similar increase of the locking range width with the absolute value of the absorber voltage was found in Ref. [42] where the experimental dependence of the locking range versus the absolute value of the reverse bias was presented.

Now let us consider the dependence of the locking range width on the linewidth enhancement factors in the gain and absorber sections. When these factors are sufficiently large the mode-locking regime usually breaks up. To avoid this break up, we consider a laser operation close to the lasing threshold when the pump parameter is small $g_0 = 1.25$. Fig. 3.8a illustrates the dependence of the locking range on the both linewidth enhancement factors. We see the increase of the locking range with the two linewidth enhancement factors, $\alpha_g = \alpha_q$. In Fig. 3.8b $\alpha_q = 1$ was fixed and α_g changed. It is seen from this figure that the locking range remains almost constant with the increase of α_g up to $\alpha_g \approx 1.7$. When $1.7 \leq \alpha_g \leq 2$ the locking range width starts to increase. At $\alpha_g \geq 2$ we observed a disappearance of the mode-locked regime for the chosen parameter values. Finally, we have found that for nonzero α-factors, $\alpha_q = 1$, $\alpha_g = 1.7$, and $g_0 = 1.25$, the dependencies of the locking range width on the laser parameters are qualitatively similar to those shown in Fig. 3.7 corresponding to $\alpha_g = \alpha_q = 0$.

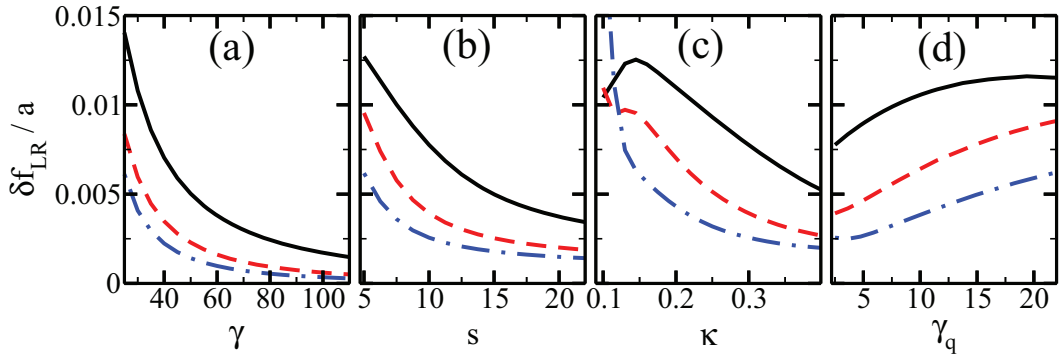

Figure 3.7: Dependence of the ratio $\delta f_{LR}/a$ on parameters of the model equations (3.1)-(3.3), $\alpha_g = \alpha_q = 0$. Solid black, red dashed, and blue dash-dotted lines correspond to $g_0 = 1.25$, $g_0 = 2.0$, and $g_0 = 2.75$, respectively. Other parameter values are as in Table 3.1.

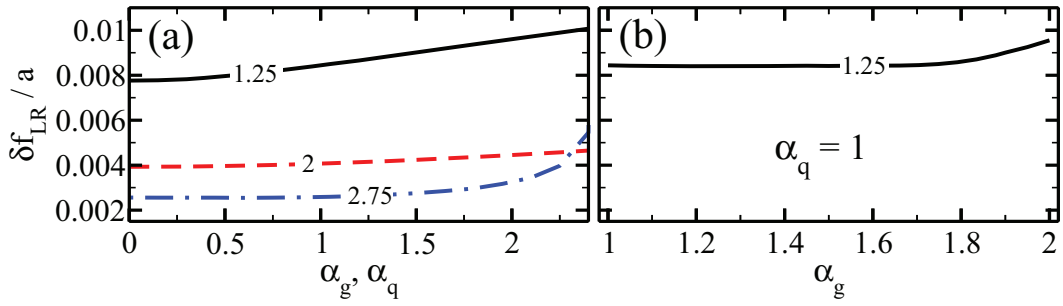

Figure 3.8: Dependence of the ratio $\delta f_{LR}/a$ on the linewidth enhancement factors $\alpha_g = \alpha_q$ (a) and α_g with fixed $\alpha_q = 1$ (b). Black solid, red dashed, and blue dash-dotted lines correspond to $g_0 = 1.25$, $g_0 = 2.0$, and $g_0 = 2.75$, respectively. Other parameter values are as in Table 3.1.

3.7 Asymmetry of the HML regions

In this section we discuss possible reasons for the locking range asymmetry, which was observed experimentally in hybrid mode-locked laser [42]. Up to now we have considered the harmonic modulation function $F = F_0$ defined by Eq. (3.4). In this case, when modulation amplitude a is small, the locking tongue was nearly symmetric with respect to zero detuning. This fact is verified rigorously from the locking condition described by the Eq. (3.27), where minimal and maximal values of δf corresponding to the lower and upper locking range boundaries have the same absolute value and differ only by their signs.

In experiments the absorber voltage modulation is harmonic. This modulation leads to a periodic change of the saturable absorber relaxation rate γ_q whose dependence on the voltage is nonlinear in general. In Ref. [124] an exponential dependence of the carrier relaxation time on the voltage applied to the absorber section was suggested. Hence, a realistic profile of the function F differs significantly from the harmonic one. Below in this section we consider modulation functions given by a sequence of pulses which are significantly broader or narrower than half of modulation period. An example of such modulation functions is

$$F = F_{\pm}(t) = \pm[1 - 2\cos^{10}(\pi f_M t)]. \tag{3.28}$$

These functions are schematically presented in Fig. 3.9. Note that the analytic expression defined by Eq. (3.28) containing a cos function was chosen in order to simplify numerical calculations. The power 10 in (3.28) describes the level of anharmonicity of the modulation. The choice of this power was rather arbitrary: on one hand, it should be sufficiently large to introduce a sufficiently strong anharmonicity, on the other hand, it should not be too large in order to avoid computational problems.

As for the harmonic modulation case (3.4), the period, the maximal value, and the minimal value of these functions are given by $1/f_M$, 1, and -1, respectively. However, the mean values $\langle F_{\pm}\rangle = f_M \int_0^{1/f_M} F_{\pm}(t)dt = \pm\frac{65}{128}$ of the two functions defined by Eq. (3.28) are not equal to zero, unlike the case of harmonic modulation. Therefore, the mean value of the absorber relaxation rate $\bar{\gamma}_q^{\pm}(a) \stackrel{def}{=} \langle\gamma_q(1 + aF_{\pm})\rangle$ depends on the amplitude a.

Locking tongues for the modulation functions (3.28) are shown in Fig. 3.9. The dependence of the pulse repetition frequency of the free-running mode-locked laser on the saturable absorber relaxation rate, $f_P = f_P(\gamma_q)$ is presented in the inset in this figure. One can see that the frequency f_P is a decreasing function of the relaxation rate. The dash-dotted lines in Fig. 3.9 show the dependence of the pulse repetition frequency detuning evaluated at the mean absorber relaxation rate $\bar{\gamma}_q^{\pm}(a)$:

$$\delta f_P^{\pm}(a) \stackrel{def}{=} f_P\left(\bar{\gamma}_q^{\pm}(a)\right) - f_P\left(\gamma_q\right). \tag{3.29}$$

We see that when the amplitude a increases, the dash-dotted lines defined by relation (3.29) move in the same direction as the locking tongues having these dash-dotted lines

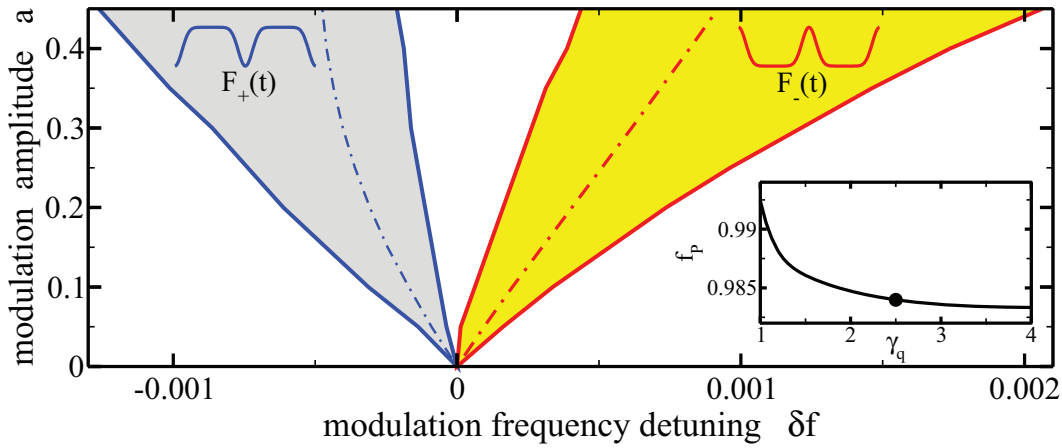

Figure 3.9: Domains of hybrid mode-locking for pulsed modulation profiles $F_{\pm}$ defined by Eq. (3.28). These profiles are shown inside the corresponding tongues. Dash-dotted curves in the middle of the locking tongues represent frequency shifts $\delta f_P(a)$ defined by Eq. (3.29). Inset shows the dependence of the pulse repetition frequency f_P of the free-running laser on the absorber relaxation rate γ_q. Thick bullet indicates the value of γ_q used in numerical simulations of the locking tongues and the corresponding value of the pulse repetition rate $f_P(\gamma_q)$ of the free-running laser. $g_0 = 2.5$. Other parameter values are as in Table 3.1.

inside. Therefore, one can conclude that the asymmetry of the locking tongues presented in Fig. 3.9 is related to the dependence of the pulse repetition frequency f_P on the mean absorber relaxation rate, which is changing with the increasing amplitude a of voltage modulation in the absorber section.

3.8 Experimental evidence of HFM hybrid mode-locking

Here we present the first experimental evidence of subharmonic half frequency voltage modulation (VM) hybrid mode-locking in a quantum-dot laser Ref. [87]. Experiments were performed at TU Berlin by D. Arsenijević. The text presented in this section below is published in a common publication Ref. [87]: R. Arkhipov, A. Pimenov, M. Radziunas, D. Rachinskii, A. G. Vladimirov, D. Arsenijević, H. Schmeckebier, and D. Bimberg. Hybrid mode-locking in semiconductor lasers: simulations, analysis and experiments, IEEE Journal of Selected Topics in Quantum Electronics, Vol. 19, p.100208, 2013 . The structure is grown by molecular beam epitaxy on an n^+-doped GaAs substrate. The active region contains 10 layers of InAs QDs in a 'dots-in-a-well' structure in order to shift the emission wavelength to 1310 nm. The wafer is processed using dry etching techniques yielding a 4-μm wide waveguide ridge. For high frequency applications BCB interlayers are used. The 1985-μm long laser chip consists of a 285-μm long reverse biased saturable absorber section and a 1680-μm forward biased gain section which are separated by a dry etched 20-μm gap. While the saturable absorber facet is high-reflection (99%) coated, the gain section facet is left as cleaved. The electrical spectra have been measured using a 50-GHz electrical spectrum analyzer in combination with a high-speed photodetector having a bandwidth larger than 50-GHz.

In the absence of external VM, after selecting appropriate gain section injection current and absorber voltage, the laser chip demonstrated stable passive mode-locking pulsations with $f_P \sim 20.62$-GHz pulse repetition frequency corresponding to the inverse round-trip time of the laser radiation in the cavity, see upper RF spectrum in panel (a) of Fig. 3.10. As is typical for passive mode-locking, the RF spectral line was relatively broad, indicating a significant timing jitter of the emitted pulses.

In case of hybrid mode-locking a broadband bias tee and probe head were used to apply a modulated bias to the absorber of the laser chip. The peak-to-peak amplitude of the modulated voltage was set to 3.2 V (14 dBm), which was the upper limit available in the experiments. First we consider the case when the frequency f_M of the external VM applied to the absorber section is close to f_P. By properly tuning f_M hybrid mode-locking was achieved in a certain locking range. This range is indicated by the horizontal arrow at the bottom of Fig. 3.10(a). The RF spectra of the hybrid mode-locked laser are shown in the lower parts of panels (a) and (b) in Fig. 3.10. The wide span of the RF spectrum (panel (b)) has a spectral peak only at $\sim f_P$ and its second harmonic, and has no low frequency components which are typical for Q-switched or irregular mode-locking with modulated amplitudes The narrow span RF spectra (panel (a)) show a significant improvement of the spectral linewidth, which indicates a considerable reduction of the pulse timing jitter. It is noteworthy that the frequency f_P (peak frequency of the upper

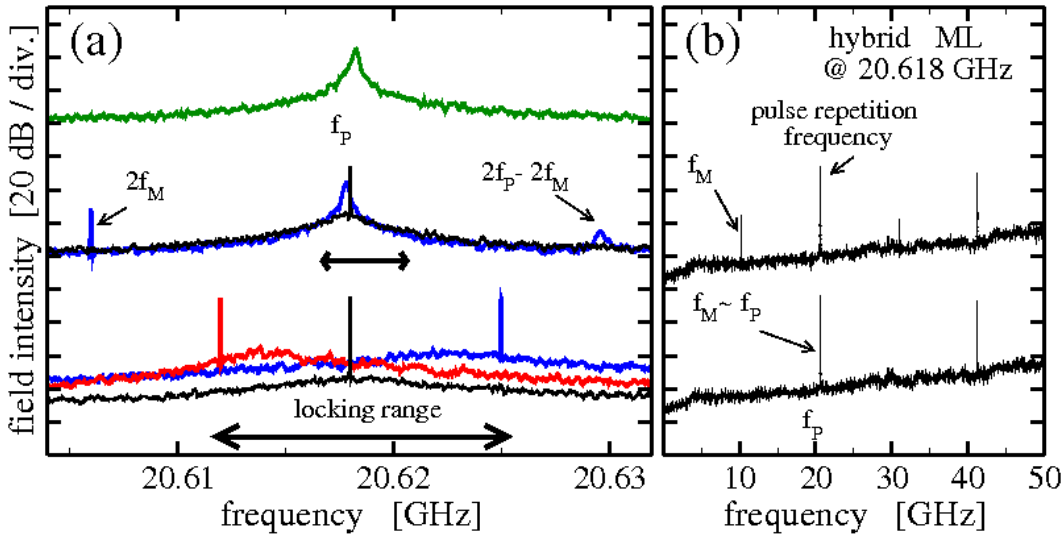

Figure 3.10: Measured RF spectra of passively and hybrid mode-locked laser. Gain section bias current, SA voltage, and peak-to-peak amplitude of VM are 100 mA, -3 V, and 3.2 V, respectively [87]: R. Arkhipov, A. Pimenov, M. Radziunas, D. Rachinskii, A. G. Vladimirov, D. Arsenijević, H. Schmeckebier, and D. Bimberg. Hybrid mode-locking in semiconductor lasers: simulations, analysis and experiments, IEEE Journal of Selected Topics in Quantum Electronics, Vol. 19, p.100208, 2013 © 2013 IEEE. (a) top: passive mode-locking; middle: HFM hybrid mode-locking (black) and non-synchronized state (blue); bottom: standard hybrid mode-locking in the middle (black) and at the boundaries (red and blue) of the locking range. Thick horizontal arrows indicate locking ranges in the classical and HFM hybrid mode-locked cases. (b): large frequency span overview of the standard (above) and HFM (below) hybrid mode-locking spectra shown by corresponding black curves in panel (a).

RF spectrum in panel (a)) is located almost at the center of the estimated locking range. This suggests that in this case the locking tongue is almost symmetric with respect to $f_M = f_P$ line in the VM frequency / VM amplitude plane.

Next, f_M close to $f_P/2 \approx 10.31\,\mathrm{GHz}$ was taken. As it can be seen from the upper curve of panel (b), in this case the RF spectrum demonstrates peaks at frequencies f_M, f_P, and their higher harmonics. A narrow span of the RF spectrum represented by gray curve in the middle part of panel (a) also indicates the presence of the combination tone $\sim (f_P - 2f_M)$. The middle part of panel (a) also gives an illustration of the synchronization between the VM and the passive mode-locking pulsations. The nonlinear nature of the interaction between optical fields and carriers in the laser cavity together with a nonlinear dependence of laser parameters on the modulation amplitude [124] imply the presence of spectral peaks at higher harmonics of the modulation frequency f_M. In the HFM experiments the role of the second-harmonic peak at $2f_M$ is similar to that of the spectral peak at f_M in standard hybrid mode-locking. Namely, for sufficiently large detuning between the frequencies $2f_M$ and f_P both these spectral components are present in the RF spectra: see blue curve in the middle part of panel (a). As soon as the frequency separation becomes sufficiently small, the broad spectral peak at f_P locks to the sharp spectral line at $2f_M$ (black curve in the middle part of panel (a)), which implies the appearance of HFM hybrid mode-locking. Since the amplitude of the second harmonic of VM at $2f_M$ is smaller than that of the first harmonic at f_M, the locking range in standard hybrid mode-locking is wider than the locking range of a HFM hybrid mode-locked laser, see black horizontal arrow below corresponding spectra in panel (a), which is in agreement with our simulations. Furthermore, HFM hybrid mode-locking is characterized by a smaller height of the sharp spectral peak [compare black spectra at the middle and at the bottom of panel (a)] and, hence, by a larger pulse timing jitter as compared to standard mode-locking. We note also that while the pulse repetition frequency remains close to f_P, strictly speaking, the period of the laser intensity time trace in the HFM hybrid mode-locking state is approximately twice larger than that in a PML laser, $1/f_M \approx 2/f_P$. This means that two consequent mode-locked pulses are slightly different (see also numerical results presented in Fig. 3.3(b) and bifurcation diagram in Fig 3.4). An increase of the VM amplitude could lead to a larger locking range, and at the same time to a growth of the difference between a pair of subsequent pulses.

3.9 Conclusions

We have studied theoretically hybrid mode-locking in a two-section edge-emitting semiconductor laser in the framework of DDE model. Dependence of the locking range on the laser parameters has been investigated numerically and analytically. The voltage modulation in the saturable absorber section of the device was represented by modulated carrier relaxation rate in this section. It has been demonstrated numerically that the locking range increases almost linearly with the increase of the modulation amplitude. We have shown that the asymmetry of the locking range is related to the dependence

of the averaged absorber relaxation rate on the modulation amplitude a, which has an impact on the frequency of the passive mode-locking pulsations.

Analytical estimates of the locking range width have been obtained using an asymptotic approach. According to these estimates the locking range in hybrid mode-locked lasers increases with the decrease of the spectral filtering bandwidth γ and decreases with the increase of ration of absorber/gain saturations s and field intensity attenuation per round-trip κ.

Locking tongues, where the pulse repetition rate is synchronized to the frequency of the external modulation, have been found theoretically for modulation frequencies f_M close to f_P (standard hybrid mode-locking), $2f_P$ (SHM hybrid mode-locking), and $f_P/2$ (HFM hybrid mode-locking). Unlike standard and SHM hybrid mode-locking, for which the dependence of the locking range width on the modulation amplitude a was almost linear, the locking range of HFM hybrid mode-locking, corresponding to a resonance $1:2$, is smaller and increases nonlinearly with a.

Finally, we have described experimental evidence of such kind of HFM hybrid mode-locking in a 20-GHz quantum-dot laser. Similarly to the results of our numerical simulations HFM hybrid mode-locking region is sufficiently smaller than that of the standard case.

4 Semiconductor mode-locked lasers with coherent dual mode optical injection

In this chapter, we study the dynamics of a PML semiconductor laser with dual frequency coherent optical injection using a delay differential equation model.

4.1 Introduction

An efficient approach to improving the characteristics of pulses emitted by PML lasers is based on the use of optical injection from a single mode laser. When one of the slave laser modes is locked to the external single frequency signal, this results in the reduction of the phase noise and suppression of waveform instabilities and leads to the PML laser's optical spectrum narrowing as was demonstrated experimentally in [45, 46, 127]. However, single mode injection does not allow one to control the repetition rate of mode-locked pulses [45, 46]. On the other hand, the hybrid mode-locking technique does not affect the individual line frequency noise [45, 47]. High quality optical frequency combs with narrow lines and small RF beating noise can be generated by injecting two coherent tones into PML lasers [43–47]. A schematic representation of a PML laser with coherent dual mode optical injection is presented in Fig. 4.1. A coherent output from a CW laser is sent through a Mach-Zehnder amplitude modulator producing two coherent sidebands with a suppressed carrier frequency. These two sidebands are then injected into the PML laser. When the frequency separation of two injected frequencies is close to the pulse repetition frequency of the free-running PML laser, the laser pulse repetition rate is synchronized to this separation frequency. Semiconductor lasers with dual mode optical injection were studied experimentally in [44–47]. Experimental study demonstrated a reduction of the timing jitter, modal optical linewidth, and RF linewidth along with time-bandwidth product improvement. In Ref. [46, 128] it was demonstrated experimentally and theoretically that single and dual mode optical injection resulted in optical spectrum narrowing of the PML laser and a red shifting of optical spectrum in the frequency domain from the master laser frequency. In the numerical simulations this shift was observed when the linewidth enhancement factor in the gain section is larger than that in the saturable absorber section, $\alpha_g > \alpha_q$.

The locking regions where the pulse repetition frequency of the laser is synchronized to the separation frequency between two injected frequencies (RF locking range) were studied experimentally in Ref. [47]. An InP quantum dash mode-locked laser with pulse repetition frequency 21 GHz was used for measurements. It was demonstrated experimentally that the locking range increases linearly with the injection field power.

Another interesting feature, which was observed experimentally, is that the locking range width is larger for negative absorber voltages than for positive voltages.

In this chapter we perform a theoretical analysis of the dynamics of a dual mode optically injected PML laser using a set of delay differential equations similar to that considered in the previous chapter. We calculate numerically the width of the locking range as a function of the injected field power and model parameters in the two following cases. In the first one the frequency separation between two injected frequencies was varied at vanishing optical frequency detuning, $\delta_\omega = 0$, see Fig. 4.1 where the notation δ_ω is defined. We refer to the locking range obtained in this situation as an RF locking range since the frequency separation between two injected frequencies varied in this case is determined by the modulation RF f_M of optical modulator, see Fig. 4.1. In the second situation the locking range was calculated by changing the optical frequency detuning δ_ω keeping the value of modulation frequency f_M constant and equal (or multiple) pulse repetition frequency of free-running PML laser. We call the locking range studied in this case the optical locking range since optical frequency detuning δ_ω is changed. We demonstrate theoretically that optical locking range is wider than RF locking range, which is in agreement with the experimental data obtained with 10 GHz PML quantum dot laser.

Finally, for sufficiently small injected field amplitudes we derive an asymptotic formula for the width of the locking range. We demonstrate that this formula is in good agreement with the results of direct numerical simulations of the model equations. Using this asymptotic formula we study the dependence of RF and optical locking range widths on the model parameters. Some results of this Chapter are included in a common publication [88] which is currently under preparation.

4.2 Model Equations

Our analysis is based on a set of delay differential equations describing the time evolution of the electric field amplitude at the entrance of the laser absorber section, $A(t)$, saturable gain, $G(t)$, and saturable absorption, $Q(t)$ in the gain and SA parts of the device, respectively. In the case of externally injected mode-locked laser this model can be written in the following form:

$$\frac{1}{\gamma}\frac{dA}{dt} = -A + \sqrt{\kappa} e^{\frac{(1-i\alpha_g)G(t-T)-(1-i\alpha_q)Q(t-T)}{2}+i\nu} A(t-T) + \mathcal{E}_i(t), \tag{4.1}$$

$$\frac{dG}{dt} = g_0 - \gamma_g G - e^{-Q}\left(e^G - 1\right)|A|^2, \tag{4.2}$$

$$\frac{dQ}{dt} = \gamma_q(q_0 - Q) - s\left(1 - e^{-Q}\right)|A|^2. \tag{4.3}$$

The parameter ν describes detuning between the central frequency of the spectral filter and the closest cavity mode. As in the previous chapter the cold cavity field round-trip time in the simulations T is normalized to 1.

Let us assume that for vanishing injection $\mathcal{E}_i(t) = 0$ the model equations (4.1)-(4.3)

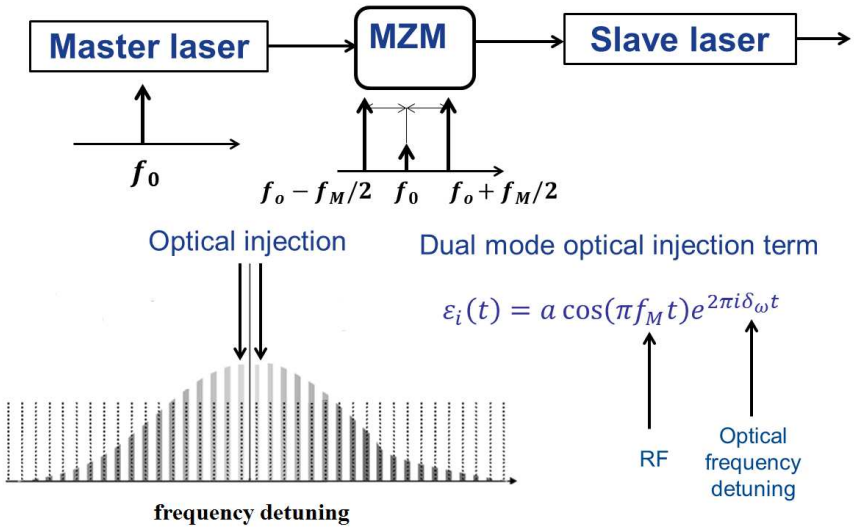

Figure 4.1: Schematic representation of a passively mode-locked laser with coherent dual mode optical injection. Radiation from CW master laser passes through Mach-Zehnder modulator producing two coherent sidebands with a suppressed carrier frequency. The two sidebands are injected into the PML laser (slave laser). When the frequency separation between the two injected modes is close to the inverse cavity round-trip time, pulse repetition frequency synchronizes to this frequency separation.

have a linearly-stable fundamental mode-locked solution

$$A(t) = A_0(t)e^{i\Omega t}, \quad G(t) = G_0(t), \quad Q(t) = Q_0(t),$$

where A_0, G_0, and Q_0 are periodic functions with the period T_0 close to the cavity round trip time T, $f_P = 1/T_0$ is the corresponding repetition frequency.

In this chapter we assume that optically injected field $\mathcal{E}_i(t)$ is given by

$$\mathcal{E}_i(t) = a\cos(\pi n f_M t)\ e^{i2\pi\delta_\omega t}, \quad n = 1, 3, 5, \ldots \tag{4.4}$$

where $f_M = nf_P + \delta_f$ ($\delta_f \ll 1$) is the frequency spacing between two injected tones (modulation frequency), δf is a small detuning from the pulse repetition frequency of uninjected laser f_P, δ_ω is a an optical frequency detuning that corresponds to the detuning between the master CW laser frequency and the central mode of free-running PML laser. It is noteworthy, that it is experimentally possible to change both these detuning factors, δ_f and δ_ω.

Note that in this chapter we simulate and analyze the PML lasers with dual-mode injection (4.4) which is symmetric or almost symmetric with respect to the zero reference frequency. For example, for $\nu = \pi$ and $\alpha_{g,q} = 0$ the central frequency of the spectral

filtering element is located exactly in the middle between two adjacent optical modes of the PML laser, i.e. $\Omega = -\pi f_P$, see Fig. 4.2a .

4.3 Numerical calculation of the locking regions

In this section we present the results of numerical calculation of the regions where the dual-mode optical injection entrains the frequency of the PML laser.

We consider a specific case of $\nu = \pi$. In this situation the spectrum of PML laser is symmetric with respect the zero frequency detuning when $\alpha_g = \alpha_q = 0$. The optical spectra of the PML laser, that is typically calculated, together with the indication of the frequencies of optical injection are shown in Fig. 4.2 (for $n = 1$) and Fig. 4.3 (for $n = 3$). Upper and lower panels of these figures correspond to the cases of vanishing and nonvanishing factors $\alpha_{g,q}$, respectively. When $n = 1$, see Fig. 4.2, the frequency separation between two injected modes f_M is close to the pulse repetition frequency f_P, $f_M \approx f_P$. When $n = 3$, the frequency f_M is close to third harmonic of the frequency f_P, $f_M \approx 3f_P$, see Fig. 4.3.

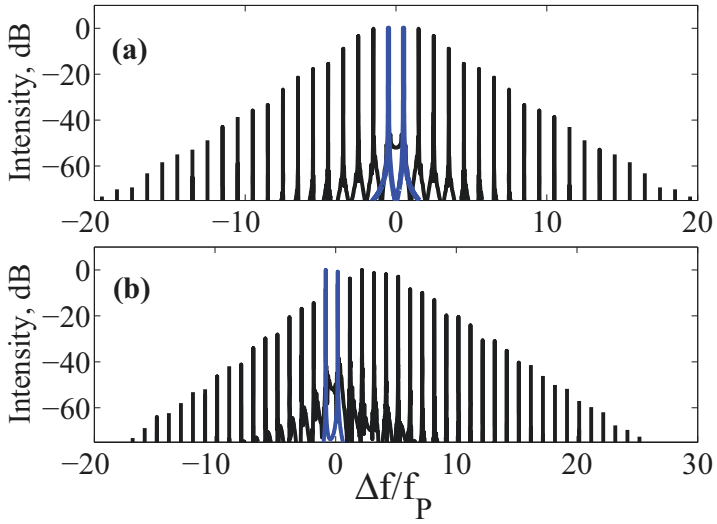

Figure 4.2: Spectrum of the free-running PML semiconductor laser (black solid line) and injection field spectrum (blue line), $n = 1$, (a): $\alpha_g = \alpha_q = 0$, (b): $\alpha_g = 2$ and $\alpha_q = 1$.

To calculate the locking regions of a mode-locked laser with dual frequency injection we used the same numerical procedure as in our previous studies of hybrid mode-locked lasers, see Chapter 3. The boundaries of the RF locking range were determined by changing the RF detuning δ_f at vanishing optical frequency detuning, $\delta_\omega = 0$. Similarly, the boundaries of the optical frequency locking range were calculated by changing the value of optical frequency detuning δ_ω at vanishing RF detuning, $\delta_f = 0$. Fig. 4.4

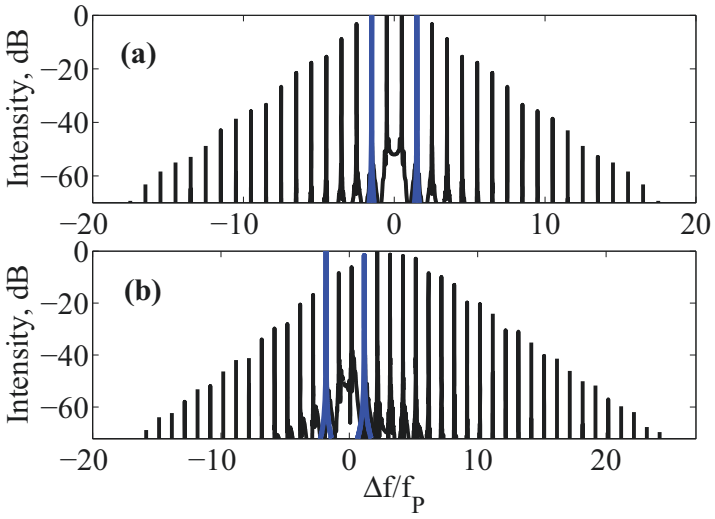

Figure 4.3: Spectrum of the free-running PML semiconductor laser (black solid line) and injection field spectrum (blue line), $n = 3$, (a): $\alpha_g = \alpha_q = 0$, (b): $\alpha_g = 2$ and $\alpha_q = 1$.

and Fig. 4.5 illustrate the local maxima of the field intensity time-trace $|A(t)|^2$ and the intensities $|A(t_k)|^2$ evaluated at equidistant time moments t_k separated by T_0 for every considered δ_f (δ_ω) when $n = 1$ and $\alpha_g = \alpha_q = 0$.

When the frequencies of the injected field come close enough to modes in the mode-locking comb, see Fig. 4.2, these modes become locked to the external injection and the pulse repetition rate becomes equal to f_M. In the case when $n = 1$, the intensity of the mode-locking regime is strictly periodic with the period $1/f_M$ and all the recorded intensity maxima have the same value at fixed detuning δ_ω (or δ_f). For frequency detuning outside the locking interval we have observed regimes with irregular or quasi-periodic pulsed laser intensity, which correspond to multiple intensity maxima at fixed detunings δ_ω and δ_f and a cloud of points in Fig. 4.4 and Fig. 4.5 .

By estimating the locking range at different values of the injection field amplitude a we obtain the locking regions (locking tongues) in the space of three parameters: RF and optical frequency detuning δ_f, δ_ω, and the injected field amplitude a. The boundaries of the two-dimensional RF locking region calculated at the vanishing optical frequency detuning $\delta_\omega = 0$ are shown in Fig. 4.6(a). Similarly, an optical frequency locking region calculated at the vanishing RF detuning $\delta_f = 0$ is presented in Fig. 4.6(b). It can be seen from Fig. 4.6 that the locking ranges grow almost linearly with the injection field amplitude a. Furthermore, our simulations demonstrate that the optical frequency locking range shown in Fig. 4.6(b) is about ten times wider than the RF locking range shown in Fig. 4.6(a). Similar situation was observed experimentally in Ref. [88]. Solid curves in Fig. 4.6 correspond to the case of zero linewidth enhancement factors, $\alpha_g = \alpha_q = 0$, while the blue dashed curves refer to the case when $\alpha_g = 2$ and

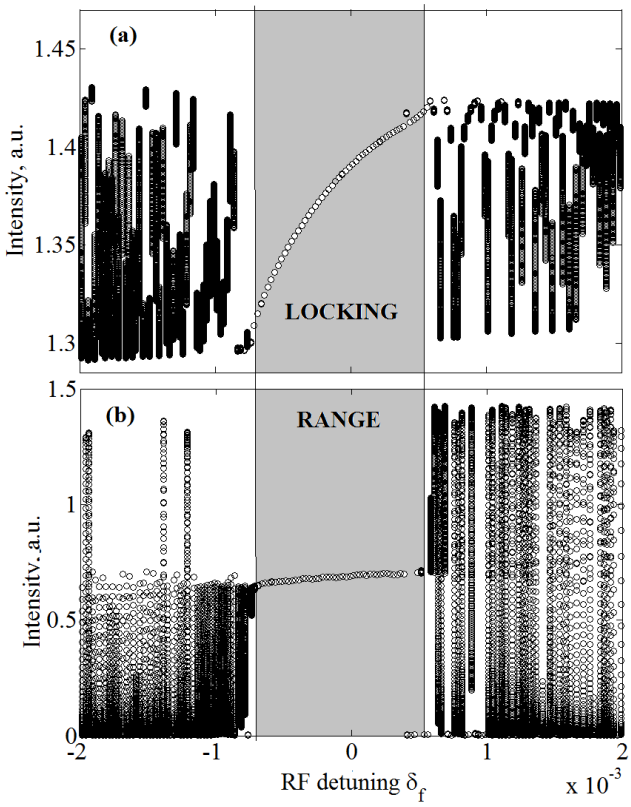

Figure 4.4: Numerical estimation of the RF locking range of PML semiconductor laser with dual mode optical injection. (a): Local maxima of the intensity time-trace and (b): stroboscopic map points of emitted field intensity at fixed injection field amplitude a = 0.008. On the x-axis is RF detuning δ_f. Optical frequency detuning $\delta_\omega = 0$, and $\alpha_g = \alpha_q = 0$. Other parameters are as in Table 3.1.

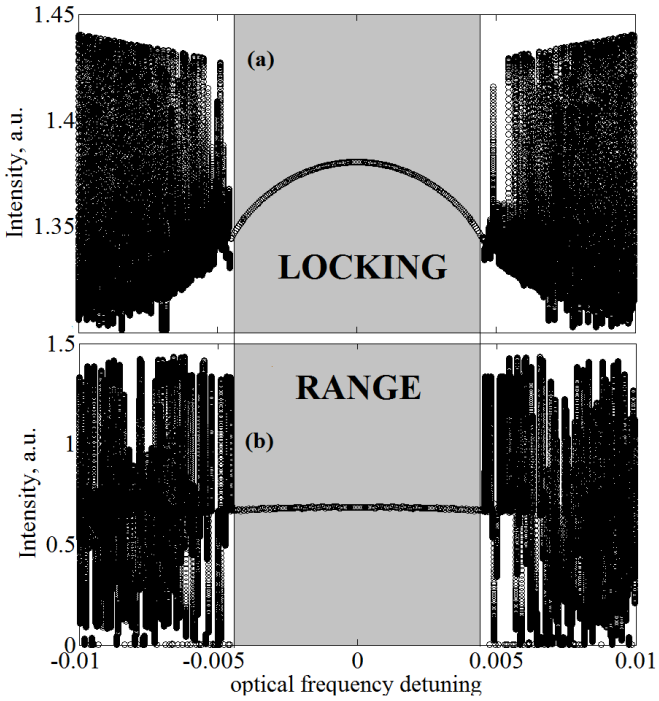

Figure 4.5: Numerical estimation of the optical locking range of passively ML semiconductor laser with dual mode optical injection. (a): Local maxima of the intensity timetrace and (b): stroboscopic map points of emitted field intensity at fixed injection field amplitude a = 0.008. On the x axis is optical frequency detuning δ_ω. RF detuning $\delta_f = 0$ and $\alpha_g = \alpha_q = 0$. Other parameters are as in Table 3.1.

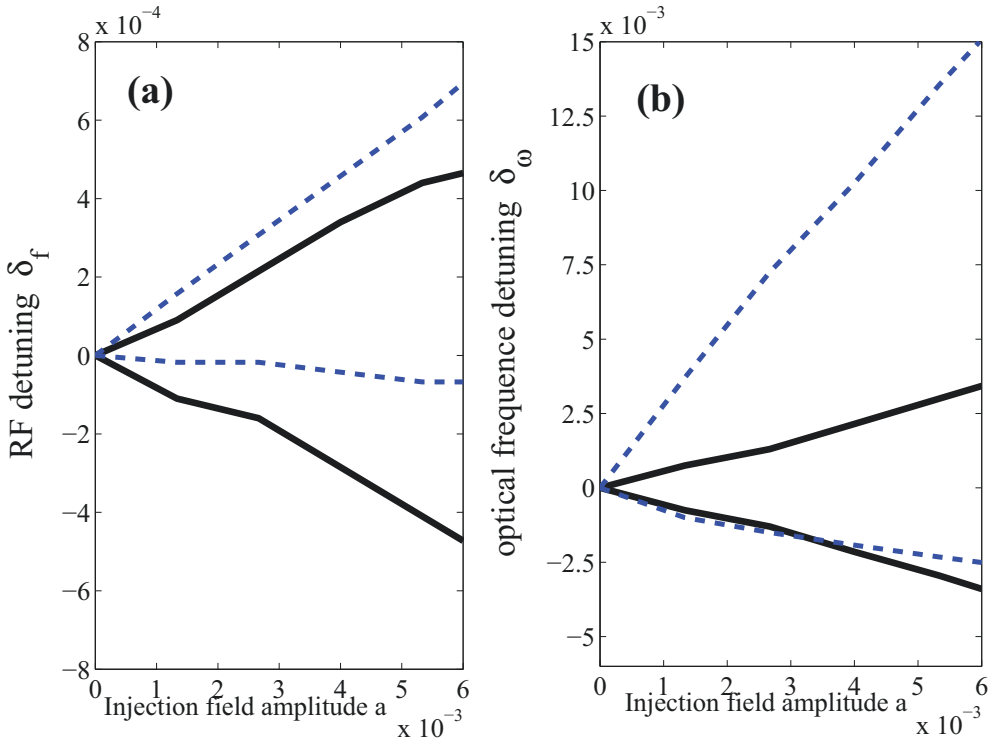

Figure 4.6: RF locking region at $\delta_\omega = 0$ (a) and optical frequency locking region at $\delta_f = 0$ (b). Optical injection mode separation factor $n = 1$. Black solid curves correspond to $\alpha_g = \alpha_q = 0$, blue dashed curves to $\alpha_g = 2, \alpha_q = 1$. Other parameters are as in Table 3.1

$\alpha_q = 1$. One can see from this figure that in the case of vanishing α-factors both optical and RF locking ranges are symmetric with respect to the zero frequency detuning. On the contrary, in the case of non-vanishing α-factors (blue dashed lines) locking ranges are asymmetric and are shifted to larger values of frequency detuning. This asymmetry is related to the increase of the pulse repetition frequency of free-running PML laser with the injection amplitude. Similar asymmetry was observed experimentally in a quantum dot PML laser, see Ref. [88]. Furthermore, it is seen from Fig. 4.6 that while the RF locking range has approximately the same width for zero and nonzero α-factors, the optical locking range in the case of non-vanishing α-factors is approximately 3 times larger than in the case of zero α-factors.

Next, we have simulated the PML laser with a dual-mode injection with the frequency separation close to $3 \cdot 2\pi f_P$ [i.e., $n = 3$ in Eq. (4.4)]. The spectrum of the free-running PML laser and the two injected frequencies are presented in Fig. 4.3. The boundaries of the RF locking region calculated at vanishing optical frequency detuning $\delta_\omega = 0$ and the boundaries of the optical locking domain obtained for vanishing RF detuning $\delta_f = 0$ are shown in Fig. 4.7(a) and Fig. 4.7(b), respectively. One can see from this figures that both RF and optical locking range have approximately the same values in the case of vanishing α-factors (black curves in Fig. 4.7(a) and Fig. 4.7(b).) Both locking tongues are symmetric with respect to the zero frequency detuning, since injection frequencies are symmetric with respect of it. Also from Fig. 4.7 it follows that the RF locking range in the case of non-vanishing α-factors is approximately ten times smaller than the optical locking range, see blue curves in Fig. 4.7(a) and Fig. 4.7(b). These locking ranges are also asymmetric with respect to the zero frequency detuning. As in the case $n = 1$ this asymmetry is related to the dependence of the pulse repetition frequency on the injected field amplitude and spectral shift of laser modes due to the non-vanishing α-factors. Comparing Fig. 4.6 and Fig. 4.7 one can conclude that RF and optical locking ranges have approximately the same width when the frequency separation between two injected frequencies is close to f_P or $3f_P$ and α-factors are nonzero. A similar situation was observed in the previous chapter in our study of hybrid mode-locked lasers. It was found in Chapter 3 that when the frequency of the external modulation voltage is close to f_P and $2f_P$, the size of the locking regions is similar.

4.4 Asymptotic analysis

In this section we derive an asymptotic formula for the RF and optical locking range. For simplicity, we set $\nu = \pi$, consider the case of vanishing α-factors, $\alpha_{g,q} = 0$, and assume a "symmetric" optical injection (4.4) with $n = 1$.

Similarly to the asymptotic analysis of the previous chapter we use the method of multiple time scales assuming small, but nonvanishing injection amplitude a. For this reason we introduce the "fast" and the "slow" time $\tau_0 = t$ and $\tau_1 = at$, and denote the corresponding differential operators by $D_0 = \frac{\partial}{\partial \tau_0}$ and $D_1 = \frac{\partial}{\partial \tau_1}$. As in the previous Chapter we consider the solutions of the model equations (4.1)–(4.3) in the following form: $A(t) = A_0[\tau_0+\theta(\tau_1)]e^{i\varphi(\tau_1)}+aA_r^1[\tau_0+\theta(\tau_1),\tau_1]e^{i\varphi(\tau_1)}+iaA_i^1[\tau_0+\theta(\tau_1),\tau_1]e^{i\varphi(\tau_1)}+...$,

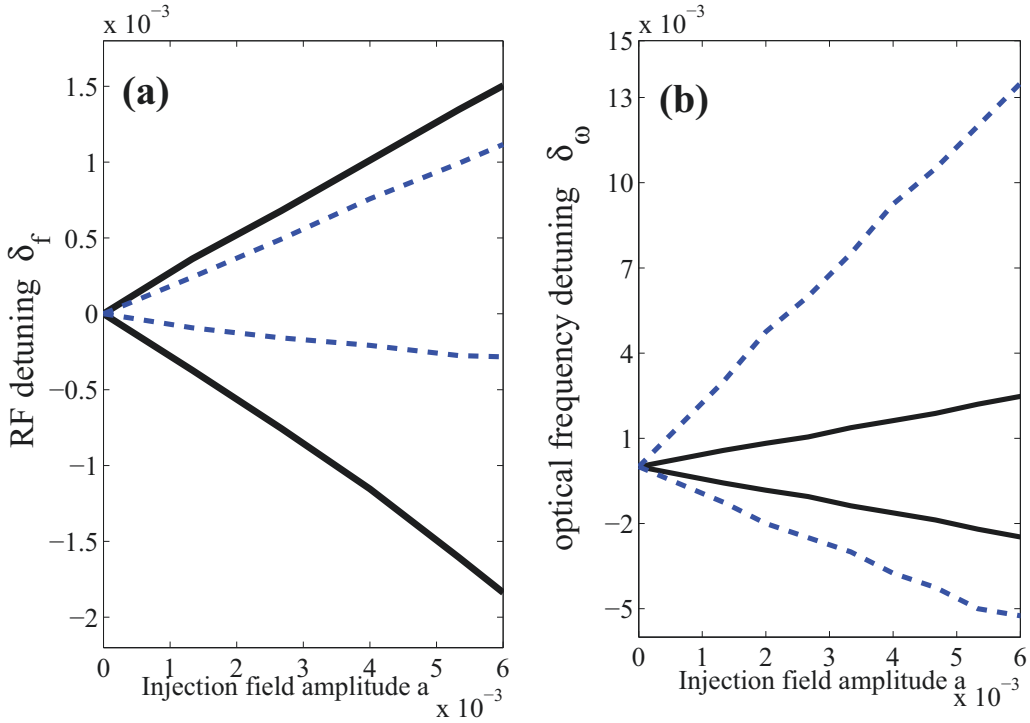

Figure 4.7: RF locking region at $\delta_\omega = 0$ (a) and optical frequency locking region at $\delta_f = 0$ (b). Optical injection mode separation factor $n = 3$. Black solid curves corresponds to the case $\alpha_g = \alpha_q = 0$, blue dashed curves: $\alpha_g = 2, \alpha_q = 1$. Other parameters are as in Table 3.1.

$G(t) = G_0[\tau_0 + \theta(\tau_1)] + aG^1[\tau_0 + \theta(\tau_1), \tau_1]e^{i\varphi(\tau_1)} + ...$, $Q(t) = Q_0[\tau_0 + \theta(\tau_1)] + aQ^1[\tau_0 + \theta(\tau_1), \tau_1]e^{i\varphi(\tau_1)} + ...$. Then substituting these expansions into (4.1)-(4.3) and collecting first order terms in the small parameter a, we obtain an inhomogeneous linear equation for the complex vector of small perturbations $\delta\psi^1(t) = \left[A_r^1, A_i^1, G^1, Q^1\right]^t$:

$$-\frac{d}{dt}\delta\psi^1(t) + \mathcal{L}(t)\delta\psi^1(t) + \mathcal{M}(t-T)\delta\psi^1(t-T) = \mathcal{F}_0(t). \tag{4.5}$$

Jacobian matrices $\mathcal{L}$ and $\mathcal{M}$ were considered in the previous chapter [see Eqs. (3.7)-(3.8)] and will not be presented here. The right side of the Eq. (4.5) is given by

$$\mathcal{F}_0 = \begin{pmatrix} -\left(\dot{A}_0 + T\ddot{A}_0 + \gamma T\dot{A}_0\right) D_1\theta + a\cos[\pi f_M(t-\theta)]\cos[2\pi\delta_\omega(t-\theta) - \varphi(\tau_1)] \\ -\left(A_0 + T\dot{A}_0 + T\gamma A_0\right) D_1\varphi + a\cos[\pi f_M(t-\theta)]\sin[2\pi\delta_\omega(t-\theta) - \varphi(\tau_1)] \\ -\dot{G}_0 D_1\theta \\ -\dot{Q}_0 D_1\theta \end{pmatrix}. \tag{4.6}$$

Here we used notations: $\dot{A}_0 = \frac{dA_0}{d\tau_0}$, $\ddot{A}_0 = \frac{d^2A_0}{d\tau_0^2}$, $\dot{G}_0 = \frac{dG_0}{d\tau_0}$ and $\dot{Q}_0 = \frac{dQ_0}{d\tau_0}$.

The homogeneous Eq. (4.5) with $\mathcal{F}_0 = 0$ has two solutions corresponding to the two symmetries of the free-running laser equations (4.1) - (4.3). One of them corresponds to the symmetry with respect to time shifts $A(t) \to A(t+t')$, $G(t) \to G(t+t')$, $Q(t) \to Q(t+t')$, the other with respect to phase shifts $A(t) \to A(t)e^{i\phi}$, $G(t) \to G(t)$, $Q(t) \to Q(t)$, see Ref. [105] and Chapter 3. Two periodic vectors-solutions of the homogeneous linear problem Eq. (4.5) are given by [105]:

$$\psi = (0, A_0, 0, 0)^t, \chi = \left(\dot{A}_0, 0, \dot{G}_0, \dot{Q}_0\right)^t. \tag{4.7}$$

The solutions of the adjoint problem

$$\psi^\dagger = \left(0, \psi_1^\dagger, 0, 0\right), \chi^\dagger = \left(\chi_1^\dagger, 0, \chi_2^\dagger, \chi_3^\dagger\right). \tag{4.8}$$

satisfy the following system of differential equations which can be solved numerically [105]:

$$\frac{d\chi_1^\dagger}{dt} = \gamma\chi_1^\dagger + 2e^{-Q_0}(e^{G_0} - 1)A_0\chi_2^\dagger + 2s(1 - e^{-Q_0})A_0\chi_3^\dagger + \gamma\sqrt{\kappa}e^{\frac{G_0-Q_0}{2}}\chi_1^\dagger(t+T), \tag{4.9}$$

$$\frac{d\chi_2^\dagger}{dt} = (\gamma_g + e^{G_0-Q_0}|A_0|^2)\chi_2^\dagger + 0.5\gamma\sqrt{\kappa}e^{\frac{G_0-Q_0}{2}}A_0\chi_1^\dagger(t+T), \tag{4.10}$$

$$\frac{d\chi_3^\dagger}{dt} = -e^{-Q_0}(e^{G_0}-1)|A_0|^2\chi_2^\dagger + (\gamma_q + se^{-Q_0}|A_0|^2)\chi_3^\dagger - 0.5\gamma\sqrt{\kappa}e^{\frac{G_0-Q_0}{2}}A_0\chi_1^\dagger(t+T), \tag{4.11}$$

$$\frac{d\psi_1^\dagger}{dt} = \gamma\psi_1^\dagger + \gamma\sqrt{\kappa}e^{\frac{G_0-Q_0}{2}}\psi_1^\dagger(t+T). \tag{4.12}$$

The neutral modes satisfy the following orthonormalization conditions with inner product defined in the previous chapter, Eq. (3.10): $\langle\psi^\dagger,\psi\rangle = \langle\chi^\dagger,\chi\rangle = 1, \langle\psi^\dagger,\chi\rangle = \langle\chi^\dagger,\psi\rangle = 0$.

According to the Fredholm alternative, the system of equations (4.5) is solvable if the right side $\mathcal{F}_0(t)$ of this system, as a function of $\tau_0 = t$, is orthogonal to each of the adjoint functions $\psi^\dagger$ and $\chi^\dagger$.

From the orthogonality condition $\langle\mathcal{F}_0(t),\psi^\dagger\rangle = 0$ one can obtain the following differential equation for φ:

$$D_1\varphi = ac_1\int_0^{T_0}\cos[\pi f_M(t-\theta)]\sin[2\pi\delta_\omega(t-\theta)-\varphi(\tau_1)]\psi_1^\dagger(t)dt, \tag{4.13}$$

here $c_1 \equiv 1/\int_0^{T_0}\left(A_0+\gamma TA_0+T\dot{A}_0\right)\psi_1^\dagger(t)dt$.

From the orthogonality condition $\langle\mathcal{F}_0(t),\chi^\dagger\rangle = 0$ one can obtain the following equation for θ:

$$D_1\theta = ac_2\int_0^{T_0}\cos[\pi f_M(t-\theta)]\cos[2\pi\delta_\omega(t-\theta)-\varphi(\tau_1)]\chi_1^\dagger(t)dt, \tag{4.14}$$

here $c_2 \equiv \frac{1}{\int_0^{T_0}(\dot{A}_0+\gamma T\dot{A}_0+T\ddot{A}_0)\chi_1^\dagger(t)+\dot{G}_0\chi_2^\dagger(t)+\dot{Q}_0\chi_3^\dagger(t)dt}$.

Using the formula $f_M = f_P + \delta_f$ we obtain from Eqs. (4.13)-(4.14):

$$D_1\varphi = ac_1\int_0^{T_0}\cos(\pi f_P t+\pi\delta_f t-\pi f_P\theta)\sin(2\pi\delta_\omega t-2\pi\delta_\omega\theta-\varphi)\psi_1^\dagger(t)dt, \tag{4.15}$$

$$D_1\theta = ac_2\int_0^{T_0}\cos(\pi f_P t+\pi\delta_f t-\pi f_P\theta)\cos(2\pi\delta_\omega t-2\pi\delta_\omega\theta-\varphi)\chi_1^\dagger(t)dt. \tag{4.16}$$

For simplification, we introduce the new variables Θ and Φ defined by the formulas: $\Theta = \pi\delta_f t - \pi f_P\theta$ and $\Phi = 2\pi\delta_\omega t - \varphi$. In the new variables the equations for φ and θ become

$$D_1\Phi = 2\pi\delta_\omega - ac_1\int_0^{T_0}\cos(\pi f_P t+\Theta)\sin(\Phi)\psi_1^\dagger(t)dt, \tag{4.17}$$

$$D_1\Theta = \pi\delta_f - a\pi f_P c_2\int_0^{T_0}\cos(\pi f_P t+\Theta)\cos(\Phi)\chi_1^\dagger(t)dt. \tag{4.18}$$

Here we neglected the term $2\pi\delta_\omega\theta$ since $\delta_\omega \ll 1$. Using the formula $\cos(\alpha+\beta) = \cos\alpha\cos\beta - \sin\alpha\sin\beta$ Eqs. (4.17)-(4.18) can be rewritten as:

$$D_1\Phi = 2\pi\delta_\omega - ac_1\left[k_{1c}\cos\Theta - k_{1s}\sin\Theta\right]\sin\Phi, \tag{4.19}$$

$$D_1\Theta = \pi\delta_f - a\pi f_P c_2\left[k_{2c}\cos\Theta - k_{2s}\sin\Theta\right]\cos\Phi, \tag{4.20}$$

where $k_{1c} = \int_0^{T_0}\cos(\pi f_P t)\psi_1^\dagger(t)dt$, $k_{1s} = \int_0^{T_0}\sin(\pi f_P t)\psi_1^\dagger(t)dt$, $k_{2c} = \int_0^{T_0}\cos(\pi f_P t)\chi_1^\dagger(t)dt$, and $k_{2s} = \int_0^{T_0}\sin(\pi f_P t)\chi_1^\dagger(t)dt$.

In the case when the pulse repetition frequency of PML laser is synchronized to the

frequency separation between externally injected modes, time derivatives of Θ and Φ in Eqs. (4.19)-(4.20) should be equal to zero: $D_1\Phi = 0$, i.e. $\Phi = \Phi_0 = const$, $D_1\Theta = 0$, i.e. $\Theta = \Theta_0 = const$. Finally, the equations for the width of RF locking range $\delta_{f,LR}$ and optical locking range $\delta_{\omega,LR}$ can be written in the form:

$$\delta_{f,LR} = af_P c_2 \left[k_{2c}\cos\Theta_0 - k_{2s}\sin\Theta_0\right]\cos\Phi_0, \tag{4.21}$$

$$\delta_{\omega,LR} = \frac{ac_1}{2\pi}\left[k_{1c}\cos\Theta_0 - k_{1s}\sin\Theta_0\right]\sin\Phi_0, \tag{4.22}$$

or in more compact form:

$$\delta_{f,LR} = af_P c_2\sqrt{k_{2c}^2 + k_{2s}^2}\cos(\Theta_0 - \alpha_2)\cos\Phi_0, \tag{4.23}$$

$$\delta_{\omega,LR} = \frac{ac_1}{2\pi}\sqrt{k_{1c}^2 + k_{1s}^2}\cos(\Theta_0 - \alpha_1)\sin\Phi_0, \tag{4.24}$$

where $\alpha_2 = \arctan\frac{-k_{2s}}{k_{2c}}$ and $\alpha_1 = \arctan\frac{-k_{1s}}{k_{1c}}$. Since $|\cos(\Theta_0 - \alpha_{1,2})| < 1$ when the optical frequency detuning $\delta_\omega = 0$ one can obtain the following estimations for the half-width of the RF locking range:

$$\delta_{f,LR} = af_P c_2\sqrt{k_{2c}^2 + k_{2s}^2}. \tag{4.25}$$

Similarly when the RF frequency detuning $\delta_f = 0$ for the width of the optical locking range we get:

$$\delta_{\omega,LR} = \frac{ac_1}{2\pi}\sqrt{k_{1c}^2 + k_{1s}^2}. \tag{4.26}$$

One can see from the expressions (4.25)-(4.26) that both RF and optical locking ranges are proportional to the first power of the injection field amplitude a. This is in agreement with the experimental observations. Using Eqs. (4.25)-(4.26) we calculated the boundaries of the locking range and compared them with those obtained by numerical simulations. Equations similar to (4.25)-(4.26) can be obtained for the case $n = 3$ when optical frequency separation between two injected frequencies close to $3 \cdot 2\pi f_P$, the only difference being that the term f_P in Eq. (4.25) would be replaced with $3f_P$. The same replacement would be done in derivation of the coefficients k_{1c}, k_{1s}, k_{2c} and k_{2s} .

In Figs. 4.8-4.9 the half-width of the locking range is compared to that calculated by direct numerical integration of (4.1)-(4.3) with $\alpha_{g,q} = 0$ and an optical injection given by Eq. (4.4) with $n = 1$ and $n = 3$, respectively. It is seen that the asymptotic relations give a good approximation of the locking region even for relatively large injected field amplitudes a. Our numerical simulations and asymptotic analysis indicate that optical-frequency locking range is about 10 times larger than RF locking range in the adjacent mode injection case $n = 1$ (see Fig. 4.8).

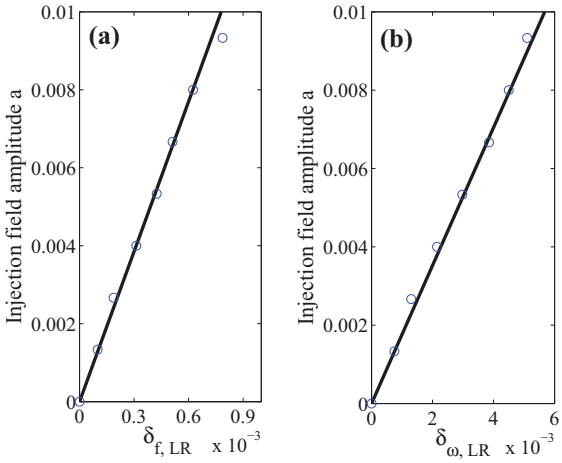

Figure 4.8: Locking range half-width as a function of the injection field amplitude a for $n = 1$ and (a): RF locking range, (b): optical locking range. Black solid line shows the results obtained by asymptotic analysis, circles show the numerical simulations.

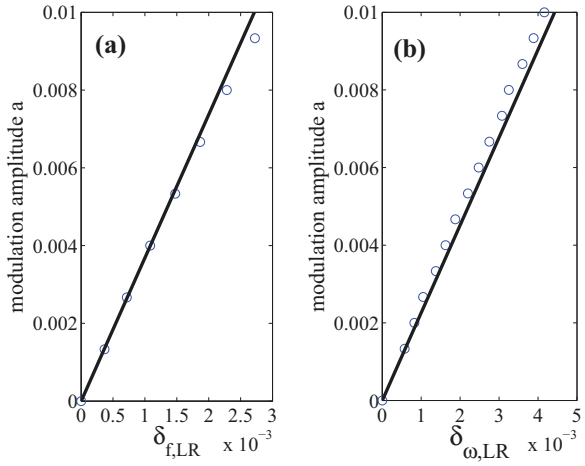

Figure 4.9: Locking region halfwidth as a function of the injection field amplitude a for $n = 3$ and (a): RF locking range, (b): optical locking range. Black solid line shows the results obtained by asymptotic analysis, circles show the numerical simulations.

4.5 Parameter study

In Eqs. (4.25)-(4.26) the ratios $\delta_{f,LR}/a$ and $\delta_{\omega,LR}/a$ characterize the capacity of the mode-locking regime to be locked by the dual mode injection frequencies. The dependence of these ratios on the parameters of Eqs. (4.1)-(4.3) is illustrated in Figs. 4.10 and 4.11 for different values of the parameter g_0 and zero α-factors. It was demonstrated experimentally that locking range width increases with the absolute value of negative voltage applied to the absorber section [47]. Since it is known that the absorber relaxation rate γ_q increases with the absolute value of the reverse voltage, we studied the dependence of the locking range on γ_q. It is seen from Figs. 4.10 and 4.11 that both RF locking range and optical frequency locking range have parabolic dependence on γ_q.

Our simulations predict that the RF locking range is smaller than the optical locking range for all values of the parameters. This fact is in agreement with the experimental data obtained with 10 GHz quantum dot PML laser [88]. We have found that both RF and optical locking range (Figs. 4.10-4.11) decrease with an increase of the intensity attenuation factor per cavity round-trip κ, the saturation parameter s, and the spectral filtering bandwidth γ. Similar behavior of a hybrid mode-locked laser has been discussed in the previous chapter. A decrease of the locking range with an increase of γ suggests that the inclusion of an additional spectral filtering section into the laser cavity can lead to an increase of the locking range. This fact was mentioned in Ref. [105] where a PML laser with a single-frequency coherent injection was studied theoretically and in Ref. [42] where hybrid mode-locking was studied theoretically and experimentally.

4.6 Conclusion

We have performed a theoretical study of the dynamics of a PML laser subject to dual mode coherent optical injection. It has been demonstrated that in the case of zero α-factors, the RF and optical locking ranges increased almost linearly with the injection field amplitude. When α-factors are nonzero the RF and optical locking ranges are asymmetric with respect to the pulse repetition frequency of the free-running PML laser. This asymmetry is related to the increase of the pulse repetition frequency with the injection amplitude. Our numerical simulations indicate that the optical locking range is approximately ten times larger than RF locking range both in the case of vanishing and non-vanishing α-factors. Our simulations predict that the RF locking range is smaller than optical locking range for all values of the parameters considered in this chapter. This fact is in the agreement with the experimental data obtained with a mode-locked quantum dot laser [88].

We have also demonstrated numerically that optical locking range is approximately 10 times larger than that of the RF when the frequency separation between 2 injected modes is close to the third harmonic of the free-running PML laser repetition frequency. The values of the locking range width calculated in this case for non-zero α-factors had similar values when compared to the injection locking of two adjacent modes.

Analytical estimates of the the locking range width have been obtained using an

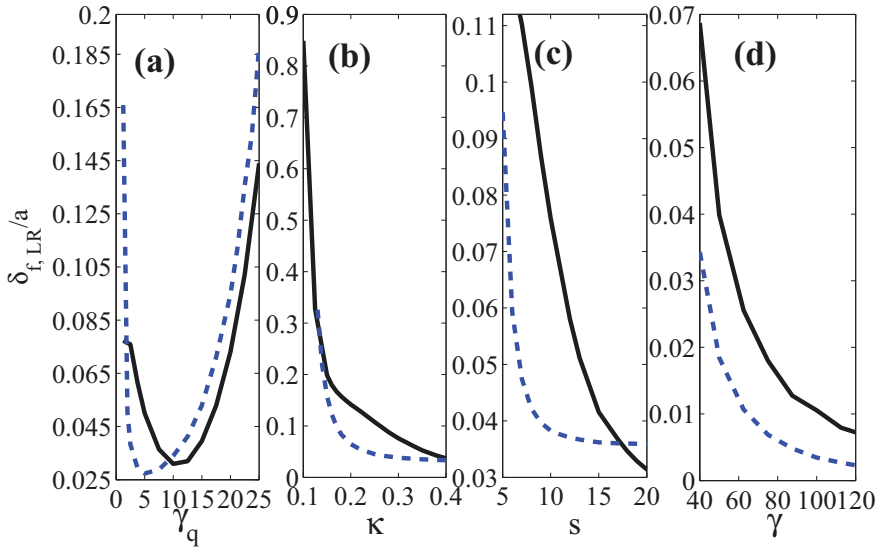

Figure 4.10: Dependence of $\delta_{f,LR}/a$ on the model parameters, $\alpha_g = \alpha_q = 0$. Black solid and blue dashed lines correspond to $g_0 = 1.25$ and $g_0 = 2$ respectively. Other parameters are as in Table 3.1.

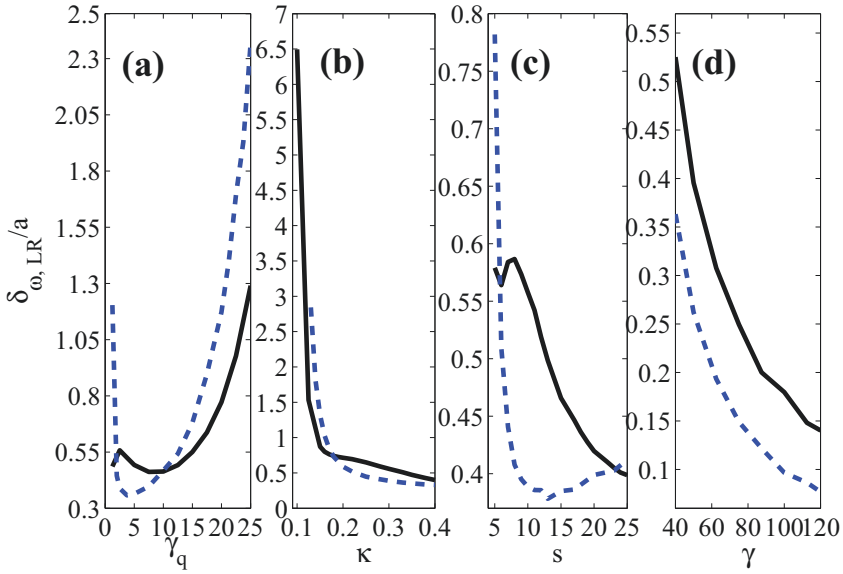

Figure 4.11: Dependence of $\delta_{\omega,LR}/a$ on the model parameters, $\alpha_g = \alpha_q = 0$. Black solid and blue dashed lines correspond to $g_0 = 1.25$ and $g_0 = 2$ respectively. Other parameters are as in Table 3.1.

asymptotic approach. According to these estimates the optical locking range and RF locking range have parabolic dependence on the absorber relaxation rate γ_q and decrease with an increase of the parameters γ, s, and κ, which describe the spectral filtering bandwidth, the ratio of the saturation intensities in the gain and absorber sections, and linear attenuation per cavity round trip, respectively. A similar tendency was observed in our previous study of hybrid mode-locking in Chapter 3.

5 Pulse repetition-frequency multiplication in a coupled cavity mode-locked semiconductor laser

Using a delay differential equation model with two time delays, we investigate the dynamics of a semiconductor laser with an active cavity coupled to an external passive cavity. Our numerical simulations indicate that when the coupling between the two cavities is strong enough and the round-trip time of the active cavity is an integer multiple of the round-trip time of the external passive cavity, a harmonic mode-locking regime can develop in the laser with the pulse repetition period close to the passive cavity round trip time.

5.1 Introduction

Passively mode-locked semiconductor lasers generate short optical pulses with high repetition rates varying from few to hundreds of GHz. They have important applications in optical telecommunications, sampling, and division multiplexing [20–25]. The optical spectrum of these lasers is a frequency comb with the line spacing equal to the pulse repetition rate of the mode-locked regime. This repetition rate is limited by the operational frequencies of the optical modulators and by the fact that the active medium length must be sufficiently large to achieve laser generation [48]. Therefore, different methods for pulse repetition frequency multiplication in such lasers have been used. Among them are the schemes employing colliding pulse mode-locking [129], the group delay dispersion in optical fibers (temporal fractional Talbot effect in optical fibers) [49, 50], chirped fiber Bragg grating based on the same Talbot effect [51, 130], and a number of uniform fiber Bragg gratings [48]. Another method of increasing the pulse repetition rate in a mode-locked laser is based on the use of a Fabry-Perot interferometer as an external spectral filter. This method is attractive due to its simplicity and robustness since commercially available Fabry-Perot filters may be employed [53, 56]. Experimentally it was realized by different authors, see, for example, Refs. [53–57]. The idea of this method is the following [53], see Fig.5.1. If the separation between transmission peaks of the Fabry-Perot interferometer is exactly m times (m is an integer number) larger than the pulse repetition rate of the laser, then only those laser modes will be transmitted through the Fabry-Perot filter which coincide with the transmission lines of this filter. Since this leads to an increase of the separation between the resulting laser modes by m times, one can expect that the repetition frequency can be increased m times [53]. In the example presented in Fig.5.1 $m = 2$. Typical solid state mode-locked femtosecond

lasers have free spectral range from about 100 MHz to 1 GHz [131, 132]. On the other hand, for the precision measurements of astronomical objects, a comb spacing of 10 to 30 GHz is ideal [132]. This is why filtering of femtosecond-laser frequency combs by an external Fabry-Perot cavity is used to generate a broad spectrum of resolvable lines for astronomical measurements, for instance, in astronomical spectrograph calibration (see reviews [132–134]).

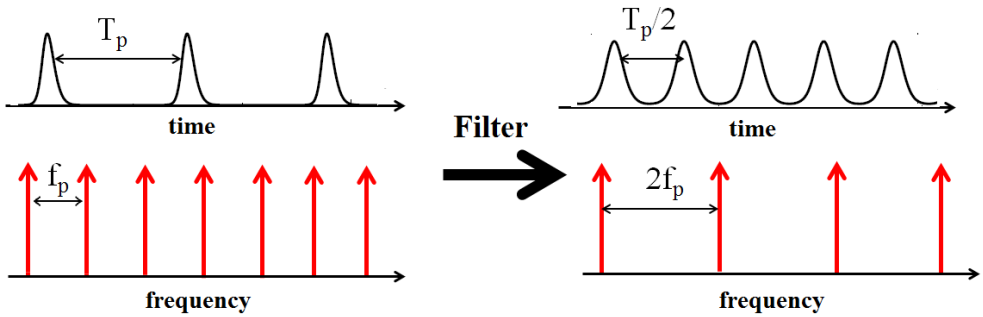

Figure 5.1: Rate multiplication example showing laser intensity versus frequency and time. Laser modes with frequency spacing f_P produce a pulse train with period $T_p = 1/f_P$. An external Fabry Perot cavity filter passes only modes with frequency spacing $2f_P$. This yields a pulse train with period $T = T_p/2$.

The problem of mode selection in single section semiconductor lasers is one of the most important problems in the control of laser radiation parameters [135]. In particular, semiconductor lasers with a fixed and predetermined number of primary modes are of interest for a number of applications. For example, two-color devices are useful for terahertz generation by photomixing [136]. In order to achieve a single mode operation in Fabry-Perot semiconductor lasers different methods have been used. In a distributed feedback laser, a Bragg grating in the active cavity can result in single mode emission [137]. An alternative technique that can modify the lasing spectrum is the incorporation of a number of scattering centers in the form of slots into the laser cavity [138, 139]. This technique enables the design of single mode lasers, two mode lasers, or passively mode-locked discrete mode lasers [140, 141].

Furthermore, systems consisting of optically coupled lasers can exhibit a very rich variety of different dynamical phenomena and have much in common with other nonlinear systems [142–146]. For example, in optically coupled phase locked lasers the break up of phase-locking can lead to the appearance of chaotic dynamics [144]. The nonlinear dynamics in passively mode-locked semiconductor lasers is an active area of research [147]. In [100–103, 148] the dynamics of passively mode-locked semiconductor lasers was studied theoretically using a system of delay differential equations model.

Optical bistability has been intensively investigated for decades because of its potential application to all-optical logic and signal processing, see e.g. [149]. The existence of optical bistability in the system comprising a cavity mode and an ensemble of two-level atoms was demonstrated theoretically in [150]. It was shown that two stable CW regimes

may coexist in this system and a hysteresis was observed between these regimes when the frequency of the external harmonic signal was changed. Optical bistability was also studied theoretically and experimentally in optically injected semiconductor lasers [151], semiconductor lasers with optical feedback [152, 153], two coupled semiconductor lasers [154], optically injected two-section semiconductor lasers [155], and other laser systems.

In this chapter using a delay differential equations model we study the dynamics of passively mode-locked semiconductor ring laser coupled to an external passive cavity. The external cavity in this case is used as a filter which suppresses certain longitudinal modes of the passively mode-locked laser. We demonstrate an increase of pulse repetition frequency f_P by a factor of 2 and 3 when the external cavity length is two and three times smaller than the active cavity. We study the dependence of these mode-locked regimes on the model parameters and coupling coefficients between the two cavities. We demonstrate that changing the relative phase between the two electric fields in the two cavities leads to a periodic appearance of mode-locking windows with the pulse repetition rates $2f_P$ and $3f_P$, respectively. The period and width of these mode-locking windows depend on the passive cavity length.

Finally we demonstrate the existence of optical bistability between a mode-locked regime and irregular pulsations in the model equations. We have found that a bistable behavior arises when the relative phase between electric fields in two cavities and the pumping power are changed.

The results of this chapter are published in own publication: R. M. Arkhipov, A. Amann, A. G. Vladimirov "Pulse repetition-frequency multiplication in a coupled cavity passively mode-locked semiconductor lasers", Applied Physics B, V. 118(4), pp. 539-548 (2015).

5.2 Model Equations

Our analysis is based on a set of delay differential equations (DDE) describing the time evolution of the electric field amplitudes in the active cavity $A_1(t)$ and in the external cavity $A_2(t)$, as well as the saturable gain $G(t)$, and the saturable absorption $Q(t)$ in the gain and saturable absorber sections of the active cavity (see Fig. 5.2). This model is given by:

$$\frac{dA_1}{dt} = -\gamma_1 A_1 + \gamma_1\sqrt{\kappa}\sqrt{\kappa_1}e^{\frac{(1-i\alpha_g)G(t)-(1-i\alpha_q)Q(t)}{2}}A_1(t-T_1)e^{i\psi} + \\ +\gamma_1\sqrt{1-\kappa}\sqrt{\kappa_2}A_2(t-T_2)e^{i\phi}, \tag{5.1}$$

$$\frac{dA_2}{dt} = -\gamma_2 A_2 + \gamma_2\sqrt{1-\kappa}\sqrt{\kappa_1}e^{\frac{(1-i\alpha_g)G(t)-(1-i\alpha_q)Q(t)}{2}}A_1(t-T_1)e^{i\psi} + \\ +\gamma_2\sqrt{\kappa}\sqrt{\kappa_2}A_2(t-T_2)e^{i\phi}, \tag{5.2}$$

$$\frac{dG}{dt} = g_0 - \gamma_g G - e^{-Q}\left(e^{G}-1\right)|A_1(t-T_1)|^2, \tag{5.3}$$

$$\frac{dQ}{dt} = \gamma_q(q_0 - Q) - s\left(1 - e^{-Q}\right)|A_1(t - T_1)|^2. \tag{5.4}$$

Here T_1 (T_2) is the round trip time in the active (passive) cavity. The parameters ϕ and ψ describe the phase shifts of the fields A_1 and A_2 after the round trip in the active and passive cavity, respectively. Equations (5.1)-(5.4) generalize the model of a passively mode-locked semiconductor laser proposed in [100–102] to the case of two coupled cavities. The parameters κ, κ_1, and κ_2 describe the reflectivities of the mirrors 3, 2, and 5, respectively, see Fig. 5.2. Typical values and a short description of the model parameters are given in Table 5.1. Each of the two coupled cavities has its own spectral filtering element. Since the passive cavity is empty, we assume that the spectral filtering bandwidth is much larger in the passive cavity than in the active one, $\gamma_2 \gg \gamma_1$. Below, we will consider the case when $\psi = 0$ for simplicity. The effect of the phase ϕ on the dynamics of coupled cavity laser is studied in Section 5.5. Let the active cavity round-trip time be equal to 25 ps. This corresponds to the pulse repetition frequency close to 40 GHz in the absence of external cavity and to $T_1 = 2.5$ in the normalized units of Eqs. (5.1)-(5.4) [102], where the time is normalized to the carrier relaxation time in the absorber section (10 ps).

Table 5.1: Typical parameter values used in simulations

spectral filtering bandwidth in the active cavity	γ_1	15
spectral filtering bandwidth in the passive cavity	γ_2	50
non-resonant field intensity attenuation factor per cavity round-trip	$\kappa_1 = \kappa_2$	0.3
linewidth enhancement factor in gain section	α_g	0
linewidth enhancement factor in saturable absorber section	α_q	0
pump parameter	g_0	0.5
unsaturated absorption	q_0	2
carrier relaxation rate in gain section	γ_g	0.01
carrier relaxation rate in saturable absorber section	γ_q	1
ratio of gain and absorber saturation intensities	s	10
optical phase shift in the active cavity	ψ	0
optical phase shift in the passive cavity	ϕ	0
active cavity round trip time	T_1	2.5
passive cavity round trip time	T_2	$T_1/2, T_1/3$

5.3 Results of numerical simulations

5.3.1 80-GHz mode-locking regimes

In this section we present the results of numerical simulations of Eqs. (5.1)-(5.4) with the parameter values given in Table 5.1. We demonstrate that when the external cavity

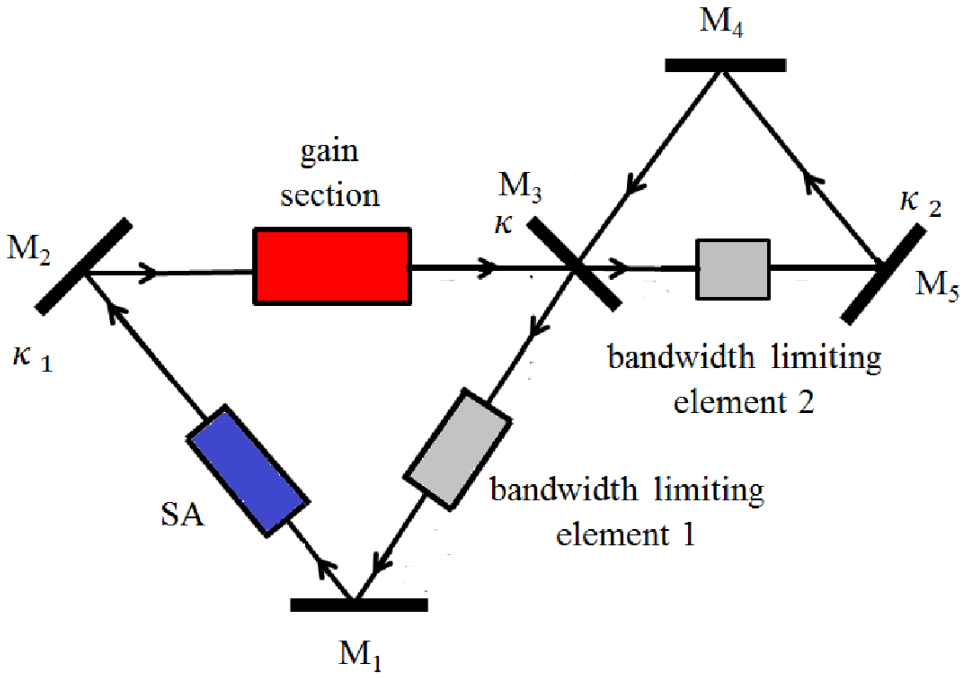

Figure 5.2: Schematic representation of mode-locked laser coupled to an external passive cavity. The active cavity contains gain section, saturable absorber section, and a spectral filtering element with the bandwidth γ_1. External passive cavity contains only a spectral filtering element with the bandwidth γ_2 which is assumed to be much larger than that of the active cavity, $\gamma_2 \gg \gamma_1$. Parameters κ, κ_1, and κ_2 are the reflectivities of the mirrors M_3, M_2, and M_5, respectively.

length is approximately twice smaller than the laser cavity length, $T_2 \approx T_1/2$, an increase of the pulse repetition frequency by a factor of 2 can be achieved. First, we study the evolution of dynamical regimes with an increase of the reflectivity κ of mirror 3. The bifurcation diagram in Fig. 5.3 shows the laser pulse peak intensity as a function of κ. To calculate this diagram we have used the following procedure. First, at each given value of the parameter κ Eqs. (5.1)-(5.4) have been integrated from $t = 0$ to $t = 5000$ in order to skip the transient behavior. Next, during the time interval from $t = 5000$ to $t = 7000$, the maxima of the intensity time trace $|A_1(t)|^2$ have been plotted.

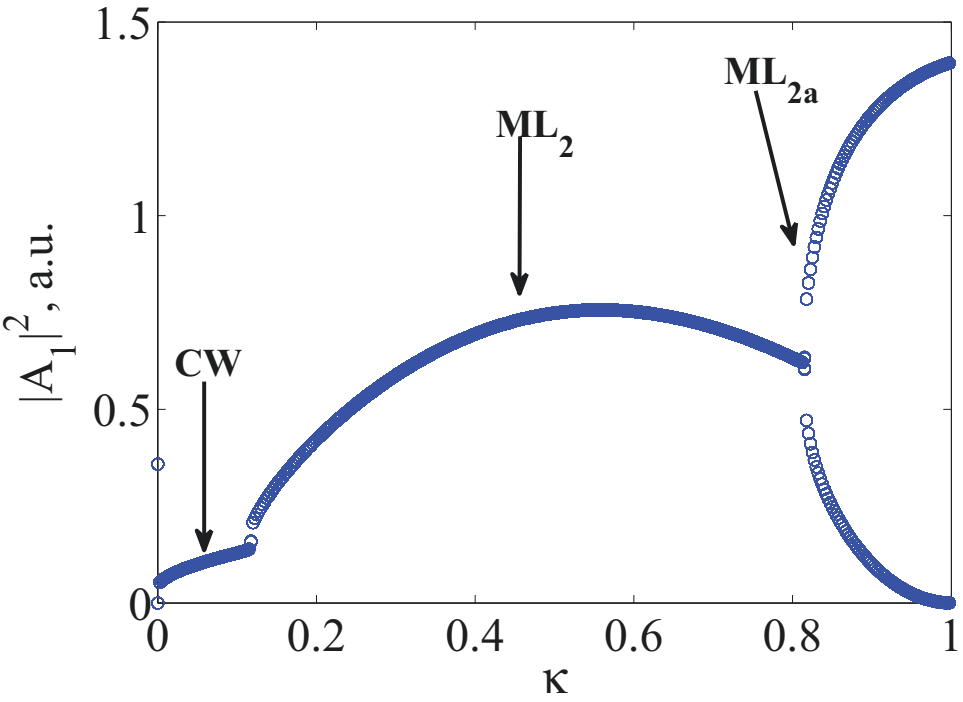

Figure 5.3: Bifurcation diagram presenting the sequence of dynamical regimes taking place with an increase of the reflectivity κ. $T_2 = T_1/2$, other parameter values are given in Table 5.1. CW, ML_2, and ML_{2a} indicate a continuous wave, an 80 GHz mode-locking regime, and an 80 GHz mode-locking regime with 2 pulses in the cavity having different peak powers, respectively.

In Fig. 5.4 four different examples of the laser intensity time trace are given. When the reflectivity κ is small (the case of strong coupling) the laser operates in a CW regime with the electric field intensity independent of time. The intensity time trace illustrating this regime is shown in Fig. 5.4a. This regime is indicated as CW in Fig. 5.3. An increase of κ leads to the appearance a harmonic mode-locking regime (ML_2) with the pulse repetition frequency close to 80 GHz (see Fig. 5.4b). In this regime the laser emits two pulses per active cavity round trip time T_1. The peak intensity of these pulses increases

with κ for $\kappa \leq 0.5$. A further increase of the reflectivity κ up to 0.8 leads to a decrease of the pulse peak intensity. When κ becomes larger than 0.8 a transition to a regime ML_{2a} with two pulses in the cavity with different peak intensities takes place via period doubling bifurcation (Figs. 5.4c). One of these pulses has larger pulse peak power and the other is smaller than the peak power of the harmonic mode-locking regime with two identical pulses shown in Fig. 5.4b. Finally, at large coupling strengths $\kappa = 1$ the laser undergoes a transition to a fundamental mode-locking regime with the repetition frequency 38.88 GHz, see Fig. 5.4d.

Fig. 5.5 has been obtained in a similar way to Fig. 5.3, but with the pump parameter g_0 taken as a bifurcation parameter instead of κ. As seen from Fig. 5.5, when the linear gain g_0 is small enough, the laser exhibits a Q-switching regime QS with the laser intensity oscillating at a low frequency (2 GHz), which is approximately one order of magnitude smaller than the pulse repetition frequency f_P of the fundamental mode-locking regime. The corresponding time trace and power spectrum are presented in Fig. 5.6. Q-switching regimes in passively mode-locked quantum dot lasers were studied theoretically using a DDE nodel in [103]. For values of the parameter g_0 within the interval $0.161 < g_0 < 0.361$ the laser operates in a CW regime (not indicated in Fig. 5.5). With further increases in the pump parameter g_0, a transition to a harmonic mode-locking regime with a repetition rate that is approximately twice higher takes place as shown in Fig. 5.4b. Finally, for large $g_0 > 1.5$ a CW regime becomes stable.

5.3.2 120-GHz mode-locking regimes

In this subsection we study the dynamics of a passively mode-locked semiconductor laser coupled to an passive cavity of length $L/3$, where L is the active cavity length ($T_2 = T_1/3$). In the simulations we have used the parameter values $q_0 = 3$, $\kappa_1 = 0.3$, and $\kappa_2 = 0.9$. Other parameter values are given in Table 5.1. Similar to the case discussed in the previous section, when the coupling strength κ is large enough one can expect the appearance of a harmonic mode-locking regime with a "multiplied" pulse repetition frequency $3f_P$. Such regimes were observed in numerical simulations of a model of passively mode-locked semiconductor laser without external cavity ($\kappa = 1$) at sufficiently large values of the pumping parameter g_0 [102].

A bifurcation diagram illustrating the dependence of the pulse peak power $|A_1|^2$ on the reflectivity κ is presented in Fig. 5.7. When $\kappa \lessapprox 0.05$ the laser exhibits periodic pulsations (ML_{3a}) with the period close to $2T_1/3$ determined by the sum of the length of the two cavities. Two intensity time traces of this regime corresponding to $\kappa = 0.01$ and $\kappa = 0.03$ are plotted in in Figs. 5.8a,b. At slightly larger reflectivities the laser starts to operate in a CW regime (see Fig. 5.8c). When κ becomes close to 0.07 harmonic mode-locking regime with the "multiplied" pulse repetition frequency close to $3f_P$ appears. The field intensity time trace for this regime is shown in Fig. 5.8d. Finally, at sufficiently large κ a transition from the harmonic mode-locking regime to a CW regime takes place.

To study the effect of the injection current on the harmonic mode-locking regime with the pulse repetition frequency $3f_P$, we present a bifurcation diagram illustrating the dependence of pulse peak power $|A_1|^2$ on the pump parameter g_0 in Fig. 5.9. This

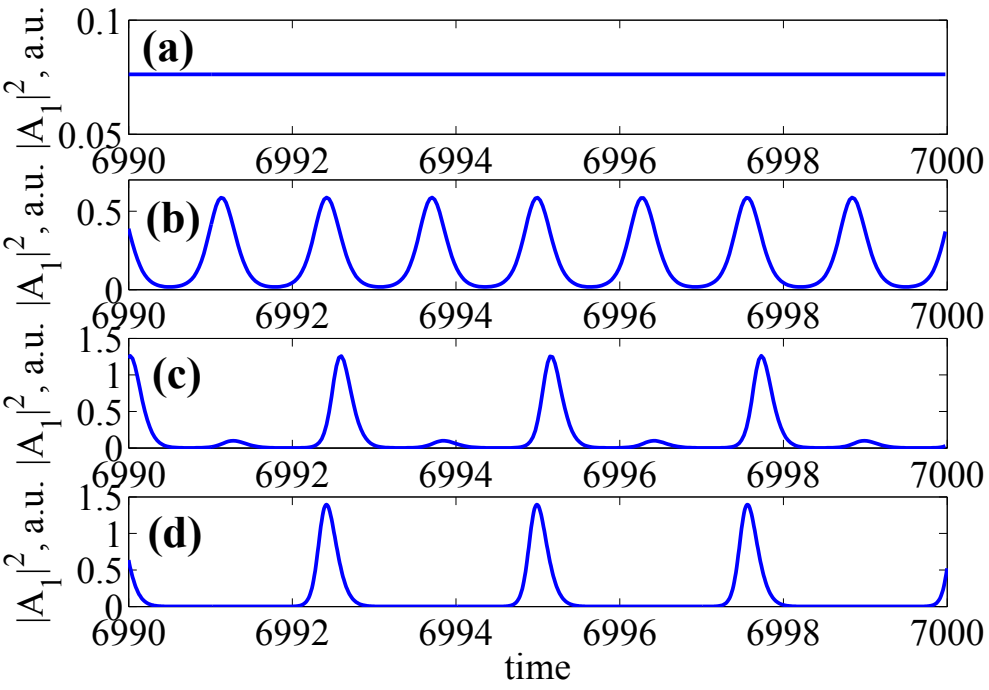

Figure 5.4: Intensity time traces at different values of the reflectivity parameter κ. (a): CW regime, $\kappa = 0.02$, (b): 80 GHz mode-locking ML_2, $\kappa = 0.3$, (c): harmonic mode-locking regime with two pulses having different peak powers ML_{2a}, $\kappa = 0.9$, (d): 40-GHz fundamental ML regime, $\kappa = 1$.

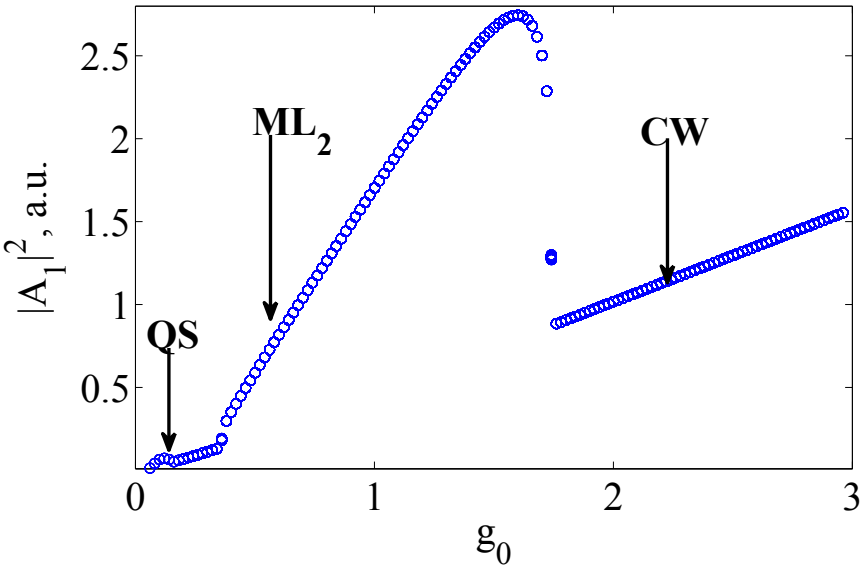

Figure 5.5: Pulse peak power $|A_1|^2$ versus g_0, $\kappa = 0.3$, $T_2 = T_1/2$. Other parameter values are given in Table 5.1. Q-switching regime shown in Fig. 5.6 is indicated as QS.

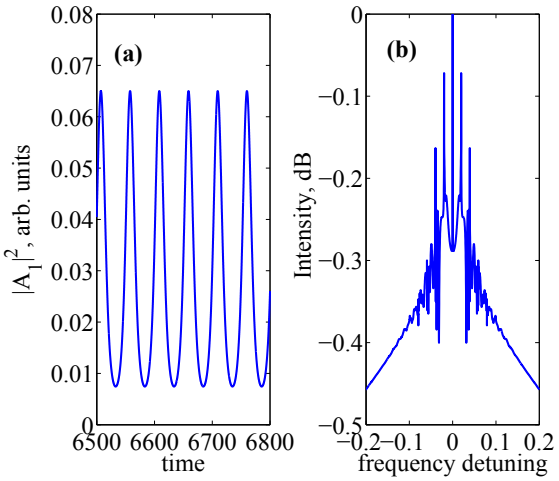

Figure 5.6: Laser intensity time traces for $g_0 = 0.1$ and $\kappa = 0.3$ (a). Power spectrum (b). Other parameter values are the same as in Fig. 5.5.

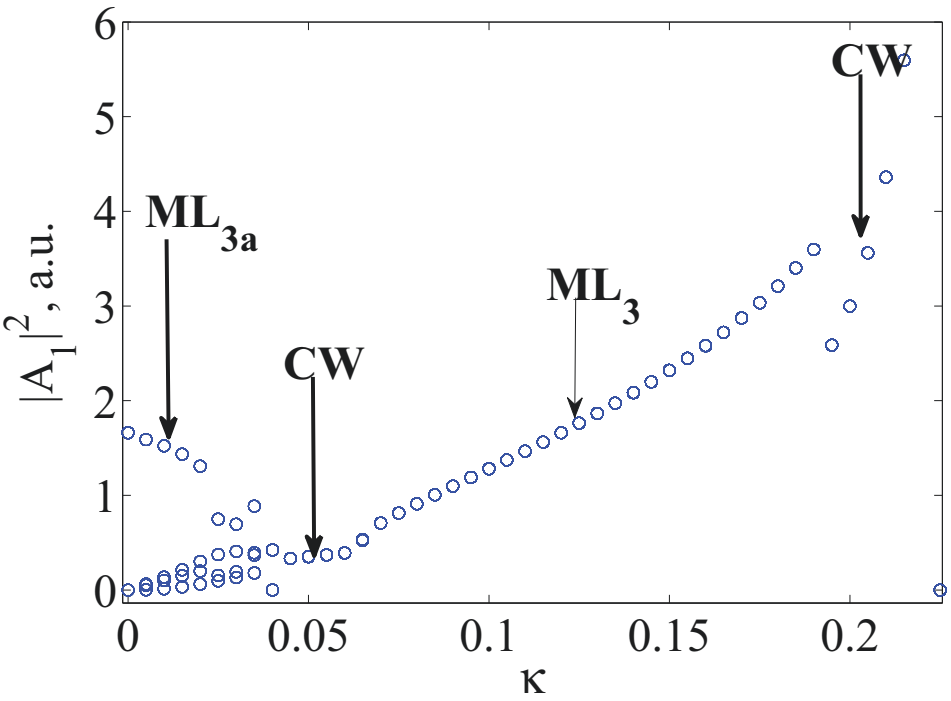

Figure 5.7: Bifurcation diagram illustrating pulse peak power $|A_1|^2$ as a function of reflectivity κ, $T_2 = T_1/3$, $q_0 = 3$, $\kappa_1 = 0.3$, and $\kappa_2 = 0.9$. Other parameter values are given in Table 5.1. Mode-locking regimes with three pulses in the cavity having different peak powers are indicated ML_{3a}. Intensity time trace of this regime is shown in Figs. 5.8a,b. ML_3 indicates harmonic mode-locking regime with the pulse repetition rate close to 120 GHz, see Fig. 5.8d.

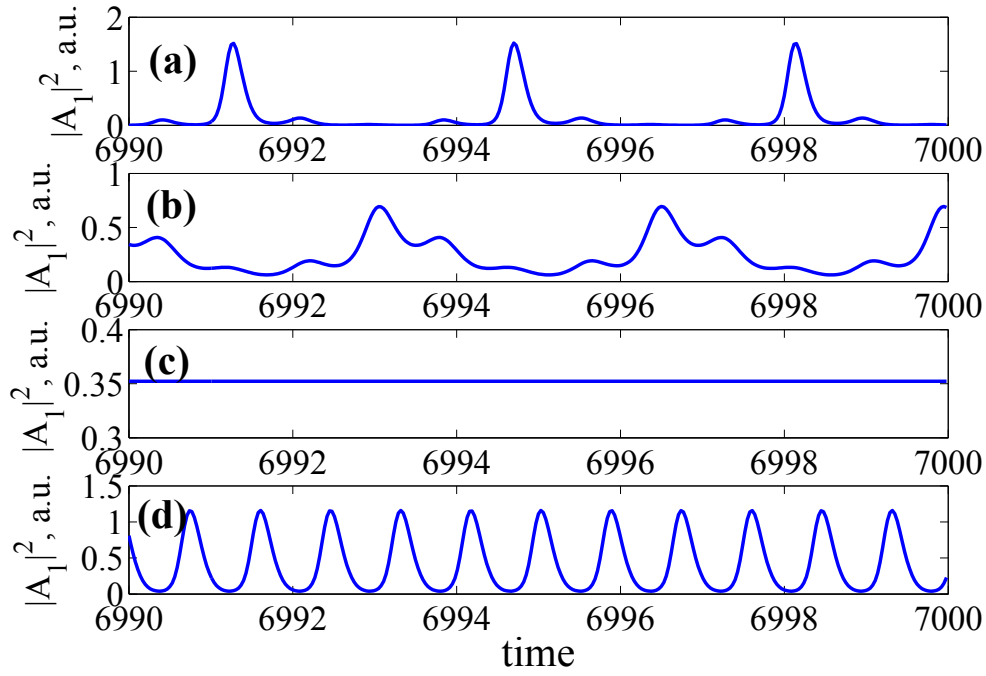

Figure 5.8: Laser intensity time traces for different values of the reflectivity κ. (a): ML_{3a} regime of periodic pulsations with the period determined by the sum of the round trip times of the two cavities, $2T_1/3$, $\kappa = 0.01$, (b): ML_{3a} regime, $\kappa = 0.03$, (c): CW regime, $\kappa = 0.05$, (d): 120 GHz mode-locking regime ML_3, $\kappa = 0.15$. Other parameter values are the same as in Fig. 5.7.

figure corresponds to the fixed value of the reflectivity $\kappa = 0.15$, for which this regime occurs in Fig. 5.7. When g_0 is small enough the laser operates in Q-switching (QS) regime (see Fig. 5.10), which corresponds to a periodic pulse train with the pulse peak power oscillating at a low frequency close to 1.7 GHz. When g_0 becomes close to 0.3, a harmonic mode-locking regime with the pulse repetition frequency close to $3f_P$ (ML_3) appears, as seen in Fig. 5.8d. Finally, for $g_0 > 0.66$ a CW regime becomes stable.

Our analysis indicates that harmonic mode-locking regimes with the pulse repetition rate $3f_P$ can be observed not only in the case when the passive cavity is three times shorter than the active one $T_2 = T_1/3$, but also for $T_2 = 2T_1/3$. In both these cases every third mode of the active cavity coincides with a certain mode of the external passive cavity and, hence, mode-locking regimes with the pulse repetition rate $3f_P$ can be expected. A bifurcation diagram obtained for the case $T_2 = 2T_1/3$ is similar to that shown in Fig. 5.7.

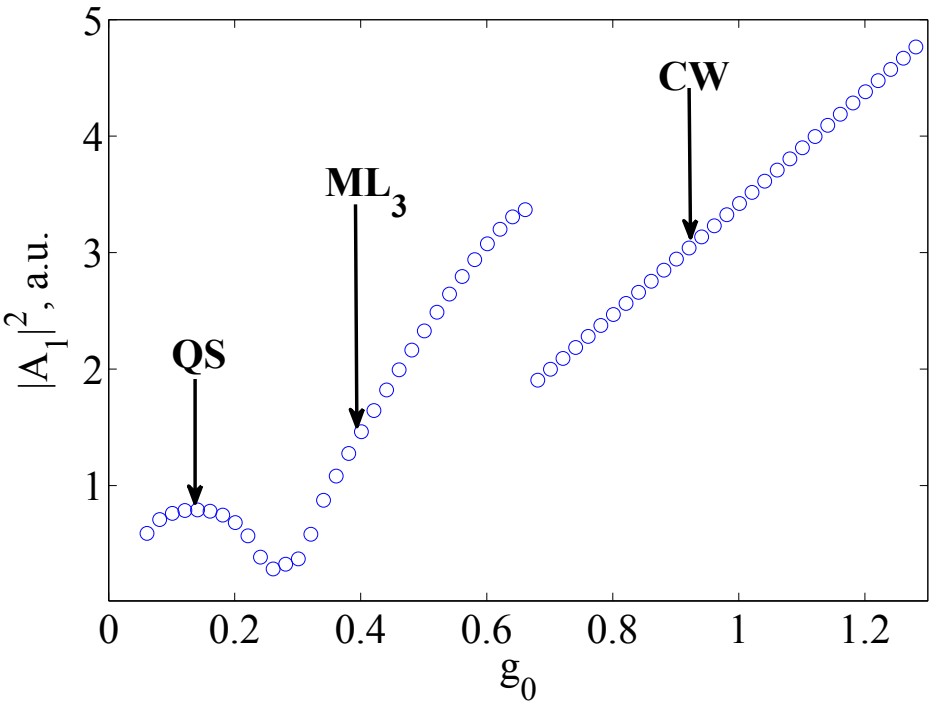

Figure 5.9: Pulse peak power $|A_1|^2$ versus g_0, $T_2 = T_1/3$, $\kappa = 0.15, \kappa_1 = 0.3$, and $\kappa_2 = 0.9$. Other parameters are the same as in Fig. 5.7.

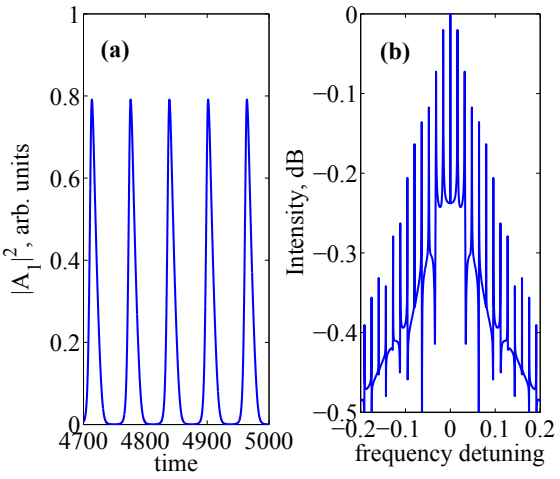

Figure 5.10: (a): Intensity time traces illustrating Q-switching regime for $g_0 = 0.14$. (b): Spectrum. $T_2 = T_1/3$, $\kappa = 0.15, \kappa_1 = 0.3$, $\kappa_2 = 0.9$. Other parameters are the same as in Fig. 5.9.

5.4 Nonzero linewidth enhancement factors

In this section we study the effect of the linewidth enhancement factors on the dynamics of Eqs. (5.1)-(5.4). It is known that for sufficiently large linewidth enhancement factors, a mode-locking regime can be destabilized and irregular pulsations can appear. The influence of the α-factors on the dynamics of a passively mode-locked semiconductor laser without external cavity was studied in [102]. Fig. 5.11 was obtained by taking the linewidth enhancement factors as bifurcation parameters. It is seen in Fig. 5.11a, which corresponds to $\alpha_q = 1.0$, that the largest pulse peak powers were observed in the case when the linewidth enhancement factors in the two sections are approximately equal: $\alpha_g \approx \alpha_q$. This can be intuitively explained as follows [102]. Since gain and loss enter in equation (5.1) with opposite signs, the contributions of the gain and absorption sections into the pulse chirp must compensate each other, at least partially, when the two linewidth enchancement factors have the same sign. When α_g is increased the pulse peak power decreases, and a transition to irregular pulsations and CW regime takes place (starting from $\alpha_g \simeq 1.7$). Similar behavior was observed for $\alpha_g = \alpha_q$, see Fig. 5.11b: the pulse peak power decreases with an increase of the two linewidth enhancement factors and a transition to irregular pulsations regime takes place at $\alpha_g = \alpha_q \simeq 3$. It was found in [102] that this transition is associated with the intermittency between mode-locking solution and chaotic intensity pulsations. Slightly above the transition point, time intervals characterized by an almost regular mode-locking behavior alternate with irregular spiking. The duration of the "regular" time intervals decreases with an increase of α_g, and, finally, irregular pulsations regime develops. The break up of a mode-locking regime can be explained by the presence of intracavity dispersion. When the linewidth

enhancement factors are large, frequencies of the laser modes become nonequidistant due to the strong intracavity dispersion and the mode-locking regime disappears.

5.5 Influence of the relative phase ϕ

In the previous section we assumed that the phase shift in both cavities is equal to zero, $\phi = \psi = 0$. This means that the frequency of the central mode of the active cavity coincides with that of the passive cavity. In order to satisfy this condition it is necessary to make the optical length of the external cavity n times smaller than the optical length of the active cavity ($L_2 = L_1/n$, n-integer number) with the precision to a small fraction of the wavelength. However, since in reality it is rather difficult to build the two cavities with such a high precision, it is interesting to consider the dynamics of the coupled cavity laser in the case when the central mode of the passive cavity is shifted in frequency with respect to that of the active cavity, $\phi \neq 0$. To this end we take the phase ϕ as the bifurcation parameter and perform numerical integration of the model equations (5.1)-(5.4) with the parameters given in Table 5.1, $T_2 = T_1/2$, and $\kappa = 0.5$. A bifurcation diagram illustrating the dependence of the pulse peak power $|A_1|^2$ on the parameter ϕ is presented in Fig. 5.12. It is seen that this dependence has a multi-resonant character and is periodic with the period equal to 2π. This periodicity can be easily understood by taking into account the invariance of equations (5.1)-(5.2) under the transformation $\phi \rightarrow \phi + 2\pi$. In Fig. 5.12 the values of ϕ characterized by a single-valued pulse peak power (the peak powers of all pulses in the intensity time trace are equal, see Fig. 5.13a) correspond to mode-locking regimes with the pulse repetition frequency close to $2f_p$. The pulse peak power of this regime achieves its maximum at $\phi = k\pi$ with $k = 0, \pm1, \pm2....$ Finally, near $\phi = (1/2 + k)\pi$ regimes with non-periodic pulsations (NPP) of the pulse peak power are observed. The intensity time traces of these regimes corresponding to a cloud of points in Fig. 5.12 are shown in Fig. 5.13b for $\phi = 0.5\pi$.

Resonant behavior similar to that presented in Fig. 5.12 was observed in the case $T_2 = T_1/3$ as well, see Fig. 5.14. However, in this case the maximal pulse peak power of the harmonic mode-locking regime at $\phi = k\pi$, $k = 0, \pm2, \pm4, \pm6...$ and $\phi \approx 0.66k\pi$, $k = \pm1, \pm2...$ is larger than that in the case $T_2 = T_1/2$ and the windows of non-periodic pulsations are located around $\phi = 0.4\pi, \pi, 1.7\pi, ...$ The nonperiodic regimes appear as a result of destabilization of harmonic mode-locking due to the interference between the electric fields in the two cavities. Note that the resonant behavior shown Fig. 5.12 is similar to the dependence of the transmission function of a Fabry-Perot cavity on the relative phase ϕ [156].

5.6 Optical bistability

Bistable devices are important in the field of optical signal processing for their use as optical logic elements. In the present section we demonstrate the appearance of optical bistability in the model equations (5.1)-(5.4). We consider the case of nonzero linewidth

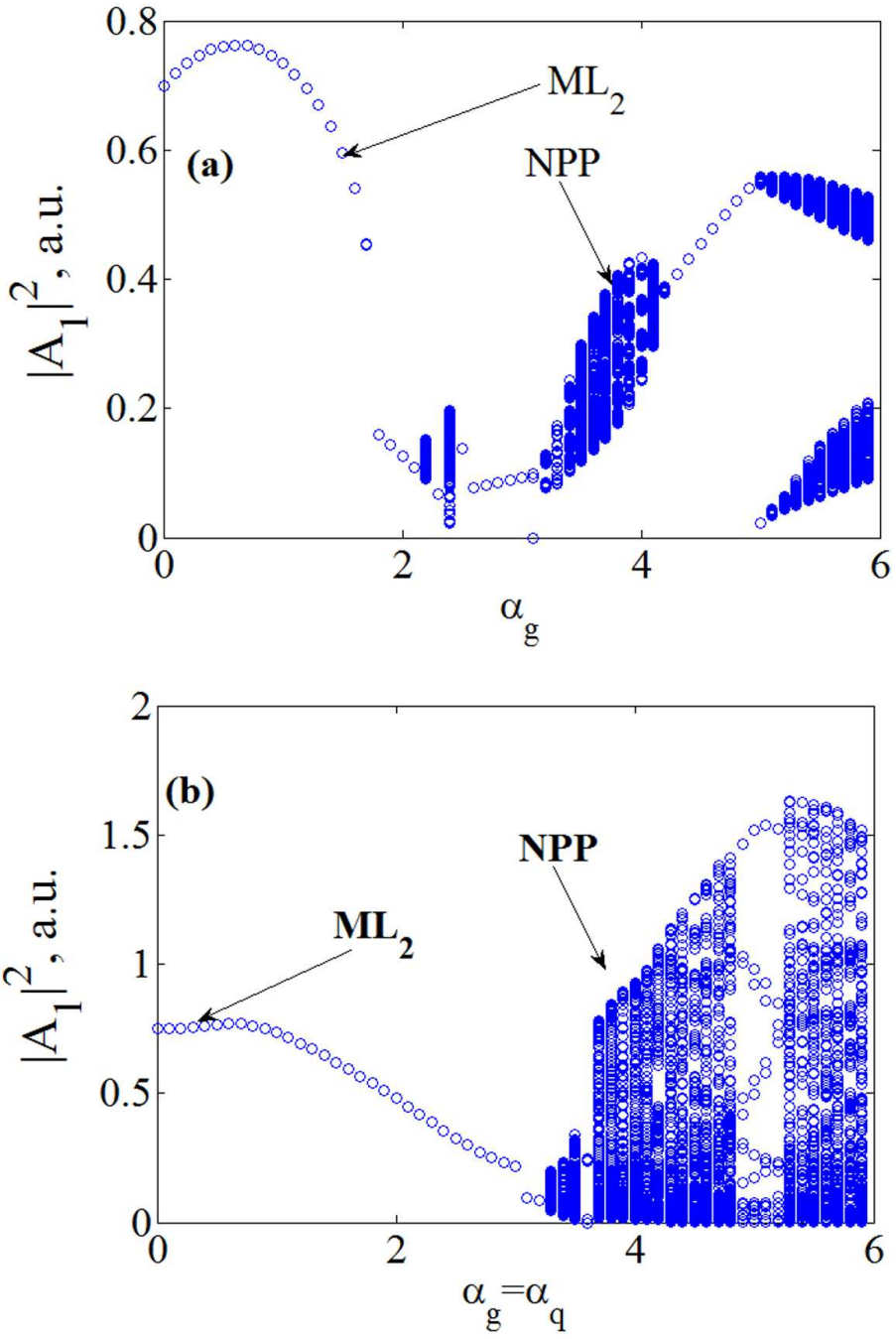

Figure 5.11: Bifurcation diagrams obtained by changing the linewidth enhancement factors α_g and α_q. $T_2 = T_1/2$. (a) Pulse peak power α_g, $\alpha_q = 1.0$, (b) Pulse peak power vs $\alpha_g = \alpha_q$, $\kappa = 0.5$. Other parameters are given in Table 5.1.

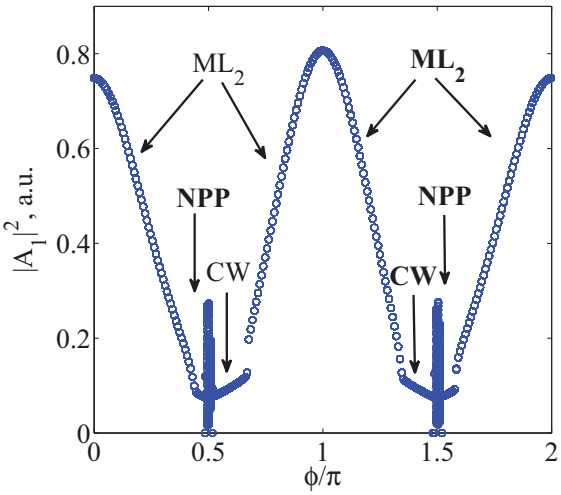

Figure 5.12: Pulse peak power $|A_1|^2$ versus ϕ. $\kappa = 0.5$, $\kappa_1 = 0.3$, $\kappa_2 = 0.3$, and $T_2 = T_1/2$. Other parameters are given in Table 5.1. NPP indicates a regime with non-periodic pulsations of the electric field, see Fig. 5.13b.

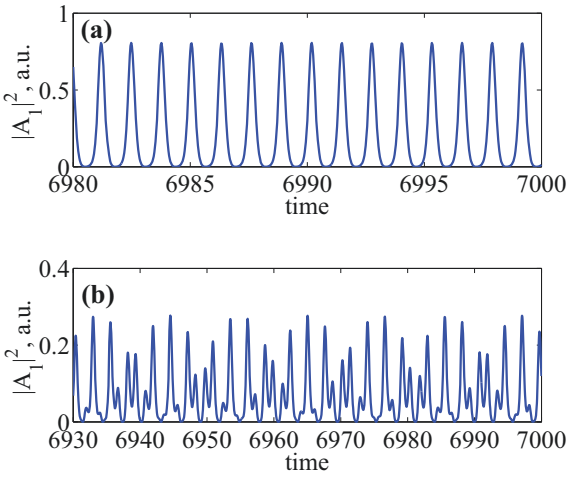

Figure 5.13: Intensity time traces $|A_1(t)|^2$ calculated for different values of the parameter ϕ. (a): 80 GHz mode-locking, $\phi = \pi$, (b): regime of non-periodic pulsations NPP, $\phi = 0.5\pi$. $\kappa_1 = \kappa_2 = 0.3$, $\kappa = 0.5$, and $T_2 = T_1/2$. Other parameter values are given in Table 5.1.

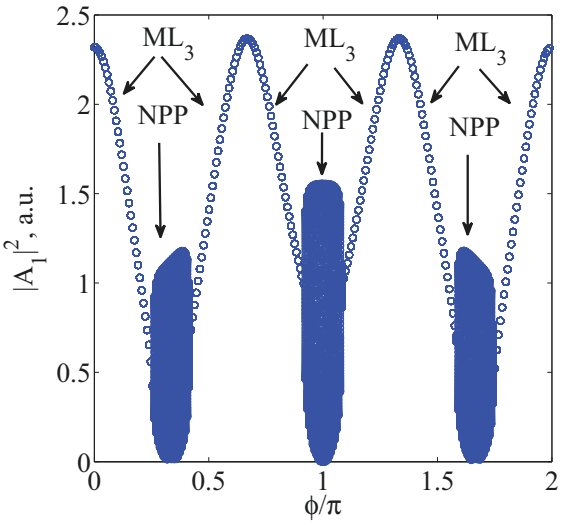

Figure 5.14: Bifurcation diagram of the pulse peak power $|A_1|^2$ versus ϕ. $\kappa = 0.15$, $\kappa_1 = 0.3$, $\kappa_2 = 0.9$, and $T_2 = T_1/3$. Other parameter values are given in Table 5.1.

enhancement factors in the gain and absorber sections, $\alpha_g = 3$ and $\alpha_q = 1$. Fig. 5.15 shows the dependence of the pulse peak power $|A_1|^2$ on the phase ϕ for $T_2 = T_1/3$. This figure was obtained by numerical integration of the model equations at each value of the parameter ϕ on an equidistant grid with the solution calculated at the previous value of ϕ taken as an initial condition. After the integration the pulse peak powers were plotted versus the phase ϕ. This procedure was repeated with stepwise increasing and stepwise decreasing of the phase parameter ϕ. Black circles and red crosses in Fig. 5.15 correspond to the case when the parameter ϕ was increased and decreased, respectively. It is seen from the figure that within the intervals $0.64\pi \lessapprox \phi \lessapprox 0.74\pi$ and $1.3\pi \lessapprox \phi \lessapprox 1.4\pi$ the laser exhibits a bistability between harmonic mode-locked states (ML_3) with the repetition rate close to 120 GHz and non-periodic regimes (NPP). Furthermore, our simulations demonstrated that the appearance of optical bistability in the system is related to nonzero linewidth enhancement factors in the gain and absorber sections.

In typical experiments on optical bistability the laser output power is measured as a function of the injection current [152–154]. The diagram shown in Fig. 5.16 was obtained in similar ways those in Fig. 5.5 and Fig. 5.9 but with the pump parameter g_0 taken as a bifurcation parameter instead of the detuning ϕ. It corresponds to the case when the external cavity length is three times smaller than that of the active cavity, $T_2 = T_1/3$. It is seen from this figure that when the pump parameter is small the laser operates in a Q-switching regime (QS). With an increase of g_0 a transition to harmonic mode-locking regime with the pulse repetition rate close to 120 GHz (ML_{3f}) takes place, see the black circles in Fig. 5.16. Finally, at $g_0 \approx 1.5$ the laser starts to operate in CW regime (CW_f). When the pump parameter is decreased (red crosses in Fig. 5.16) the laser starts from

a CW regime (CW_b in Fig. 5.16), but the electric field intensity in this case is larger than that of the regime CW_f. The regime CW_b is stable for $g_0 \succeq 0.65$. Below this value a transition to a harmonic mode-locking regime with frequency close to $3f_P$ (ML_{3b}) takes place. A further decrease of g_0 leads to a transition to a Q-switching regime QS coinciding with that obtained by increasing g_0.

The physical mechanisms responsible for the appearance of bistability can differ. For example, it was demonstrated in Ref. [154] that bistability in two coupled semiconductor lasers arises due to the gain saturation that is strongly affected by the mutual coupling of the two cavities.

To demonstrate that the bistability shown in Fig. 5.16 is related to the presence of the nonzero linewidth enhancement factors in the model equations we integrate these equations with α_g taken as a bifurcation parameter, and $g_0 = 2.98$, see Fig. 5.17. Red crosses and black circles were obtained by decreasing the parameter α_g from $\alpha_g = 3$ to $\alpha_g = 0$ along the branches CW_b and CW_f, respectively, see Fig. 5.16. The result of these simulations is plotted in Fig. 5.17. It is seen from Fig. 5.17 that two stable CW branches coexist for $\alpha_g < \alpha_g^* \approx 0.55$. However, at small $\alpha_g < \alpha_g^*$ the branch CW_f with smaller laser intensity becomes unstable and bistability disappears.

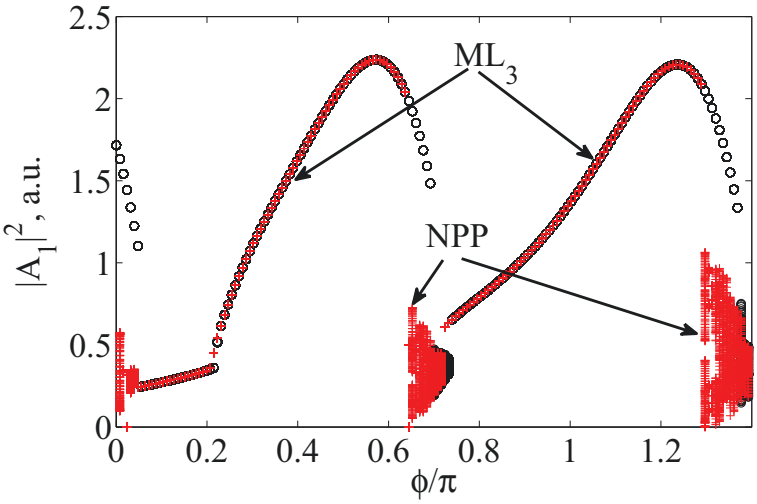

Figure 5.15: Bifurcation diagram of the pulse peak power $|A_1|^2$ versus ϕ. $q_0 = 3$, $\kappa = 0.15$, $\kappa_1 = 0.3$, $\kappa_2 = 0.9$, $T_2 = T_1/3$, $\alpha_g = 3, \alpha_q = 1$. Black circles (red crosses) correspond to the case when ϕ was increased (decreased). Other parameter values are given in Table 5.1.

5.7 Conclusions

In summary, we have studied the dynamics of a 40-GHz passively mode-locked semiconductor laser coupled to an external passive cavity. Our analysis was based on a set of

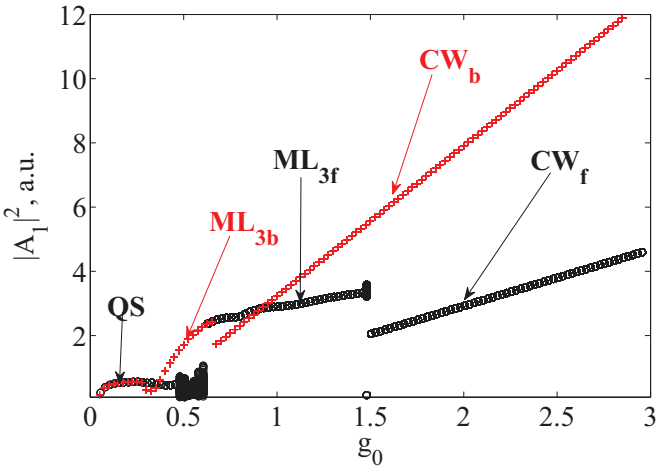

Figure 5.16: Bifurcation diagram of the pulse peak power $|A_1|^2$ versus pump parameter g_0. $q_0 = 3$, $\kappa = 0.15$, $\kappa_1 = 0.3$,$\kappa_2 = 0.9$, $T_2 = T_1/3$, $\alpha_g = 3, \alpha_q = 1$, and $\phi = 0$. Black circles (red crosses) correspond to the case when g_0 was increased (decreased). Other parameter values are given in Table 5.1. CW_f and CW_b indicate two bistable CW regimes. ML_{3f} and ML_{3b} correspond to harmonic mode-locking regimes with the pulse repetition frequency close to 120 GHz.

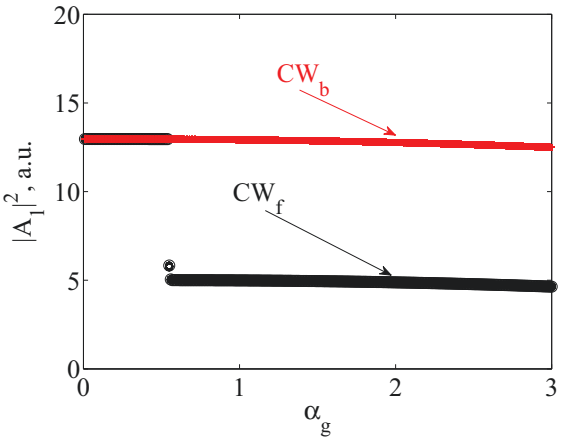

Figure 5.17: Bifurcation diagram of the pulse peak power $|A_1|^2$ versus α_g. $g_0 = 2.98$. Other parameter values are the same as in Fig. 5.16.

delay differential equations governing the time evolution of the electric field envelopes in the two cavities, saturable gain, and saturable absorption. We have shown that the dynamical behavior of the laser depends strongly on the length of the external cavity, the coupling strength between the two cavities, pumping parameter, and the relative phase ϕ. If the length of the external cavity is two or three times smaller than that of the active cavity and the coupling between two cavities is strong enough, it is possible to generate mode-locking pulses with the "multiplied" repetition frequency close to $2f_P$ or $3f_P$, respectively.

We have investigated the effect of the linewidth enhancement factors on the dynamics of a coupled cavity mode-locked laser. In particular, our numerical simulations indicate that at large linewidth enhancement factors mode-locking regimes with the pulse repetition rates $2f_P$ and $3f_P$ can be destroyed and, as a result, irregular pulsations regime can develop. A beak-up of the mode-locking regimes can be attributed the intermode distance variation due to the intracavity dispersion.

We have studied the effect of the phase ϕ describing the relative position of the frequency combs associated with active and passive cavity on the system behavior. Numerical simulations indicate that the pulse peak power has a periodic dependence on ϕ and that there are transitions between nonperiodic and mode-locking regimes when ϕ changes. This periodic dependence seems to have a similar nature as the dependence of the transmission function of a Fabry-Perot cavity on the electric field phase.

We have demonstrated the existence of optical bistability between different laser operation regimes. The bistability arises only when the linewidth enhancement factors are nonzero in the gain and the saturable absorber sections. At zero or sufficiently small linewidth enhancement factors no bistability was observed in our numerical simulations.

6 Transient Cherenkov radiation from a periodic resonant medium

This chapter studies in a theoretical context the optical response of a one-dimensional string made of dipoles with a periodically varying density excited by a spot of light moving along the string at superluminal (subluminal) velocity. Cherenkov radiation in such system is rather unusual, possessing both a transient and resonant character. We show that under certain conditions, in addition to the resonant Cherenkov peak, another Doppler-like frequency appears in the radiation spectrum. Both linear (small-signal) and nonlinear regimes as well as different string topologies are considered.

6.1 Introduction

The problem of superluminal motion and its existence in nature has attracted the attention of various researchers for a considerable time. At the turn of 20th Century, physicists O. Heaviside and A. Sommerfeld considered the radiation of charged particles moving in a vacuum at a velocity greater than the velocity of light in a vacuum c (see [61, 62, 67, 69–74, 157, 158] and references therein). The special theory of relativity does not allow such motion and their works were forgotten for many years. Further analysis has shown that only those motions that involve signal (information) transfer at the superluminal velocity are prohibited, with this strong prohibition being related to the violation of the causality principle [61, 62, 69, 158].

Superluminal objects and sources are well-studied today [67, 69–74]. In Refs. [10, 106–109] the possibility of superluminal propagation of the pulse maxima in an amplifying medium was demonstrated experimentally and theoretically. In the experiment in Refs. [106, 107] a laser pulse from a Q-switched ruby laser was split into 2 beams. The first, more powerful beam propagated through the Ruby optical amplifier. The second beam propagated in the air. This beam served as a reference for comparison with the amplified pulse. Both beams were detected by photodetectors. The output signals from these photodetectors were fed to an oscilloscope for visual observation. The experiments resulted in a pulse maxima propagated through the amplifier at a velocity $6-9$ times larger than the velocity of light in vacuum c. Moreover, experimental investigation provided in Refs. [106, 107] demonstrated that the shape of the pulse propagated through the amplifier did not change in the case of nonlinear amplification (when the pulse energy is greater than the saturation energy of the amplifier). Due to nonlinear amplification of the light pulse on the leading edge and absorption on the trailing edge the pulse envelope (pulse maxima) has an additional movement forward. This leads to the superluminal propagation of the pulse maxima. This phenomenon was mentioned in Chapter 2. Current exper-

imental investigations provided in [159] demonstrated superluminal pulse propagation due to gain-assisted linear anomalous dispersion in caesium gas.

Different superluminal sources of electromagnetic radiation were studied in [67]. In particular, radiation by charges moving faster than light in vacuum is considered in [70].

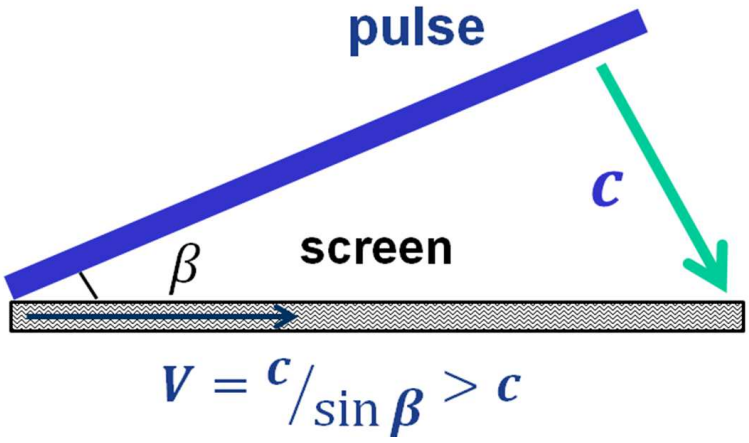

Figure 6.1: A short pulse of light illuminates a flat screen. The intersection point of the beam and medium moves over the screen at the velocity $V = c/\sin\beta > c$, β is the angle of the incidence [66].

If a charged particle moves faster than light in some medium the so called Cherenkov radiation occurs [58–64]. It typically appears in a cone shape with the angle depending on the ratio of the particle velocity to the speed of light in the media. Similar conical emissions can also appear in nonlinear optical parametric processes [75–79]. Not only particles but also spots of light can propagate faster than the phase velocity of light in particular mediums [65–67, 160–164]. Those can be optical pulses and solitons in fibers or filaments [165–172] as well as in other optical systems [173–181]. Spots of light formed by a rotating projector, searchlight (or pulsar in astrophysics) at a fairly remote screen can also move at a superluminal velocity. If the projector rotates at angular velocity Ω, the velocity of the spot of light V on the screen located at distance R is determined by $V = \Omega R$. The model of rotating searchlights was applied to pulsars in astrophysics in [66, 182, 183]. For example, for the pulsar NP 0532 in the Crab Nebula $\Omega \approx 200$ rad/s and the velocity V of the spot on the earth at the distance $R \approx 2000$ parsec $\approx 6 \cdot 10^{21}$ cm is given by $V = \Omega R \simeq 1.2 \cdot 10^{24}$ cm/sec [66, 182, 183]. The intersection point of two interfering laser beams that propagates at the velocity $V = c/\cos\frac{\alpha}{2} > c$ (α being the angle between two interfering waves) can also move at a velocity exceeding that of light [67, 184] (see Fig. 6.3). Similar situation occurs when a short plane-wave impulse crosses a flat screen (or the plane diffraction grating) [67, 185]. In this case, the intersection of the pulse and screen moves along the screen at the velocity $V = c/\sin\beta > c$ (here β is the angle of wave incidence) [65, 66]. This situation is illustrated in Fig. 6.1.

Cherenkov radiation in different periodically modulated media was also considered

[173, 186, 187]. Despite the great number of different configurations studied in the context of Cherenkov radiation, in all those cases such radiation has the same nature. Namely, it is a result of the interference of the secondary waves emitted by the moving physical object. The temporal shape of the radiating wave and thus the spectrum of radiation can be significantly different depending on the particular situation. For instance, the spectrum of radiation induced by a charged particle moving faster than the phase velocity of light is rather unstructured [61, 62]. In many cases, resonances may occur [67, 185]. Other important example is the Purcell-Smith radiation appearing as a charged particle moves in the vicinity of a periodic structure [185, 188]. The appearance of resonance Cherenkov radiation for optical soliton propagation is demonstrated in [189].

In this chapter, we consider the Cherenkov-type radiation in the case of a one-dimensional (1D) string formed by resonant two-level particles (dipoles) with a spatially periodic modulated number density. Our consideration is rather general, we bear in mind optical nanoantenna or quantum dots arrays [190–197] as well as thin microcapillaries. A similar geometry was recently realized experimentally in [163].

In this chapter we show, that the Cherenkov radiation emission exhibits an unusual character. It possesses a narrow-band spectrum with the central frequency at the resonance of the dipoles. We show also that in presence of inhomogeneities in the dipole density, a new Doppler-like frequency appears in the spectrum in a linear regime, when the pump is weak and in nonlinear regime when pump is strong. We consider both a straight and a circularly-shaped string. By increasing the pump the nonlinear response of the two-level atoms becomes important. In this case the radiation intensity at a new frequency may even significantly overcome the radiation intensity at a resonant frequency.

The majority of the results of this Chapter were published in own publication [164] and in the recent publication [198]. Some part of the text presented below is reprinted with permission from [198]: R. M. Arkhipov, I. Babushkin, M. K. Lebedev, Yu. A. Tolmachev, and M. V. Arkhipov. Transient Cherenkov radiation from an inhomogeneous string excited by an ultrashort laser pulse at superluminal velocity. Physical Review A, Vol. 89(4) p. 043811, 2014.

6.2 Physical considerations

We consider the geometry illustrated in Fig. 6.2(a). A short, spectrally broadband optical plane wave pulse is emitted by source 1, passing through beam expander (lenses 2 and 3) which spatially extends the pulse. We assume that source produce a significantly broadband and flat spectrum [199–207] and includes the resonance frequency ω_0 of the dipoles in the string. After beam expander this spatially extended short in time and in the axial direction pulse has the form of thin "sheet of light" 4. This "sheet of light" illuminates at the angle β the string medium parallel to z-axis.

A similar situation of superluminal excitation of the string by the intersection point of two laser beams is presented in Fig. 6.3. Radiation from an ultrashort laser pulse

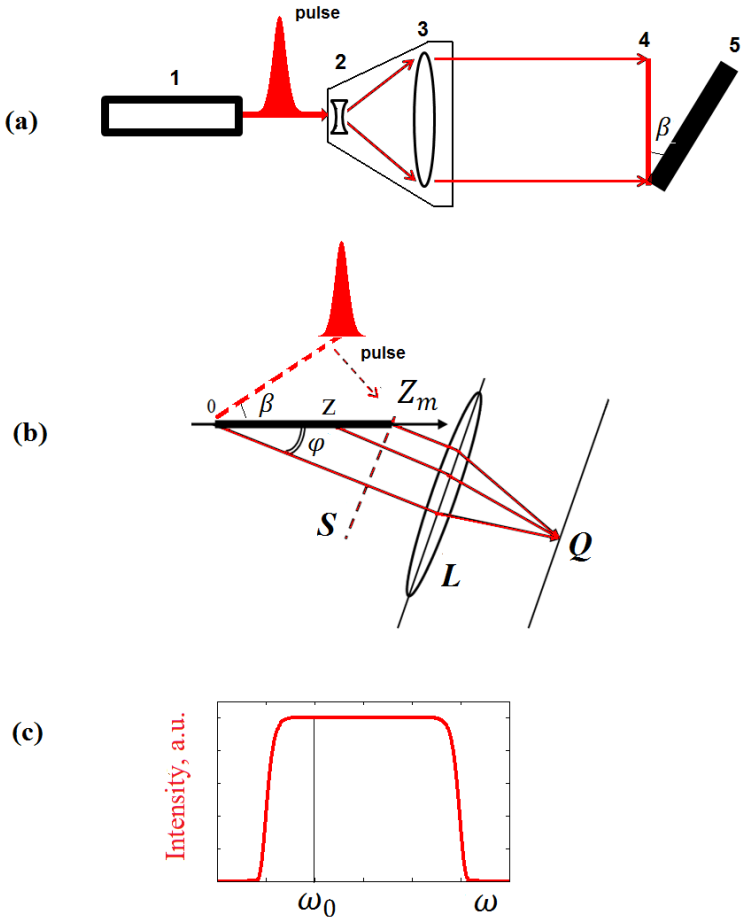

Figure 6.2: (a) Excitation of a string at superluminal velocity. 1 - a short spectrally broadband laser pulse source, 2,3 -lenses, 4 the plane pulse wave. The intersection of the plane pulse and the medium moves along the string at the velocity $V = c/\sin\beta > c$. (b) The observation geometry of the string of the length Z_m emission. The observer is placed far away from the string or in the focus of a lens L which collects the radiation of the string parallel to the z-axis. (c) The source must produce significantly broadband and flat spectrum [199–207], which includes also the resonance frequency ω_0 of the dipoles forming the string.

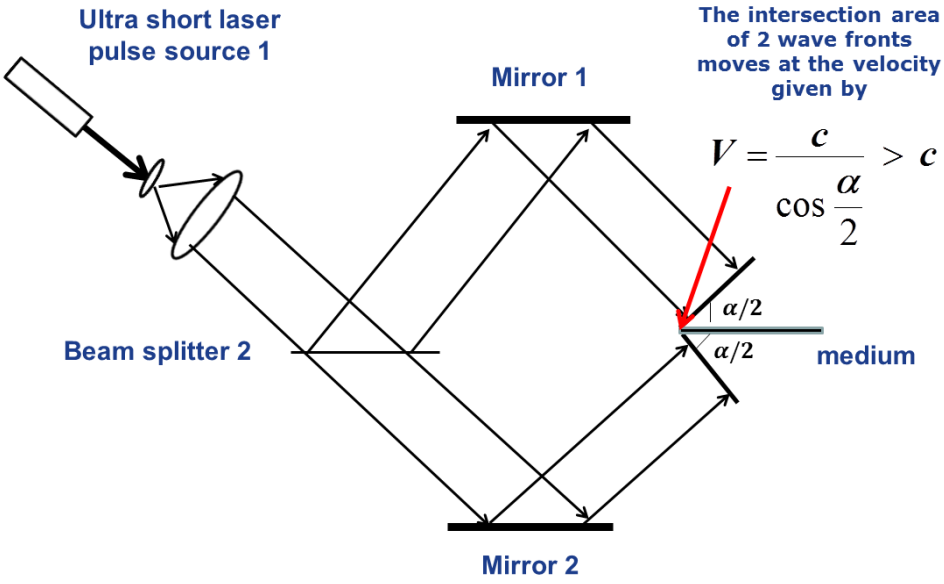

Figure 6.3: Excitation of a string at superluminal velocity. The intersection point of 2 laser beams propagates over the medium at the velocity $V = c/\cos\frac{\alpha}{2} > c$.

originating from source 1 passes through the beam splitter 2 and reflects from mirrors 1 and 2. As a result two intersecting beams are formed. If the resonant string is placed along the propagation of the intersection point of two beams, superluminal excitation of the string occurs.

In our consideration we assume that the string consists of oscillators (dipoles) with the resonance frequency ω_0 and decay constant γ, whose number density $N(z)$ varies periodically along the string with the spatial period Λ_z.

Moreover, we assume that the string is thin. Its thickness is less than the wavelength of light corresponding to the resonance frequency ω_0. Such quasi-1D geometry of the system suggests that, if the irradiation and observation angles β and φ are not zero (cf. Fig. 6.2(a)), the secondary radiation emitted by any dipole will never hit another dipole on its way to the observer.

The electric field created by this excitation observed at the remote position Q is determined by the solution of the wave equation

$$\Box\mathbf{E} = \mu_0\partial_{tt}\mathbf{P}, \tag{6.1}$$

where $\Box = \partial_{xx} + \partial_{yy} + \partial_{zz} - 1/c^2\partial_{tt}$ is the d'Alembert operator and c is the velocity of light in vacuum. In particular, if the source is a single dipole, that is, $\mathbf{P} \propto \delta(\mathbf{r})$, the observed secondary emission at the point $\mathbf{r}'$ is:

$$\mathbf{E}(\mathbf{r}', t) \propto \partial_{tt}\mathbf{P}(\mathbf{r}, t - |\mathbf{r} - \mathbf{r}'|/c). \tag{6.2}$$

We will normalize the latter relation so that the coefficient of proportionality between $\mathbf{E}$ and $\omega_0^2\mathbf{P}$ is 1.

The total response of dipoles to excitation field $\mathbf{E}_e(t)$ at the point Q is described by the sum of the responses of separate dipoles over the whole string. The response comes to the point Q delayed in time. Let us denote $\mathbf{g}_e(t)$ the response of a single dipole to the excitation field. Therefore, the resulting expression for the electric field at the point Q will be:

$$\mathbf{E}(t, Q) = \int_0^{Z_m} N(z)\mathbf{g}_e(\tilde{t}, z)dz, \tag{6.3}$$

where $\tilde{t}$ is the delayed time depending on the geometry of the system and $N(z)$ the dipole density.

The physical nature of the oscillators forming the string can be very different. In particular, one can use a string of optical nanoantennas made of the conducting material. Such nanoantennas have indeed the resonance frequencies defined by their plasmonic resonances, which are highly flexible and are determined by the geometry and size of the structures [190–193]. Using such structures the resonance frequency ω_0 can be tuned to a wide range from teraherz up to the visible spectrum. Semiconductor quantum dots arrays [194–197] can be also used. One may remark that in the case of semiconductors, strong nonlinearities accomplished by the possibility of a pump allow for the use of such thinner-than-wavelength layers as active elements in quantum wells and quantum dot lasers [208–215].

In the case when the exciting pulse is weak and the dipole response is linear, its response to the excitation pulse $\mathbf{E}_e(t)$ is described by the polarization $\mathbf{P}(t)$

$$\ddot{\mathbf{P}} + \gamma\dot{\mathbf{P}} + \omega_0^2\mathbf{P} = g\mathbf{E}_e(t), \tag{6.4}$$

where g is the coupling strength to the field.

In a linear regime we also assume that the excitation pulse duration is smaller (or comparable) than the resonant period of oscillators $T_0 = 2\pi/\omega_0$, so that its spectrum not only includes ω_0 but at the same time is significantly broad and flat [see Fig. 6.2(c)]. Such pulses can be obtained, for instance, in the teraherz range using a gaseous ionization-based source pumped by ultrashort optical pulses [199–207].

In this case the response of the oscillators can be described to a high degree of precision by the following expression

$$g_e(t) \approxeq e^{-\gamma t}\cos(\omega_0 t)\Theta(t), \tag{6.5}$$

where $\Theta(t)$ is the Heaviside step-function.

In the case when the pumping pulse has a large enough amplitude, the response of the string becomes nonlinear. Interaction of two-level dipoles with the strong optical field is described by system of optical Bloch equations [10, 29]:

$$\frac{du(t,z)}{dt} = -\Delta\omega v(t,z) - \frac{1}{T_2}u(t,z), \tag{6.6}$$

$$\frac{dv(t,z)}{dt} = -\Delta\omega u(t,z) - \frac{1}{T_2}v(t,z) + \Omega_R(t,z)w(t,z), \tag{6.7}$$

$$\frac{dw(t,z)}{dt} = -\frac{1}{T_1}(w(t,z)+1) - \Omega_R(t,z)v(t,z). \tag{6.8}$$

Here u, v represent the components of the medium polarization that are in-phase and out of phase with the driving E field correspondingly, w - population difference, T_1 is the time relaxation of the population difference, T_2 is the time relaxation of the polarization, $\Delta\omega$ is the frequency detuning between the electric field and the resonance frequency of the medium, $\Omega_R = \frac{d_{12}E_0(t)}{\hbar}$ - the Rabi frequency of the driving field, d_{12} - the transition dipole moment, and E_0 - the amplitude of the driving field. This system of equations is commonly used for describing the interaction of short optical pulses with the two-level medium, in particular taking into account the coherent interaction considered in Chapter 2 [10, 29]. Note, that Eqs. (6.6)-(6.8) are derived in the rotating wave approximation that is inapplicable to the broad spectra and short pulses mentioned above. Thus, below our consideration is limited by relatively long pump pulses. We assume that the excitation pulse has a Gaussian shape given by: $E_p(t) = E_0 \exp\left(\frac{-t^2}{\tau_p^2}\right)$. In the case of $\Delta\omega = 0$ and if the duration of the excitation pulse is much shorter than T_1, T_2: $\tau_p << T_1, T_2$ one can obtain the following solution of the optical Bloch equations for the polarization $P(t,z)$ and population difference $n(t,z) = N_0 w(t,z)$ (N_0 is the concentration of the two-level atoms) [10, 29]:

$$n(t,z) = N_0 w(t,z) = N_0 \cos\Phi(t,z), \tag{6.9}$$

$$P(t,z) = d_{12}N_0 v(t,z) = d_{12}N_0 \sin\Phi(t,z), \tag{6.10}$$

where

$$\Phi(t,z) = \frac{d_{12}}{\hbar}\int_{-\infty}^{t} E(t',z)dt', \tag{6.11}$$

is the pulse area considered in Chapter 2 [10, 29].

The system of optical Bloch equations (6.6)-(6.8) has a simple physical interpretation [10, 29]. The change of n and P can be represented as the rotation of a unit Bloch vector $\rho = (v,w)^t$ in the (v,w) plane. In this case the function Φ given by (6.11) is the angle of rotation of this vector. For example, $\Phi = \pi$ corresponds to a rotation of the Bloch vector at angle π and corresponding complete transition of the atom to the upper excited level (π pulse), and $\Phi = 2\pi$ corresponds to an excitation of the atom to the excited level and then return to the ground level (2π pulse). These pulses are considered in Chapter 2.

6.3 Straight string: linear response

In this section we consider the case when our string has the form of a straight line of length Z_m [Fig. 6.2(b)]. We assume that the radiation is registered at a very large distance from the string (or at the focal point Q of the lens L). We consider that the string consists of identical dipole oscillators with resonance frequency ω_0 (λ_0 is the corresponding wavelength) and decay rate γ. The number density of oscillators along the Oz axis varies periodically with the period Λ_z:

$$N(z) = \frac{1}{2}\left(1 + a\cos\frac{2\pi}{\Lambda_z}z\right), \tag{6.12}$$

where $a \leq 1$ is the amplitude of density oscillations. Below, for simplicity, we take $a = 1$.

At the initial moment $t = 0$ the excitation pulse crosses the point $z = 0$ and starts to propagate at velocity V along the string from point $z = 0$ to point $z = Z_m$. In this analysis we assume that the exciting pulse is linearly polarized and the polarization plane is perpendicular to the plane of Fig. 6.2(b). The oscillators start to emit electromagnetic radiation according to the response law (6.5). Consider the secondary radiation propagating at the angle φ to the string, which reaches the observer at the point Q, see Fig. 6.2(b).

The electric field emitted by the oscillator located in z (as being observed in the same point) is proportional, according to (6.5), to:

$$E(t,z) \cong \exp\left[-\frac{\gamma}{2}\left(t - \frac{z}{V}\right)\right]\cos\left[\omega_0\left(t - \frac{z}{V}\right)\right]\Theta\left[t - \frac{z}{V}\right], \tag{6.13}$$

where the argument with the time delay $t - \frac{z}{V}$ describes the excitation pulse appears at the point z at the moment delayed by z/V. Instead of observation point Q we can consider the electric field at the reference plane S orthogonal to the direction φ passing through the end of the string point Z_m. The propagation time from this reference plane to Q is constant and will be omitted in the following analysis.

The time of light propagation from the point z at the string to the reference plane S is $\frac{Z_m - z}{c}\cos\varphi$. Thus, the electric field emitted by the dipoles located at the point z at the reference plane is given by the expression:

$$E_{ref}(t,z) \cong \exp\left[-\frac{\gamma}{2}f(t,z)\right]\cos\left[\omega_0 f(t,z)\right]\Theta\left[f(t,z)\right], \tag{6.14}$$

where $f(t,z) = t - \frac{z}{V} - \frac{Z_m - z}{c}\cos\varphi$.

The total field observed in observation point Q is obtained by the integration of (6.14) over the whole string:

$$E(t,\varphi) = \int_0^{Z_m} N(z)\exp\left[-\frac{\gamma}{2}f(t,z)\right]\cos\left[\omega_0 f(t,z)\right]\Theta\left[f(t,z)\right]\,dz. \tag{6.15}$$

The analytical solution of (6.15) in the case of $\gamma = 0$ is given in the last section. As one can see from analytical calculation, see Eq. (6.37), the response contains the resonance frequency of the oscillators ω_0 together with a new component given by the expression:

$$\Omega_1 = 2\pi \frac{V/\Lambda_z}{|\frac{V}{c}\cos\varphi - 1|}. \tag{6.16}$$

The inverse numerator of (6.16) is the time interval which the excitation pulse needs to cross the single oscillation period of dipole density $N(z)$. When this time is equal to the period of the medium oscillations:

$$\lambda_0/c = \Lambda_z/V, \tag{6.17}$$

formula (6.16) leads to:

$$\Omega_{1_D} = \frac{\omega_0}{|\frac{V}{c}\cos\varphi - 1|}. \tag{6.18}$$

This relation (6.18) formally coincides with that one for the Doppler frequency shift [65, 66], so we will call it the Doppler-like frequency but will keep in mind that its physical origin differs from that of the Doppler effect.

Equation (6.16) is valid for arbitrary values of the excitation pulse velocity V and has the same form as the one appearing in the case of Purcell-Smith radiation studied experimentally in Refs. [185, 188]. In the experiments by Smith and Purcell, a fine beam of electrons passed over a flat optical reflective diffraction grating of period Λ_z [185]. However, the velocity of the electrons is smaller than the velocity of light c. To the contrary, in our case the velocity of excitation can be much faster than c.

Now we study the temporal and spectral shape of the linear string response defined by Eq. (6.15) and its dependence on the system parameters.

We start with the numerical simulations (6.15) for the normalized parameters: $\frac{V}{c} = 2$, $\frac{Z_m}{\Lambda_z} = 9.55$, $\frac{\Lambda_z}{\lambda_0} = 5$, $\frac{\omega_0}{\gamma} = 22.22$. The real-world values of the parameters corresponding to this set depend on the resonance frequency of the oscillators in the string ω_0. For example, taking $\omega_0 = 2\pi \times 10$ ps^{-1} (the frequency for which the δ-function assumption from Fig. 6.2(c) is especially easy fulfilled), we will obtain the following values for other parameters: $\Lambda_z = 150\mu m$, $Z_m = 1.4$ mm, and $\gamma = 2.8$ ps^{-1}. Another example is the pump at optical frequencies $\omega_0 = 2\pi \times 375$ ps^{-1}, $\Lambda_z = 4$ μm, $Z_m = 40\mu m$, $\gamma = 106.04$ ps $^{-1}$.

The numerical solution of the integral (6.15) and corresponding spectrum are illustrated in Fig. 6.4 for the above mentioned parameters, and $\varphi = 0$ (the observation point is on the same line as the string) in Fig. 6.4(a,b). The case when the angle $\varphi = 60$ degrees is shown in Fig. 6.4(c,d). This angle corresponds to the Cherenkov emission angle (6.19).

As one can see from this Fig. 6.4, the resonant response at $\omega = \omega_0$ exists in both cases. But when $\varphi = 0$ an additional frequency defined by Eq. (6.16) arises in the spectrum of medium response, see Fig. 6.4b. As it is seen in Fig. 6.4(a), the new frequency (6.16) appears in the transient process for the time interval from $t_1 \approx 20T_0 = 20$ to $t_2 \approx 47T_0$.

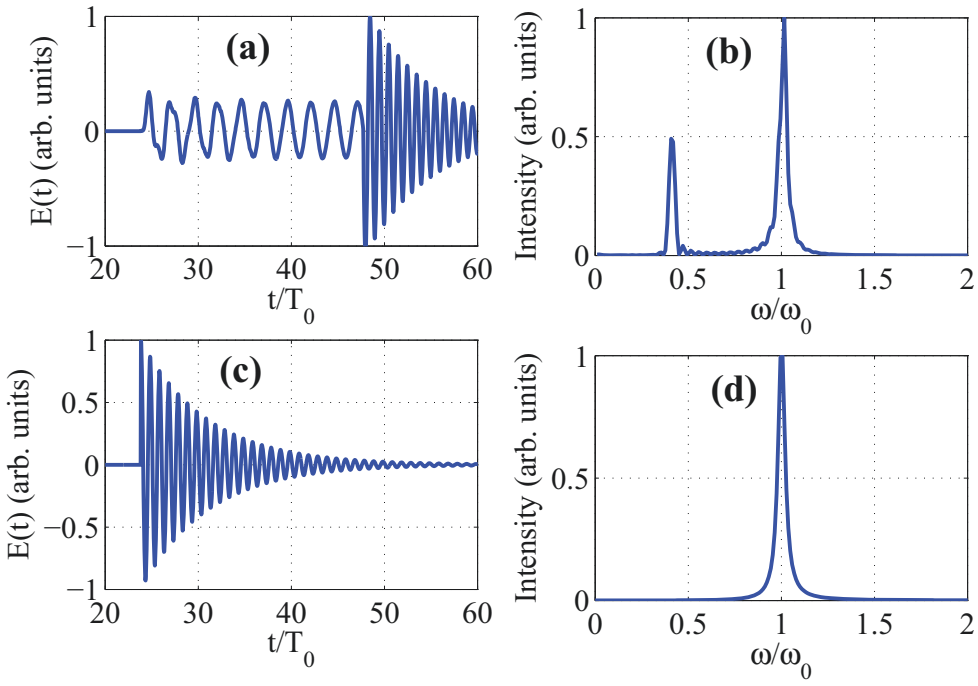

Figure 6.4: Time dependence of the field $E(t)$ according to Eq. (6.15) (a,c) and its spectral intensity $I(\omega)$ (b,d) normalized to their maximal values vs. normalized time t/T_0 and frequency ω/ω_0, for $\frac{V}{c} = 2$, $\frac{Z_m}{\Lambda_z} = 9.55$, $\frac{\Lambda_z}{\lambda_0} = 5$, $\frac{\omega_0}{\gamma} = 22.22$ for the observation angle $\varphi = 0$ (a,b) and $\varphi = 60°$ (c,d), the later corresponds to the Cherenkov emission angle.

At the moment t_1 the excitation pulse reaches the end of the string. During the period t_1 to t_2, the radiation from the points $z = Z_m$ to $z = 0$ arrives at the observation point that is $z = Z_m$ in this example. As the result of the interference of the incoming waves, a transition process occurs. It lasts until the moment t_2. Only the decaying emission with the frequency ω_0 remains at the later time.

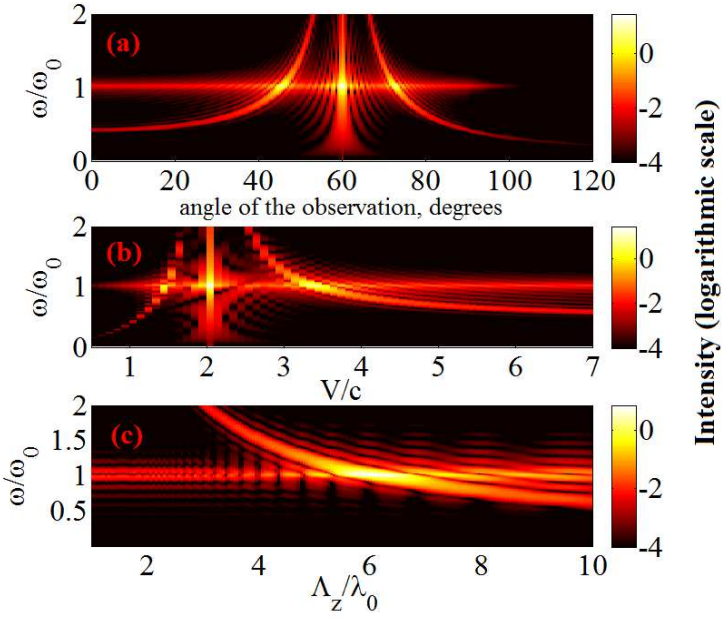

Figure 6.5: Dependence of the spectral intensity $I(\omega)$ of the string response according to Eq. (6.15) on the observation angle φ (a), the excitation velocity V (b) and on the string density modulation period Λ_z (c). The other parameters coincide with those ones given in Fig. 6.4(c,d). The spectral intensity is presented on a logarithmic scale.

For the superluminal velocity of the excitation the denominator of (6.16) can be equal to zero if:

$$\cos\varphi_0 = c/V. \tag{6.19}$$

This expression coincides with the condition for Cherenkov radiation [63, 64]. Case of Cherenkov emission angle is plotted in Fig. 6.4(c). This angle corresponds also to the zeroes-order diffraction peak of the grating formed by $N(z)$. Under the parameters of Fig. 6.4c, $\varphi_0 = 60$ degrees. When the condition (6.19) is fulfilled, we have $\Omega_1 = \infty$, and the radiation from all points of the grating (the resonance medium) comes to the reference plane simultaneously, thus no transient process occurs.

The +1st- and -1st diffraction orders maxima are defined by the expression:

$$\cos\varphi_{\pm 1} = \frac{\pm\lambda_0}{\Lambda_z} + \frac{c}{V}. \tag{6.20}$$

For the parameters of Fig. 6.5(a) the angles are $\varphi_{+1} = 45.57$ and $\varphi_{-1} = 72.54$ degrees correspondingly. For those angles, we have $\omega_0 = \Omega_1$ as well. For all values of φ different from the one given by (6.20), the Doppler-like frequency $\Omega_1 \neq \omega_0$. It should be noted, however, that in this case the radiation intensity in the transient regime is smaller than for the Cherenkov angle.

Dependence of the spectrum of the solution of (6.15) on the system parameters is presented in Fig. 6.5. Fig. 6.5(a) illustrates the dependence of spectral intensity on the observation angle φ, Fig. 6.5(b) illustrates this dependence on the excitation speed V and the dependence on the grating period Λ_z is presented in Fig. 6.5(c) From these figures one can clearly see the frequency branch corresponding to the resonance frequency, $\omega = \omega_0$, as well as another one corresponding to the Doppler-like frequency given by (6.16).

According to Eq. (6.16), Ω_1 decreases with increasing of V/c for $V/c > 2$ and increases for $V/c < 2$. From Eq. (6.16) it also follows that $\Omega_1 \to \infty$ for $V \to 2c$ (when $\varphi = 60$ degrees). This also coincides with the typical behavior of the Doppler frequency shift. As can be seen from Fig. 6.5(c), Ω_1 decreases with increasing values of Λ_z/λ_0.

Above we have considered the case when the string is excited by a short pulse of light propagating at the superluminal velocity. Another interesting case if the excitation spot moves at the subluminal velocity. An example of numerical solution of the integral (6.15) assuming $V/c = 0.7$ and $\varphi = 0$ are shown in Fig. 6.6. Other parameters of this example are the same as in the Fig. 6.4. The additional Doppler-like frequency component arises during the transient process from $t_1 \approx 47T_0$ to $t_2 \approx 70T_0$. At moment t_1 the radiation from the point $z = 0$ reaches the end of the medium located at the point $z = Z_m$. At moment t_2 the radiation from the point $z = Z_m$ appears at the observation point. After transient process ends, only decaying oscillations at the frequency ω_0 remain.

Fig. 6.7 illustrates the dependence of the string response spectrum on the observation angle φ and on the grating period Λ_z. As one can see, the situation in the case $V < c$ is slightly differs to the case of the superluminal velocity considered above. In particular, Ω_1 decreases with an increase of φ and the Cherenkov angle at which $\Omega_1 = \infty$ is never achieved. From Fig. 6.7b it follows that Ω_1 decreases with an increase of Λ_z as in the case of superluminal excitation.

6.4 Straight string: strong pump and nonlinear dynamics

In the present section we investigate the radiation of a straight string in the case when the pump is strong enough, so that the response of the string is significantly nonlinear.

Taking into account that the secondary radiation never comes back to the string, and no nonlinear propagation takes place (unless the observation angle $\varphi = 0$) using the

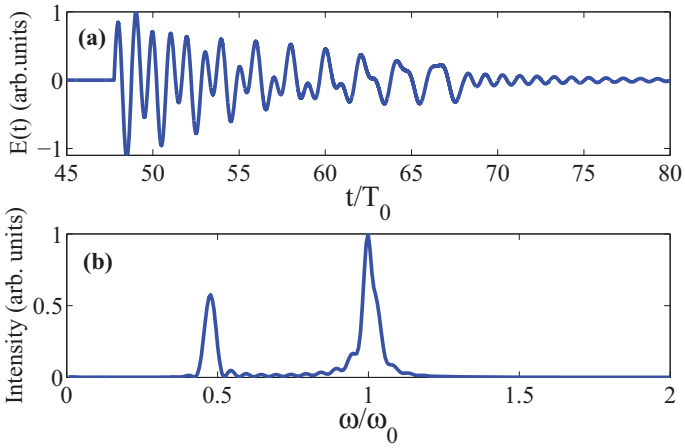

Figure 6.6: Time dependence (a) of the string response field $E(t)$ according to (6.15), and (b) its spectral intensity $I(\omega)$ normalized to the maximum values vs. normalized time t/T_0 and frequency ω/ω_0, for $\frac{V}{c} = 0.7$, $\frac{Z_m}{\Lambda_z} = 9.55$, $\frac{\Lambda_z}{\lambda_0} = 5$, $\frac{\omega_0}{\gamma} = 22.22$ and observation angle $\varphi = 0$.

Eq. (6.10) we obtain for the electric field emitted by the string:

$$E(t,\varphi) = \int_0^{Z_m} N(z) P\left[f(t,z)\right] \sin\left[\omega_0 f\left(t,z\right)\right] dz. \tag{6.21}$$

We consider pulses with a relatively narrow spectrum to be consistent with the approximations for which (6.10) was derived. The pulses we consider have nevertheless still short enough duration to clearly observe the frequency Ω_1. The result of numerical solution of the integral (6.21) assuming the parameters of Fig. 6.4 and the observation angle $\varphi = 71$ degrees, total pulse area $\Phi = \pi/2$, Rabi frequency $\Omega_R = 0.07\omega_0$, and Gaussian pulse duration $\tau_p = 2T_0$ is presented in the Fig. 6.8. We consider the pulse with a duration of 2 periods of medium oscillation T_0. A system of optical Bloch equations in the form (6.6)-(6.8) was used for the analysis of a such few-cycle pulse evolution in two-level media in Refs. [216, 217].

As in the linear case, the two frequencies ω_0 and Ω_1 are observed as shown in Fig. 6.8(b). Fig. 6.9 illustrates the dependence of the secondary emission spectrum on the total pulse area Φ (cf. Eq.(6.11)). The pulse area was changed via modification of the pulse amplitude (Rabi frequency), keeping the pulse duration constant, $\tau_p = 2T_0$. In Fig. 6.9 one can observe two branches corresponding to the resonance frequency ω_0 and to the Doppler-like Ω_1. Analysis of Fig. 6.9 shows that in strongly nonlinear regime when the pulse area is large the radiation at the resonance frequency ω_0 has smaller intensity than that at

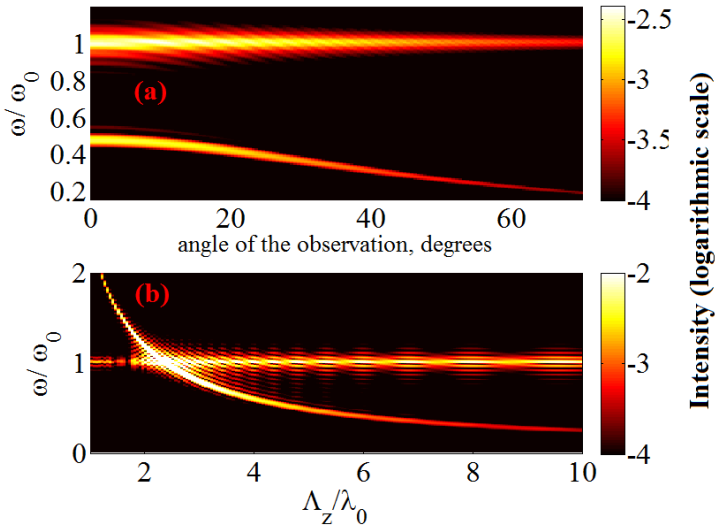

Figure 6.7: Dependence of the spectral intensity $I(\omega)$ of the string response according to Eq. (6.15) on the observation angle φ (a), and the string density modulation period Λ_z (b). The other parameters coincide with ones in Fig. 6.6. Note the logarithmic scale in the plot.

the new frequency Ω_1. The periodic structure revealed in Fig. 6.9 in dependence on Φ is explained by the phase relations between the periodic term $\sin\Phi$ entering $P(t,z)$ [cf. Eqs.(6.21) (6.10) and (6.11)] and the period of spatial inhomogeneity of dipole density $N(z)$.

We considered the case of the interaction of single pulse with a string of two-level atoms in a nonlinear regime. Let us now consider the case when we have a periodic pulse train, obtained for example from mode-locked laser. The envelope of this pulse train can be represented as:

$$E(t) = \sum_{k=1}^{N_i} E_0 \exp\left(-\frac{(t-kT_i)^2}{\tau_p^2}\right), \tag{6.22}$$

where N_i is a number of pulses and T_i - the pulse repetition period. The spectrum of such a pulse train is a frequency comb with the central frequency ω_0 and intermode frequency spacing $f_{rep} = 1/T_i$. If for some angle φ the frequency Ω_1 is close to mf_{rep} (m is integer number) one can expect the arising of the radiation at the frequency Ω_1 at this angle. Fig. 6.10 illustrates the time dependence of $v(t), E(t), \Phi(t)$. It can be seen that pulse area Φ changes in a stepwise manner and the medium polarization which is proportional to $\sin\Phi$ (see Eq. (6.10)) is a sequence of rectangular pulses. The result of numerical solution of the integral (6.21) with periodic pulse train in the form (6.22) is presented in Fig. 6.11, assuming the parameters of Fig. 6.8 and the observation angle

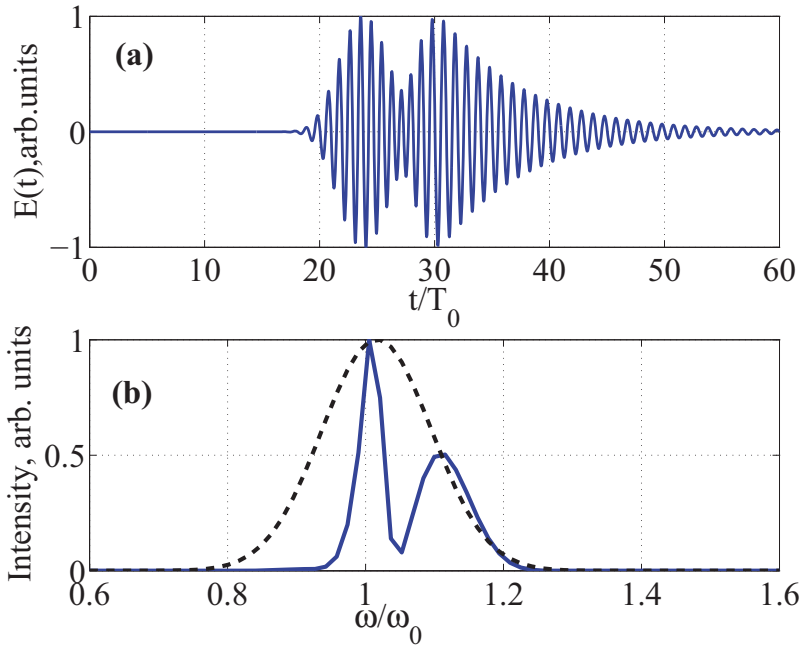

Figure 6.8: Time dependence (a) of the string response field $E(t)$ according to Eq. (6.21), and (b) solid line - its spectral intensity $I(\omega)$ normalized to the maximum values vs. normalized time t/T_0 and frequency ω/ω_0, for the parameters of Fig. 6.4 and total pulse area $\Phi = \pi/2$, $\Omega_R = 0.07\omega_0$, $\tau_p = 2T_0$, dashed line - spectrum of the excitation pulse).

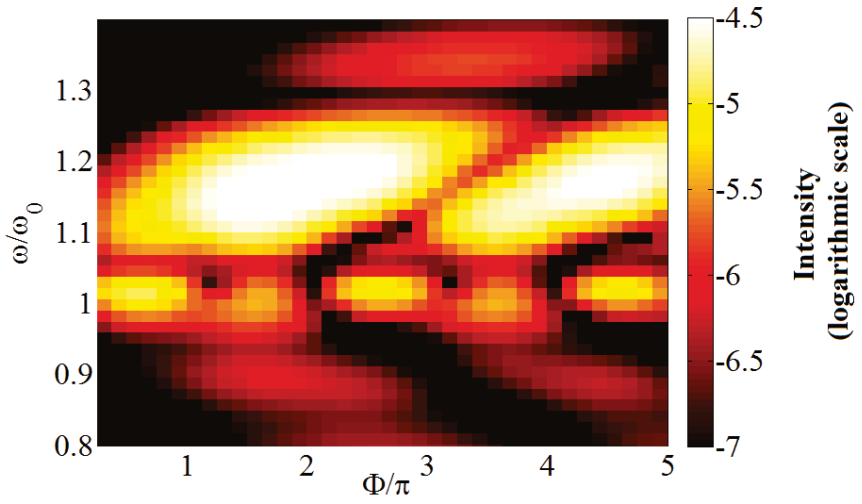

Figure 6.9: Dependence of the radiation spectrum on the pulse area Φ. Other parameters are as in the Fig. 6.8.

$\varphi = 70.97$ degrees, $\omega_0/\gamma = 40$, $T_i = 10\tau_p$, $\Omega_1 = 3f_{rep}$, $N_i = 5$. The electric field dynamics are similar to that of Fig. 6.8. The presence of the frequency Ω_1 can be seen.

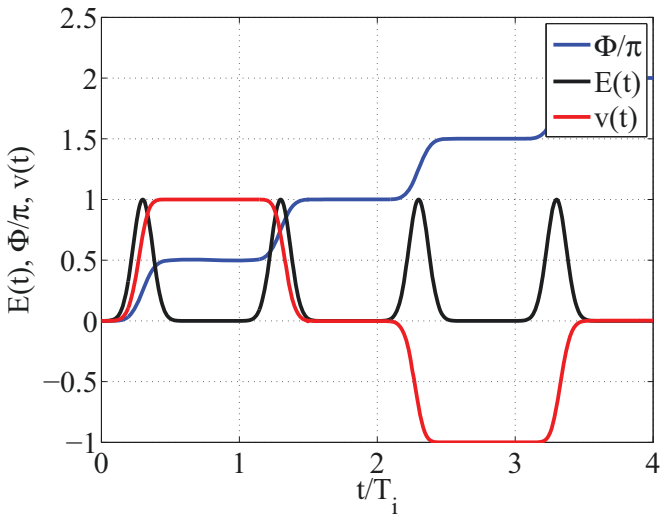

Figure 6.10: Time dependence of the $v(t)$, pumping electric field amplitude $E(t)$ given by Eq. (6.22) and pulse area Φ. Other parameters are as in the Fig. 6.8.

6.5 Circular string: radiation is measured at the center of the circle, the linear and nonlinear response dynamics

In this section we consider a completely different topology of the string schematically presented in Fig. 6.12. The string made of the dipoles with the same resonance frequency ω_0 as in the previous section. We assume that the dipoles are arranged along the circle of radius R. The dipole density is modulated along the string in a periodic way with the angular period Λ_ϕ as:

$$N(\phi) = \frac{1}{2}\left(1 + a\cos(\frac{2\pi}{\Lambda_\phi}\phi)\right). \tag{6.23}$$

As in (6.12), we assume the modulation amplitude $a = 1$. In the center of the circle a source of a short spectrally broad optical pulse (see Fig. 6.2(c)) is located, that quickly rotates so that the cross-section point (red point in Fig. 6.12) moves at the velocity V along the circle.

Under this excitation the dipoles of the string emit secondary waves. Here we will calculate the string response field $E(t)$ observed in the center of circle. Each element dE_ϕ located at the point whose angular coordinate is ϕ emits the electric field given by

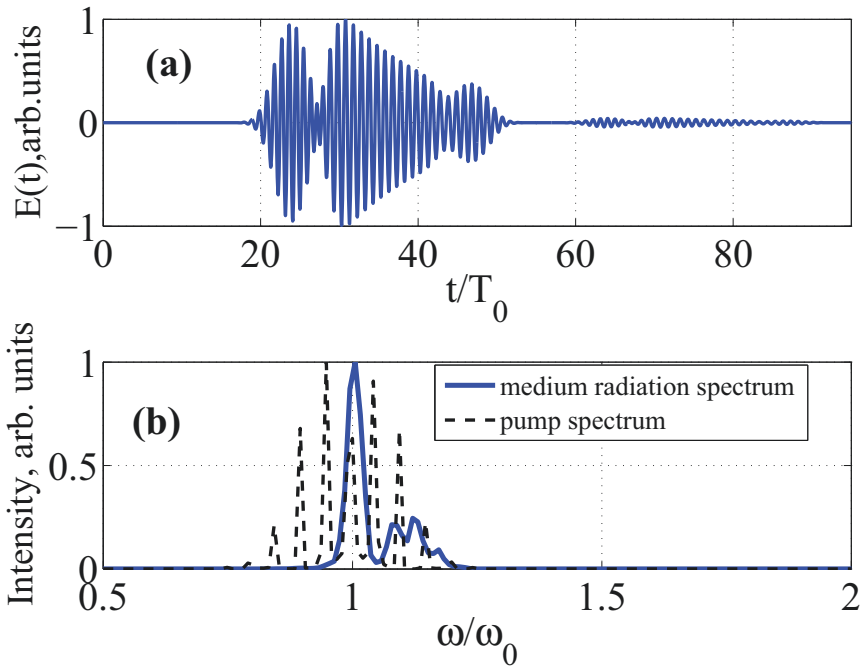

Figure 6.11: Time dependence (a) of the string response field $E(t)$ according to (6.21), and (b) blue solid line - its spectral intensity $I(\omega)$ normalized to the maximum values vs. normalized time t/T_0 and frequency ω/ω_0, for the parameters of Fig. 6.4 and total pulse area $\Phi = \pi/2$, $\Omega_R = 0.07\omega_0$, $T_i = 10\tau_p$, $\Omega_1 = 3f_{rep}$, $\omega_0/\gamma = 40$ $\tau_p = 2T_0$,$N_i = 5$, black dashed line: spectrum of the excitation pulse train (6.22).

the expression:

$$dE_\phi(t) = N(\phi) \exp\left[-\frac{\gamma}{2} f_\phi(t,\phi)\right] \cos\left[\omega_0 f_\phi(t,\phi)\right] \Theta\left[f_\phi(t,\phi)\right] d\phi, \tag{6.24}$$

where $f_\phi(t,\phi) = t - \frac{R\phi}{V} - \frac{R}{c}$. For one round pass of the excitation, the total electric field is obtained by integration (6.24) over ϕ:

$$E(t) = \int_0^{2\pi} N(\phi) \exp\left[-\frac{\gamma}{2} f_\phi(t,\phi)\right] \cos\left[\omega_0 f_\phi(t,\phi)\right] \Theta\left[f_\phi(t,\phi)\right] d\phi. \tag{6.25}$$

The analytical solution of Eq. (6.25) in the case of $\gamma = 0$ is given in the last section. As one can see from analytical calculation the response contains the resonance frequency of oscillators ω_0 together with a new component given by the formula:

$$\Omega_2 = 2\pi \frac{V/\Lambda_\phi}{R}. \tag{6.26}$$

Let us discuss the physical meaning of Eq. (6.26). This is the frequency at which the intersection point of the pulse and string crosses the inhomogeneity oscillations. Under the condition

$$\frac{V}{c} = \frac{\Lambda_\phi R}{\lambda_0}, \tag{6.27}$$

the new frequency is equal to the resonance one, $\Omega_2 = \omega_0$.

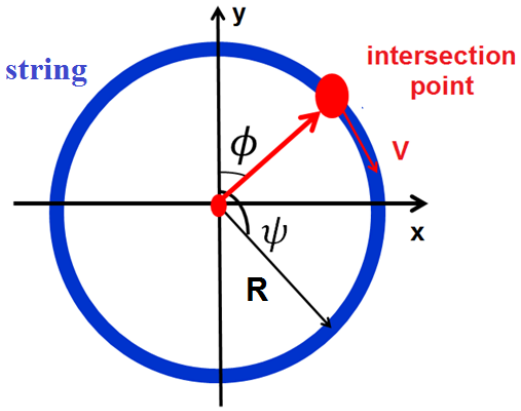

Figure 6.12: Circular geometry of the string. The source of a short pulse with a broad spectrum (c) is located in the center of the circle and quickly rotates. The cross-section of the pulse and medium (red dot) moves at the velocity V along the string (blue circle). As in the previous case, the string is made of dipoles characterized by the resonance frequency ω_0 and the dipoles number density is modulated along the string periodically with the angular period Λ_ϕ.

Note, that Eq. (6.26) is valid in the case when the observer is located anywhere on the axis passing through the center of the circle perpendicularly to its plane.

Let us consider now the numerical examples taking the following parameters: $V/c = 3.75$, $\frac{\Lambda_\phi R}{\lambda_0} = 2$, $\omega_0/\gamma = 22.2$, $\omega_0/\Omega_2 = 0.53$. Assuming $\omega_0 = 2\pi \times 10$ ps^{-1} and $R = 3$ cm, we obtain $\Lambda_\phi = 0.002$ rad^{-1}, $\gamma = 2.8$ ps^{-1}. The electric field calculated using (6.25) is shown in Fig. 6.13. For these parameters, the new frequency Ω_2 is approximately two times larger than the resonance frequency ω_0 of oscillators. The high-amplitude beatings clearly seen in Fig. 6.13. Once the transition process is finished, the observer at O sees only the ordinary decaying oscillations at the resonance frequency. This conclusion is also valid in the case when the excitation pulse moves at a subluminal velocity, or even at the velocity of light. In all these cases, the radiation spectrum at the center of circle will possess a new frequency Ω_2, with only the exception given by Eq. (6.27).

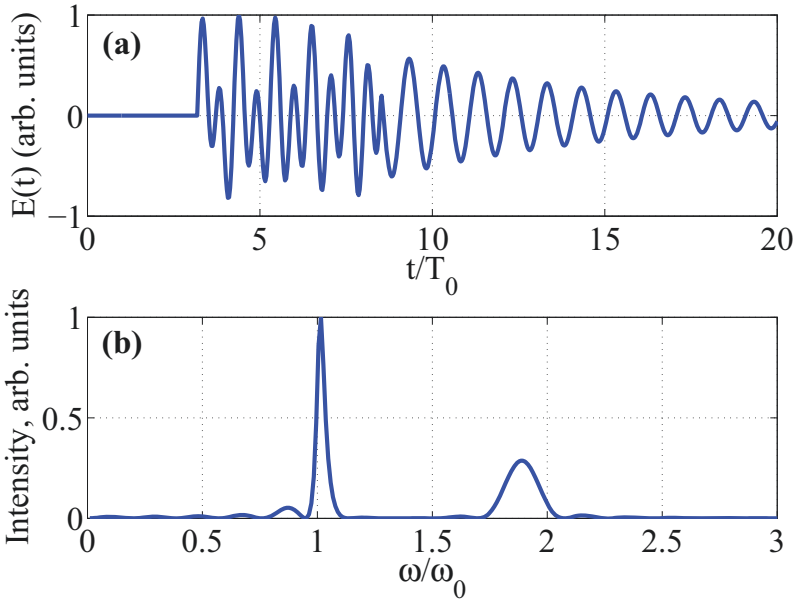

Figure 6.13: (a) Time dependence of the electric field $E(t)$ excited by the string and (b) the corresponding intensity spectrum $I(\omega)$ in the center of the circle for the circular scheme depictured in Fig. 6.12 and the parameters $V/c = 3.75$, $\frac{\Lambda_\phi R}{\lambda_0} = 2$, $\omega_0/\gamma = 22.2$, $\omega_0/\Omega_2 = 0.53$.

In order to illustrate the dependence Ω_2 on the parameters of system, we present the radiation spectrum in dependence on V, see Fig. 6.14(a) and R, see Fig. 6.14(b). Other parameters are taken as in Fig. 6.13. As can be easily seen from Fig. 6.14, the new frequency increases with V and decreases with R which is in agreement with Eq. (6.26).

In the circular case considered here the Cherenkov resonance corresponds to the R value defined by Eq. (6.27).

Up to now we considered the linear response of the string when pump radiation is

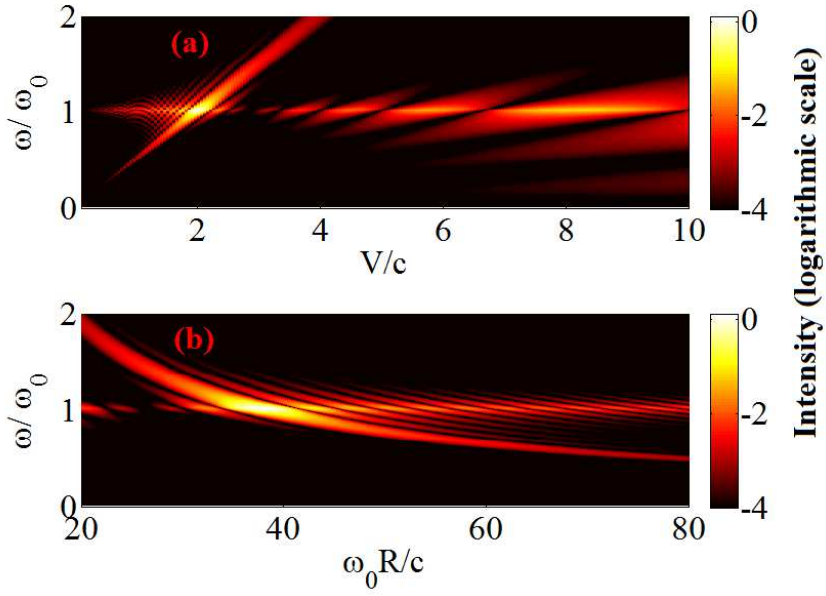

Figure 6.14: (a) Dependence of the radiation spectrum on the normalized propagation speed V of the excitation and the radius of the circle R (b). Other parameters are as in the Fig. 6.13.

weak. Let us now consider the nonlinear response of the circular string when pumping is strong. The expression for total electric field is similar to Eq. (6.21) and has the form:

$$E(t) = \int_0^{2\pi} N(\phi) P\left[f_\phi(t,\phi)\right] \sin\left[\omega_0 f_\phi\left(t,\phi\right)\right] d\phi. \tag{6.28}$$

Fig. 6.15 shows the dependence of the secondary emission spectrum on the total pulse area Φ. As in the previous section the pulse area was changed via modification of the Rabi frequency (pulse amplitude), keeping the pulse duration constant. In Fig. 6.15 one can observe two branches corresponding to the resonance frequency ω_0 and to the frequency shift Ω_2. Analysis of Fig. 6.15 shows that as in the case of straight string in strongly nonlinear regime when the pulse area is large the radiation at the resonance frequency ω_0 has even smaller intensity than that at the frequency Ω_2. The periodic structure revealed in Fig. 6.15 in dependence on Φ is explained by the phase relations between the periodic term $\sin\Phi$ entering $P(t)$ [cf. Eqs.(6.28) (6.10) and (6.11)] and the period of spatial inhomogeneity of dipole density $N(\phi)$.

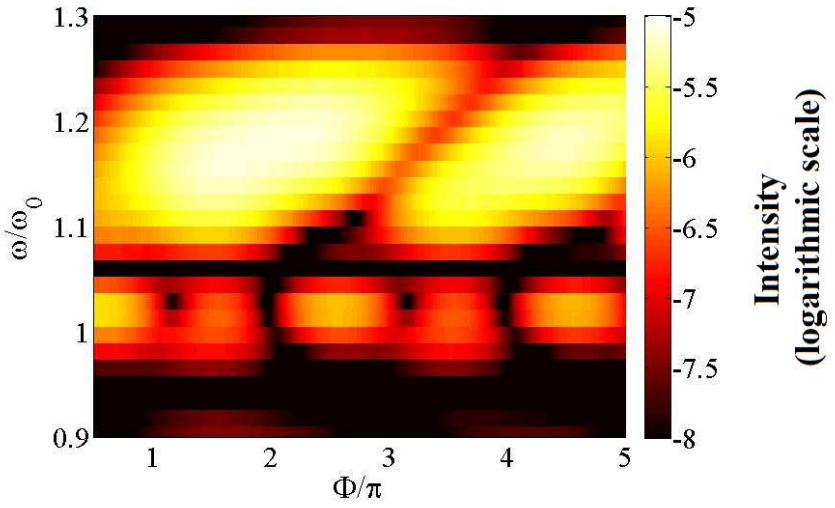

Figure 6.15: Dependence of the radiation spectrum on the pulse area Φ when $V/c = 2.3$, $\frac{\Lambda_\phi R}{\lambda_0} = 2$, $\omega_0/\gamma = 22.2$, $\omega_0/\Omega_2 = 1.15$, $\tau_p = 2T_0$.

6.6 Circular string: radiation is measured at the circle, the linear response

It is interesting to consider the case when the radiation propagates along the ring and is measured at some point with polar coordinate ψ (Fig. 6.12). We assume that the medium radiation can propagate only along a circle as in whispering gallery lasers [218–220], and not along the chord. In this case it is easy to obtain an expression for the electric field at the point ψ:

$$E(t,\psi) = \int_0^{2\pi} N(\phi) \cos\left[\omega_0 f_\psi\left(t,\psi\right)\right] \Theta\left[f_\psi\left(t,\psi\right)\right] d\phi. \tag{6.29}$$

Here $f_\psi\left(t,\psi\right) = t - \frac{R\phi}{V} - \frac{R(\psi-\phi)}{c}$.

Since we assumed that the light can propagate only along the circle, the term $\frac{R(\psi-\phi)}{c}$ in (6.29) corresponds to the time of the radiation propagation from the oscillator, located at a point with polar angle ϕ to the observation point ψ. The calculation of this integral shows (see the last expression in the last section) that the spectrum of the transition process, in addition to the fundamental frequency of the medium, also contains a new frequency:

$$\Omega_3 = 2\pi \frac{V/\Lambda_\phi}{|1 - \frac{V}{c}|R}. \tag{6.30}$$

Unlike the previous case, the new frequency depends on the ratio $\frac{V}{c}$.

We now discuss the physical sense of (6.30). The numerator of this formula is the fre-

quency of the incident pulse excitation of the system of oscillators periodically arranged along the circle. For the observer located at the point ψ, the process would seem to have a frequency Ω_3. Under the condition of resonance (6.27) formula (6.30) becomes

$$\Omega_{3D} = \frac{\omega_0}{|1 - \frac{V}{c}|}, \tag{6.31}$$

and coincides with the formula for the frequency shift due to the Doppler effect when the source is moving towards a stationary receiver.

In order to illustrate the dependence Ω_3 on the parameters of system, we present the radiation spectrum in dependence on V (Fig. 6.16a) and R (Fig. 6.16b). As can be easily seen from (6.30), the new frequency increases with the V when $V/c < 1$ and decreases with an increase of V when $V/c > 1$. Also V decreases with an increase of the R.

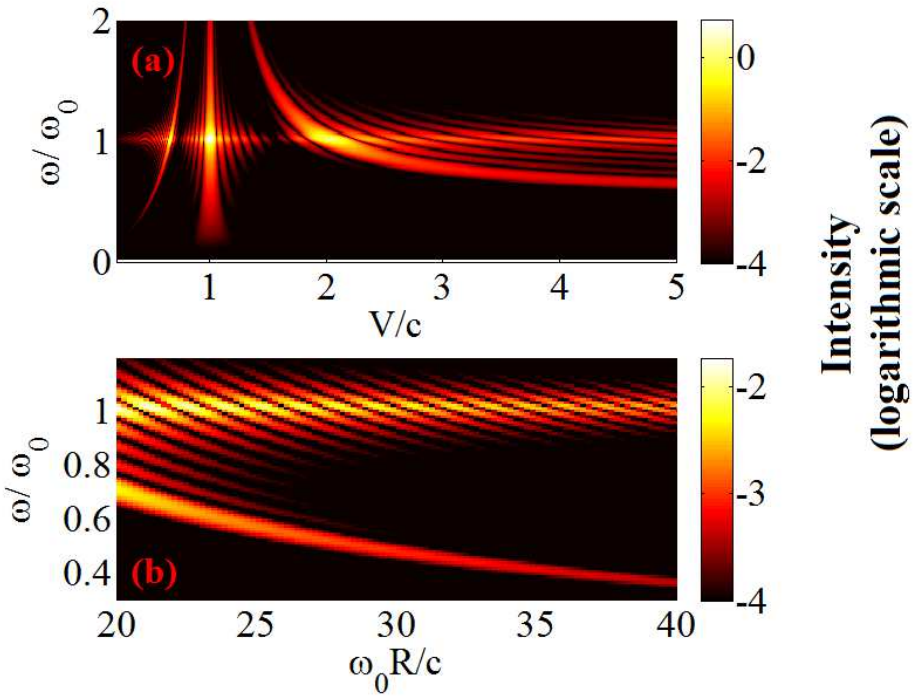

Figure 6.16: (a) Dependence of the radiation spectrum on the normalized propagation speed V of the excitation and the radius of the circle R (b) for $\psi = 2\pi$.

If the excitation propagates at the velocity c, the denominator in (6.30) for the new frequency is equal to 0. In this case the radiation from all points on the circle converges to point ψ simultaneously, the transient process is absent. Accordingly, there will not be any new frequency in the spectrum.

6.7 Analytical solutions of Eqs. (6.15), (6.25) and (6.29).

In this section we provide an analytical solutions of (6.15), (6.25) and (6.29) when $\gamma = 0$. To obtain such an expression we first rearrange the argument of the Θ - function in Eq.(6.15) as $f(t,z) = t - \frac{z}{V} - \frac{Z_m - z}{c}\cos\varphi = t - z/W - \frac{Z_m}{c}\cos\varphi$, where W is the effective velocity defined as:

$$\frac{1}{W} = \frac{1}{V} - \frac{1}{c/\cos\varphi}. \tag{6.32}$$

One can see that W can be interpreted as the velocity of the projection of the cross-section point to the axis parallel to the observation plane in Fig. 6.2(b). Using this parameter we can rewrite the integral for the pulse response in the form:

$$E(t) = \int N(z) h_0\left(t' - \frac{z}{W}\right) dz, \tag{6.33}$$

where $t' = t - \frac{Z_m \cos\varphi}{c}$, and the function $h_0(t)$ denotes the response of a dipole located at $z = 0$ and excited with the excitation in the form of delta-function $\delta(t)$: $h_0(t) = \cos(\omega_0 t)\Theta(t)$.

The integral in (6.33) for the string placed at the interval $[0, Z_m]$ has a different form depending on the sign of W. That is, it can be written as:

$$E(t) = \int_0^{Wt'} N(z) h_0\left(t' - \frac{z}{W}\right) dz \,\text{for}\, W > 0, \tag{6.34}$$

$$E(t) = \int_{Z_m}^{Wt'} N(z) h_0\left(t' - \frac{z}{W}\right) dz \,\text{for}\, W < 0. \tag{6.35}$$

If $W > 0$, the emitting element of the string moves in a positive direction starting from zero, as seen by the observer. In the opposite situation, when $W < 0$, it is seen as moving in a negative direction from Z_m to 0.

Eqs.(6.34)-(6.35) are valid for $0 < t < Z_m/|W|$ (transient regime) assuming $\nu_z = \frac{2\pi}{\Lambda_z}$. In particular for $W > 0$ one can obtain:

$$E(t) = \frac{W}{\omega_0}\sin\left(\omega_0 t'\right) + \frac{W}{W^2\nu_z^2 - \omega_0^2}\left[\nu_z W \sin\left(\nu_z W t'\right) - \omega_0 \sin\left(\omega_0 t'\right)\right]. \tag{6.36}$$

On the other hand, for $W < 0$ we have:

$$E(t) = \frac{W}{\omega_0}\sin\left(\omega_0(t' - \frac{Z_m}{W})\right) + \\ + \frac{W^2\nu_z\sin(\nu_z W t') - \nu_z W^2\sin(\nu_z Z_m)\cos\left[\omega_0(t' - \frac{Z_m}{W})\right]}{\nu_z^2 W^2 - \omega_0^2} - \\ - \frac{\omega_0 W\cos(\nu_z Z_m)\sin\left[\omega_0(t' - \frac{Z_m}{W})\right]}{\nu_z^2 W^2 - \omega_0^2}. \tag{6.37}$$

The last equations contain the oscillating terms at the frequencies ω_0 and $\Omega_1 = \nu_z W$ which coincides with the (6.16).

For $t \geq Z_m/W$, that is when the excitation impulse exits the string, we have:

$$E(t) = \int_0^{Z_m} N(z)\cos\left[\omega_0\left(t' - \frac{z}{W}\right)\right]dz = \\ = \frac{W}{\omega_0}\left[\sin(\omega_0 t') - \sin\left(\omega_0(t' - \frac{Z_m}{W})\right)\right] + \\ \frac{\nu_z W^2\sin(\nu_z Z_m)\cos\left[\omega_0(t' - \frac{Z_m}{W})\right]}{\nu_z^2 W^2 - \omega_0^2} + \\ + \frac{\omega_0 W\cos(\nu_z Z_m)\sin\left[\omega_0(t' - \frac{Z_m}{W})\right] - W\omega_0\sin(\omega_0 t')}{\nu_z^2 W^2 - \omega_0^2}. \tag{6.38}$$

This term describes the oscillations with frequency ω_0 after the transition process stops.

In the case of circular geometry (when radiation is measured at the center), for transient process ($\frac{R}{c} < t < \frac{2\pi R}{V} + \frac{R}{c}$ if $V > c$) one can obtain

$$E(t) = \int_{Vt''/R}^{2\pi} N(\phi)\cos\left[\omega_0\left(t'' - \frac{R\phi}{V}\right)\right]d\phi = -\frac{V}{R\omega_0}\sin\left(\omega_0(t'' - \frac{2\pi R}{V})\right) + \\ + \frac{V^2\nu_\phi\sin(2\pi\nu_\phi)\cos\left[\omega_0(t'' - \frac{2\pi R}{V})\right]}{\nu_\phi^2 V^2 - R^2\omega_0^2} + \frac{R\omega_0 V\cos(2\pi\nu_\phi)\sin\left[\omega_0(t'' - \frac{2\pi R}{V})\right]}{\nu_\phi^2 V^2 - R^2\omega_0^2} - \\ - \frac{V^2\nu_\phi\sin(\Omega_2 t'')}{\nu_\phi^2 V^2 - R^2\omega_0^2}. \tag{6.39}$$

Here $t'' = t - \frac{R}{c}$, $\nu_\phi = \frac{2\pi}{\Lambda_\phi}$. The last expression contains terms oscillating at the frequencies Ω_2 and ω_0. After the transition process ends ($V > c$, $t > \frac{2\pi R}{V} + \frac{R}{c}$), we have:

$$E(t)=\int_0^{2\pi}N(\phi)\cos\left[\omega_0\left(t''-\frac{R\phi}{V}\right)\right]d\phi=\frac{V}{R\omega_0}\left[\sin\left(\omega_0 t''\right)-\sin\left(\omega_0(t''-\frac{2\pi R}{V})\right)\right]+$$
$$+\frac{V^2\nu_\phi\sin(2\pi\nu_\phi)\cos\left[\omega_0(t''-\frac{2\pi R}{V})\right]}{\nu_\phi^2V^2-R^2\omega_0^2}+\frac{R\omega_0V\left[\cos(2\pi\nu_\phi)\sin\left[\omega_0(t''-\frac{2\pi R}{V})\right]-\sin\left(\omega_0 t''\right)\right]}{\nu_\phi^2V^2-R^2\omega_0^2}. \tag{6.40}$$

which contains only terms oscillating at the frequency ω_0.

In the case when radiation is measured at the point ψ at the circle one can obtain for the transient regime ($\frac{R\psi}{V}<t<\frac{R\psi}{V}+\frac{R\psi}{c}$ and if $V>c$):

$$E(t)=\int_{W_0t'''/R}^{2\pi}N(\phi)\cos\left[\omega_0\left(t'''-\frac{R\phi}{W_0}\right)\right]d\phi=-\frac{W_0}{R\omega_0}\sin\left(\omega_0(t'''-\frac{2\pi R}{W_0})\right)+$$
$$+\frac{W_0^2\nu_\phi\sin(2\pi\nu_\phi)\cos\left[\omega_0(t'''-\frac{2\pi R}{W_0})\right]}{\nu_\phi^2W_0^2-R^2\omega_0^2}+\frac{R\omega_0W_0\cos(2\pi\nu_\phi)\sin\left[\omega_0(t'''-\frac{2\pi R}{W_0})\right]}{\nu_\phi^2W_0^2-R^2\omega_0^2}- \tag{6.41}$$
$$-\frac{W_0^2\nu_\phi\sin(\Omega_3t''')}{\nu_\phi^2W_0^2-R^2\omega_0^2}.$$

Here $t'''=t-\frac{R\psi}{c}$ and $\frac{1}{W_0}=\frac{1}{V}-\frac{1}{c}$. This expression contains terms oscillating with the frequencies ω_0 and Ω_3.

6.8 Conclusion

In this Chapter the secondary radiation excited by a moving intersection of a short spectrally broadband pulse and a resonant string made of identical dipoles is discussed for both linear and circular string geometry. In such a situation, Cherenkov radiation naturally appears. In contrast to many other cases where Cherenkov radiation is unstructured and has no clear frequency resonance, the present one demonstrates obvious resonant properties. That is, the response spectrum is centered at the resonant frequency of the dipoles comprising the string. In addition, as our analysis shows, a new Doppler-like frequency appears in the presence of the string density oscillations.

We point out also that the new Doppler-like frequency (Ω_1 in the case of the straight string and Ω_2 or Ω_3 in the circular case) appears in the transient regime, when some of the secondary waves excited by the exciting pulse have not yet reached the observation plane. The dynamics of the radiation after this moment is trivial and contains only decaying oscillations on the resonant frequency ω_0. In the strong-signal regime, when the nonlinearity in the string response becomes significant, the radiation intensity at the new frequency may even be significantly larger than the radiation intensity at the resonant frequency.

The behavior described here can be applied, for instance, to the pulse shape of broad-

band pulses using a rather compact setup. The frequency of new component can be used to determine the velocity of motion of superluminal excitations in a resonant medium and for the determination of a spatial structure of the scattering system by the spectrum of the scattered wave.

Author thanks Prof. Dr. Yu. A. Tolmachev, Dr. M. V. Arkhipov, Dr. I. Babushkin and Dr. I. A. Chekhonin for helpful discussions of the results obtained in this Chapter.

7 Conclusions

In the present thesis, the problems related to the generation of short optical pulses in mode-locked lasers were studied theoretically. The main part of this work explores the physical principles which can be used for the control of the pulse duration and pulse repetition frequency. The possibility of coherent mode-locking - generation of ultrashort pulses in a two-section laser due to coherent interaction of light with gain and absorber was predicted theoretically. Coherent mode-locking technique allows to generate ultrashort optical pulses with spectral width larger than the spectral width of the gain medium. A totally new approach revealing the main features and physical mechanism of this remarkable phenomena based on the area theorem was presented for the first time. The last part involves the prediction of new type of Cherenkov radiation in a resonant medium excited by ultrashort light pulses. The results presented in the five original chapters are in brief the following.

In Chapter 2 a theoretical analysis of the possibility of passive mode-locking in a two-section laser due to the coherent character of the interaction of radiation with amplifying and absorbing media was presented. We considered a simpler and practically more attractive scheme when the gain and absorber sections are spatially separated, but not implemented within the same sample as it was considered in the literature earlier [30–36]. An important feature of coherent mode-locking is the possibility of generation of short optical pulses with spectral bandwidth wider than the bandwidth of the active medium. It was shown that the regime of the coherent mode-locking is self-starting and, hence, the injection of an external seeding pulse is not necessary to achieve this regime. Qualitative consideration of coherent passive mode-locking based on the area theorem of McCall and Hahn and its graphical representation was performed for the first time. The examples of limit cycles of generation were presented. An analytical expression for the self-starting condition of coherent mode-locking was derived. The analysis based on the McCall and Hahn area theorem shows that the parameters of coherent mode-locked pulses depend on the ratio of the transition dipole moment of the absorber to the transition dipole moment of the amplifier. When this ratio increases the duration of the laser pulse decreases. When the ratio is smaller than 1 or greater than 3 a regime with multiple pulses per a cavity round-trip arises. In order to perform numerical experiments for studying coherent mode-locking in a two-section lasers, a numerical model of a laser based on the Maxwell-Bloch equations under the slowly varying envelope approximation was developed. Results of the numerical simulations demonstrated the existence of a coherent mode-locking regime in a two-section laser with ring or linear cavity in a wide range of parameters. It was found that scenarios of coherent mode-locking calculated numerically differ from those previously found in a soliton laser. Unlike the soliton laser considered in [30], which requires a high-Q cavity, in our study the requirement of high-

Q cavity is not necessary for the appearance of coherent mode-locking in two-section lasers. Numerical simulations showed that coherent mode-locking can exist in lasers with cavities having a low Q-factor.

Unfortunately, there is no experimental evidence of coherent mode-locking so far. All existing passively mode-locked laser systems operate in the regimes, in which the pulse spectral bandwidth is smaller than the gain bandwidth of the active medium, so that the medium coherence time T_2 is short compared to the pulse duration. The effect of self-induced transparency (SIT) discovered and explained by MacCall and Hahn more than 40 years ago has a fundamental importance. A practical application of the SIT in photonics and optoelectronics devices has not been found. An implementation of coherent mode-locking in two-section lasers could be the first important practical application of the phenomenon of SIT. By employing the technique of coherent mode-locking, one can use narrowband active media for producing wideband pulses, and, therefore, the bandwidth of the gain medium will not be the ultimate limit on the laser pulse duration.

In Chapters 3 and 4 we used the DDE model to analyze synchronization phenomena in passively mode-locked semiconductor lasers. This model is commonly used to study the nonlinear dynamics of PML semiconductor lasers and can reproduce experimentally observed dynamical regimes. The DDE model is much simpler for numerical simulations than the traveling wave model and allows to obtain some analytical results using asymptotic analysis. In Chapter 3 this model was used to investigate hybrid mode-locking in semiconductor lasers. The phenomenon of the locking of the laser repetition frequency to the frequency of the external modulation known as frequency entrainment was studied. The interval of modulation frequencies where this locking takes place is usually referred to as the locking range. The locking range width was calculated numerically and estimated analytically using a perturbation approach. Results of this analytical estimation are in very good agreement with those obtained from a numerical integration of the model equations. Moreover, we investigated the possibility of hybrid mode-locking when the frequency of the external signal is not only close to pulse repetition rate of the free-running laser (standard case) but twice larger (SHM) or twice smaller (HFM) than this rate. In the standard and SHM cases the locking range has approximately the same width. But in the HFM case the locking range was significantly smaller, strongly nonlinear and asymmetric. This fact is in a qualitative agreement with the experimental data obtained using quantum dot mode-locked lasers. Furthermore, asymmetry of the locking range was also observed in the numerical simulations. This asymmetry is related to the nonlinear dependence of the pulse repetition frequency on the amplitude of the external signal. A similar asymmetry was observed in the experimental study of a quantum dot mode-locked semiconductor laser in Ref. [42].

Another method for stabilization of the pulse repetition frequency in semiconductor lasers is based on the dual mode coherent optical injection into a PML laser. This technique was studied theoretically in Chapter 4 in the framework of the DDE model. We investigated the phenomenon of synchronization of the pulse repetition rate to the difference of the two injected frequencies. Our investigation demonstrated that this synchronization can be achieved in the two following cases. In the first case the frequency separation between two injected modes was changed keeping the master laser frequency

constant (RF locking range). In the second case the master laser frequency was changed keeping the separation frequency constant (optical locking range). We found that the RF locking range width is ten times smaller than the optical locking range width. This fact is in agreement with the recent experimental results obtained with a PML semiconductor quantum dot laser [88]. The asymptotic formulas for the RF and optical locking range in the limit of weak external optical injection and vanishing linewidth enhancement factor were derived. The results obtained from these formula were in good agreement with those obtained by numerical integration of the model equations. Using an asymptotic analysis the dependence of the locking range on the model parameters was investigated. It was shown that both RF and optical locking ranges have quadratic dependence on the absorber relaxation rate, and decrease with the increase of the linear losses, ratio of gain/absorber saturation intensities, and spectral bandwidth of the gain medium.

In Chapter 5 using a DDE model with two time delays the possibility of pulse repetition rate multiplication in a passively mode-locked laser coupled to an external passive cavity was demonstrated numerically. In this case the external cavity acts as a spectral filter which can suppress certain modes in the spectrum of a free-running mode-locked laser. Our numerical simulations indicated the presence of the second (third) harmonic mode-locking regimes when the round-trip of the laser cavity is two (three) times larger than the round-trip time of the external passive cavity. The influence of the phase ϕ describing the relative position of the two frequency combs associated with the active and the passive cavities, respectively, on the system dynamics was studied. Numerical simulations showed that the pulse peak power depends periodically on this phase and that there are transitions between nonperiodic and mode-locking regimes when the phase is changed. Existence of optical bistability between different laser operation regimes was demonstrated numerically. The bistability arises when the linewidth enhancement factors are nonzero in the gain and the saturable absorber sections. At zero or sufficiently small linewidth enhancement factors no bistability was observed in the numerical simulations.

In Chapter 6 the Cherenkov radiation arising when a resonant string of dipoles with spatial harmonic variation of the atomic density is excited by an ultrashort light pulse propagating at superluminal velocity was studied. It was pointed out that this radiation arises in the transient regime and contains both the resonance frequency of the medium and an additional Doppler-like frequency. Analytical expressions for this additional frequency were obtained in the case of the linear and circular string topologies. The additional frequency arises in the linear and nonlinear regimes when pump pulse power is weak and strong, respectively. In the nonlinear regime the intensity of the radiation at the additional frequency is larger than the intensity of radiation at the resonance frequency. Further analysis will be focused on the investigation of superluminal pulse propagation in an optically dense medium that could be accompanied by coherent and collective phenomena [117].

Bibliography

[1] F. J. McClung and R. W. Hellwarth. Giant optical pulsations from ruby. Journal of Applied Physics, 33(3):828–829, 1962.

[2] L. E. Hargrove, R. L. Fork, and M. A. Pollack. Locking of He–Ne laser modes induced by synchronous intracavity modulation. Applied Physics Letters, 5(1): 4–5, 1964.

[3] H. W. Mocker and R. J. Collins. Mode competition and self-locking effects Q-switched Ruby laser. Applied Physics Letters, 7(10):270–273, 1965.

[4] A. J. DeMaria, D. A. Stetser, and H. Heynau. Self mode-locking of lasers with saturable absorbers. Applied Physics Letters, 8(7):174–176, 1966.

[5] D. A. Stetser and A. J. DeMaria. Optical spectra of ultrashort optical pulses generated by mode-locked glass: Nd lasers. Applied Physics Letters, 9(3):118–120, 1966.

[6] T. I. Kuznetsova, V. I. Malyshev, and A. S. Markin. Self-synchronization of axial modes of a laser with saturable filters. Soviet Physics JETP, 25(2):286–291, 1967.

[7] W. H. Glenn, M. J. Brienza, and A. J. DeMaria. Mode locking of an organic dye laser. Applied Physics Letters, 12(2):54–56, 1968.

[8] N. G. Basov, P. G. Kriukov, V. S. Letokhov, and Yu. Senatskii. Generation and amplification of ultrashort optical pulses. IEEE Journal of Quantum Electronics, 4(10):606–609, 1968.

[9] N. G. Basov, P. G. Krjukov, and V. S. Letokhov. Ultra-short light pulses. Optics Technology, 2(3):126–131, 1970.

[10] P. G. Kryukov and V. S. Letokhov. Propagation of a light pulse in a resonantly amplifying (absorbing) medium. Physics-Uspekhi, 12(5):641–672, 1970.

[11] E. P. Ippen, C. V. Shank, and A. Dienes. Passive mode locking of the cw dye laser. Applied Physics Letters, 21(8):348–350, 1972.

[12] A. Yariv. Quantum Electroncs. Wiley, New York, 1975.

[13] O. Svelto and D. C. Hanna. Principles of lasers. Springer, 1976.

[14] S. A. Akhmanov, V. A. Vysloukh, and A. S. Chirkin. Self-action of wave packets in a nonlinear medium and femtosecond laser pulse generation. Physics-Uspekhi, 29(7):642–647, 1986.

[15] J. Herrmann and B. Wilhelmi. Lasers for ultrashort light pulses. North-Holland, Amsterdam, 1987.

[16] S. A. Akhmanov and S. U. Nikitin. Physical Optics. Oxford University Press, 1997.

[17] C. Rulliere. Femtosecond laser pulses. Springer, 1998.

[18] Ya. I. Khanin. Fundamentals of laser dynamics. Cambridge Int. Science Publ., 2006.

[19] J. Diels and W. Rudolph. Ultrashort laser pulse phenomena. Academic press, 2006.

[20] P. G. Kryukov. Ultrashort-pulse lasers. Quantum Electronics, 31(2):95–119, 2001.

[21] P. G. Kryukov. Continuous-wave femtosecond lasers. Physics Uspekhi, 183:897–916, 2013.

[22] D. Bimberg, M. Grundmann, and N. N. Ledentsov. Quantum dot heterostructures. John Wiley Chichester, 1999.

[23] D. Bimberg. Quantum dot based nanophotonics and nanoelectronics. Electronics Letters, 44:168–171, 2008.

[24] E. U. Rafailov, M. A. Cataluna, and E. Avrutin. Ultrafast Lasers Based on Quantum-dot Structures: Physics and Devices. WILEY-VCH Verlag, 2011.

[25] E. U. Rafailov, M. A. Cataluna, and W. Sibett. Mode-locked quantum-dot lasers. Nature Photonics, 1:395–401, 2007.

[26] D. Arsenijević, M. Kleinert, and D. Bimberg. Passive mode-locking of quantum-dot lasers. IEEE Photonics Journal, 6:0700306, 2013.

[27] S. L. McCall and E. L. Hahn. Self-induced transparency by pulsed coherent light. Physical Review Letters, 18(21):908, 1967.

[28] S. L. McCall and E. L. Hahn. Self-induced transparency. Physical Review, 183(2): 457, 1969.

[29] L. Allen and J. H. Eberly. Optical resonance and two-level atoms. Wiley, New York, 1975.

[30] V. V. Kozlov. Self-induced transparency soliton laser via coherent mode locking. Physical Review A, 56:1607–1612, 1997.

[31] V. V. Kozlov. Self-induced-transparency soliton laser. JETP Lett., 69(12):906–911, 1999.

[32] C. R. Menyuk and M. A. Talukder. Self-induced transparency mode-locking of quantum cascade lasers. Physical Review Letters, 102(2):023903, 2009.

[33] M. A. Talukder and C. R. Menyuk. Analytical and computational study of self-induced transparency mode locking in quantum cascade lasers. Physical Review A, 79(6):063841, 2009.

[34] V. V. Kozlov, N. N. Rosanov, and S. Wabnitz. Obtaining single-cycle pulses from a mode-locked laser. Physical Review A, 84(5):053810, 2011.

[35] V. V. Kozlov and N. N. Rosanov. Single-cycle-pulse passively-mode-locked laser with inhomogeneously broadened active medium. Physical Review A, 87(4): 043836, 2013.

[36] V. V. Kozlov and N. N. Rosanov. Numerical modeling of generation of few-cycle pulses in a mode-locked laser. Optics and Spectroscopy, 114(5):798–803, 2013.

[37] D. Bimberg. Quantum dots for lasers, amplifiers and computing. Journal of Physics D: Applied Physics, 38(13):2055, 2005.

[38] M. Kuntz, G. Fiol, M. Lämmlin, D. Bimberg, M. G. Thompson, K. T. Tan, C. Marinelli, A. Wonfor, R. Sellin, and R. V. Penty. Direct modulation and mode locking of 1.3 μm quantum dot lasers. New Journal of Physics, 6(1):181, 2004.

[39] R. Kaiser and B. Huttl. Monolithic 40-GHz mode-locked MQW DBR lasers for high-speed optical communication systems. IEEE Journal of Selected Topics in Quantum Electronics, 13(1):125–135, 2007.

[40] M. Kuntz, G. Fiol, M. Laemmlin, C. Meuer, and D. Bimberg. High-speed mode-locked quantum-dot lasers and optical amplifiers. Proceedings of the IEEE, 95(9): 1767–1778, 2007.

[41] M. G. Thompson, A. R. Rae, M. Xia, R. V. Penty, and I. H. White. InGaAs quantum-dot mode-locked laser diodes. IEEE Journal of Selected Topics in Quantum Electronics, 15(3):661–672, 2009.

[42] G. Fiol, D. Arsenijević, D. Bimberg, A. G. Vladimirov, M. Wolfrum, E. A. Viktorov, and P. Mandel. Hybrid mode-locking in a 40 GHz monolithic quantum dot laser. Applied Physics Letters, 96(1):011104–011104, 2010.

[43] W. Lee and P. J. Delfyett. Dual-mode injection locking of two independent mode-locked semiconductor lasers. Electronics Letters, 40(19):1182–1183, 2004.

[44] T. Habruseva, N. Rebrova, S. P. Hegarty, and G. Huyet. Quantum-dot mode-locked lasers with dual mode optical injection. In SPIE Photonics Europe, pages 77200Z–77200Z. International Society for Optics and Photonics, 2010.

[45] T. Habruseva, G. Huyet, and S. P. Hegarty. Dynamics of quantum-dot mode-locked lasers with optical injection. IEEE Journal of Selected Topics in Quantum Electronics, 17(5):1272–1279, 2011.

[46] T. Habruseva, N. Rebrova, S. P. Hegarty, and G. Huyet. Mode-locked semiconductor lasers with optical injection. In Quantum Dot Devices, pages 65–91. Springer, 2012.

[47] E. Sooudi, S. Sygletos, A. D. Ellis, G. Huyet, J. G. McInerney, F. Lelarge, K. Merghem, R. Rosales, A. Martinez, and A. Ramdane. Optical frequency comb generation using dual-mode injection-locking of quantum-dash mode-locked lasers: properties and applications. IEEE Journal of Quantum Electronics, 48(10):1327–1338, 2012.

[48] N. K. Berger, B. Levit, S. Atkins, and B. Fischer. Repetition-rate multiplication of optical pulses using uniform fiber Bragg gratings. Optics Communications, 221 (4):331–335, 2003.

[49] H. Takara, S. Kawanishi, and M. Saruwatari. High-repetition-rate optical pulse generation by using chirped optical pulses. Electronics Letters, 34:792–793, 1998.

[50] S. Arahira, S. Kutsuzawa, Y. Matsui, D. Kunimatsu, and Y. Ogawa. Repetition-frequency multiplication of mode-locked pulses using fiber dispersion. Journal of Lightwave Technology, 16(3):405–410, 1998.

[51] S. Longhi, M. Marano, P. Laporta, O. Svelto, M. Belmonte, B. Agogliati, L. Arcangeli, V. Pruneri, M. N. Zervas, and M. Ibsen. 40-GHz pulse-train generation at 1.5 μm with a chirped fiber grating as a frequency multiplier. Optics Letters, 25(19):1481–1483, 2000.

[52] J. Azana and M. A. Muriel. Technique for multiplying the repetition rates of periodic trains of pulses by means of a temporal self-imaging effect in chirped fiber gratings. Optics Letters, 24:1672–1674, 1999.

[53] T. Sizer. Increase in laser repetition rate by spectral selection. IEEE Journal of Quantum Electronics, 25(1):97–103, 1989.

[54] U. Keller, W. H. Knox, and H. Roskos. Coupled-cavity resonant passive mode-locked Ti: sapphire laser. Optics Letters, 15(23):1377–1379, 1990.

[55] D. K. Serkland, G. D. Bartolini, W. L. Kath, P. Kumar, and A. V. Sahakian. Rate multiplication of a 59-GHz soliton source at 1550 nm. Journal of Lightwave Technology, 16(4):670–677, 1998.

[56] K. Yiannopoulos, K. Vyrsokinos, D. Tsiokos, E. Kehayas, N. Pleros, G. Theophilopoulos, T. Houbavlis, G. Guekos, and H. Avramopoulos. Pulse repetition frequency multiplication with spectral selection in Fabry-Perot filters. IEEE Journal of Quantum Electronics, 40(2):157–165, 2004.

[57] M. S. Kirchner, D. A. Braje, T. M. Fortier, A. M. Weiner, L. Hollberg, and S. A. Diddams. Generation of 20 GHz, sub-40 fs pulses at 960 nm via repetition-rate multiplication. Optics Letters, 34(7):872–874, 2009.

[58] P. A. Cherenkov. Vidimoe svechenie chistykh zhidkostei pod deistviem γ-radiatsii (Visible glow of pure liquids under γ-irradiation). Dokl. Akad. Nauk SSSR, 2(10): 451, 1934.

[59] P. A. Čerenkov. Visible radiation produced by electrons moving in a medium with velocities exceeding that of light. Physical Review, 52(4):378, 1937.

[60] I. E. Tamm and I. M. Frank. Kogerentnoe izluchenie bystrogo elektrona v srede (The coherent radiation of a fast electron in a medium). Dokl. Akad. Nauk SSSR, 14:107, 1937.

[61] J. V. Jelley. Cerenkov Radiation and Its Applications. Pergamon Press, London, 1958.

[62] L. D. Landau, E. M. Liftshitz, and L. P. Pitaevskii. Electrodynamics of Continuous Media. Pergamon Press, New York, 1984.

[63] I. M. Frank. A conceptual history of the Vavilov-Cherenkov radiation. Physics-Uspekhi, 27(5):385–395, 1984.

[64] B. M. Bolotovskii. Vavilov-Cherenkov radiation: its discovery and application. Physics-Uspekhi, 52(11):1099–1110, 2009.

[65] I. M. Frank. Effect Dopplera v prelomlyaushei srede. Izv. Akad. Nauk SSSR, Ser. Fiz, 6(3):3–31, 1942.

[66] B. M. Bolotovskii and V. L. Ginzburg. The Vavilov-Cerenkov effect and the Doppler effect in the motion of sources with superluminal velocity in vacuum. Physics-Uspekhi, 15(2):184–192, 1972.

[67] B. M. Bolotovskii and A. V. Serov. Radiation of superluminal sources in empty space. Physics-Uspekhi, 48(9):903–915, 2005.

[68] G. A. Askar'yan. Cerenkov and transition radiation from electromagnetic waves. Sov. Phys. JETP, 15:943–946, 1962.

[69] D. A. Kirzhnits and V. N. Sazonov. Superluminal motions and the special relativity theory. In Einstein Collection, pages 84–111. Nauka, Moskow, 1974.

[70] B. M. Bolotovskiĭ and V. P. Bykov. Radiation by charges moving faster than light. Physics-Uspekhi, 33(6):477–487, 1990.

[71] E. Recami, F. Fontana, and R. Garavaglia. Special relativity and superluminal motions: a discussion of some recent experiments. International Journal of Modern Physics A, 15(18):2793–2812, 2000.

[72] E. Recami. Superluminal motions? A bird's-eye view of the experimental situation. Foundations of Physics, 31(7):1119–1135, 2001.

[73] E. Recami, M. Zamboni-Rached, K. Z. Nóbrega, C. A. Dartora, and F. Hernandez. On the localized superluminal solutions to the Maxwell equations. IEEE Journal of Selected Topics in Quantum Electronics, 9(1):59–73, 2003.

[74] G. B. Malykin and E. A. Romanets. Superluminal motion (review). Optics and Spectroscopy, 112(6):920–934, 2012.

[75] L. You, J. Mostowski, J. Cooper, and R. Shuker. Cone emission from laser-pumped two-level atoms. Physical Review A, 44:R6998–R7001, Dec 1991.

[76] L. You, J. Mostowski, and J. Cooper. Cone emission from laser-pumped two-level atoms. II. analytical model studies. Physical Review A, 46:2925–2938, 1992.

[77] W. Chalupczak, W. Gawlik, and J. Zachorowski. Conical emission as cooperative fluorescence. Physical Review A, 49:R2227–R2230, 1994.

[78] B. D. Paul, J. Cooper, A. Gallagher, and M. G. Raymer. Theory of optical near-resonant cone emission in atomic vapor. Physical Review A, 66:063816, 2002.

[79] V. Vaičaitis and E. Gaižauskas. Conical fluorescence emission from sodium vapor excited with tunable femtosecond light pulses. Physical Review A, 75:033808, 2007.

[80] E. M. Belenov and P. P. Vasil'ev. Coherent effects in generation of ultrashort light pulses in a semiconductor injection laser. Zh. Eksp. Teor. Fiz., 96(5):1629–1637, 1989.

[81] P. P. Vasil'ev. Role of a high gain of the medium in superradiance generation and in observation of coherent effects in semiconductor lasers. Quantum Electronics, 29(10):842, 1999.

[82] D. L. Boiko and P. P. Vasilev. Superradiance dynamics in semiconductor laser diode structures. Optics Express, 20(9):9501–9515, 2012.

[83] A. Capua, O. Karni, G. Eisenstein, and J. P. Reithmaier. Electron wavefunction probing in room-temperature semiconductors: direct observation of rabi oscillations and self-induced transparency. arXiv preprint arXiv:1210.6803, 2012.

[84] O. Karni, A. Capua, G. Eisenstein, V. Sichkovskyi, V. Ivanov, and J. P. Reithmaier. Rabi oscillations and self-induced transparency in InAs/InP quantum dot semiconductor optical amplifier operating at room temperature. Optics Express, 21(22):26786–26796, 2013.

[85] H. Choi, V. Gkortsas, L. Diehl, D. Bour, S. Corzine, J. Zhu, G. Höfler, F. Capasso, F. Kärtner, and T. B. Norris. Ultrafast Rabi flopping and coherent pulse propagation in a quantum cascade laser. Nature Photonics, 4(10):706–710, 2010.

[86] A. Gordon, C. Y Wang, L. Diehl, F. X. Kärtner, A. Belyanin, D. Bour, S. Corzine, G. Höfler, H. C. Liu, and H. Schneider. Multimode regimes in quantum cascade lasers: From coherent instabilities to spatial hole burning. Physical Review A, 77 (5):053804, 2008.

[87] R. Arkhipov, A. Pimenov, M. Radziunas, D. Rachinskii, A. G. Vladimirov, D. Arsenijević, H. Schmeckebier, and D. Bimberg. Hybrid mode-locking in semiconductor lasers: simulations, analysis and experiments. IEEE Journal of Selected Topics in Quantum Electronics, 19:100208–1100208, 2013.

[88] R. M. Arkhipov, A. Pimenov, M. Radziunas, T. Habruseva, G. Huyet, and A. G. Vladimirov. Semiconductor mode-locked lasers with coherent dual mode optical injection: simulations, analysis and experiment. Under preparation.

[89] U. Keller. Recent developments in compact ultrafast lasers. Nature, 424(6950): 831–838, 2003.

[90] U. Keller, K. J. Weingarten, F. X. Kartner, D. Kopf, B. Braun, I. D. Jung, R. Fluck, C. Honninger, N. Matuschek, and J. Aus der Au. Semiconductor saturable absorber mirrors (SESAM's) for femtosecond to nanosecond pulse generation in solid-state lasers. IEEE Journal of Selected Topics in Quantum Electronics, 2(3):435–453, 1996.

[91] P. G. Kryukov and V. S. Letokhov. Fluctuation mechanism of ultrashort pulse generation by laser with saturable absorber. IEEE Journal of Quantum Electronics, QE-8:766–782, 1972.

[92] V. S. Letokhov. Generation of ultrashort light pulses in a laser with a nonlinear absorber. Sov. Phys. JETP, 28:562, 1969.

[93] H. Haus. Theory of mode locking with a slow saturable absorber. IEEE Journal of Quantum Electronics, 11(9):736–746, 1975.

[94] H. A. Haus. Theory of mode locking with a fast saturable absorber. Journal of Applied Physics, 46(7):3049–3058, 1975.

[95] H. A. Haus. Mode-locking of lasers. IEEE Journal of Selected Topics in Quantum Electronics, 6(6):1173–1185, 2000.

[96] G. H. C. New. Pulse evolution in mode-locked quasi-continuous lasers. IEEE Journal of Quantum Electronics, 10(2):115–124, 1974.

[97] F. X. Kartner, I. D. Jung, and U. Keller. Soliton mode-locking with saturable absorbers. IEEE Journal of Selected Topics in Quantum Electronics, 2(3):540–556, 1996.

[98] F. X. Kurtner, J. A. der Au, and U. Keller. Mode-locking with slow and fast saturable absorbers-What's the difference? IEEE Journal of Selected Topics in Quantum Electronics, 4(2):159–168, 1998.

[99] R. Paschotta and U. Keller. Passive mode locking with slow saturable absorbers. Applied Physics B, 73(7):653–662, 2001.

[100] A. G. Vladimirov, D. Turaev, and G. Kozyreff. Delay differential equations for mode-locked semiconductor lasers. Optics Letters, 29(11):1221–1223, 2004.

[101] A. G. Vladimirov and D. V. Turaev. A new model for a mode-locked semiconductor laser. Radiophysics and Quantum Electronics, 47(10-11):769–776, 2004.

[102] A. G. Vladimirov and D. Turaev. Model for passive mode locking in semiconductor lasers. Physical Review A, 72(3):033808, 2005.

[103] A. G. Vladimirov, U. Bandelow, G. Fiol, D. Arsenijević, M. Kleinert, D. Bimberg, A. Pimenov, and D. Rachinskii. Dynamical regimes in a monolithic passively mode-locked quantum dot laser. JOSA B, 27(10):2102–2109, 2010.

[104] D. Rachinskii A. G. Vladimirov and M. Wolfrum. Modeling of passively mode-locked semiconductor lasers (in Nonlinear Laser Dynamics: From Quantum Dots to Cryptography). Wiley-VCH, 2012.

[105] N. Rebrova, G. Huyet, D. Rachinskii, and A. G. Vladimirov. Optically injected mode-locked laser. Physical Review E, 83:066202, 2011.

[106] N. G. Basov, R. V. Ambartsumyan, V. S. Zuev, P. G. Kryukov, and V. S. Letokhov. Nonlinear amplification of light pulses. Sov. Phys. JETP, 23(1):16–22, 1966.

[107] R. V. Ambartsumyan, N. G. Basov, V. Zuev, P. G. Kryukov, and V. S. Letokhov. Short-pulse Q-switched laser with variable pulse length. IEEE Journal of Quantum Electronics, 2(9):436–441, 1966.

[108] A. N. Oraevsky. Superluminal waves in amplifying media. Physics-Uspekhi, 41 (12):1199–1209, 1998.

[109] N. N. Rozanov. Superluminal localized structures of electromagnetic radiation. Physics-Uspekhi, 48(2):167–171, 2005.

[110] I. A. Poluéktov, Yu. M. Popov, and V. S. Roitberg. Coherent effects in the propagation of ultrashort light pulses in resonant media. Part I (review). Soviet Journal of Quantum Electronics, 4(4):423, 1974.

[111] D. V. Novitsky. Ultrashort pulses in an inhomogeneously broadened two-level medium: soliton formation and inelastic collisions. Journal of Physics B: Atomic, Molecular and Optical Physics, 47(9):095401, 2014.

[112] R. M. Arkhipov, I. Babushkin, and M. V. Arkhipov. Self-induced transparency self-starting stable coherent mode-locking in a two-section laser. Under preparation.

[113] M. D. Crisp. Propagation of small-area pulses of coherent light through a resonant medium. Physical Review A, 1(6):1604, 1970.

[114] J. E. Rothenberg, D. Grischkowsky, and A. C. Balant. Observation of the formation of the zero-area pulse. Physical Review Letters, 53:552–555, 1984.

[115] E. Lippert and J. D. Macomber. Dynamics during spectroscopic transitions: basic concepts. Springer Verlag, 1995.

[116] P. A. Apanasevich. Basics of the theory of interaction of light with matter. Minsk, Nauka i Tehnika, 1977.

[117] M. V. Arkhipov, R. M. Arkhipov, and S. A. Pulkin. Effects of inversionless lasing in two-level media from the point of view of specificities of the spatiotemporal propagation dynamics of radiation. Optics and Spectroscopy, 114(6):831–837, 2013.

[118] R. M. Arkhipov, M. V. Arkhipov, V. S. Egorov, I. A. Chekhonin, M. A. Chekhonin, and S. N. Bagaev. Effective excitation of polaritonic modes in optical cavity with resonant inversionless medium. Nauchno-Tekhnicheskii Zh. Priborostroenie, 7:42–48, 2012.

[119] P. Siddons. Light propagation through atomic vapours. Journal of Physics B Atomic Molecular Physics, 47(9):3001, 2014.

[120] D. Bimberg, G. Fiol, M. Kuntz, C. Meuer, M. Laemmlin, N. N. Ledentsov, and A. R. Kovsh. High speed nanophotonic devices based on quantum dots. Physica Status Solidi (a), 203(14):3523–3532, 2006.

[121] M. G. Thompson, C. Marinelli, K. T. Tan, K. A. Williams, R. V. Penty, I. H. White, I. N. Kaiander, R. L. Sellin, D. Bimberg, and D. Kang. 10 GHz hybrid mode-locking of monolithic InGaAs quantum dot lasers. Electronics Letters, 39 (15):1121–1122, 2003.

[122] H. Schmeckebier, G. Fiol, C. Meuer, D. Arsenijević, and D. Bimberg. Complete pulse characterization of quantum dot mode-locked lasers suitable for optical communication up to 160 Gbit/s. Optics Express, 18(4):3415–3425, 2010.

[123] E. A. Viktorov, P. Mandel, A. G. Vladimirov, and U. Bandelow. Model for mode locking in quantum dot lasers. Applied Physics Letters, 88(20):201102–201102, 2006.

[124] E. A. Viktorov, T. Erneux, P. Mandel, T. Piwonski, G. Madden, J. Pulka, G. Huyet, and J. Houlihan. Recovery time scales in a reversed-biased quantum dot absorber. Applied Physics Letters, 94(26):263502–263502, 2009.

[125] V. I. Arnold and M. Levi. Geometrical methods in the theory of ordinary differential equations. Springer-Verlag New York, 1983.

[126] C. M. Bender and S. A. Orszag. Multiple-scale analysis. In Advanced Mathematical Methods for Scientists and Engineers I. Springer, 1999.

[127] N. Rebrova, T. Habruseva, G. Huyet, and S. P. Hegarty. Stabilization of a passively mode-locked laser by continuous wave optical injection. Applied Physics Letters, 97(10):101105–101105, 2010.

[128] T. Habruseva, N. Rebrova, S. P. Hegarty, and G. Huyet. Quantum-dot mode-locked lasers with dual mode optical injection. In SPIE Photonics Europe, pages 77200Z–77200Z. International Society for Optics and Photonics, 2010.

[129] R. L. Fork, B. Greene, and C. V. Shank. Generation of optical pulses shorter than 0.1 psec by colliding pulse mode locking. Applied Physics Letters, 38(9):671–672, 1981.

[130] J. Azana and M. A. Muriel. Technique for multiplying the repetition rates of periodic trains of pulses by means of a temporal self-imaging effect in chirped fiber gratings. Optics Letters, 24(23):1672–1674, 1999.

[131] W. Sibbett, A. A. Lagatsky, and C. Brown. The development and application of femtosecond laser systems. Optics Express, 20(7):6989–7001, 2012.

[132] D. A. Braje, M. S. Kirchner, S. Osterman, T. Fortier, and S. A. Diddams. Astronomical spectrograph calibration with broad-spectrum frequency combs. The European Physical Journal D, 48(1):57–66, 2008.

[133] Z. Jiang, C. Huang, D Leaird, and A. M. Weiner. Optical arbitrary waveform processing of more than 100 spectral comb lines. Nature Photonics, 1(8):463–467, 2007.

[134] T. Steinmetz, T. Wilken, C. Araujo-Hauck, R. Holzwarth, T. W. Hänsch, L. Pasquini, A. Manescau, S. D'Odorico, M. T. Murphy, and T. Kentischer. Laser frequency combs for astronomical observations. Science, 321(5894):1335–1337, 2008.

[135] P. W. Smith. Mode selection in lasers. Proceedings of the IEEE, 60(4):422–440, 1972.

[136] M. Tani, O. Morikawa, S. Matsuura, and M. Hangyo. Generation of terahertz radiation by photomixing with dual-and multiple-mode lasers. Semiconductor Science and Technology, 20(7):S151, 2005.

[137] L. A. Coldren and S. W. Corsine. Diode Lasers and Photonic Integrated Circuitss. New York:Wile, 1995.

[138] B. Corbett and D. McDonald. Single longitudinal mode ridge waveguide 1.3 μm Fabry-Perot laser by modal perturbation. Electronics Letters, 31(25):2181–2182, 1995.

[139] S. O'Brien, A. Amann, R. Fehse, S. Osborne, E. P. O'Reilly, and J. M. Rondinelli. Spectral manipulation in Fabry-Perot lasers: perturbative inverse scattering approach. JOSA B, 23(6):1046–1056, 2006.

[140] S. Osborne, S. O'Brien, K. Buckley, R. Fehse, A. Amann, J. Patchell, B. Kelly, D. R. Jones, J. O'Gorman, and E. P. O'Reilly. Design of single-mode and two-color fabry–pérot lasers with patterned refractive index. IEEE Journal of Selected Topics in Quantum Electronics, 13(5):1157–1163, 2007.

[141] S. O'Brien, S. Osborne, D. Bitauld, N. Brandonisio, A. Amann, R. Phelan, B. Kelly, and J. O'Gorman. Optical synthesis of terahertz and millimeter-wave frequencies with discrete mode diode lasers. IEEE Transactions on Microwave Theory and Techniques, 58(11):3083–3087, 2010.

[142] A. F. Glova. Phase locking of optically coupled lasers. Quantum Electronics, 33 (4):283–306, 2003.

[143] D. A. Usikov R. Z. Sagdeev and G. M. Zaslavsky. Nonlinear Physics: from the Pendulum to Turbulence and Chaos. Chur: Harwood, 2008.

[144] H. Haken. Laser light dynamics. North-Holland Pub. Co, 1985.

[145] H. E. Hagemeier and S. R. Robinson. Field properties of multiple coherently combined lasers. Applied Optics, 18(3):270–280, 1979.

[146] M. B. Spencer, J. Lamb, and E. Willis. Theory of two coupled lasers. Physical Review A, 5(2):893, 1972.

[147] E. A. Avrutin, J. H. Marsh, and E. L. Portnoi. Monolithic and multi-gigahertz mode-locked semiconductor lasers: Constructions, experiments, models and applications. In IEE Proceedings-Optoelectronics, volume 147, pages 251–278. IET, 2000.

[148] A. G. Vladimirov, A. S. Pimenov, and D. Rachinskii. Numerical study of dynamical regimes in a monolithic passively mode-locked semiconductor laser. IEEE Journal of Quantum Electronics, 45(5):462–468, 2009.

[149] H. Gibbs. Optical bistability: controlling light with light. Elsevier, 1985.

[150] A. N. Oraevsky. Resonant properties of a system comprising a cavity mode and two-level atoms and frequency bistability. Quantum Electronics, 29(11):975–978, 1999.

[151] T. Erneux, E. A. Viktorov, B. Kelleher, D. Goulding, P. Hegarty, S, and G. Huyet. Optically injected quantum-dot lasers. Optics Letters, 35(7):937–939, 2010.

[152] P. Glas, R. Müller, and A. Klehr. Bistability, self-sustained oscillations, and irregular operation of a gaas laser coupled to an external resonator. Optics Communications, 47(4):297–301, 1983.

[153] S. Bauer, O. Brox, J. Kreissl, B. Sartorius, M. Radziunas, J. Sieber, H. J. Wünsche, and F. Henneberger. Nonlinear dynamics of semiconductor lasers with active optical feedback. Physical Review E, 69(1):016206, 2004.

[154] N. K. Dutta, G. P. Agrawal, and M. W. Focht. Bistability in coupled cavity semiconductor lasers. Applied Physics Letters, 44(1):30–32, 1984.

[155] A. Pimenov, E. A. Viktorov, S. P. Hegarty, T. Habruseva, G. Huyet, D. Rachinskii, and A. G. Vladimirov. Bistability and hysteresis in an optically injected two-section semiconductor laser. Physical Review E, 89:052903, 2014.

[156] M. Born and E. Wolf. Principles of Optics: Electromagnetic Theory of Propagation, Interference and Diffraction of Light. Cambridge University Press, 6 edition, 1997.

[157] B. M. Bolotovskii. Teoriya effekta Vavilova-Cherenkova. Uspekhi Fizicheskikh Nauk, 75(10):295–350, 1961.

[158] A. P. Kobzev. The mechanism of Vavilov-Cherenkov radiation. Physics of Particles and Nuclei, 41(3):452–470, 2010.

[159] L. J. Wang, A. Kuzmich, and A. Dogariu. Gain-assisted superluminal light propagation. Nature, 406(6793):277–279, 2000.

[160] L. F. Mironenko, V. O. Rapoport, and D. S. Kotik. Vavilov-Čerenkov and Doppler effects from a superluminal radio-beam spot in the lower ionosphere. Radiophysics and Quantum Electronics, 42(8):651–659, 1999.

[161] K. T. McDonald. Radiation from a superluminal source. arXiv preprint physics/0003053, 2000.

[162] E. G. Doil'nitsyna and A. V. Tyukhtin. Energetic characteristics of radiation of oscillating dipoles travelling in some dispersive and moving media. Int. J. Geomagn. Aeron, 6, 2006.

[163] Z. Yu. Chen, J. Li, Q. Peng, J. Li, J. Dan, and S. Chen. Experimental study of radio-frequency Cherenkov radiation by a line focused laser pulse obliquely incident on a wire target. Chinese Journal of Physics, 49(3), 2011.

[164] M. V. Arkhipov, R. M. Arkhipov, and Yu. A. Tolmachev. Emission of a spatially modulated resonant medium excited with superluminal velocity. Optics and Spectroscopy, 112(2):243–248, 2012.

[165] P. K. A. Wai, H. H. Chen, and Y. C. Lee. Radiations by "solitons" at the zero group-dispersion wavelength of single-mode optical fibers. Physical Review A, 41: 426–439, Jan 1990.

[166] V. I. Karpman. Radiation by solitons due to higher-order dispersion. Physical Review E, 47:2073–2082, 1993.

[167] V. I. Karpman. Stationary and radiating dark solitons of the third order nonlinear Schrödinger equation. Physics Letters A, 181(3):211 – 215, 1993.

[168] N. Akhmediev and M. Karlsson. Cherenkov radiation emitted by solitons in optical fibers. Physical Review A, 51:2602–2607, 1995.

[169] A. Demircan, Sh. Amiranashvili, and G. Steinmeyer. Controlling light by light with an optical event horizon. Physical Review Letters, 106:163901, 2011.

[170] A. Demircan, S. Amiranashvili, C. Brée, C. Mahnke, F. Mitschke, and G. Steinmeyer. Rogue events in the group velocity horizon. Scientific Reports, 2, 2012.

[171] Driben R. and I. Babushkin. Accelerated rogue waves generated by soliton fusion at the advanced stage of supercontinuum formation in photonic-crystal fibers. Optics Letters, 37(24):5157–5159, 2012.

[172] A. V. Yulin, R. Driben, B. A. Malomed, and D. V. Skryabin. Soliton interaction mediated by cascaded four wave mixing with dispersive waves. Optics Express, 21 (12):14481–14486, 2013.

[173] C. Luo, M. Ibanescu, S. G. Johnson, and J. D. Joannopoulos. Cerenkov radiation in photonic crystals. Science, 299:368–371, 2003.

[174] M. I. Bakunov, A. V. Maslov, and S. B. Bodrov. Cherenkov radiation of terahertz surface plasmon polaritons from a superluminal optical spot. Physical Review B, 72(19):195336, 2005.

[175] C. D'Amico, A. Houard, M. Franco, B. Prade, A. Mysyrowicz, A. Couairon, and V. T. Tikhonchuk. Conical forward THz emission from femtosecond-laser-beam filamentation in air. Physical Review Letters, 98(23):235002, 2007.

[176] Q. L. Hu, S. B. Liu, and W. Li. Cherenkov radiation of a fast electron in ultrashort intense laser plasmas. Physics of Plasmas, 14(12):123101, 2007.

[177] M. I. Bakunov, S. B. Bodrov, A. V. Maslov, and M. Hangyo. Theory of terahertz generation in a slab of electro-optic material using an ultrashort laser pulse focused to a line. Physical Review B, 76:085346, 2007.

[178] J. Q. Yao, P. X. Liu, D. G. Xu, Y. J. Lv, and D. Lv. THz source based on optical Cherenkov radiation. Science China Information Sciences, 55(1):27–34, 2012.

[179] G. Burlak. Spectrum of cherenkov radiation in dispersive metamaterials with negative refraction index. Progress In Electromagnetics Research, 132:149–158, 2012.

[180] S. Liu, P. Zhang, W. Liu, S. Gong, R. Zhong, and Y. Zhang. Surface polariton Cherenkov light radiation source. Physical Review Letters, 109:153902, 2012.

[181] D. E. Fernandes, S. I. Maslovski, and M. G. Silveirinha. Cherenkov emission in a nanowire material. Physical Review B, 85:155107, 2012.

[182] V. L. Ginzburg. Pulsars (theoretical concepts). Physics-Uspekhi, 14(2):83–103, 1971.

[183] V. L. Ginzburg and V. V. Zheleznyakov. On the pulsar emission mechanisms. Annual Review of Astronomy and Astrophysics, 13(1):511–535, 1975.

[184] J. Salo, J. Fagerholm, A. T. Friberg, and M. M. Salomaa. Unified description of nondiffracting X and Y waves. Physical Review E, 62(3):4261, 2000.

[185] S. J. Smith and E. M. Purcell. Visible light from localized surface charges moving across a grating. Physical Review, 92:1069–1069, 1953.

[186] S. Longhi, M. Marano, M. Belmonte, and P. Laporta. Superluminal pulse propagation in linear and nonlinear photonic grating structures. IEEE Journal of Selected Topics in Quantum Electronics, 9(1):4–16, 2003.

[187] J. R. Zurita-Sánchez, H. Abundis-Patiño, J, and P. Halevi. Pulse propagation through a slab with time-periodic dielectric function ε (t). Optics Express, 20(5): 5586–5600, 2012.

[188] K. J. Woods, J. E. Walsh, R. E. Stoner, H. G. Kirk, and R. C. Fernow. Forward directed Smith-Purcell radiation from relativistic electrons. Physical Review Letters, 74:3808–3811, May 1995.

[189] D. V. Skryabin and A. V. Gorbach. Colloquium: Looking at a soliton through the prism of optical supercontinuum. Reviews of Modern Physics, 82(2):1287–1299, 2010.

[190] L. Novotny and N. van Hulst. Antennas for light. Nature Photonics, 5(2):83–90, 2011.

[191] P. Biagioni, J. Huang, and B. Hecht. Nanoantennas for visible and infrared radiation. Reports on Progress in Physics, 75(2):024402, 2012.

[192] J. Sun, E. Timurdogan, A. Yaacobi, E. S. Hosseini, and M. R. Watts. Large-scale nanophotonic phased array. Nature, 493(7431):195–199, Jan 2013.

[193] C. Feuillet-Palma, Y. Todorov, A. Vasanelli, and C. Sirtori. Strong near field enhancement in THz nano-antenna arrays. Scientific Reports, 3, 2013.

[194] A. Hartmann, Y. Ducommun, K. Leifer, and E. Kapon. Structure and optical properties of semiconductor quantum nanostructures self-formed in inverted tetrahedral pyramids. Journal of Physics: Condensed Matter, 11(31):5901, 1999.

[195] M. Felici, P. Gallo, A. Mohan, B. Dwir, A. Rudra, and E. Kapon. Site-controlled InGaAs quantum dots with tunable emission energy. Small, 5(8):938–943, 2009.

[196] A. Mohan, M. Felici, P. Gallo, B. Dwir, A. Rudra, J. Faist, and E. Kapon. Polarization-entangled photons produced with high-symmetry site-controlled quantum dots. Nature Photonics, 4(5):302–306, 2010.

[197] G. Juska, V. Dimastrodonato, L. O. Mereni, A. Gocalinska, and E. Pelucchi. Towards quantum-dot arrays of entangled photon emitters. Nature Photonics, 7 (7):527–531, 2013.

[198] R. M. Arkhipov, I. Babushkin, M. K. Lebedev, Yu. A. Tolmachev, and M. V. Arkhipov. Transient Cherenkov radiation from an inhomogeneous string excited by an ultrashort laser pulse at superluminal velocity. Physical Review A, 89(4): 043811, 2014.

[199] R. Klaus. Table-top sources of ultrashort THz pulses. Reports on Progress in Physics, 70(10):1597–1632, 2007.

[200] M. D. Thomson, M. Kress, T. Löffler, and H. G. Roskos. Broadband THz emission from gas plasmas induced by femtosecond optical pulses: From fundamentals to applications. Laser Photonics Review, 1(4):349–368, 2007.

[201] K. Y. Kim, J. H. Glownia, A. J. Taylor, and G. Rodriguez. Terahertz emission from ultrafast ionizing air in symmetry-broken laser fields. Optics Express, 15(8): 4577–4584, 2007.

[202] K. Y. Kim, A. J. Taylor, J. H. Glownia, and G. Rodriguez. Coherent control of terahertz supercontinuum generation in ultrafast laser-gas interactions. Nature Photonics, 2(10):605–609, Oct 2008.

[203] I. Babushkin, S. Skupin, and J. Herrmann. Generation of terahertz radiation from ionizing two-color laser pulses in ar filled metallic hollow waveguides. Optics Express, 18(9):9658–9663, 2010.

[204] I. Babushkin, W. Kuehn, C. Köhler, S. Skupin, L. Bergé, K. Reimann, M. Woerner, J. Herrmann, and T. Elsaesser. Ultrafast spatiotemporal dynamics of terahertz generation by ionizing two-color femtosecond pulses in gases. Physical Review Letters, 105(5):053903, 2010.

[205] C. Köhler, E. Cabrera-Granado, I. Babushkin, L. Bergé, J. Herrmann, and S. Skupin. Directionality of terahertz emission from photoinduced gas plasmas. Optics Letters, 36(16):3166–3168, 2011.

[206] I. Babushkin, S. Skupin, A. Husakou, C Köhler, E. Cabrera-Granado, L Bergé, and J. Herrmann. Tailoring terahertz radiation by controlling tunnel photoionization events in gases. New Journal of Physics, 13(12):123029, 2011.

[207] L. Bergé, S. Skupin, C. Köhler, I. Babushkin, and J. Herrmann. 3D numerical simulations of THz generation by two-color laser filaments. Physical Review Letters, 110:073901, 2013.

[208] K. Iga, F. Koyama, and S. Kinoshita. Surface emitting semiconductor lasers. IEEE Journal of Quantum Electronics, 24:1845–1855, 1988.

[209] T. E. Sale. Vertical cavity surface emitting lasers. Research Studies Press Ltd, New-York, 1995.

[210] W. W. Chow, K. D. Choquette, M. H. Crawfod, and Kevin L. Lear. Design, fabrication, and visibl vertical-cavity surface-emitting lasers. IEEE Journal of Quantum Electronics, 33(10):1810–1824, 1997.

[211] N A. Loiko and I. V. Babushkin. Competition of orthogonally polarized transverse fourier modes in a vcsel. Journal of Optics B: Quantum and Semiclassical Optics, 3(2):S234, 2001.

[212] I. V. Babushkin, N. A. Loiko, and T. Ackemann. Secondary bifurcations and transverse standing-wave patterns in anisotropic microcavity lasers close to the first laser threshold. Physical Review A, 67(1):013813, 2003.

[213] I. V. Babushkin, N. A. Loiko, and T. Ackemann. Eigenmodes and symmetry selection mechanisms in circular large-aperture vertical-cavity surface-emitting lasers. Physical Review E, 69:066205, 2004.

[214] M. Schulz-Ruhtenberg, I. V. Babushkin, N. A. Loiko, T. Ackemann, and K. F. Huang. Transverse patterns and length-scale selection in vertical-cavity surface-emitting lasers with a large square aperture. Applied Physics B, 81(7):945–953, 2005.

[215] M. Schulz-Ruhtenberg, I. V. Babushkin, N. A. Loiko, K. F. Huang, and T. Ackemann. Polarization properties in the transition from below to above lasing threshold in broad-area vertical-cavity surface-emitting lasers. Physical Review A, 81(2): 023819, 2010.

[216] J. Xiao, Z. Wang, and Z. Xu. Area evolution of a few-cycle pulse laser in a two-level-atom medium. Physical Review A, 65(3):031402, 2002.

[217] X. Jian, W. Zhong-yang, and X. Zhi-zhan. Spectrum of a few-cycle laser pulse propagating in a two-level atom medium. Chinese Physics, 10(10):941, 2001.

[218] K. J. Vahala. Optical microcavities. Nature, 424(6950):839–846, 2003.

[219] V. S. Ilchenko and A. B. Matsko. Optical resonators with whispering-gallery modes-part II: applications. IEEE Journal of Selected Topics in Quantum Electronics, 12(1):15–32, 2006.

[220] A. N. Oraevsky. Whispering-gallery waves. Quantum Electronics, 32(5):377–400, 2002.

List of publications

Refereed publications

[B1] R. M. Arkhipov, A. Amann, A. G. Vladimirov, Pulse repetition-frequency multiplication in a coupled cavity passively mode-locked semiconductor lasers, Appl. Phys. B, **118**, 539 (2015).

[B2] M. V. Arkhipov, R. M. Arkhipov, A. A. Shimko, I. Babushkin, Mode-Locking in a laser with a coherent absorber, JETP Letters, **101**, 232 (2015).

[B3] R. M. Arkhipov, M. V. Arkhipov, I. V. Babushkin, On coherent mode-locking in a two-section laser, JETP Letters, **101**, 149 (2015).

[B4] R. Arkhipov, I. Babushkin, M. K. Lebedev, Yu. A. Tolmachev, and M. V. Arkhipov, Transient Cherenkov radiation from an inhomogeneous string excited by an ultrashort laser pulse at superluminal velocity, Phys. Rev. A, **89**, 043811 (2014).

[B5] S. Joshi, C. Calò, N. Chimot, M. Radziunas, R. Arkhipov, S. Barbet, A. Accard, A. Ramdane, and F. Lelarge, Quantum dash based single section mode locked lasers for photonic integrated circuits, Opt. Express **22**, 1742 (2014).

[B6] R. Arkhipov, A. Pimenov, M. Radziunas, A. G. Vladimirov, D. Arsenjević, D. Rachinskii, H. Schmeckebier, and D. Bimberg, Hybrid mode-locking in edge-emitting semiconductor lasers: Simulations, analysis and experiments, IEEE J. Sel. Top. Quantum Electron., **19**, 1100208/1 (2013).

[B7] M. V. Arkhipov, R. M. Arkhipov, and S. A. Pulkin, Effects of inversionless lasing in two-level media from the point of view of specificities of the spatiotemporal propagation dynamics of radiation, Optics and Spectroscopy **114(6)**, 831 (2013).

[B8] M. V. Arkhipov, R. M. Arkhipov, and Yu. A. Tolmachev, Emission of a spatially modulated resonant medium excited with superluminal velocity, Optics and Spectroscopy, **112(2)**, 243 (2012).

[B9] R. M. Arkhipov, M. V. Arkhipov, V. S. Egorov, I. A. Chekhonin, M. A. Chekhonin, and S. N. Bagaev, Effective excitation of polaritonic modes in optical cavity with resonant inversionless medium, Nauchno-Tekhnicheskii Zh. Priborostroenie (in Russian) **7**, 42 (2012)

[B10] R. M. Arkhipov, I. Babushkin, and M. V. Arkhipov Self-induced transparency self-starting stable coherent mode-locking in a two-section laser, under preparation.

[B11] R. Arkhipov, A. Pimenov, M. Radziunas, T. Habruseva, G. Huyet, and A. G. Vladimirov, Semiconductor mode-locked lasers with coherent dual mode optical injection: simulations, analysis and experiment, under preparation.

Conference Proceedings

[B12] R. M. Arkhipov, M. Radziunas, A. G. Vladimirov, Theoretical analysis of the influence of external periodic forcing on nonlinear dynamics of passively mode-locked semiconductor lasers, in: Proceedings of the XIV school seminar "Wave Phenomena in Inhomogeneous Media (Waves-2014)" (in Russian), Moscow, Russia, May 26-31, 2014, Lomonosov Moscow State University, Faculty of Physics, Section 9 "Nonlinear dynamics and Information systems", pp.3-6, 2014.

[B13] R. M. Arkhipov, M. V. Arkhipov, Mode-locking in two-section and single- section lasers due to coherent interaction of light and matter in the gain and absorbing media, in: Proceedings of the XIV school seminar "Wave Phenomena in Inhomogeneous Media (Waves-2014)" (in Russian), Moscow, Russia, May 26-31, 2014, Lomonosov Moscow State University, Faculty of Physics, Section 6 "Coherent and Nonlinear Optics", pp. 43-45, 2014.

[B14] R. M. Arkhipov, I. Babushkin, M. V. Arkhipov, Yu. A. Tolmachev, Spectral and temporal characteristics of a transient Cherenkov radiation from a periodic resonant medium excited by an ultrashort laser pulse at superluminal velocity, in: SPIE OPTO, International Society for Optics and Photonics, p. 89840S, 2014.

[B15] R. Arkhipov, A. Pimenov, M. Radziunas, A. G. Vladimirov, Theoretical Analysis of Hybrid and Dual Mode Injected Semiconductor Mode-Locked Lasers, Proc. of the International Nano-Optoelectronics Workshop, August 19-30, 2013, Cargese, France (Corsika), pp B3-B4.

[B16] R. M. Arkhipov, I. Babushkin, M. V. Arkhipov, Yu. A. Tolmachev Spectral and Temporal Characteristics of Radiation from a Periodic Resonant Medium Excited at the Superluminal Velocity, in: Proceedings of the conference ICONO/LAT-2013, June 18-22, Moscow, Russia, Section "Diffractive Optics and Nanophotonics", pp. 14-15, invited talk, 2013.

[B17] R. M. Arkhipov, M. Radziunas, A. G. Vladimirov, Numerical Simulation of Passively Mode-Locked Semiconductor Lasers under Dual Mode Optical Injection Regime, in:

Proceedings of the conference ICONO/LAT-2013, June 18-22, Moscow, Russia, Section "Solid-State Lasers, Materials and Applications", pp. 111-112, 2013.

[B18] R. M. Arkhipov, M. Radziunas, A. G. Vladimirov, Numerical simulations of the influence of injection of biharmonic radiation on the regime of passive mode-locking in semiconductor laser, in: Proceedings of the seminar "Waves-2013" (in Russian), Moscow, Russia, May 20-25, 2013, Lomonosov Moscow State University, Faculty of Physics, Section 5 "Nonlinear dynamics and Information systems", pp. 9-12, 2013

[B19] M. V. Arkhipov, R. M. Arkhipov, S. N. Bagaev, V. S. Egorov, I. A. Chekhonin, M. A. Chekhonin, Ultrafast laser beam scanning by resonant light-induced spacial periodic structures, in: Proceedings of the seminar "Waves-2013" (in Russian), Moscow, Russia, May 20-25, 2013, Lomonosov Moscow State University, Faculty of Physics, Section 6 "Coherent and Nonlinear Optics", pp. 6-9, 2013.

A: Derivation of the system of Maxwell-Bloch equations for a distributed laser model

In the present Appendix as in Refs. [12, 16, 18] we will apply density matrix formalism to derive the system of Maxwell-Bloch equations (2.8)-(2.12) describing the behavior of slow envelopes of the electric field, polarization and population difference of a two-level system. We assume that laser medium contains only two-levels. As a result the density matrix is reduced to 2×2 matrix with elements $\rho_{11}, \rho_{12}, \rho_{21}, \rho_{22}$.

According to Ref. [12] the system of equations determined the evolution of nonlinear density matrix element and population difference including time relaxations of the polarization T_2 and population inversion T_1 has the following form:

$$\frac{d\rho_{21}(t)}{dt} = -\frac{\rho_{21}(t)}{T_2} - i\omega_{12}\rho_{21} + \frac{id_{12}}{\hbar}\Delta\rho(t)E(t). \tag{1}$$

$$\frac{d}{dt}\Delta\rho(t) = -\frac{\Delta\rho(t) - \Delta\rho_0}{T_1} + \frac{2id_{12}E(t)}{\hbar}(\rho_{21} - \rho_{21}^*). \tag{2}$$

Here $\Delta\rho = \rho_{11} - \rho_{22}$ population difference between ground level and excited level of two-level system, $\Delta\rho_0$ is the population difference in the absence of the electric field, ω_{12} is medium transition frequency, d_{12} is transition dipole moment, and $E(t)$ the electric field.

The ensemble average $\langle d \rangle$ of the dipole moment of the atom that is induced by field $E(t)$ is given by [12]:

$$\langle d \rangle = d_{12}(\rho_{12} + \rho_{21}). \tag{3}$$

Represent electric field and nondiagonal element of the density matrix in the form:

$$E(t) = A(t)\cos(\omega t) + B(t)\sin(\omega t). \tag{4}$$

$$\rho_{21} = \sigma_{21}(t)e^{-i\omega t} = (P_c(t) + iP_s(t))e^{-i\omega t}. \tag{5}$$

Here $A(t)$, $B(t)$ are the slow envelopes of the electric field, σ_{21} is the slow envelope of the density matrix element ρ_{21}, P_c and P_s are the real and imaginary part of σ_{21} respectively. By substituting (4)-(5) in (1)-(2) and keeping only terms with $e^{-i\omega t}$ time dependence and neglecting the terms having $e^{-i2\omega t}$ and $e^{i2\omega t}$ time dependence, we obtain

the following system of optical Bloch equations:

$$\frac{d}{dt}P_c(t) = -\frac{P_c}{T_2} - \Delta\omega P_s(t) - \frac{d_{12}}{2\hbar}\Delta\rho(t)B(t), \tag{6}$$

$$\frac{d}{dt}P_s(t) = -\frac{P_s}{T_2} + \Delta\omega P_c(t) + \frac{d_{12}}{2\hbar}\Delta\rho(t)A(t), \tag{7}$$

$$\frac{d}{dt}\Delta\rho(t) = -\frac{\Delta\rho(t) - \Delta\rho_0}{T_1} - \frac{2d_{12}}{\hbar}\left(A(t)P_s(t) - B(z,t)P_c(t)\right). \tag{8}$$

Here $\Delta\omega$ is the frequency detuning between optical the frequency of optical field ω and medium resonance frequency ω_{12}.

Medium polarization is related with P_c, P_s, the concentration of two-level atoms N_0 by the following relation [12]:

$$P = N_0\langle d\rangle = N_0 d_{12}(\rho_{12} + \rho_{21}) = 2N_0 d_{12}(P_c\cos(\omega t) + P_s\sin(\omega t)). \tag{9}$$

Below we will derive the system of equations describing the propagation of the electric field in two-level medium.

We take the scalar field and the medium polarization in the form:

$$E(z,t) = A(z,t)\cos(\omega t - kz) + B(z,t)\sin(\omega t - kz). \tag{10}$$

$$P(z,t) = 2N_0 d_{12}(P_c(z,t)\cos(\omega t - kz) + P_s(z,t)\sin(\omega t - kz)). \tag{11}$$

Here k is the wave number. Equations (10)-(11) are substituted into the wave equation:

$$\frac{\partial^2 E(z,t)}{\partial t^2} - c^2\frac{\partial^2 E(z,t)}{\partial z^2} = -\frac{4\pi}{c^2}\frac{\partial^2 P(z,t)}{\partial t^2}. \tag{12}$$

In the obtained expressions we used the following approximation (slow varying envelope approximations): $\frac{\partial F}{\partial t} << \omega_0 F$, $\frac{\partial F}{\partial z} << kF$, $\frac{\partial^2 F}{\partial t^2} << \omega_0\frac{\partial F}{\partial t}$, $\frac{\partial^2 F}{\partial z^2} << k\frac{\partial F}{\partial z}$, where $F = A, B, P_c, P_c$ [12]. Using these approximations we obtain the system of Maxwell equations describing the evolution of slow envelopes of the electric field in two-level medium:

$$\frac{\partial A(z,t)}{\partial t} + c\frac{\partial A(z,t)}{\partial z} = -4\pi\omega d_{12}N_0 P_s(z,t), \tag{13}$$

$$\frac{\partial B(z,t)}{\partial t} + c\frac{\partial B(z,t)}{\partial z} = 4\pi\omega d_{12}N_0 P_c(z,t). \tag{14}$$

The coupled set of equations (6)-(8) with the equations (13)-(14) is our final system of equations which we used for developing of the numerical model of a two-section laser.

B: Symbols and conventions

$\mathrm{Re}z$	Real part of z
$\mathrm{Im}z$	Imaginary part of z
$\Theta(x)$	Heaviside function $\Theta(x) = \begin{cases} 1, & \text{if} x > 0 \\ 0, & \text{if} x < 0 \end{cases}$
c	velocity of light in vacuum, $c = 2.99792458 \cdot 10^{10}\,\mathrm{cm/s}$
$\hbar$	Planck constant, $\hbar = 1.054571726 \cdot 10^{-27}\,\mathrm{erg\cdot\ s}$
ω	carrier frequency of the optical field
ω_{12}	center frequency
$\Delta\omega$	frequency detuning of the radiation field ω from transition frequency ω_{12}, $\Delta\omega = \omega - \omega_{12}$
ω_0	resonance frequency
τ_p	pulse duration
E_0	electric field amplitude
Ω_R	Rabi frequency, $\Omega_R = \frac{d_{12}E_0}{\hbar}$
d_{12}	transition dipole moment
T_1	population difference relaxation time
T_2	polarization relaxation time
$\Delta\rho_0$	population difference at equilibrium
T	cold cavity round-trip time
α_g	linewidth enhancement factor in the gain section
α_q	linewidth enhancement factor in the saturable absorber
γ	spectral filtering bandwidth
κ	non-resonant field intensity attenuation factor per cavity round-trip
g_0	pump parameter
q_0	unsaturated absorption
γ_g	gain relaxation rate
γ_q	saturable absorber relaxation rate
s	ratio of gain/absorber saturation intensities
f_P	pulse repetition frequency of mode-locked laser
f_M	modulation frequency

SIT	Self-Induced Transparency
QCL	Quantum Cascade Laser
DDE	Delay Differential Equation
VM	Voltage Modulation
SA	Saturable Absorber
HML	Hybrid Mode-Locking
SHM	Second-Harmonic Modulation
HFM	Half-Frequency Modulation

Acknowledgments

I would like to thank my scientific supervisors Dr. A. G. Vladimirov, Dr. M. Radziunas and PD Dr. U. Bandelow for giving me the opportunity to work on an exciting topic modeling passively mode-locked lasers.

I am deeply grateful Dr. M. V. Arkhipov for helpful discussions of all results presented in this thesis.

I would also like to thank Dr. I. Babushkin who helped me with the interpretation of some results of Chapters 2 and 6 and whose advise helped improve these Chapters.

I am very grateful to Dr. A. Pimenov for helpful discussions on the modeling of mode-locked lasers.

I am very thankful to Prof. Dr. Yu. A. Tolmachev for the helpful discussions about the superluminal motions and Cherenkov radiation.

Furthermore, I would to thank Dr. I. A. Chekhonin for helpful discussion of the results of Chapter 2 devoted to coherent mode-locking and for introducing me to the physics of coherent phenomena when I was a master student.

I would like to thank Dr. S. Amiranashvili for helpful discussions of some results obtained in the thesis.

I am very thankful to Prof. A. Ramdane, Dr. A. Martinez, Dr. F. Lelarge, Dr. R. Rosales, C. Calò, Dr. G. Huyet, Dr. T. Habruseva, D. Arsenjević, and H. Schmeckebier for helpful discussions of experimental results obtained with mode-locked lasers.

I am very thankful to Dr. A. Amann for helpful discussions of the results of Chapter 5.

Finally, I would like to thank all members of the research group “Laser Dynamics” at WIAS for the brilliant work atmosphere.

Selbständigkeitserklärung

Hiermit erkläre ich, die Dissertation selbstständig und nur unter Verwendung der angegebenen Hilfen und Hilfsmittel angefertigt zu haben.

Ich habe mich anderwärts nicht um einen Doktorgrad beworben und besitze keinen entsprechenden Doktorgrad.

Ich erkläre die Kenntnisnahme der dem Verfahren zugrunde liegenden Promotionsordnung der Mathematisch-Naturwissenschaftlichen Fakultät der Humboldt-Universität zu Berlin.

Berlin, den 23.09.2014 Rostislav Arkhipov